Testing Gravitational Physics on Large and Small Scales



Dina Traykova

Supervisors: Prof Pedro G. Ferreira and Dr Emilio Bellini

Department of Physics

Sub-department of Astrophysics

University of Oxford

Thesis submitted for the degree of

Doctor of Philosophy

July, 2021

Declaration

I declare that the contents of this thesis are mainly based on original research, with references to all previous works when appropriate, and that I have not previously submitted any part of it for consideration for any other degree or qualification.

Chapter 2 is based on work done in collaboration with Carlos García-García, Emilio Bellini, Pedro G. Ferreira and Miguel Zumalacárregui and published in PRD [1]. Chapter 3 - based on work with Emilio Bellini, Pedro G. Ferreira, Carlos García-García, Johannes Noller and Miguel Zumalacárregui, accepted for publication in PRD [2]. Chapter 4 - on a paper in collaboration with Emilio Bellini and Pedro G. Ferreira, published in JCAP [3]. Chapter 5 is based on work with Katy Clough, Thomas Helfer, Pedro G. Ferreira, Emanuele Berti and Lam Hui, submitted for publication in PRD [4].

Dina Traykova

July, 2021

Acknowledgements

First and foremost, I would like to thank my supervisors Pedro Ferreira, Emilio Bellini and Katy Clough for their incredible patience, support and guidance they have given me throughout my DPhil, and without the invaluable help, encouragement and advice from whom this thesis would not exist. I would also like to give special thanks Carlos García-García for all his help, advice and friendship, and also for very kindly agreeing to give me comments on this draft.

I also thank my collaborators, Miguel Zumalacárregiu, Johannes Noller, Thomas Helfer, Emanuele Berti, Lam Hui and everyone in the GRChombo collaboration for sharing their wealth of knowledge with me and always having extremely useful comments and suggestions. Thanks as well to my friends and colleagues in the Oxford Astrophysics department for the many nice conversations about science, life, the Universe and everything over a cup of coffee or a pint of ale.

Huge thanks to my amazing family, especially to mum, dad, my grandparents and my sister for tirelessly cheering me on along the way and all the care and support they have given me throughout the years. Thanks as well to all my friends, especially Tom, Mazzy, Char, Jack, Becky, Hanlin, Irene, Andrea and Tom dW for fun conversations and good company, always being up for an adventure, sending me treats, making me coffee, and being very understanding and cheering me up when I have been stressed and tired.

Abstract

Einstein's theory of General Relativity has long been considered the standard theory of gravity, as it provides us with an extremely good description of how objects interact gravitationally at all scales. The Standard Model of cosmology, based on General Relativity, provides an excellent description of how astrophysical objects and matter interact. However, it requires the addition of two exotic ingredients: cold dark matter and dark energy, in order to correctly account for some observational phenomena, such as the accelerated expansion of the universe and the flat galaxy rotation curves that we observe. This has prompted the exploration of alternative theories of gravity, which can account for these observations without invoking the need for one or both of these exotic types of matter.

In this thesis we build different tools for testing such alternatives at large and small scales. The majority of the work focuses on testing beyond General Relativity models on large scales using cosmological probes. We derive theory-informed priors, find suitable forms for the time evolution of the functions parametrising specific sets of extensions to General Relativity, and put constraints on their parameters from cosmological data. In the last chapter we shift the focus to small scales, where we numerically confirm an expression for the drag force on a moving black hole. This result can be used to test a model of dark matter using the gravitational wave signal from a black hole binary merger. With the growing amount of gravitational wave data, testing alternative theories of gravity in this way is becoming an increasingly popular area of research. The future direction of this work is to apply the methods we commonly use for testing gravity on large scales, as described in this work, to test beyond General Relativity theories on small scales using gravitational wave data.

Notation

Throughout this work we use the following notation and conventions:

- We set the speed of light to unity, $c = 1$; The reduced Planck mass, $M_P^2 = 1/8\pi G$, is often also set to 1.
- Throughout we use the metric signature: $(-,+,+,+)$.
- Greek indices (e.g. μ, $\nu = 0, \ldots 3$) denote four-dimensional spacetime vectors and tensors; Latin script is used for three-dimensional ones (e.g. i, $j = 1, 2, 3$).
- Where no summation sign is present, the Einstein summation convention is implied.
- The Minkowski spacetime metric throughout this work will be denoted as $\eta_{\mu\nu} = \mathrm{Diag}(-1, 1, 1, 1)$, whereas $g_{\mu\nu}$ is the full four-dimensional symmetric metric tensor.
- We use dots (e.g. $\dot{H}$) to denote a derivative with respect to physical time t and primes (e.g. H') for derivatives with respect to conformal time τ.
- The Hubble parameter in physical and conformal time is written as $H = \dot{a}/a$ and $\mathcal{H} = a'/a$, respectively.
- Total derivatives are denoted by d, partial derivatives by ∂ and covariant ones by ∇. Commas and semicolons denote partial and covariant derivatives, respectively (e.g. for a scalar field ϕ we can write $\partial_\mu \phi \equiv \phi_{,\mu}$ and $\nabla_\mu \phi \equiv \phi;\mu$).

Contents

Abstract iv

Notation v

List of Figures x

List of Tables xv

1 Introduction 1

1.1 General Relativity . . . 1

1.1.1 Why go beyond? . . . 2

1.1.2 Theoretical framework . . . 4

1.2 Modified Gravity . . . 6

1.2.1 Landscape . . . 6

1.2.2 Scalar-tensor gravity . . . 7

1.2.3 The Horndeski class . . . 7

1.3 The $3+1$ decomposition . . . 8

1.4 Parametrising Horndeski . . . 10

1.4.1 Effective field theory . . . 10

1.4.2 Stability Conditions . . . 11

1.4.3 Minimal set of parameters . . . 11

1.5 Cosmology . . . 13

1.5.1 Background expansion . . . 13

1.5.2 Distance measures . . . 14

1.5.3 Perturbation theory . . . 15

1.5.4 Growth of matter overdensities . . . 16
1.5.5 Correlation functions and power spectra . . . 17
1.6 Probing gravity on large scales . . . 18
1.6.1 Time evolution of DE/MG functions . . . 18
1.6.2 Including theoretical priors . . . 19
1.6.3 Cosmological Data . . . 20
1.7 Parameter Inference . . . 23
1.8 Gravity on small scales . . . 24
1.8.1 Probing physics with gravitational waves . . . 24
1.8.2 Numerical solutions in strong gravity . . . 25

2 Quintessence priors **27**
2.1 Introduction . . . 27
2.2 Quintessence . . . 30
2.3 Establishing Physical Priors . . . 34
2.4 Parameterising quintessence . . . 38
2.5 Results . . . 40
2.6 Comparison with current data . . . 47
2.7 Discussion . . . 50

3 Shift-symmetric Horndeski priors **52**
3.1 Introduction . . . 53
3.2 Shift-Symmetric Scalar-Tensor Gravity . . . 55
3.3 Establishing Physical Priors . . . 59
3.4 Approximating the time dependence of w and $\alpha_{\rm B}$ . . . 63
3.5 Results . . . 67
3.6 Comparison with current data . . . 72
3.7 Discussion . . . 77

4 Beyond Horndeski **80**
4.1 Introduction . . . 80
4.2 Theoretical framework . . . 82

4.2.1 Background . . . 86
4.2.2 Stability conditions . . . 87
4.2.3 Recent implications from GW170817 and GRB 170817A . . . 88
4.2.4 Perturbations . . . 89
4.3 Phenomenology of beyond Horndeski theories . . . 91
4.3.1 The quasi-static approximation . . . 91
4.3.2 Matter power spectrum . . . 96
4.3.3 The growth rate of structure . . . 97
4.3.4 CMB power spectra . . . 99
4.4 Results . . . 101
4.4.1 Method . . . 101
4.4.2 Datasets . . . 102
4.4.3 Constraints on the beyond Horndeski parameters . . . 105
4.5 Discussion . . . 110

5 Dynamical friction from scalar dark matter 112
5.1 Introduction . . . 112
5.2 Framework . . . 117
5.2.1 Background metric . . . 117
5.2.2 Scalar field evolution . . . 119
5.2.3 Diagnostic quantities . . . 120
5.2.4 Numerical methods . . . 123
5.3 Background on dynamical friction . . . 124
5.4 Results . . . 129
5.5 Discussion . . . 135

6 Discussion and conclusions 137
6.1 Conclusions . . . 137
6.2 Future Directions . . . 140

References 142

Appendices 173

A Shift-symmetric Horndeski priors **173**

A.1 Discontinuities for models crossing $\alpha_{\rm B} = 2$ 173

B Beyond Horndeski **177**

B.1 Implementing the equations into `hi_class` 177

C Dynamical friction from scalar dark matter **181**

C.1 Code validation 181

C.1.1 Code validation and coordinate choice 181

C.1.2 Convergence testing and error estimation 183

C.2 Large and small β approximations 186

C.3 Real scalar field 187

List of Figures

1.1 Relevant experiments for testing GR at different scales. 2

1.2 The left panel illustrates the principle foliation of spacetime into three-dimensional hypersurfaces. On the right is the definition of the lapse function, α, and shift vector β^i on two adjacent hypersurfaces. 9

1.3 A diagram summarising the approach for constructing theoretical priors for scalar-tensor theories. 20

2.1 A schematic of the loci of *freezing* and *thawing* models on the (w_0, w_a) plane. 32

2.2 Effect of the initial conditions on the dynamics of the model $U \propto \phi^{-2}$ with initial conditions $\phi_i = M_P$ and $\phi_i' \equiv \mathrm{d}\phi/\mathrm{d}\tau|_i = H_0$. 33

2.3 w_0-w_a distributions for the Monomial (left panel), EFT (central panel) and Modulus (right panel). 36

2.4 Freezing behaviour for inverse power-law potentials (monomial quintessence $N < 0$). 37

2.5 Distribution of the maximum relative error of the observables for each Quintessence model compared to its fit in the $w_0 - w_a$ plane, i.e. $\tilde{\Delta}\mathcal{O} \equiv |\mathcal{O}(\mathrm{Fit})/\mathcal{O}(\mathrm{Quintessence}) - 1|$. 42

2.6 Density plots, one for each Quintessence model, showing the time evolution of the relative difference between $w(a)$ obtained from the original realisation and after fitting it in the $w_0 - w_a$ plane. 42

2.7 For each model, we show the exact (blue solid lines) probability distribution of w_0 normalised to 1 for $w_0 = -1$. The approximate analytic model defined in Eq. (2.13) is also shown (orange dashed lines). 43

2.8 For each model, Axion excluded since it can be parametrised solely in terms of w_0, we show the conditional probability distribution of w_a given specific values of w_0 (coloured solid lines). 44

2.9 Distributions of the observables obtained integrating the field equations of motion (solid black line) compared to those obtained sampling from our parametrisation. 45

2.10 Distribution of $\{w_0, w_a\}$ for the CMB+BAO+RSD+SN combined datasets and the theoretical priors. 48

2.11 Constraints on $\{w_0, w_a\}$ for the four different quintessence models from the CMB+BAO+RSD+SN combined datasets and including the priors. 50

3.1 Distributions of the parameters of the action for the $\Lambda = 0$ (green) and $\Lambda \neq 0$ (blue) variants of the shift-symmetric model, where we have fixed $d_{01} = -1$. 57

3.2 Distributions of the parameters of $\dot{\phi}_0^2/\Lambda_2^2$ and $\ddot{\phi}_0/\Lambda_3^3$, where ϕ_0 is the amplitude of the scalar field today. 58

3.3 Distributions of the parameters given different ways of sampling. 61

3.4 The time evolution of w (left) and $\alpha_{\rm B}$ (right) for two representative models and their approximate fits using the parametrisations we choose. 64

3.5 Probability distributions of the $\{w_0, w_a, \hat{\alpha}_{\rm B}, m\}$ parameters obtained minimising Eq. (3.14) as explained in Sections 3.4 and 3.5. 65

3.6 Diagram summarising the method presented in Section 3.4 that we use for determining the correct evolution functions of the model, $w(a)$ and $\alpha_{\rm B}(a)$ and the set of coefficients $\{w_0, w_a, \hat{\alpha}_{\rm B}, m\}$ that best fit the observables computed from the Lagrangian. 66

3.7 Left panel: distribution of the maximum relative deviation between the observables computed from the theory ($\mathcal{O}(c_{01}, c_{02}, d_{01}, d_{02})$) and the parametrisation ($\mathcal{O}(w_0, w_a, \hat{\alpha}_{\rm B}, m)$) at $z < 10$ for each fit. Right panel: distribution of the relative error between the $D_A(z_{\rm rec})$ computed from the theory and the parametrisation for each fit. 68

3.8 Approximate fit to the probability distribution of the $\{X_1, X_2, X_3, X_4\}$ for the $\Lambda = 0$ model. In black, the contours from the original set of parameters transformed by Eq. (3.16). In green, those obtained from a multivariate Gaussian distribution. 69

3.9 Probability density distributions of the $\{w_0, w_a, \hat{\alpha}_{\rm B}, m\}$ parameters for the $\Lambda = 0$ (lower left) and $\Lambda \neq 0$ (upper right) shift-symmetric theories studied. We compare the exact distributions obtained fitting the observables with those obtained sampling from the new Gaussianised space $\{X_1,\ X_2,\ X_3\, X_4\}$ and transforming back using Eq. (3.16). 70

3.10 Probability density distributions of the $\{w_0, w_a, \hat{\alpha}_{\rm B}, m\}$ parameters for the $\Lambda = 0$ (lower left) and $\Lambda \neq 0$ (upper right) shift-symmetric theories studied. We compare the exact distributions obtained fitting the observables with those obtained sampling from the new Gaussianised space $\{X_1,\ X_2,\ X_3\, X_4\}$ and transforming back using Eq. (3.16). 71

3.11 Comparison between data and the prior distributions for the two shift-symmetric variants we have considered, $\Lambda = 0$ (lower left corner) and $\Lambda \neq 0$ (upper right). 73

3.12 Probability distributions of Ω_Λ from the analysis with data alone (grey solid line), our priors (green solid line). 75

4.1 The evolution of μ_Ψ (left) and μ_Φ (right) as a function of scale factor. . . . 93

4.2 The ratio between the two terms contributing to the deviation from GR in the QSA equations, Eqs. (4.31) and (4.31) for 4 different values of $\hat{\alpha}_{\rm H}$ as a function of scale factor. 95

4.3 The effects of $\hat{\alpha}_{\rm H}$ on the matter power spectrum at $z = 0$. On the right graph we show the relative difference between the models we are considering and a fiducial ΛCDM model. 96

4.4 Relative difference of the growth rate, f, between 4 models with different $\hat{\alpha}_{\rm H}$ and ΛCDM. 98

4.5 On the left is the relative difference of the CMB lensing potential for different values of $\hat{\alpha}_{\rm H}$ and ΛCDM. And on the right is the deviation from ΛCDM of the lensing parameter, $\Sigma(a) - 2$. 99

4.6 The unlensed CMB temperature power spectrum for different values of $\alpha_{\rm H}$, compared to ΛCDM. 100

4.7 Distance measurements, D_V, (left) and the growth of structure, $f\sigma_8$, (right) for best fit lines of a set of MG models compared to ΛCDM. 104

4.8 Constraints on Ω_ν and $\hat{\alpha}_{\rm H}$ from the combination of CMB+BAO (red) and CMB+BAO+RSD (blue) datasets. 107

4.9 Constraints on the MG parameters, $\hat{\alpha}_{\rm B}, \hat{\alpha}_{\rm M}, \hat{\alpha}_{\rm H}$, and the DE equation of state parameters, w_0 and w_a. 108

4.10 Constraints on $\hat{\alpha}_{\rm B}$, $\hat{\alpha}_{\rm M}$ and $\hat{\alpha}_{\rm H}$ from the combination of CMB+BAO+RSD datasets. 109

5.1 Image illustrating our numerical setup: the density distribution, ρ, of the scalar cloud around a BH that is boosted relative to the matter rest frame. 114

5.2 The time evolution (from left to right) of the density profiles of the cloud for two different velocities and the same scalar mass. 115

5.3 Analytic approximation for the nonrelativistic case for a scalar field cloud (dotted line) and with a relativistic correction term (dashed line) and a further correction for a pressure-like term, as for supersonic collisional fluids (solid line). 127

5.4 The diagram shows schematically the regime covered by our simulations in the $\alpha_{\rm s} = \mu M$ - velocity plane. 128

5.5 Dynamical friction force as a function of time extracted from one of our simulations, showing that the total force we extract from our simulations is independent of the value of $r_{\rm in}$. 130

5.6 Time evolution of the total force F_x extracted from the simulations. The four blocks show the the different scalar field masses we consider. 131

5.7 Scaling of the total force, F, on the BH due to the scalar field with relative velocity v. 132

5.8 This plot shows the scaling of the pressure correction factor κ with scalar mass, $\alpha_{\rm s}$. 134

A.1 We show the relative deviation of the CMB temperature-temperature (top panel) and the matter (bottom panel) power spectra w.r.t. a fiducial model for different values of $\alpha_{\rm B}$ ($a = 1$). 176

C.1 Agreement between the time-integrated quantities defined in Eq. (C.2). . . . 182

C.2 Top panel: evolution of the force extracted from the simulations for $\mu = 0.05$ and $v = 0.3$ at three different resolutions. Bottom panel: relative difference between the solutions at the high/low resolutions and the medium one. We also show the difference in the solutions between the low and medium resolutions divided by a convergence factor of 2^4, showing that we achieve fourth-order convergence. 184

C.3 The top panel shows the evolution of the force extracted from the simulations for $\mu = 1$ and $v = 0.8$ at three different resolutions. The bottom panel shows the relative differences in the force between the different resolutions and showing fourth-order convergence. 185

C.4 The expressions in Eqs. (5.31)–(5.33) as a function of the relative velocity v of the BH with respect to the scalar field, for the four values of $\alpha_{\rm s}$ that we simulate. 187

C.5 Time evolution of the force in the case of a real (solid green lines) and complex (dashed black lines) scalar field, showing the agreement between the two cases. 188

List of Tables

2.1 Specific forms of the quintessence potential $V(\phi)$ for the studied models. . . 32

2.2 Parameters distributions. U$[a, b]$ stands for the uniform distribution between a and b and $\mathrm{U}_{\mathbb{Z}}$ is the uniform distribution in the integers. 35

2.3 Fit parameters for $\mathcal{P}[w_0]$ [Eq. (2.13)] model distributions 44

2.4 Fit parameters for $\mathcal{P}[w_a|w_0]$ [Eq. (2.15)] model distributions. Recall that $\langle w_a\rangle(w_0, \beta_i)$ and $\sigma(w_0, \sigma_i)$ are given by Eqs. (2.14) and (2.16), respectively. 44

2.5 Confidence limits of w_0 and w_a each model from the analysis with data alone (where "Data" is the combination CMB+BAO+RSD+SN), as well as from the combined analysis including also the theoretical priors for each model. . 49

3.1 Best fit and confidence limits of w_0 and w_a for the data set CMB+BAO+RSD+SN, the theoretical priors and the combined analysis for the shift-symmetric models both with and without Λ, ($\Lambda = 0$ and $\Lambda \neq 0$). 77

4.1 List of BAO measurements used in this work. 102

4.2 List of RSD measurements used in this work. 102

4.3 Constraints (95%) and marginalised mean values of α_{H} for the different datasets combinations and different sets of other parameters being varied. . 104

4.4 Best fit likelihoods for each model and probe, when running the full CMB+BAO+RSD dataset. 106

5.1 Parameters that vary in our simulations for each value of α_{s}, which compares the Compton wavelength of the scalar to the BH size. 131

Chapter 1

Introduction

1.1 General Relativity

Einstein's theory of general relativity (GR) is the foundation of modern cosmology, the physics describing black holes, and many other phenomena involving strong gravitational fields. The theory was built on the mathematical principles of differential geometry [5, 6]. Einstein claimed that there are a few key principles that a theory must obey in order to be a successful description of gravity: the principle of general covariance, the equivalence principle, and Mach's principle.

At the beginning of the 20^{th} century, Newton's law of gravity had long been the accepted theory to describe the gravitational force between masses, however the nature of this force was unexplained. GR provided a much more consistent formulation of gravity and thus quickly gained popularity. Moreover, it was extremely successful in predicting some observed astrophysical phenomena that had been unexplained before that. One such prediction was the correct orbit of Mercury and other planets. Gravitational redshift is another interesting consequence of GR, which predicts that as photons climb out of a gravitational well, their wavelength will lengthen. Possibly one of the most useful applications of GR to everyday life is the satellite navigational systems, where relativistic effects are accounted for to periodically adjust the rates of the satellite clocks. Another major success of GR is its ability to predict novel effects of gravity, such as gravitational lensing, gravitational waves (GW) and gravitational time dilation. These predictions sparked a wave of new astrophysical experiments aiming to test them and many of these have now been

confirmed.

1.1.1 Why go beyond?

Despite the incredible success of General Relativity, alternative theories have been proposed since Einstein first published it, suggesting a wide range of possible extensions.

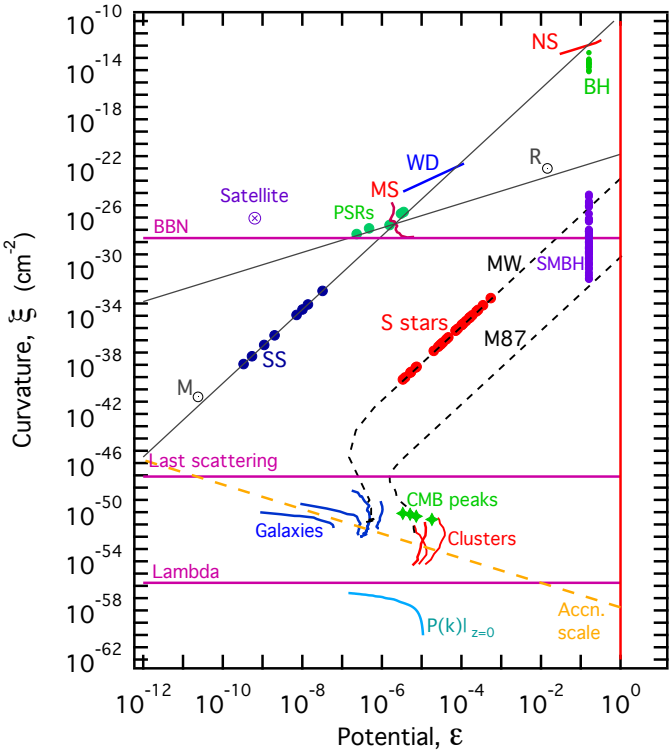


Figure 1.1: Relevant experiments for testing GR at different scales. The x-axis shows the Newtonian gravitational potential, $\varepsilon = GM/(rc^2)$ for a test particle at a distance r from an object of mass M, quantifying the distance scale. On the y-axis is the Kretschmann scalar, which measures the approximate magnitude of the Riemann curvature, $\xi = \left(R^{\alpha\beta\gamma\delta}R_{\alpha\beta\gamma\delta}\right)^{1/2}$, where R is the Riemann tensor. Figure from [7].

Even though it has been shown that GR works extremely well over 15 orders of magnitude in length scale [7] and it remains to this date the most complete theory of gravity, at very large and very small scales current constraints are less tight. This is where deviations from GR become significant and need to be tested. Fig. 1.1 shows a range of experiments for constraining beyond GR models and the scales at which they apply. The relevant experiments (and the scales they probe) for this thesis are the cosmological tests, such as galaxy and galaxy clustering surveys, cosmic microwave background (CMB) experiments and matter power spectrum ($P(k)$) measurements (at large scales, $\varepsilon \sim 10^{-9} - 10^{-4}$) and

the gravitational wave detections of binary mergers of compact objects, such as black holes (BH) and neutron stars (NS) (at small scales, $\varepsilon \sim 10^{-1}$); details on the other tests in this plot can be found in Ref. [7].

The discovery of the 'dark universe' provided yet another reason to search for alternative theories of gravity. For a while now there has been evidence that a significant amount of an additional source of matter, called dark matter (DM), is needed in order to explain the observed rotation curves of galaxies [8–10]. More recently it was also found that the expansion of the universe is accelerating at late times, confirmed by three independent sources, namely, Supernovae Type Ia [11–14], measurements of large scale structure clustering [15–17] and the CMB [18–25]. Even after many years of research, the origin of this so-called 'dark energy' (DE), causing the observed late-time acceleration, remains a mystery (see e.g. [26–29] for a review).

The simplest and currently most successful model that can explain the existence of the 'dark sector' is the Lambda cold dark matter (ΛCDM) model (the standard cosmological model). It is based on GR with the addition of cold dark matter (CDM) and a cosmological constant, Λ. If GR is the correct description of gravity, only about 5% of the current energy content of the universe would be in the form of baryonic matter, of which the visible universe is composed; the rest would have to come from some unknown 'dark' source, the exotic properties of which prompts further exploration of alternative models.

The aim of this thesis is to explore and test specific beyond GR models on both large and small scales. In Chapters 2–4 we test specific dark energy and modified gravity models on large scales with cosmology, by building theoretical priors to combine with data and improve the constraints on certain parameters in Chapters 2 and 3, and exploring the phenomenology of a general class of theories in Chapter 4. In Chapter 5 we numerically test a semi-analytic model for the effects of a dark matter cloud on a moving black hole, the result of which can be used to test a specific dark matter model on small scales with gravitational wave data.

1.1.2 Theoretical framework

Einstein's field equations describe how curvature relates to matter and have the general form,

$$G_{\mu\nu} \equiv R_{\mu\nu} - \frac{1}{2}Rg_{\mu\nu} = \frac{8\pi G}{c^4}T_{\mu\nu}\,. \tag{1.1}$$

The LHS of this equation describes the curvature of spacetime via the Einstein tensor, $G_{\mu\nu}$. $R_{\mu\nu}$ is the Ricci tensor, R (the Ricci scalar) is its trace, and $g_{\mu\nu}$ is the four-dimensional symmetric metric tensor. On the RHS, the matter content of spacetime is represented by the stress-energy tensor, $T_{\mu\nu}$; G is Newton's constant, c is the speed of light. These equations govern a wide range of phenomena, such as the expansion of the universe, the formation of all structure within it, the dynamics and evolution of black holes and the propagation of gravitational waves. Originally derived from fundamental principles, these equations have also been shown (simultaneously by Einstein and Hilbert) to derive form an action of the form,

$$S = \int \mathrm{d}^4x\sqrt{-g}\left[\frac{R}{16\pi G} + \mathcal{L}_m(\psi_i, g_{\mu\nu})\right], \tag{1.2}$$

where the first part is the Einstein-Hilbert action (representing the curvature sector) and $\mathcal{L}_m$ is the Lagrangian of the matter fields, ψ_i, coupled to the metric $g_{\mu\nu}$; g is the determinant of the metric $g_{\mu\nu}$.

The four-dimensional metric $g_{\mu\nu}$ encodes the information about the geometry of spacetime and the effects this has on the matter distribution. It describes a Lorentzian manifold with a line interval, $\mathrm{d}s^2 = g_{\mu\nu}\mathrm{d}x^\mu\mathrm{d}x^\nu$, where x^μ are the spacetime coordinates. From the metric one can obtain the affine connection,

$$\Gamma^\mu_{\nu\lambda} = \frac{1}{2}g^{\mu\alpha}\left(\frac{\partial \mathrm{g}_{\alpha\nu}}{\partial \mathrm{x}^\lambda} + \frac{\partial \mathrm{g}_{\alpha\lambda}}{\partial \mathrm{x}^\nu} - \frac{\partial \mathrm{g}_{\nu\lambda}}{\partial \mathrm{x}^\alpha}\right) \tag{1.3}$$

and the Ricci tensor, related to the second-order derivatives of the metric, $g_{\mu\nu}$, has the form,

$$R_{\mu\nu} = \frac{\partial\Gamma^\alpha_{\mu\nu}}{\partial \mathrm{x}^\alpha} - \frac{\partial\Gamma^\alpha_{\mu\alpha}}{\partial \mathrm{x}^\nu} + \Gamma^\alpha_{\mu\nu}\Gamma^\beta_{\alpha\beta} - \Gamma^\alpha_{\mu\beta}\Gamma^\beta_{\alpha\nu}\,. \tag{1.4}$$

Following a variational principle one can arrive again at the Einsteins field equations, as

defined in Eq. (1.1). Starting from a specific action it is possible to derive the equations of motion for any modification to the curvature part of this action.

Depending on the symmetries of the metric and on the matter content one can obtain different geometries of spacetime. One of the most well-known solutions in GR is described by the Friedmann-Lemaître-Robertson-Walker (FLRW) metric in a homogeneous and isotropic universe [30–33],

$$\mathrm{d}s^2 = -\mathrm{d}t^2 + a(t)^2 \left(\frac{\mathrm{d}r^2}{1-kr^2} + r^2 \mathrm{d}\theta^2 + r^2 \sin^2 \mathrm{d}\phi^2 \right) , \tag{1.5}$$

where t is physical time, $a(t)$ is the scale factor, which describes the expansion of the universe and k is the curvature of the universe. This provides the basis of modern cosmology on large scales. With this spacetime metric and knowledge of the evolution history of the universe, GR allows us to constrain its matter and energy content. Another useful solution, describing a spherical object and the vacuum spacetime around it, is the Schwarzschild metric with a line element [34],

$$\mathrm{d}s^2 = -\left(1 - \frac{2M}{r}\right) \mathrm{d}t^2 + \left(1 - \frac{2M}{r}\right)^{-1} \mathrm{d}r^2 + r^2 \mathrm{d}\theta^2 + r^2 sin^2\theta \mathrm{d}\phi^2 \, , \tag{1.6}$$

where M is the mass of the object. It is usually applied to compact objects such as black holes and neutron stars. This can be extended to masses with angular momentum, described by the Kerr metric [35], as well as one with an electric charge, given by the Reissner-Nordström metric [36].

The matter content of the universe is described by the stress-energy tensor, which for a perfect fluid has the form,

$$T_{\mu\nu} = (\rho + p) u_\mu u_\nu + p g_{\mu\nu} \, , \tag{1.7}$$

where ρ is the relativistic energy density, p is the isotropic pressure, and u^μ is the tangent velocity four-vector.

1.2 Modified Gravity

1.2.1 Landscape

There are a multitude of different ways to modify the equations of GR and construct a theory consistent with current observations. Lovelock's theorem [37, 38] states that under a specific set of assumptions from a local gravitational action containing only the four-dimensional spacetime metric, $g_{\mu\nu}$, and up to second-order of its derivatives, Einstein's field equations plus a cosmological term are the only possible solution. Violating these assumptions can provide us with a way to avoid Lovelock's theorem and construct different sets of modified gravity theories. Here we give a brief overview of some of the most popular sets:

- Additional fields: One of the simplest and most heavily developed ways to avoid Lovelock's theorem is the addition of an extra fundamental field coupled to the metric $g_{\mu\nu}$, allowing us to modify the LHS of Einstein's equations (1.1) in countless different ways.

- Breaking Lorentz invariance: Although, Lorentz invariance is a key ingredient in building a viable theory of gravity, it is possible to construct a theory such that the Lorentz invariance is an emergent symmetry that is broken at very high energies (e.g. Hoŕava–Lifshitz gravity [39]).

- Massive gravity: A consequence of diffeomorphism invariance, another one of the fundamental symmetries of GR, is that gravity must be mediated by a massless spin-2 field.

- Higher dimensions: In higher (than four) dimensions the Einstein field equations are not the only unique solution, even when all of the assumptions of the Lovelock's theorem remain intact. These models serve as the basis of string theories.

The class of theories that we will look at in this thesis are scalar-tensor theories with an additional scalar field; see e.g. [40, 41] for a review on various modified gravity theories.

1.2.2 Scalar-tensor gravity

Scalar-tensor theories present a particularly good model for describing late-time acceleration of the universe, as a slow-rolling scalar field potential can mimic a cosmological constant extremely well. The equations of motion can be derived from a generalised Einstein-Hilbert action [Eq. (1.2)], with an additional field (minimally or non-minimally) coupled to the metric. In their simplest form they include up to first-order derivatives in the action, leading to at most second-order derivatives in the equations of motion. They are characterised by an action of the form [42],

$$S = \int d^4x\sqrt{-g}\Big\{\frac{1}{16\pi G}\left[\omega(\phi)R - K(X,\phi)\right] + \mathcal{L}_m(\psi_i, g_{\mu\nu})\Big\}\,, \tag{1.8}$$

where ϕ is the additional scalar field and $2X = -g^{\mu\nu}\nabla_\mu\phi\nabla_\nu\phi$ is its canonical kinetic term. From this action one can recover GR+Λ by fixing $\omega = 1$ and $K = \Lambda$, quintessence models (with $\omega = 1$ and $K = X - V$, where V is a quintessence potential that can have a variety of different forms [43, 44], used in Chapter 2), axion-like scalar DM models [45–49] (also with $\omega = 1$ and $K = X - V$, relevant for Chapter 5), Brans-Dicke [42], $f(R)$ [50–53], k-essence [54, 55], Chameleon [56–58], symmetron [59], and other models.

1.2.3 The Horndeski class

The most general scalar-tensor theory that leads to at most second-order equations of motion is the Horndeski class [60–62]. It includes, as special cases, a wide range of DE/MG models, such as all the first-order derivative of the field actions mentioned above, plus kinetic gravity braiding [63], covariant galileons [64], the shift-symmetric sub-set (explored in Chapter 3) and others; for a review see [41, 65]. The general Horndeski action is given by [60–62]

$$S[g_{\mu\nu},\phi] = \int \mathrm{d}^4x\,\sqrt{-g}\Big[\sum_{i=2}^{5}\frac{1}{8\pi G_\mathrm{N}}\mathcal{L}_i(g_{\mu\nu},\phi) + \mathcal{L}_\mathrm{m}(g_{\mu\nu},\psi_M)\Big]\,. \tag{1.9}$$

The sum is over four Lagrangians defined as,

$$\begin{aligned}
\mathcal{L}_2 &= G_2(\phi,\, X)\,, \\
\mathcal{L}_3 &= -\,G_3(\phi,\, X)\Box\phi\,, \\
\mathcal{L}_4 &= G_4(\phi,\, X)R + G_{4X}(\phi,\, X)\left[(\Box\phi)^2 - \phi_{;\mu\nu}\phi^{;\mu\nu}\right]\,, \\
\mathcal{L}_5 &= G_5(\phi,\, X)G_{\mu\nu}\phi^{;\mu\nu} \\
&\quad -\frac{1}{6}G_{5X}(\phi,\, X)\Big[(\Box\phi)^3 + 2\phi_{;\mu}{}^{\nu}\phi_{;\nu}{}^{\alpha}\phi_{;\alpha}{}^{\mu} - 3\phi_{;\mu\nu}\phi^{;\mu\nu}\Box\phi\Big]\,,
\end{aligned} \tag{1.10}$$

where $\phi_{;\mu} \equiv \nabla_\mu\phi$, $\phi_{;\mu\nu} \equiv \nabla_\mu\nabla_\nu\phi$, $G_i(\phi,\, X)$ are arbitrary functions of the scalar field ϕ and its canonical kinetic term X. The subscripts ϕ and X denote partial derivatives ($G_{iX} \equiv \partial G_i/\partial X$).

In building "healthy" extensions to GR by adding a scalar field, one needs to take care to avoid Ostrogradsky instabilities [66, 67], especially in the case where higher (than first) order derivatives of the scalar field are present in the action. The theorem states that a system described by a non-degenerate Lagrangian containing higher than first-order time derivatives of a field, which leads to a linearly unstable Hamiltonian, suffers from ghost-like instabilities [68]; it can also be extended to theories with third-order equations of motion [69]. The conditions under which these instabilities can be avoided are discussed in Section 1.4.2.

It is possible to extend the Horndeski class to include higher (than second) order derivatives of the field in the equations while keeping the action up to second-order (and avoiding Ostrogradsky instabilities), [70, 71]. This is the so-called beyond Horndeski class of models, discussed in Chapter 4.

1.3 The $3+1$ decomposition

A commonly used approach in evolving any physical system in time is to formulate the evolution as an initial value problem. In the Einstein equations, however, space and time are treated equally. It is possible to disentangle their roles in a clear way by using the $3+1$ Arnowitt-Deser-Misner (ADM) decomposition [72], in which spacetime is split into a three-dimensional space and time, with the time slices, t_i, defined on adjacent (uniformly

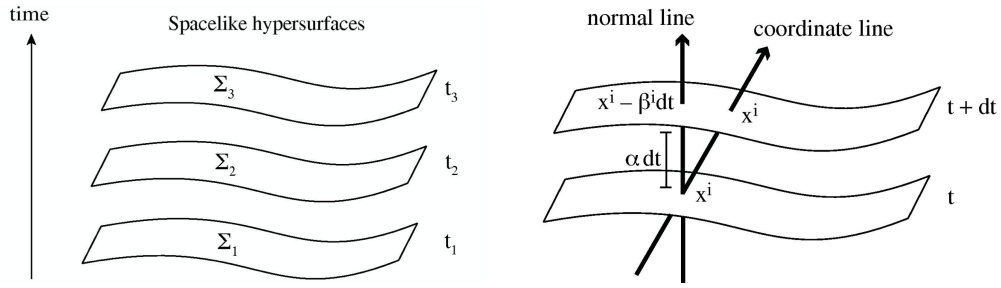


Figure 1.2: The left panel illustrates the principle foliation of spacetime into three-dimensional hypersurfaces. On the right is the definition of the lapse function, α, and shift vector β^i on two adjacent hypersurfaces, where x^i are the spatial coordinates and dt is a single time step. Image from [73]

distributed) spacelike hypersurfaces, Σ_i, as shown on left panel of Fig. 1.2. The ADM decomposition of a four-dimensional metric $g_{\mu\nu}$ has the form,

$$\mathrm{d}s^2 = -\alpha^2 \mathrm{d}t^2 + \gamma_{ij}(\mathrm{d}x^i + \beta^i \mathrm{d}t)(\mathrm{d}x^j + \beta^j \mathrm{d}t)\,, \tag{1.11}$$

where the physical time, t, relates to proper time, τ, as $\mathrm{d}t = \alpha \mathrm{d}\tau$, α is the lapse of proper time dτ between the hypersurfaces measured by an observer moving along the normal direction, β^i is the relative velocity between this observer and the lines of constant spatial coordinates, called the shift vector, x^i are the spatial coordinates, and γ_{ij} is the three-dimensional projection tensor that measures the proper distances within each hypersurface. An illustration of the definition of α and β^i is shown on the right panel of Fig. 1.2. The unit normal vector to the spatial hypersurfaces, n^μ, has time and space components

$$n^\mu = (1/\alpha, -\beta^i/\alpha)\,, \qquad n_\mu = (-\alpha, 0)\,, \tag{1.12}$$

and is also related to the four-velocity of the Euclidean observer.

The four-dimensional curvature, R, can be expressed in terms of the intrinsic three-dimensional curvature of the hypersurfaces, ${}^{(3)}R$, and the extrinsic curvature, $K_{\mu\nu}$, which describes how the spatial hypersurfaces are immersed in spacetime,

$$K_{\mu\nu} = -P^\alpha_\mu \nabla_\alpha n_\nu\,, \tag{1.13}$$

where $P^\alpha_\mu = \delta^\alpha_\mu + n^\alpha n_\mu$ is the projection operator onto the spacelike hypersurfaces. These

are related though the Gauss-Codazzi equations,

$$R = {}^{(3)}R + K_{\mu\nu}K^{\mu\nu} - K^2 - 2\nabla_\lambda(n^\nu\nabla_\nu n^\lambda - n^\lambda\nabla_\nu n^\nu)\,, \tag{1.14}$$

where K and R are the traces of the extrinsic and intrinsic curvature tensors, respectively. Using these quantities the action of a particular theory can be expressed in terms of the ADM quantities. For example, in the case of GR it has the form,

$$S_{\rm GR} = \frac{1}{16\pi G}\int \mathrm{d}^4x\,\alpha\sqrt{\gamma}\left({}^{(3)}R + K_{ij}K^{ij} - K^2\right)\,, \tag{1.15}$$

noting that the four-dimensional volume element, $\sqrt{-g}$, can be expresses in term of the determinant of the three-dimensional of the spatial metric, γ_{ij}, as $\sqrt{-g} = \alpha\sqrt{\gamma}$.

1.4 Parametrising Horndeski

1.4.1 Effective field theory

The effective field theory (EFT) approach to dark energy and modified gravity is a way to connect data to fundamental theory, a method that has proved very successful in particle and condensed matter physics [74, 75]. It has been shown that these methods can also be applied in cosmology, in the case of inflation [76–78] as well as models describing the late-time acceleration of the universe [79–84]. The aim of this approach is to unify a large set of existing DE/MG models, containing a single scalar degree of freedom. To this end, one needs to construct a Lagrangian that includes the perturbations about a cosmological background and that contains a metric, a single scalar field and a matter source, which is assumed to obey the weak equivalence principle, meaning that all matter fields couple to the same metric.

This approach makes use of the ADM decomposition, introduced in Chapter 1.3. The most general EFT action in the ADM decomposition for a scalar field DE, leading to at

most second-order equations of motion is given by [85, 86],

$$S = \int \mathrm{d}^4x\, \alpha\sqrt{\gamma}\left[\frac{M_*^2}{2}f(t)R - \Lambda(t) - c(t)g^{00} + \frac{M_2^4}{2}(\delta g^{00})^2 - \frac{m_3^3(t)}{2}\delta K\delta g^{00} \right.$$
$$\left. -m_4^2(t)\left(\delta K^2 - \delta K^\mu{}_\nu \delta K^\nu{}_\mu\right) + \frac{\tilde{m}_4^2(t)}{2}\,{}^{(3)}\!R\delta g^{00}\right], \tag{1.16}$$

where f, Λ, c, m_3^3, m_4^2 and $\tilde{m}_4^2$ and M_2^4 are time-dependent functions, M_* is the effective Planck mass, $\delta g^{00} = g^{00}+1$, $g^{00} = -1/\alpha$, $\delta K_{\mu\nu} = K_{\mu\nu} - H\gamma_{\mu\nu}$ and $\gamma_{\mu\nu} = g_{\mu\nu} + n_\mu n_\nu$. One should note that while this setup only allows for up to second-order time derivatives in the linear perturbation equations, it is possible for higher than second-order spatial derivatives to emerge and the conditions under which these are absent were derived in Ref. [87].

1.4.2 Stability Conditions

Starting from this action it is possible to define the stability conditions necessary to avoid Ostrogradsky instabilities by requiring the positivity of the time kinetic term of the action,

$$\mathcal{L}_{\dot{\zeta}\dot{\zeta}} \equiv 2\left(c + 2M_2^4 - 3H^2M_*^2 f - 3HM_*^2\dot{f} + 3Hm_3^3 - 6H^2m_4^2\right)D^2 + 6(M_*^2 f + 2m_4^2) > 0\,, \tag{1.17}$$

where ζ describes the scalar perturbations of the spatial metric as defined in Ref. [88] and

$$D = \frac{2(M_*^2 f + 2m_4^2)}{2H(M_*^2 f + 2m_4^2) + M_*^2\dot{f} - m_3^3}\,. \tag{1.18}$$

Here we only present a brief overview, for a more detailed description and derivation of all the expressions here see Refs. [87, 89].

1.4.3 Minimal set of parameters

These results have been reformulated in Ref. [90] by introducing four dimensionless function of time, which can be expressed as combinations of the functions of the Horndeski Lagrangian, $G_i(\phi, X)$, in Eq. (1.10). This approach allows us to clearly parametrise deviations from GR by separating the properties of the background expansion (H_0 and Ω_m) and perturbations (parametrised by four additional functions of time, which are independent of each other, the background and the matter sector); a very useful property, as we know

from observations that the background expansion history is close to ΛCDM. The physical meanings of the four functions describing the perturbations are as follows:

- $\alpha_{\rm K}$ is the kinetic energy of scalar perturbations,
- $\alpha_{\rm B}$ represents the mixing of the kinetic terms of the metric and the scalar field,
- $\alpha_{\rm M}$ is the time derivative of the effective Planck mass, M_*^2,
- $\alpha_{\rm T}$, which measures the deviation of the speed of gravitational waves c_T from the speed of light.

These are functions of the G_i parameters of the Lagrangian in Eq.(1.10) and their derivatives with respect to the scalar field ϕ and its canonical kinetic term X. They represent the common factors in front of evolution variables in the perturbed Einstein and scalar field equations.

It is possible to re-express the Horndeski action in terms of these parameters, as well as the scalar and two metric perturbations, π, Ψ and Φ, respectively, and which has the form [91],

$$
\begin{aligned}
S = \int {\rm d}^4x a^3 M_*^2 \Bigg\{ & \left[\dot{H} + \frac{1}{2M_*^2}\left(\rho_{\rm m} + p_{\rm m} + 2(M_*^2 H \alpha_{\rm B})^{\cdot}\right) + H^2(\alpha_{\rm B} - \alpha_{\rm M} + \alpha_{\rm T})\right]\frac{(\nabla\pi)^2}{a^2} \\
& + \frac{1}{2}H^2\alpha_{\rm K}\dot{\pi}^2 - 3\dot{\Psi}^2 + (1+\alpha_{\rm T})\frac{(\nabla\Psi)^2}{a^2} + 2H\alpha_{\rm B}\nabla\Phi\nabla\pi - 2H(\alpha_{\rm M} - \alpha_{\rm T})\frac{\nabla\Psi\nabla\pi}{a^2} \\
& + 6H\alpha_{\rm B}\dot{\pi}\dot{\Psi} + H^2(6\alpha_{\rm B} - \alpha_{\rm K})\Phi\dot{\pi} - 2\frac{\nabla\Phi\nabla\Psi}{a^2} \\
& - 6H(1+\alpha_{\rm B})\dot{\Psi}\Phi + H^2\left(\frac{1}{2}\alpha_{\rm K} - 3(1+2\alpha_{\rm B})\right)\dot{\Phi}^2 + ...\Bigg\},
\end{aligned}
\tag{1.19}
$$

including only the terms that are quadratic in derivatives of the metric or scalar perturbations. The exact form of the α functions and the perturbed Einstein and scalar field equations can be found in Chapter 4.

Particular DE models have different $\alpha_i \neq 0$ and thus constraining these parameters with data could indicate classes of models that are consistent with measurements. For example the detection of an electromagnetic counterpart [92, 93] to the gravitational wave event GW190817 [94] was used to rule out a large set of models belonging to the Horndeski

class that allowed the speed of gravitational waves to deviate from the speed of light (i.e. $\alpha_{\rm T} \neq 0$) [95–98]. The α_i parameters can be related to the Lagrangian coefficients of Eq. (1.16) as described in Refs. [89, 91] (see in particular bottom row of Table 1 in [91]), after removing some redundancies in the original EFT description, which were pointed out in Ref. [99].

1.5 Cosmology

In this section we briefly summarise the observable quantities used to test the background expansion of the universe and the growth of structure.

1.5.1 Background expansion

The standard model of cosmology is based on the cosmological principle, which states that there is no preferred location or a direction in the universe (it is homogeneous and isotropic). It is seen observationally in galaxy distributions and the CMB that this is indeed the case on scales larger than 100 Mpc [100–103].

From Einstein's equations (1.1) for the FLRW metric in Eq.(1.5) and the stress-energy tensor for perfect fluids [Eq.(1.7)] we can obtain the equations that govern the background expansion of the universe. The 00 component of the Einstein equations gives

$$3H^2 = \sum_i \rho_i \,, \tag{1.20}$$

where $H = \dot{a}/a$ is the Hubble parameter and the subscript i represents the different constituents of the universe. The ii component of the Einstein's equations leads to

$$\frac{\ddot{a}}{a} = -\frac{1}{3}\sum_i (\rho_i + 3p_i) \,. \tag{1.21}$$

These are the so-called Friedmann equations, which provide us with a description of the dynamics and evolution of the homogeneous universe.

From the conservation of the stress-energy tensor, $\nabla_\mu T^{\mu\nu} = 0$, one can show that for

a perfect fluid [Eq. (1.7)], the rate of change of the density of the fluid is

$$\dot{\rho}_i = -3H\rho(1 + w_i)\,, \tag{1.22}$$

where $w_i = p_i/\rho_i$ is the equation of state of the fluid. Using this equation it is possible to obtain a simple form for the evolution of the density of the different constituents of the universe,

$$\rho_i = \rho_{i,0}\, a^{-3(1+w_i)}\,, \tag{1.23}$$

when w_i is a constant. For example for CDM ($w_{\rm cdm} = 0$) and a cosmological constant ($w_\Lambda = -1$), the evolution of the density on the background level is $\rho_{\rm cdm} \propto a^{-3}$ and $\rho_\Lambda \propto$ const., respectively. In models of dynamical DE, $w_{\rm DE}$ is allowed to differ from -1 and can vary in time.

1.5.2 Distance measures

It is sometimes useful to use comoving distance coordinates $\mathrm{d}\chi = \mathrm{d}r/\sqrt{1-kr^2}$ rather than radial coordinates $\mathrm{d}r$, as they expand along with the expansion of the universe and are time-independent. Using these one can define the comoving distance to an object,

$$\chi = \frac{d_{\rm phys}(t)}{a(t)} = \int_t^{t_0} \frac{dt'}{a(t')} = \int_a^1 \frac{da'}{a'^2 H(a')}\,, \tag{1.24}$$

where $d_{\rm phys}$ is the physical distance to the object, t_0 is physical time today. This is a time-independent quantity that defines the distance a photon has travelled since it was emitted.

The angular diameter distance, $D_{\rm A}$, is defined as the ratio of an object's physical size, l, to its angular size (the angle subtended by an object of size l), θ,

$$D_{\rm A} = \frac{l}{\theta} = a(t)\chi\,, \tag{1.25}$$

for a flat FLRW universe.

It is also possible to measure the luminosity distance to an object, which can be inferred by measuring the flux, F of an object with known luminosity, L. It is related to the

comoving and angular diameter distances as,

$$D_{\rm L} = \chi(1+z) = D_{\rm A}(1+z)^2\,. \tag{1.26}$$

All of these measurements of distance would be affected by the presence of dark energy in the universe and hence will be sensitive to the value of the cosmological constant or the parameters setting the time dependence of dynamical DE models. Many surveys can measure these quantities directly, making them a very good probe for constraining the DE component of MG models.

1.5.3 Perturbation theory

At scales smaller than 100 Mpc the universe is full of structure in the form of galaxies and galaxy clusters and can no longer be assumed to be homogeneous. As discussed in Section 1.4.1 it is possible to parametrise all deviations from GR into the properties of the perturbations, which makes the measurement of these a very powerful probe of modified gravity.

Mathematically this picture can be realised by adding small perturbations to the FLRW metric and the stress-energy tensor, then computing the Einstein equations to first-order in these perturbations. In the conformal Newtonian gauge [104], the perturbed FLRW metric, considering only scalar perturbations (following the notation of [105]) can be written as

$$ds^2 = -(1+2\Psi)dt^2 + a^2(t)(1-2\Phi)\delta_{ij}dx^i dx^j\,, \tag{1.27}$$

where Ψ and Φ are the scalar potentials that characterise the perturbations.

The metric and the stress-energy tensors can be split into a sum of zeroth- and first-order perturbation components,

$$g_{\mu\nu} = g^{(0)}_{\mu\nu} + \delta g_{\mu\nu} \qquad \text{and} \qquad T_{\mu\nu} = T^{(0)}_{\mu\nu} + \delta T_{\mu\nu}\,. \tag{1.28}$$

Equating the first-order perturbation parts, one can recover the perturbed Einstein equa-

tions for a single fluid in Fourier space,

$$k^2\Phi - 3\mathcal{H}\left(\Phi' - \mathcal{H}\Psi\right) = \frac{1}{2}a^2\rho\delta\,, \tag{1.29}$$

$$k^2\left(\Phi' - \mathcal{H}\Psi\right) = \frac{1}{2}a^2(1+w)\rho\theta\,, \tag{1.30}$$

$$\Psi = -\Phi\,, \tag{1.31}$$

$$\Phi'' + 2\mathcal{H}\Phi' - \mathcal{H}\Psi' - \left(\mathcal{H}^2 + 2\mathcal{H}'\right)\Psi = -\frac{1}{2}a^2c_{\rm s}^2\delta\rho \tag{1.32}$$

where the primes denote derivatives with respect to conformal time, τ, (which relates to physical time t as $\mathrm{d}t = a\mathrm{d}\tau$), $\mathcal{H} = a'/a$ is the conformal Hubble factor, $\delta = (\rho - \bar{\rho})/\bar{\rho}$ is the density contrast for all individual matter species (with $\bar{\rho}$ – the background average density), θ is the peculiar velocity of the fluid and $c_{\rm s}^2 = \delta p/\delta\rho$ is its sound speed. These equations can be derived from the perturbed Einstein and stress-energy tensor and transformed from real to Fourier space using the fact that $\nabla \to ik$, where k is the wavenumber of the perturbations. For a detailed derivation see e.g. [50, 106].

From the conservation of the perturbed stress-energy tensor, one can obtain the continuity and Euler equations for each of the fluid species,

$$\delta' + 3\mathcal{H}(c_{\rm s}^2 - w)\delta = -(1+w)\left(\theta + 3\Phi'\right)\,, \tag{1.33}$$

$$\theta' + \left[\mathcal{H}(1-3w) + \frac{w'}{1+w}\right]\theta = -k^2\left(\frac{c_{\rm s}^2}{1+w}\delta + \Psi\right)\,. \tag{1.34}$$

1.5.4 Growth of matter overdensities

For scales much larger than the Hubble horizon ($k \ll \mathcal{H}$), where we can use the quasistatic approximation ($\Phi' = 0$), for matter and radiation (with $w = c_{\rm s}^2 =$ constant), we can see from Eqs. (1.29) and (1.20) that the perturbations of these fluid components do not grow until they re-enter the horizon, as $\delta = 2\Phi$.

On small scales, well within the horizon ($k \gg \mathcal{H}$), the growth of matter and radiation perturbations is given by

$$\delta'' + \mathcal{H}(1-3w)\delta' + \left(k^2c_{\rm s}^2 - \frac{3}{2}(1+w)\mathcal{H}^2\right)\delta = 0\,. \tag{1.35}$$

This expression describes the time evolution of density perturbations for the different fluids

at different times during the evolution of the universe (radiation, matter or DE-dominated era).

A very useful quantity that can be used to probe the growth of large scale structure is the growth rate,

$$f(a) = \frac{\mathrm{d}\,\ln \delta_{\mathrm{m}}}{\mathrm{d}\,\ln a}\,, \tag{1.36}$$

where the subscript m denotes matter. The differential equation for the growth of perturbations [Eq. (1.35)] can be rewritten in terms of the growth rate function as

$$f' + f^2 + \left(\frac{\dot{H}}{H^2} + 2\right) f = \frac{3}{2}\Omega_{\mathrm{m}}\,, \tag{1.37}$$

Some observations are directly sensitive to this function, making it a very powerful probe of MG theories.

1.5.5 Correlation functions and power spectra

Clustering of matter can be measured through the overdensity, $\delta(\boldsymbol{r})$, by a two-point correlation function,

$$\xi(\boldsymbol{r}) = \langle \delta(\boldsymbol{r_1})\delta(\boldsymbol{r_2})\rangle\ , \tag{1.38}$$

where the angle brackets denote an ensemble average. One can then define the matter power spectrum by Fourier transforming the correlation function,

$$P(k) = \int d^3\boldsymbol{r}\xi(\boldsymbol{r})e^{i\boldsymbol{k}\cdot\boldsymbol{r}} \tag{1.39}$$

Although theoretically, we are often interested in the total matter overdensity, δ_{m}, and matter power spectrum P_{m}, which is dominated by CDM, we observe the much smaller luminous component of matter, galaxies. At linear scales the matter and galaxy overdensities are related with a bias factor b as $\delta_{\mathrm{g}} = b\delta_{\mathrm{m}}$. So that the matter power spectrum is related to the galaxy power spectrum as,

$$P_{\mathrm{g}} = b^2 P_{\mathrm{m}}\,. \tag{1.40}$$

It is important to note that, while at large scales (relevant to this work), b can be approximated to a constant, at smaller scales one needs to consider the time and scale dependence of the bias factor, $b(k, a)$, for which more complex models and numerical treatment may be required.

1.6 Probing gravity on large scales

1.6.1 Time evolution of DE/MG functions

In order to constrain the free functions parametrising DE/MG models one can either measure them directly, as a function of redshift or assume a parametric form for their time evolution. On the background level, the exact form for the evolution of the DE equation of state, $w_{\rm DE}$ is unknown. A parametrisation for its time dependence that is often assumed in the literature is the Chevallier-Polarski-Linder (CPL) parameterisation [107, 108],

$$w_{\rm DE} = w_0 + w_a(1 - a)\,, \tag{1.41}$$

which can approximate most equations of state close to $a = 1$ and is widely used in current data analysis or in assessing the constraining power of future surveys [109, 110]. The perturbations, parametrised by the α_i parameters, introduced in Section 1.4.3, are most commonly assumed to scale with the fractional density parameter of DE, $\Omega_{\rm DE}$,

$$\alpha_i = \hat{\alpha}_i\, \Omega_{\rm DE}\,, \tag{1.42}$$

where $\hat{\alpha}_i$ are constant parameters. This form is motivated by the fact that the modifications to GR at the perturbation level (in the form of α_i) are expected to become important at late times (when DE also becomes significant), making it a suitable choice for theories aiming to explain the late-time acceleration of the universe. We used this parametrisation in Chapter 4, to put constraints on the additional function of beyond Horndeski class, $\alpha_{\rm H}$.

Using this approach one can constrain the functions of a general set of theories and then infer what this implies for any particular model, allowing us to compare different models more easily. However, as it relies on an assumption for the time evolution of its functions, regardless of how well-motivated a parametrisation is, it can bias our results [111]. One

alternative is to reconstruct the values of these functions at different redshifts directly from observational data, the so-called "non-parametric" approach (see e.g. [111–118]). However, Principle Component Analysis (PCA) forecasts have shown that while future surveys can constrain DE/MG parameters at several redshift bins, values at neighbouring bins are expected to be highly degenerate and many will remain unconstrained [119–123].

1.6.2 Including theoretical priors

One possible solution to these problems is to adopt a theoretically informed parametrisation, by using the properties of the underlying physical model. There are many different approaches to this. One possibility is to include a theoretically informed prior covariance matrix to the analysis with data to reduce the degeneracy in non-parametric models (see e.g. [117, 124–134]). It is also possible to use a PCA forecast to tune the strength of the prior and avoid the bias in the reconstructed evolution of the parameters (as done in Refs. [124, 127]), as well as derive the values of the function at different redshifts directly from data, by taking derivatives of the luminosity distances $D_L(z)$ (see [112, 135]). It is also possible to build theoretical priors for the CPL parameters w_0 and w_a based on a representative ensemble of quintessence potentials [136, 137] and similarly for an ensemble of more general scalar-tensor models [130].

In the work presented in Chapter 2 we develop a new method in deriving the theoretical priors for $w_{\rm DE}$ for a range of quintessence potential, extended to the shift-symmetric Horndeski model with parameters $w_{\rm DE}$ and $\alpha_{\rm B}$ in Chapter 3. The approach we used is summarised in the diagram in Fig. 1.3, where we make use of the evolution of a set of observable quantities (the Hubble parameter, H, the angular diameter distance, D_A, and the growth rate of structure, f) to find a best fit function to match those calculated from the underlying model varying the parameters of the Lagrangian along with cosmological parameters, known to have an effect on DE functions. Using this approach we eliminate the issue of biasing the results, as we do not assume a parametric form for the evolution of these functions, but rather find an expression that provides a good fit to the observable quantities that would be used to constrain the model with data.

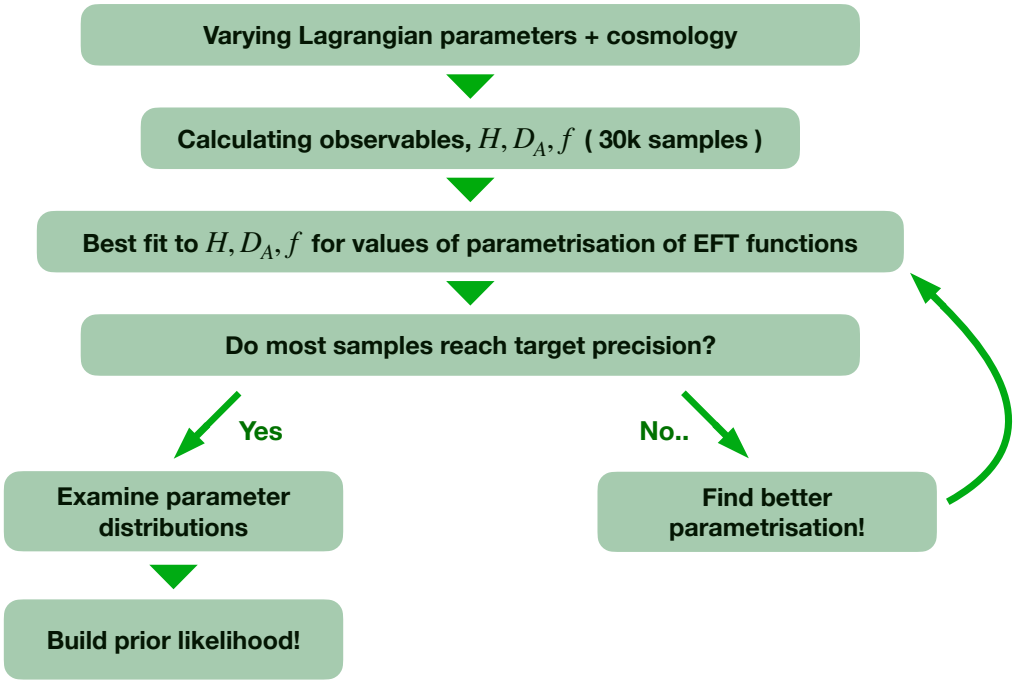


Figure 1.3: A diagram summarising the approach for constructing theoretical priors for scalar-tensor theories, developed in Chapter 2 for a range of quintessence potentials and extended to the shift-symmetric sub-class of Horndeski in Chapter 3.

1.6.3 Cosmological Data

We discuss briefly some of the cosmological probes that measure these quantities and can be used to test GR and MG (for a comprehensive review on cosmological tests of gravity see [138–140]).

Cosmic Microwave Background

The Cosmic Microwave Background (CMB) is a relic electromagnetic radiation from the epoch of recombination. It is a mostly uniform and isotropic field, which has a measured black-body spectrum with temperature $T_{\rm cmb} = 2.72$K. It is one the most powerful probes of gravity as it constrains both the homogeneous background and the growth of structure in the universe.

The temperature and polarisation power spectra of the CMB have primary anisotropies, imprinted in the surface of last scattering and secondary ones, which appear later, as the

CMB photons travel through the intervening medium to reach us. The primary anisotropies probe the early universe and can be used to constrain the standard cosmological parameters. Secondary anisotropies, such as the Integrated Sachs-Wolfe effect (ISW) [141], lensing of the CMB [142–145], and the Sunyaev–Zel'dovich (SZ) [146] effect are more relevant for DE and MG models as they can be used to constrain scalar mode perturbations and the growth rate of large scale structure. These are more relevant for DE and MG models as they can be used to constrain scalar mode perturbations and the growth rate of large scale structure.

Although very uniform across the sky, the temperature field of the CMB has fluctuations at smaller scales, defined as $\Theta(\theta,\phi) = (T(\theta,\phi) - \bar{T})/\bar{T}$, where $\bar{T}$ is the average temperature of the CMB. These fluctuations are projected onto a 2D spherical surface of the sky, so it is useful to expand them using spherical harmonics,

$$\Theta(\theta,\phi) = \sum_{\ell=0}^{\ell=\infty} \sum_{m=-\ell}^{m=\ell} a_{\ell m} Y_{\ell m}(\theta,\phi)\,, \tag{1.43}$$

where $a_{\ell m}$ are the harmonic coefficients,

$$a_{\ell m} = \int_{\theta=-\pi}^{\pi} \int_{\phi=0}^{2\pi} \Theta(\theta,\phi) Y^*_{\ell m}(\theta,\phi) d\Omega\,. \tag{1.44}$$

So the power spectrum of temperature fluctuations can be defined as,

$$C_\ell = \frac{1}{2\ell+1} \sum_{m=-\ell}^{m=\ell} \left\langle |a_{\ell m}|^2 \right\rangle\,, \tag{1.45}$$

which can be measured by CMB experiments.

Galaxy Surveys

BAO

The baryon acoustic oscillation (BAO) signature, first detected by the Sloan Digital Sky Survey (SDSS) [147] and the 2dF Galaxy Redshift Survey [148], is measured through the angular diameter distance, $D_A(z)$ [Eq. (1.25)], and the Hubble parameter, $H(z)$ [Eq. (1.20)].

During the very early stages of the universe electrons, photons and baryons were coupled

and these oscillated together as a single plasma fluid, which left an imprint on the baryon distribution at the time of baryon-photon decoupling. These oscillations have a fixed comoving scale given by the size of the sound horizon in the drag epoch (shortly after recombination, $z \sim 1100$), which was maintained as matter overdensities grew. When compared to its observed angular size at a given redshift, it can be used to infer the distance to it. This makes the BAOs a very good probe of the expansion rate of the universe since the time of recombination (e.g. [109]), and the density fractions of the different components of the universe: baryonic matter, dark matter and dark energy (e.g. [149–151]).

Redshift Space Distortions

In galaxy redshift surveys, observations along the line of sight are subject to another type of distortion caused by the peculiar velocities of the galaxies, which creates a Doppler shift in addition to the cosmological expansion redshift. These are called Redshift Space Distortions (RSD) and can present in two different ways: the "fingers of God" effect [152] – an elongation of the galaxy distribution in the direction of the observer, and the Kaiser effect [153], where the distribution appears flattened. Galaxy surveys measure RSDs through the growth rate of structure, $f(z)$, [Eq. (1.36)] at different redshifts (see e.g. [154–159]). RSDs are a very good probe of cosmology and the gravity theory that governs the evolution of perturbations.

Lensing

Photons propagate freely from the surface of last scattering and as they do their trajectories along the line of sight get deflected by matter overdensities of the large-scale structure in the intervening medium. These deflections leave an imprint on the observed CMB temperature and polarisation anisotropies in the form of small distortions and can be used to reconstruct a map of the lensing potential. Its power spectrum is a strong probe of the late-time geometry and expansion of the universe as it measures the distortions to the CMB temperature and polarisation maps caused by the clustering of matter at relatively small redshifts (CMB lensing is most efficient at $z \sim 2$).

Similarly, large-scale structure also deflects the trajectories of photons from distant galaxies. Depending on the positions of the lenses and the sources, these deflections can

induce either strong, weak or intermediate lensing effect. Strong and intermediate gravitational lensing can result in very distorted images, such as arcs and Einstein rings. Weak lensing (also known as cosmic shear), on the other hand, results in much smaller distortions quantified by the shear of the images, which tend to transform from circular to elliptical shapes. WL is detected studying the statistical properties of many distorted samples (rather than individual ones), as its effect is quite small. It is a ubiquitous source of gravitational lensing and a powerful probe of the cosmology of the intervening deflector medium.

1.7 Parameter Inference

Bayesian statistics and Markov Chain Monte Carlo (MCMC) algorithms are crucial mathematical and numerical tools in cosmological parameter estimation and model selection. Bayes' theorem states that the posterior probability of a given model H, for a parameter vector θ and data D is given by,

$$P(\theta|D,H) = \frac{P(D|\theta,H)\,P(\theta|H)}{P(D,H)}\,, \tag{1.46}$$

where $P(D|\theta,H)$ is the likelihood, $P(\theta|H)$ is any prior knowledge we might have of the model before considering the data and $P(D,H)$ is a normalising factor. In cosmology one often assumes uniform (or flat) priors, $P(\theta|H) \propto$ constant, which means that all values for a specific parameter are equally as likely and hence the posterior probability will be proportional to the likelihood. As we will see in Chapters 2 and 3 it is also possible to include theory informed priors (e.g. a Gaussian distribution) to certain parameters that may significantly change their posterior distributions. The normalising factor, $P(D,H)$, is the so-called Bayesian evidence, which is the average of the likelihood under the prior. This quantity is usually ignored when exploring the parameter space of a single model, however, it can become important when selecting a model that best fits certain data (model selection).

In very simple terms, MCMC algorithms are used to sample though a parameter space, evaluate the posterior of each sample, as given in Eq. (1.46) (which can be used to inform future guesses of the sampler) leading to convergence to a most likely region of space. For

a detailed description of MCMC algorithms see e.g. [160, 161].

1.8 Gravity on small scales

Black holes and other compact objects provide a unique laboratory for testing gravity and fundamental physics in extreme gravitational environments. Scalar DM and DE are expected to interact with baryonic matter very weakly, if at all, but will certainly interact gravitationally with compact objects. Comparing the gravitational wave signal from mergers to the predicted one from simulation can help us confirm or rule out certain beyond GR models. In the absence of couplings to standard model matter, this may be the only way to probe the properties of DM.

1.8.1 Probing physics with gravitational waves

A new era into the study of the universe was opened with the first direct detection of gravitational wave of the black hole merger GW150914 [162] and the field has advanced hugely since, with many more detections being confirmed (see e.g. [163–169]), allowing us to probe in great detail the nature of the merger objects and potentially probe their environments. In the coming years there will be a large amount of gravitational wave data from current and future surveys, including LIGO/Virgo/KAGRA [170, 171], LISA [172,173], the Einstein Telescope [174], and others, allowing for a very precise measurement of the origin and location of the sources. This can open the possibility to constrain the parameters of beyond GR theories of gravity using GW data and solve many outstanding problems in cosmology, astrophysics and particle physics.

Future GW experiments should provide a much higher sensitivity to small deviations in the waveforms from binary mergers of compact objects, allowing for a more precise reconstruction of the properties of their environments [175, 176]. These so-called "environmental" effects are expected to leave a potentially detectable imprint on the waveform. [1] For example, the presence of DM can slow down a BH moving in a binary due to a dynamical friction (DF) drag-like force induced by the DM cloud. This is expected to modify

[1] We should note that, even though, DM densities in most galaxies may not be high enough to produce a strong effect in the the signal [175], unless the environmental effects are enhanced, it is still important to characterise them.

the dynamics of the binary and cause a detectable de-phasing of the gravitational waveform [176–179]. If detected, such de-phasing effect can signal the presence of DM around BHs, as well as inform us of its properties given a specific model. In Chapter 5 of this thesis we explore this problem and numerically derive the expected scaling of the DF force with the velocity of the BH induced by a cloud of light bosonic scalar field DM.

There are many other possible ways to characterise beyond GR effects using GWs, such as the BH spin-down due to superradiance, which can drive an exponential growth of the scalar field clouds, reaching up to 10% of the mass of the BH (see e.g. [180–184]). The existence of such a field can be probed directly by measuring the spins and masses of the merging BHs. Other ways in which GW experiments can signal beyond GR physics include detecting exotic compact objects (e.g. boson stars), constraining cosmic expansion history by using GW sources with an electromagnetic counterpart as standard sirens, GW damping due to modified gravity interactions, direct detection using the GW polarisation (as alternative theories of gravity are expected to have additional polarisation modes), and others. In this thesis we only focus on the effects of de-phasing due to dynamical friction, for a detailed discussion on characterising properties of beyond GR models using GWs see e.g. [178, 185–187].

1.8.2 Numerical solutions in strong gravity

Solutions to the fully non-linear Einstein equations are very difficult to find analytically in most cases that do not exhibit many symmetries. Therefore we need to turn to numerical methods to study the dynamics and evolution of the complex systems of black holes and other compact objects in different environments, using numerical relativity (NR). The four-dimensional Einstein equations (1.1) are split into three-dimensional spatial hypersurfaces and a time-like direction, as described in Section 1.3. The ADM decomposition was later reformulated in a numerically more stable form by Baumgarte, Shapiro, Shibata and Nakamura (BSSN) [188–190], enabling stable evolution of strong gravitational spacetimes for much longer timescales.

It is also possible to treat extensions to GR perturbatively by adding them onto a fixed metric background, as done in cosmology, as current data indicates that any modifications if detected will be small. In Chapter 5 we use this formulation to evolve a scalar field profile

around a moving BH and calculate the resulting drag force on the BH. The perturbative approach allows for a much faster numerical evolution (due to all the BSSN variables that describe the evolution of the metric being fixed) and can be very useful, especially for problems where we expect the effect of perturbations onto the background metric to remain small, as in the case of a minimally coupled scalar field. However, in general, initially small effects can accumulate over time and lead to a breakdown of perturbation theory calling for the use of the full non-linear theory.

Recently a well-posed initial value problem was formulated for the Horndeski class of theories [191–194], making it possible to evolve the fully non-linear equations of Horndeski numerically. This opens the possibility to model the gravitational waveforms expected in Horndeski gravity, as done in [195], and extend our work on constraining DE/MG parameters with cosmology from Chapters 2 and 3 to the small scale regime. Chapter 5 of this thesis represents a first step in this wider research programme.

Chapter 2

Quintessence priors

The late-time acceleration of the Universe can be characterised in terms of an extra, time dependent, component of the universe – dark energy. The simplest proposal for dark energy is a scalar-tensor theory – quintessence – which consists of a scalar field, ϕ, whose dynamics is solely dictated by its potential, $V(\phi)$. Such a theory can be uniquely characterised by the equation of state of the scalar field energy momentum-tensor. We find the time dependence of the equation of state for a broad family of potentials and, using this information, we propose an analytic prior distribution for the most commonly used parametrisation. We show that this analytic prior can be used to accurately predict the distribution of observables for the next generation of cosmological surveys. Including the theoretical priors in the comparison with observations considerably improves the constraints on the equation of state.

2.1 Introduction

Cosmological observations show compelling evidence that the expansion of the Universe is accelerating [11, 12, 109, 151, 196, 197]. As discussed in Chapter 1, as yet, we have no clear understanding why, but the consensus, for now, is that the way forward is to improve observations. Fortunately, the prospects look good: a slew of powerful surveys mapping out the large scale structure of the Universe over the coming decade should be able to pin down the expansion of the Universe to sub-percent level [198–202].

An effective way of describing the accelerated expansion is to assume that it is driven

by an extra, exotic, source of dark energy, with density $\rho_{\rm DE}$ and pressure, $p_{\rm DE}$. One can then define the equation of state of dark energy as

$$w \equiv \frac{p_{\rm DE}}{\rho_{\rm DE}}\,, \tag{2.1}$$

which can, in general, depend on the scale factor of the universe, a or equivalently, in terms of redshift, $1+z \equiv 1/a$. Characterising the acceleration of the universe can then be translated into finding an accurate description of $w(a)$ [203]. Indeed, current cosmological surveys targeting dark energy have as their primary goal obtaining accurate measurements of $w(a)$.

It is often useful to use a reduced set of parameters that can accurately describe complex behaviour. A notable example is that of primordial parameters arising from inflation. There, one generally has that the evolution of perturbations at early time is governed by an extra field leading to an imprint of quasi-scale invariant perturbations on large scales. These perturbations are incredibly well described by an amplitude, A_S, a spectra index, n_S and a tensor to scalar ratio, r [204]. While one can enlarge this space of parameters, it has been repeatedly shown that these parameters capture the nature of inflationary perturbations with a high degree of accuracy. In particular, one can constrain, using the Cosmic Microwave Background (CMB) for example, the allowed values of (n_S, r) and then consider the subspace in this plane which corresponds to particular types of inflationary models [19, 205–208]. In other words, it is straightforward to identify the physical priors one should apply to $(n_S,\, r)$ for any particular inflationary model.

In this chapter we want to emulate what has been done in the case of inflation and identify an efficient and accurate parametrisation for dark energy models. To do so, we revisit the background parametrisation of the scalar field evolution in scalar-tensor theories of gravity. We will attempt to construct an accurate parametrisation over a wide range of redshifts and then identify the correct, physical, range of values for this parametrisation. In other words, we wish to construct a model for the physical priors, a functional probability distribution function, $P[\vec{\alpha}]$, where $\vec{\alpha}$ is a set of time dependent functions which uniquely describes the family of scalar-tensor theories. Here we focus on the simplest case – quintessence – that is described by a time evolving scalar field, ϕ, with a canonical kinetic

term and a potential, $V(\phi)$ [43, 44, 203, 209] (see also [28, 29] for reviews); in this case, the time dependent function that uniquely characterises a model is $w(a)$. For any particular choice of parametrisation, the problem then reduces to studying the distribution of the corresponding parameters $w(a)$ for a wide range of models (i.e. choices of $V(\phi)$) and initial conditions for the scalar field. What we propose to do here is very much in the spirit of [137] but now we wish to construct a full model for $P[w(a)]$, an approach which can be extended to full scalar-tensor theories further down the line. Note that our method is complementary to what has been done in [130, 134]. While their aim is to reconstruct $w(a)$ from observations, we use theoretical assumptions.

To go about constructing a prior for $w(a)$ one needs to adopt a parametrisation. A wide range of proposals have been put forward that attempt to fully capture its time evolution. We consider the favoured CPL parametrisation, defined in Eq. (1.41). While this parametrisation has proven to be useful in identifying qualitatively different forms of dark energy, it may not necessarily be accurate enough to fully characterise the time evolution of dark energy over a wide range of redshifts. For example, for a particular form of dark energy that we will explore in this chapter – quintessence – we have that $w > -1$ for all a which can be easily violated for certain choices of w_0 and w_a if one chooses to work with Eq. (1.41). We shall see, however, that these concerns are not borne out in practice.

Outline: In Section 2.2 we describe quintessence, presenting the underlying mathematics but also laying out the various possible regimes that have been identified for the equation of state; in Section 2.3 we discuss in some detail how we establish what are physical priors in quintessence models, singling out thawing models as the most natural in terms of intial conditions (barring the existence of tracking behaviour); in Section 2.4 we discuss the approximation scheme we will use, and present how the required accuracy is evaluated and taking particular care to explain any restrictions; in Section 2.5 we work through a range of models to construct an analytic form for the prior function for the equation of state $w(a)$; in Section 2.6 we apply it to a current selection of data, to illustrate the impact the priors have on current constraints on the equation of state; finally in Section 2.7 we discuss our proposal and its caveats.

2.2 Quintessence

Consider as a starting point, the Horndeski action in Eq. (1.9). Even if the final aim, beyond the scope of this work, is to obtain physical priors for this action in full generality, in this chapter we focus on a simpler scenario, quintessence. Quintessence models are a sub-class of Horndeski with the form

$$\begin{aligned} G_2 &= X - V(\phi)\,, \\ G_3 &= 0\,, \\ G_4 &= \frac{1}{2}M_P^2\,, \\ G_5 &= 0\,, \end{aligned}$$

where the reduced Planck mass is $M_P^2 = 1/8\pi G$. By analogy with perfect fluids, we can define the energy density and pressure of the homogeneous quintessence field as

$$\rho_{\rm DE} = \frac{1}{2}\dot{\phi}^2 + V(\phi)\,, \tag{2.2}$$

$$p_{\rm DE} = \frac{1}{2}\dot{\phi}^2 - V(\phi)\,. \tag{2.3}$$

It is useful to follow [137] and rewrite the potential as $V = M_P^2 M_H^2 A U(\phi)$, with

$$U(\phi) = f(\phi) + \sum_{n_{\rm min}}^{n_{\rm max}} c_n \xi_n b_n(\phi)\,, \tag{2.4}$$

where $M_H = 100$ Km s^{-1} Mpc^{-1}, A is the potential amplitude and $f(\phi)$ and $b_n(\phi)$ are a choice of basis functions. The leading order $f(\phi)$ is perturbatively modified by the sum. The lower limit, $n_{\rm min}$, is model specific and the truncation order, $n_{\rm max}$, is randomly chosen. Each perturbation order is weighted by a dimensionless constant, c_n, given by the theory itself and a random contribution from a set of dimensionful constants, ξ_n. These are drawn from a Normal distribution and are meant to increase the different possible $U(\phi)$ expansions. It is useful to rescale $\phi \to M_P\phi$ and $t \to M_H^{-1}t$ so that they are dimensionless.

We can now focus on a homogeneous and isotropic universe where the space-time metric is given by $\mathrm{d}s^2 = -\mathrm{d}t^2 + a^2(t)(\mathrm{d}\vec{r})^2$. The expansion rate can be derived from the Einstein

field equations to give

$$H^2 \equiv \left(\frac{\dot{a}}{a}\right)^2 = \frac{1}{3M_P^2}\left(\rho + \rho_{\rm DE}\right) , \tag{2.5}$$

where the energy density of matter and radiation is ρ. In terms of dimensionless units, the evolution equation for the scalar field is

$$\ddot{\phi} + 3H\dot{\phi} + AU_\phi = 0\,. \tag{2.6}$$

These equations completely define the dynamics of quintessence.

Given the definition of $\rho_{\rm DE}$ and $p_{\rm DE}$, one can use Eqs. (2.1) and (1.41) to determine the equation of state $w(a)$ and $\{w_0, w_a\}$. One can envisage two approaches for calculating the latter two parameters. The first one is to consider a Taylor expansion of $w(a)$ around $a = 1$ (the value of the scale factor today) giving

$$w_0 = \frac{\dot{\phi}^2 - 2AU(\phi)}{\dot{\phi}^2 + 2AU(\phi)}, \tag{2.7}$$

$$\frac{{\rm d}w}{{\rm d}a} = \frac{2A}{\dot{a}\rho_{\rm DE}^2}\left[3U(\phi)\dot{\phi}^2 H + U_{,\phi}\dot{\phi}\rho(\phi)\right]. \tag{2.8}$$

where the subsript "$,\phi$" denotes a partial derivative with respect to ϕ and the dots are derivatives with respect to cosmological time. Alternatively one can simply fit the expression in Eq. (1.41) over a range of redshifts.

It turns out that $\{w_0, w_a\}$ is a useful diagnostic for the types of behaviour that arise. In particular they allow us to distinguish between two broadly different types of regimes [210, 211] (see Fig. 2.1). In the first regime, the equation of state can be different from -1 in the past but evolves towards -1 as the dynamics of the scalar field freezes with the expansion of the Universe. This is often called the *freezing* or *cooling* regime and is satisfied (for special choices of initial conditions) by, for example, potentials of the form $U \sim \phi^n$, $n < 0$. In the second regime, the equation of state starts close to -1 and evolves towards larger values as the Universe expands. Often called the *thawing regime*, it arises, e.g. in potentials of the form $U \sim \phi^n$, $n \geq 0$.

Whether the quintessence field is in the freezing or thawing regime not only depends

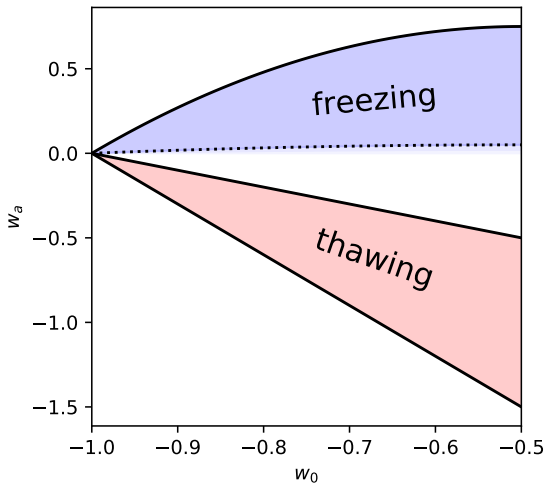


Figure 2.1: A schematic of the loci of *freezing* and *thawing* models on the (w_0, w_a) plane.

on the form of the potential but also depends heavily on the initial conditions one is considering. Furthermore, it is possible to choose potentials such that the intermediate and late-time behaviour is an attractor, independent of initial conditions. Models endowed with this behaviour are known as *tracker* models. In practice, and without tracking, natural initial conditions inevitably lead to thawing behaviour (as we will discuss in Section 2.3) and, in this chapter, we will focus on characterising these models thoroughly.

We consider a comprehensive suite of dark energy models (see [28,29] for a broad range). Building on the choices of [137] we explore and characterise the following subclasses of *thawing* potentials given by Eq. (2.4) and represented in Table 2.1:

Model	$b_n(\phi)$	c_n	$n_{\rm min}$	$f(\phi)$	ϕ_i
Monomial	0	–	–	ϕ^N	$[1,7]$
EFT	ϕ^n	$(\epsilon_{\rm F})^n$	p_E	$\sum_{i=2,4} \xi_i(\epsilon_{\rm F}\phi)^i$	$[1,10]_{\log_{10}}$
Modulus	$e^{\alpha(p_D-n)\phi}$	$(\epsilon_D)^n$	0	0	$[-1,1]$
Axion	$\cos(n\epsilon_{\rm F}\phi)$	$(\epsilon_{\rm NP})^{n-1}$	2	$1+\cos\epsilon_{\rm F}\phi$	$[-\frac{\pi}{\epsilon_{\rm F}}, \frac{\pi}{\epsilon_{\rm F}}]$

Table 2.1: Elements of the potential [Eq. (2.4)] for the studied models. Note that for EFT, $\phi_i \in [1,10]_{\log_{10}}$ stands for $\log_{10}(\phi_i) \in [0,1]$.

Monomial: $V \sim \phi^N$; N can be positive, such as the case of a massive Klein-Gordon field ($N=2$) or a scale-invariant field ($N=4$); or negative. Both cases lead to thawing behaviour, provided one solves the evolution equation from early times. It has been argued that a negative N would lead to freezing behaviour [210,211]; however, this is only true if the initial conditions are set at low redshift (see Fig. 2.2) or the kinetic energy is similar

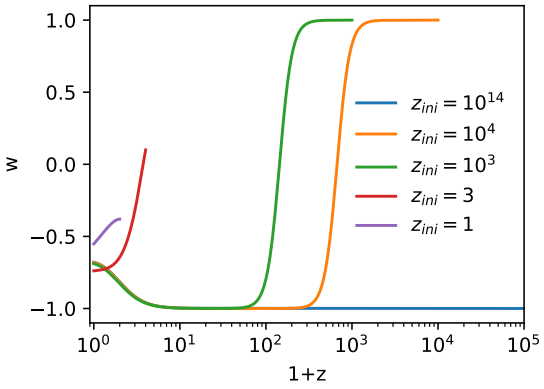


Figure 2.2: Effect of the initial conditions on the dynamics of the model $U \propto \phi^{-2}$ with initial conditions $\phi_i = M_P$ and $\phi_i' \equiv \mathrm{d}\phi/\mathrm{d}\tau|_i = H_0$. Just starting the integration close enough $z = 0$ the initial velocity of the field can survive and yield a freezing behaviour.

to the potential energy at the origin and $V(\phi_i) \gg V(\phi_0)$ (see discussion in next Section). In general, starting from deep inside the radiation epoch, the Hubble parameter is large ($\ddot{\phi} + 3\dot{\phi}H \approx 0$) and freezes the field ($\dot{\phi} = \dot{\phi}_i a^{-3}$), which only starts evolving at late times (thawing). In addition, the early dark energy constraints from CMB and Big-Bang Nucleosynthesis (BBN) ($\sim 1\%$ [22, 212]), limits the maximum value of $\dot{\phi}_i$. Recall that, during kination, $\rho_{DE} \sim \dot{\phi}^2 = \dot{\phi}_i^2 a^{-6}$.

Effective Field Theory (EFT): V is a sum of monomials suitably weighted by the corrected powers of a mass scale consistent with the view that it arises as a consistent low energy limit of a theory. This series represents corrections from operators representing high-energy physics. The series converges if the parameter ε_{F} is small, required by the super-Planckian shift symmetry that imposes $\varepsilon_F < 1$. We will call n_Q to be the number of quantum corrections.

Modulus: $V \sim \epsilon_D^n e^{\lambda_n \phi}$; the vacua potential of theories with higher order dimensions are usually proportional to exponentials of the field [28]. We consider here weighted sums of them, where ϵ_D is the compactification scale. We parametrise $\lambda_n = \alpha(p_D - n)$, so that λ_n can be positive or negative, depending on the order of the term, n, and the positive integer parameter, p_D, and is weighted by α, a positive number of $\mathcal{O}(1)$.

Axion: $V \sim 1 + \cos(\epsilon_{\mathrm{F}}\phi)$ where ϵ_{F} is related to the symmetry breaking scale; these potentials arise in theories where the field is a pseudo-Nambu Goldstone boson. Note that we are interested in a regime different to that in which axions contribute to dark

matter, in which the field oscillates around a minimum of the potential and the equation of state averages to zero.

2.3 Establishing Physical Priors

Before we attempt to construct an efficient and comprehensive parametrisation of quintessence models it is useful to explore the broad characteristics one might expect if one focuses on what we determine to be physical priors. We will focus on $\{w_0, w_a\}$, very much along the lines of [137, 210, 211, 213]. This will allow us to explain and make explicit our choices that then lead to a distribution of dynamical behaviours for each individual model.

We can split the choices into a) cosmological parameters that affect that background evolution b) parameters in the action (or more specifically, the potential $V(\phi)$ and c) initial conditions for the scalar field. With regards to a) we choose to be sufficiently general but not overly so, or the analysis is impractical. This means that we choose to vary cosmological parameters that most directly affect the background evolution and which play off against the scalar field evolution. Specifically, we restrict ourselves to just h (where the Hubble constant is $H_0 = 100\,h\,\mathrm{km\,s^{-1}Mpc^{-1}}$) and the fractional density of cold dark matter today, Ω_{cdm}; We choose the ranges $h \in U[0.6, 0.8]$ and $\Omega_{\mathrm{cdm}} \in U[0.15, 0.34]$. It is important to note that ranges are chosen to be broad enough so that we do not bias our result, but we do not explore regimes that are clearly ruled out by current observations (e.g. $H_0 = 0$) [1]. In particular, Ω_{cdm} priors might seem too broad in comparison with typical constraints. However, they were enlarged to allow for compatible results with tomographic weak lensing constraints from KiDS-450 [214] or CFHTLenS [215], which gave weaker constraints on Ω_m.

With regards to parameters in the potential, the choices are more subtle. In principle one should work within the framework of effective field theory and only include terms ("operators") with a suitable dimensionfull weighting and dimensionless parameters of $O(1)$. Indeed, one of the options makes this philosophy explicit – the case of EFT – and generally we obey this principle. Nevertheless, if used bluntly, this can severely restrict the range of behaviours; indeed it will be overwhelmingly dominated by a cosmological constant. We

[1] The other parameters are left as the hi_class default, i.e. Planck 2013 values. In general, these parameters will have little effect on our result, except, perhaps, for the lack of massive neutrinos, whose effect is degenerate with DE and could have a small impact when used with data.

Parameter	Model	Distribution
A	All	Fixed by $1 = \sum_i \Omega_i$
ξ_n	All	$\mathcal{N}(0, 1)$
N	Monomial	$\mathrm{U}_{\mathbb{Z}}[1, 7)$
$n_{\max}$	Modulus, Axion	$\mathrm{U}_{\mathbb{Z}}[10, 20]$
n_{Q}, p_E	EFT	$\mathrm{U}_{\mathbb{Z}}[5, 10]$
$\log_{10} \epsilon_{\mathrm{F,NP,D}}$	EFT, Modulus, Axion	$\mathrm{U}[-3, -1)$
p_D	Modulus	$\mathrm{U}_{\mathbb{Z}}[1, 5]$
α	Modulus	$\mathrm{U}[0, 1]$

Table 2.2: Parameters distributions. $\mathrm{U}[a, b]$ stands for the uniform distribution between a and b and $\mathrm{U}_{\mathbb{Z}}$ is the uniform distribution in the integers.

take care to allow for more general behaviour to be able to emerge.

We should note that alternatives are permissible where naturalness still plays a role (e.g. in the case of monomial potentials that break shift symmetry) or where other symmetry principles may be at play (as in the case of scale invariant potentials or axion like potentials). Furthermore, more complex operators arising from the low energy limit of higher dimensional theories and their variants (where, for example, factors of $e^{\lambda\phi}$ might emerge) are also considered.

Finally, we need to address the initial conditions for the scalar field. We assume that the initial conditions are established deep in the radiation era and there we can identify two different regimes. In the first case, the expansion of the Universe will have damped the evolution such that, in full generality, $\dot{\phi} = 0$. We can, again, use the view point of effective field theory and assume that the amplitude of the scalar field is of a $O(1)$ in terms of either Planck units or the fiducial mass scale which is used for dimensionful power counting. Alternatively, one can assume that the scalar field "scales" or "tracks" initially, i.e. that its background energy density follows that of radiation. In that case the initial value and velocity is uniquely determined by the background cosmology.

We have chosen these ranges in cosmological and potential parameters as well as in the initial conditions for the scalar field to span as broad a set of possibilities as are physically credible, very much in the spirit of [137]. A list of the ranges is presented in Table 2.2 where the parameters are described in Section 2.2. This does mean that we are excluding what we consider unphysical possibilities such as, for example, starting the scalar field with an arbitrary velocity at some low redshift – there is simply no physical mechanism that

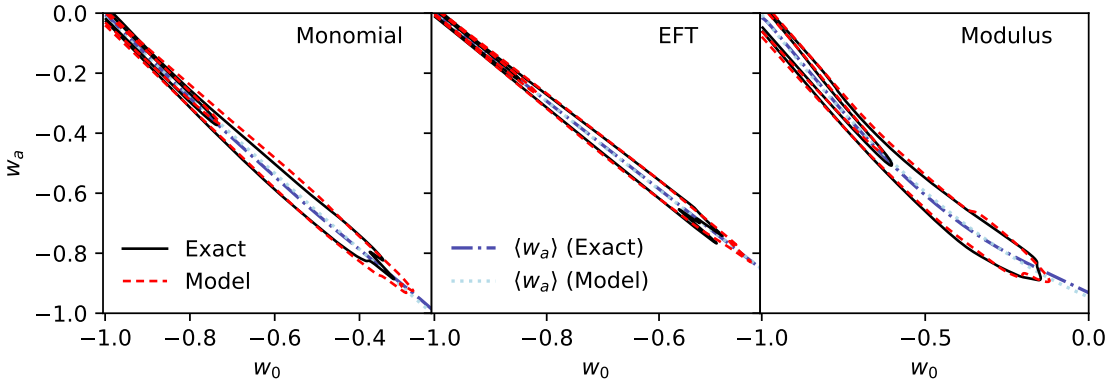


Figure 2.3: w_0-w_a distributions for the Monomial (left panel), EFT (central panel) and Modulus (right panel). All these models have $w_a \neq 0$, while Axion can be described just with $w_0 \leq -1 + 10^{-4}$ (95% C.L.). In this Figure we are comparing the prior distributions found for w_0-w_a fitting the observables (the *Exact*); i.e. minimising Eq. (2.11); and the distributions obtained with our analytic approximation (*Model*), i.e. with Eq. (2.12)-(2.15).

would put it there. Or, for example, we do not consider hugely disparate sets of parameters in the potential, as the small parameters would receive large radiative corrections in the absence of a symmetry protecting them.

We also avoid having too many higher order terms in the potential, controlled by n_{max} and n_Q, as that would make their contribution negligible. In the same way we don't have either too low or too high values of the weighting constants $\epsilon_{F,NP,D}$ that would make the higher order terms either stop contributing or explode. Similarly, we choose α and p_D priors for the Modulus so that the exponent size is controlled, despite allowing for unlikely large values such as e^5. For the monomial case, large N values would make the potential too steep making the field evolve too fast and yielding unphysical or highly tuned results. Finally, the ξ_n constants weigh randomly higher order term in the potential, leading us to take their values from a Normal distribution.

In Fig. 2.3 we can get an idea of the dominant type of behaviour for the class of models we consider, in terms of the equation of state. Focusing, for now, on the solid contours, we can see that these models lead exclusively to thawing models. The only way to change this behaviour (unless the potential tracks the dominant energy density) is to give the scalar field large initial velocities at late time (see Fig. 2.2); these are completely unphysical as they correspond to unacceptable velocities in the radiation era – i.e. there is no physical mechanism for achieving these velocities and hence, such evolution cannot be, in any way

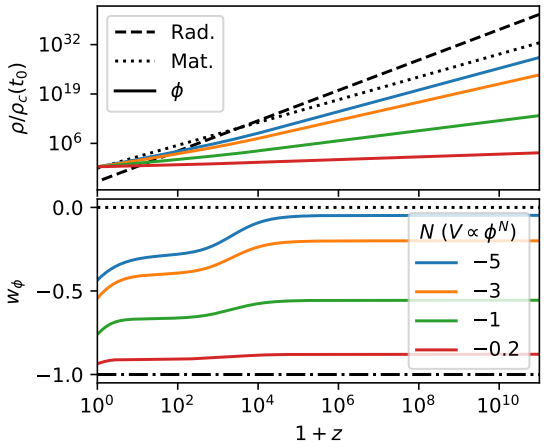


Figure 2.4: Freezing behaviour for inverse power-law potentials (monomial quintessence $N < 0$). Freezing behaviour is possible if the energy density of the field is significant at early times $V(\phi_i) \gg V(\phi_0)$ (upper panel). However, in order to achieve $w(z = 0) \approx -1$ the potential needs to be very flat ($N \approx 0$), a requirement that pushes the model towards a Λ limit (lower panel).

considered part of a set of physical priors. We note that, in the analysis of [213] such unphysical initial conditions were considered by starting the integration of the background at late redshifts ($z = 3$). This prevents the expansion of the universe to dilute the initial conditions and hence the unnatural prevalence of freezing models in their analysis. We also note that this plot pretty much reflects the findings of [137].

Freezing models can be obtained in at least two situations. In tracker models, solutions exist in which the quintessence energy density is a fraction of the dominant matter component, e.g. radiation at early times. This early dark energy contributes to the expansion rate throughout cosmic history and is thus subject to constraints from CMB and BBN [212]. Generic initial conditions will cause the field to be frozen at $\rho_{\rm DE} \sim V(\phi_i)$, entering the tracking behaviour when $V \sim \rho$. A tracking behaviour at all epochs can be achieved through an exponential potential, although a change on $V_{,\phi}/V$ is necessary for the field to freeze in [216, 217]. Other freezing models can be obtained with inverse power-law potential (i.e. monomial with $N < 0$) [218, 219]. In this case the field evolves with a fixed equation of state, rather than track the dominant matter component. However such a simple potential does not successfully freeze to $w \sim -1$ at low redshift unless N is close to zero, effectively recovering the cosmological constant behaviour, cf. Fig. 2.4. In both cases, freezing behaviour requires that the initial conditions for the field are so that

$V(\phi_i) \gg V(\phi_0)$ ($\rho_{\rm DE}(\phi_i) \gg \rho_{\rm DE}(\phi_0)$) – only thawing behaviour can occur if the initial energy density of quintessence is small, as it is the case for the priors used here. Neither purely exponential or inverse power-law potentials can act as viable freezing models – we will leave the study of other potentials with freezing behaviour for a future study.

2.4 Parameterising quintessence

We now proceed to describe the method by which we compress information about the quintessence component in such a way as to retain as much information as necessary for a reliable model comparison or likelihood analysis. In this work, as it is customary, we choose to work with the equation of state w, which enters into the equations of the observables through the energy density as

$$\rho_{\rm DE} = \rho_{\rm DE}^{(0)} \exp\left[-3\int_0^{\log(a)} {\rm d}\log(a')[1+w(a')]\right] . \tag{2.9}$$

The Hubble rate, H, and the angular diameter distance, D_A, only depend on the energy densities:

$$H^2 \propto \sum_i \rho_i \,,$$
$$D_A = \int_0^z \frac{{\rm d}z'}{H(z)} \,,$$

while the growth rate of structure, $f = {\rm d}\ln\delta_M/{\rm d}\ln a$ (where δ_M is the matter density contrast) also depends (mildly) on w,

$$(1+z)\frac{{\rm d}f}{{\rm d}z} = \frac{1}{2}\left(1 - \sum_i \frac{3w_i\rho_i}{H^2}\right) f + f^2 - \frac{3}{2}\Omega_M(z) \,.$$

In choosing a parametrisation, one has to assess how well it approximates the dynamics it is supposed to represent. To do so, one needs some kind of measure. For example, it should be good enough that evolution of distinct classes of models, once parameterised, are easily distinguishable. In practice this means one needs to construct realisations of this evolution (the equation of state, w, in this case) from realistic priors for a particular class of models and check that the parametrisation follows these realisations faithfully and in

such a way that it is clearly distinguishable from another class of models.

There is also a practical guide that guides the quality of the parametrisation. Ultimately we will use it to generate mock observables that will be compared to data. We are looking forward and assuming that the quality of the data will be such that we will have, at most, percent errors on the observables. This means that we should aim to have a parametrisation which is accurate at the sub-percent level but not much more. Another way of stating it is that the systematic errors arising from our modelling of the dark energy evolution (through the parametrisation) should be of the same order as (or marginally smaller than) the statistical and systematic errors arising from the observations themselves.

We will use the latter criteria as a practical guide in determining the quality of our parametrisation. The observables we will focus on are the angular diameter distance, $D_A(z)$, the growth rate, $f(z)$, and the Hubble parameter, over the range of redshifts which will be covered by the next generation of data sets. This is key (and a novel aspect) of the approach in this chapter.

Our starting point is a finite series expansion of w,

$$w = \sum_{m=0}^{M} c_m (1-a)^m \,, \tag{2.10}$$

Note this parametrisation does not break at high order and that higher terms contribute more at early times ($a \to 0$). It will be convenient to denote $\mathbf{c} = (c_1, c_2, \cdots, c_m)$.

While it is clear that the larger the number of coefficients (i.e the larger the M), the more accurate the parametrisation, we, naturally, want to come up with the most economical parametrisation. Even though the equation of state can have a difficult evolution, the results of [137] and the fact that it will only be relevant when dark energy is not negligible, lead us to believe that it should, universally, be described by a combination of a few smooth functions. We shall see that, for thawing models of quintessence, which is the focus of this work, the parametrisation of Eq. (1.41) is sufficient. This means we need to find a probabality distribution function for $\{w_0, w_a\}$, $\mathcal{P}[w_0, w_a]$.

Our approach is as follows [2]. For each class of theories, we generate a large number of possible evolutions for w, using the approach described in Section 2.3. We work with

[2]Our code can be found in https://gitlab.com/ardok-m/horndeski-priors

hi_class [220, 221], a modified version of the Boltzmann code CLASS [222] that incorporates Horndeski theories [60–62], to solve the cosmological equations and obtain the exact observables for each realisation. In addition, the parameters of the model must be chosen so that we are able to reproduce the phenomenology of the given model, with mild restrictions based on stability and more fundamental physics. Given an ensemble of models, parameters are obtained fitting w_0 and w_a so that they minimise the error on the observables at specific redshifts; i.e. minimising

$$\chi^2 = \sum_i \frac{(\mathcal{O}(\vec{c}) - \mathcal{O}(\phi))_i^2}{\sigma^2_{\mathcal{O}_i}}\,, \tag{2.11}$$

where $\mathcal{O}(\phi)_i$ stands for the exact D_A, H and f at the specific redshift z_i, computed solving the field equation and, therefore, depends on the specific choice of the model parameters in Table 2.1. On the other hand, $\mathcal{O}(\vec{c})$ stands for the observables computed using the parametrised w. As we will see, $\mathcal{O}(\vec{c}) \equiv \mathcal{O}(w_0, w_a)$. Finally, $\sigma_{\mathcal{O}_i}$ is the desired precision, which, in all cases, we choose it to be lower than 1% at low redshift (i.e. $z < z_{low} = 10$) [198, 199, 201], and 0.3% at recombination for D_A [223]. Note that, using the parametrisation it is possible that w crosses $w = -1$. To allow for such models that, however, reproduce the observables accurately, we use the fluid equations with the parametrised post-Friedmann (PPF) approximation [224], already implemented in CLASS.

Eq. (2.11) neglects the fact that the observables are, in general, correlated. However, we can safely disregard this contribution as Eq. (2.11) suffices to achieve the goal precision. This will be seen in following Section.

With this machinery in hand, we can study the probability distribution functions (PDFs) of $\{w_0, w_a\}$ and from them we are able to generate the PDFs for the observables, D_A, H and f.

2.5 Results

We now proceed to construct a distribution function for w_0 and w_a. To begin with, we generate ensembles of cosmologies for each of the models. We follow the procedure we discussed in Section 2.3 to generate 20,000 realisations for each class of models, which

we have seen is enough to produce stable results. Given the extra accuracy we need for $D_A(z_{rec})$, we weight the low redshift observables with $\sigma_{\mathcal{O}_i} = 10^{-3}$ and $\sigma_{D_A(z_{rec})} = 10^{-4}$ for the angular diameter distance point at recombination in Eq. (2.11). Do not confuse these variables with the maximum allowed errors. They are set lower to ensure the maximum errors are below our threshold (i.e. 1% at low redshift and 0.3% for $D_A(z_{rec})$).

Revisiting Fig. 2.3, we note that the contours for $\{w_0, w_a\}$ all have similar characteristics: a long degeneracy direction (given by the dotted line) towards the bottom right while a reasonable tight distribution along the (quasi)-orthogonal direction. This is characteristic of thawing models, as has been previously observed in [137, 225]. In the end, the field evolution for thawing models is just a slow (to be physically viable) roll down of the potential and, consequently, produces similar effects. We will exploit this structure further down.

To begin with, as explained before, we check the quality of this parametrisation by generating our proxies for the observables, now with $\{w_0, w_a\}$ and comparing, model by model, with the original full calculation. In Fig. 2.5 we can see that, apart from a very few outliers, most models lie well within our target precision. In other words, using $\{w_0, w_a\}$ we generate observables which agree with those calculated from the full evolution to better than our threshold. This gives us confidence that describing $w(a)$ in terms of two parameters is good enough for any of the planned surveys.

It is interesting to see how well the parametrised $w(a)$ approximates the full one as a function of redshift. In Fig. 2.6 we plot the maximum deviation between the two. We can see that for $z > 1$, the differences are appreciable. This is, of course, to be expected. The dark energy density at those redshift is sufficiently subdominant and will contribute very little to the observables.

With the distributions in hand for $\{w_0, w_a\}$ we can construct an analytic model. We assume that the distribution can be factorised into

$$\mathcal{P}[w_0, w_a] = \mathcal{P}[w_a|w_0]\mathcal{P}[w_0]\,. \tag{2.12}$$

We can see in Fig. 2.7, the $\mathcal{P}[w_0]$ for each model (solid line) is sharply peaked at $w_0 = -1$.

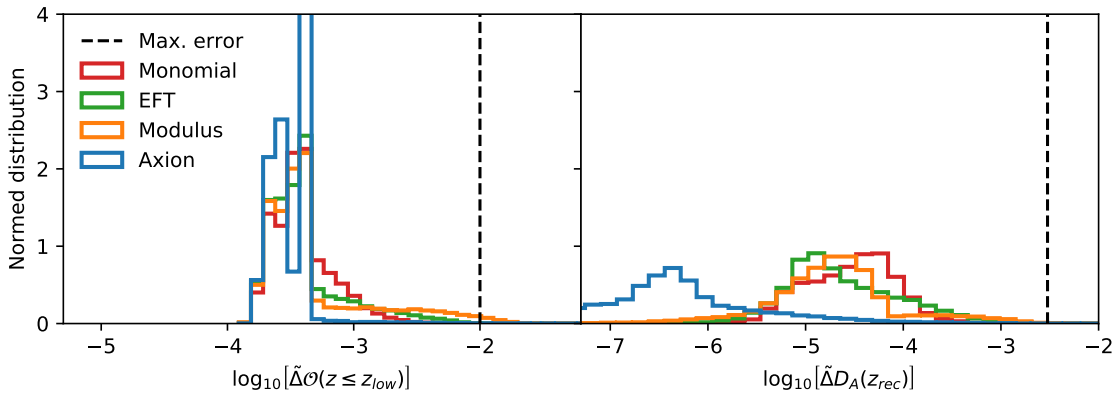


Figure 2.5: Distribution of the maximum relative error of the observables for each Quintessence model compared to its fit in the $w_0 - w_a$ plane, i.e. $\tilde{\Delta}\mathcal{O} \equiv |\mathcal{O}(\text{Fit})/\mathcal{O}(\text{Quintessence}) - 1|$. On the left panel $\mathcal{O}$ stands for any observable among H, f or D_A, whichever gives the maximum error at low redshift ($z < z_{low} = 10$). On the right panel we show the maximum error at recombination for the angular diameter distance $D_A(z_{rec})$.

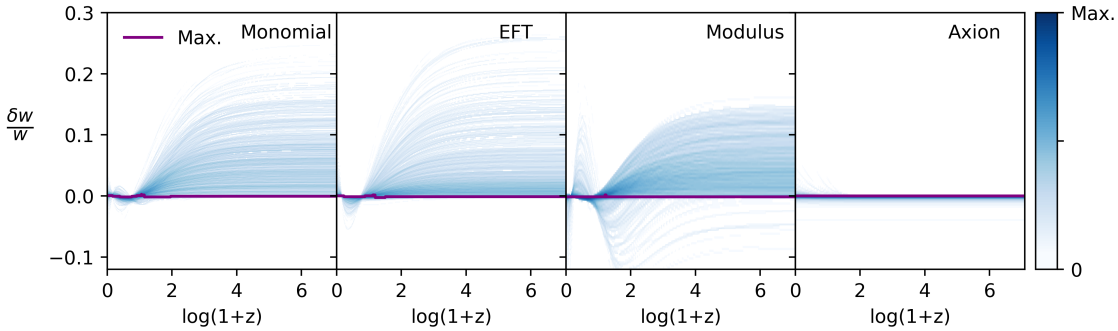


Figure 2.6: Density plots, one for each Quintessence model, showing the time evolution of the relative difference between $w(a)$ obtained from the original realisation and after fitting it in the $w_0 - w_a$ plane. Darker colours indicate the presence of more models with that particular relative difference at that redshift. The purple lines show the maximum density for each model.

While an exponential is a reasonable approximation, we find that

$$\mathcal{P}[w_0] = A_1 e^{-\left(\frac{w_0}{w_1}\right)^{\alpha_1}} + A_2 e^{-\left(\frac{w_0}{w_2}\right)^{\alpha_2}} \tag{2.13}$$

is more robust and can cover more models, where w_1 and w_2 set the widths of the two exponents. In Fig. 2.7 we see that approximate form as a dashed line.

From the contour plots in Fig. 2.3 we can also see that there is a well defined degeneracy direction in $\{w_0, w_a\}$ (the dotted lines). The degeneracy line, $\bar{w}_a(w_0)$ is well approximated

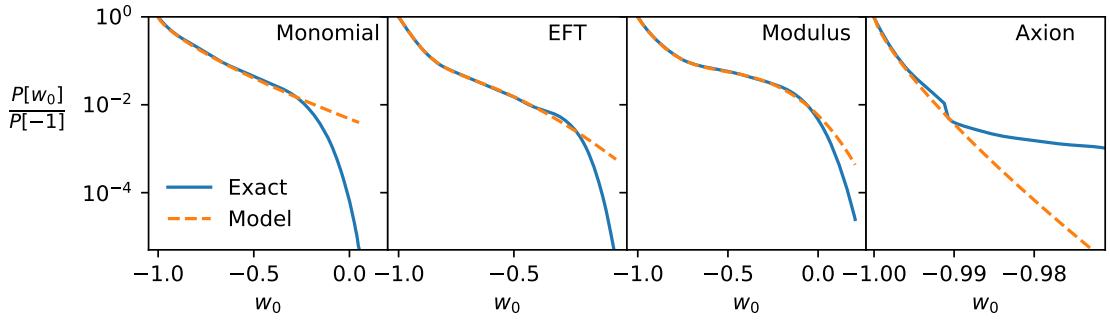


Figure 2.7: For each model, we show the exact (blue solid lines) probability distribution of w_0 normalised to 1 for $w_0 = -1$. The approximate analytic model defined in Eq. (2.13) is also shown (orange dashed lines). It is possible to appreciate the excellent agreement between the two curves down to probabilities of 10^{-2}, which includes the region preferred by the data in most models.

by a quadratic

$$\bar{w}_a(w_0) \simeq \beta_0 + \beta_1 w_0 + \beta_2 w_0^2 \,. \tag{2.14}$$

We now want to look at the conditional probability, $\mathcal{P}[w_a|w_0]$. From Fig. 2.8 we can see that, for each value of w_0, the distribution is peaked around $\bar{w}_a(w_0)$ and well approximated by a Gaussian. We thus use the ansatz

$$\mathcal{P}[w_a|w_0] = \frac{1}{\sqrt{2\pi\sigma^2(w_0)}} e^{-\left(\frac{w_a - \bar{w}_a(w_0)}{2\sigma(w_0)}\right)^2} \,, \tag{2.15}$$

where the variance is given by

$$\sigma(w_0) \simeq \sigma_0 + \sigma_1 w_0 + \sigma_2 w_0^2 \,, \tag{2.16}$$

where σ_i are the constant parameters setting the quadratic. The fits to these parameters for each class of models are given in tables 2.3 and 2.4, respectively. Although they are given with high accuracy, we have found that small changes do not affect the $\{w_0, w_a\}$ distribution and, specially, the distributions of the observables. Nevertheless, we are cautious and use three significant figures. The study of the minimum required accuracy goes beyond the scope of this work.

We can now revisit the contour plots, comparing the original ones with those from our analytical model. In Fig. 2.3 we overlay the two sets and, unsurprisingly, find very close

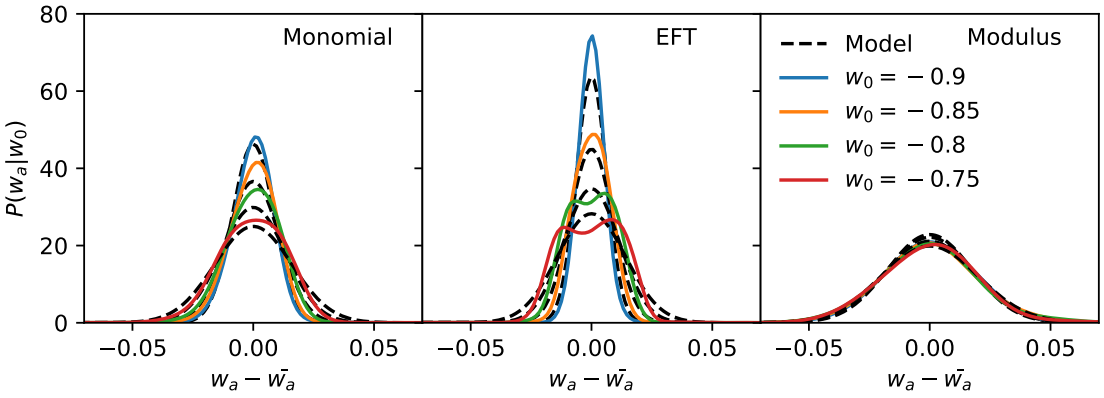


Figure 2.8: For each model, Axion excluded since it can be parametrised solely in terms of w_0, we show the conditional probability distribution of w_a given specific values of w_0 (coloured solid lines). Dashed black lines represent the same curves obtained using our analytic approximation, Eq. (2.15). The parameters of this equation have been obtained through a global fitting. This explains the discrepancy between the solid and dashed curves, but it does not affect the observables as shown in Fig. 2.9.

Model	A_1	w_1	α_1	A_2	w_2	α_2
Axion	737	0.775	-1.08×10^{-3}	0	-	-
Monomial	8.21	0.734	0.102	0	-	-
EFT	12.9	1.01	0.0499	1.05	1.76	0.383
Modulus	8.13	0.890	0.0712	0.535	3.95	0.803

Table 2.3: Fit parameters for $\mathcal{P}[w_0]$ [Eq. (2.13)] model distributions

.

agreement. The final step is now to sample from the analytic priors to generate the observables and compare them with those generated by the full scalar field evolution. In Fig. 2.9 we overlay the contours for the case with the largest differences, i.e. for the Modulus model at redshift $z = 1$. We find an excellent agreement between the two, giving us confidence that the analytic priors can be used as reasonably accurate representation of the quintessence space in future cosmological analysis. It must be noted that we checked the truth of this statement for all models at different redshifts ($z = 0.1$, 0.5, 1.0, 2.0, 5.0, and 10). In section 2.6, we will study the impact of these analytic priors when used in combination with

Model	β_0	β_1	β_2	σ_0	σ_1	σ_2
Monomial	-1.28	-1.21	0.0564	0.0769	0.108	0.0357
EFT	-1.43	-1.35	0.0882	0.0556	0.0577	0.00320
Modulus	-0.946	-0.460	0.481	0.0755	0.121	0.0628

Table 2.4: Fit parameters for $\mathcal{P}[w_a|w_0]$ [Eq. (2.15)] model distributions. Recall that $\langle w_a \rangle(w_0, \beta_i)$ and $\sigma(w_0, \sigma_i)$ are given by Eqs. (2.14) and (2.16), respectively.

.

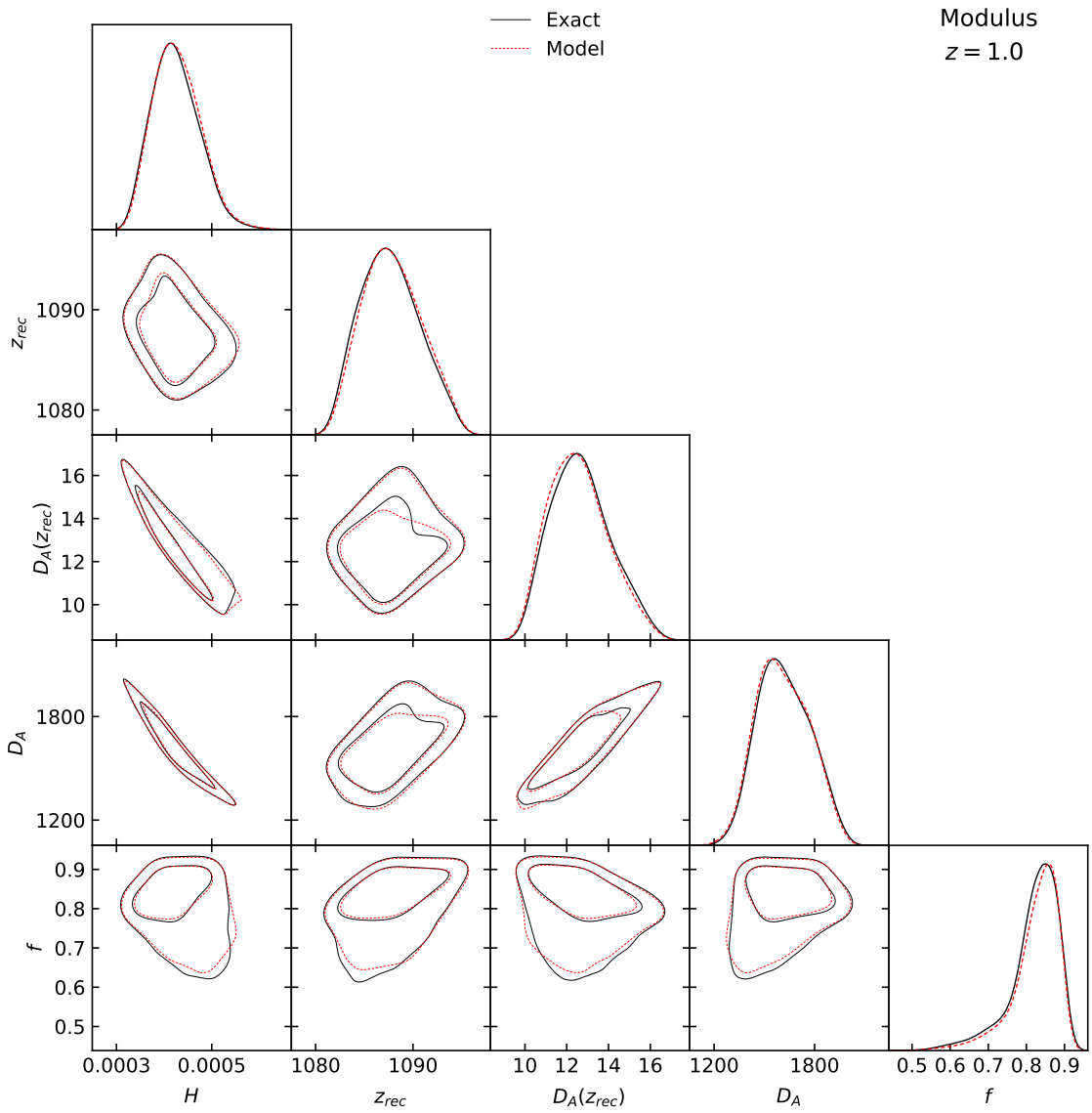


Figure 2.9: Distributions of the observables obtained integrating the field equations of motion (solid black line) compared to those obtained sampling from our parametrisation. These are the results for modulus at redshift $z = 1$, which was the case we found largest differences. However, they are small and will have little impact when the analytic expressions are used in combination with data.

actual data and see that they considerably increase the constraining power of the data.

In general, the analytic expression are stable under changes of the parameters' priors. We checked the stability of the results by approximately doubling or halving the width of the prior distributions and saw that, even though (in a very few cases) the actual numbers change, the new distributions can be still parametrised by Eqs. (2.13) and (2.15). In particular, we saw that Monomial and EFT distributions remain unchanged, while the

distributions for Axion and, more significantly, Modulus varied. The exponential potential of Modulus makes it more sensitive to changes on the field.

In the following lines we summarise some key, individual, features of each model.

Monomial: The two parameters, w_0 and w_a, suffice to reproduce the observables accurately. In fact, minimising the χ^2 with the observables [Eq. (2.11)] yields equivalent distributions to those obtained fitting the actual curves (i.e. w) at low redshift. The probability distribution of w_0, $P[w_0]$, is correctly reproduced with just one of the exponentials in Eq. (2.13). The parametrised w goes to lower values than the original one, meaning that, for a large fraction of the models, one needs $w < -1$ at early times to effectively recover the model.

EFT: The two parameters, w_0 and w_a, suffice to reproduce the observables accurately. In contrast with the monomial case, fitting w at low redshift yields different distributions for the parameters. This is a consequence of faster evolutions of the field close to $z = 0$. In addition, our prior on ϕ_i substantially enlarge the w_0-w_a distribution in comparison with that in [137]. This is a consequence of having initial values of the field considerably lower than $1/\epsilon_F$ and forcing the Friedmann equation to hold today. While in [137] $\phi_i \in [-1/\epsilon_F, 1/\epsilon_F]$ (with $\log_{10}(\epsilon_F) \in [-3, -1]$), we imposed a fixed range $\phi_i \in [1, 10]$; the smaller $(\epsilon_F \phi)^n$ terms that enter into the potential, force the potential to be (substantially) larger, leading to a large derivative, $V_{,\phi}$.

Modulus: The two parameters, w_0 and w_a, suffice to reproduce the observables accurately. The more complicated dynamics are reflected in both the fit performance and the way w is recovered in comparison with the original: the errors on the observables, although good enough, have longer tails relative to other models; in addition, in contrast with previous cases, many models have $w(w_0, w_a) > w(z)$ at early times.

Axion: Just one parameter is needed to reproduce the observables accurately: w_0. In this case, the field remains frozen for almost all its history and just starts moving very close to the present. As in the previous case, $w(w_0) > w(z)$ at early times, in a form that compensates the (small) late-time evolution of the field, but does not change the early universe dynamics.

2.6 Comparison with current data

In this section we present the constraints on the equation of state from current cosmological data and combine them with the analytical priors of the previous section. Let us briefly go through the method. We do a Bayesian analysis, sampling through w_0 and w_a along with the standard cosmological parameters in a Markov Chain Monte Carlo (MCMC) with `MontePython` [226, 227] using the Metropolis-Hastings algorithm [228, 229]. We have used the Gelman-Rubin convergence criterion [230], requiring $R - 1 < 0.01$.

We have used the following datasets:

CMB: From Planck 2015 [24, 25, 231], we use the high l temperature autocorrelation (TT) likelihood, in the range $l = 30-2508$, along with the likelihood of the joint autocorrelations of the temperature (TT), the E and B polarisation modes (EE and BB) and the cross-correlation of the temperature with the E-polarisation mode (TE) for $l = 2 - 29$ and the lensing likelihood (with temperature and polarisation lensing reconstruction) in the multipole range $l = 40 - 400$.

BAO: We use Baryon Acoustic Oscillation (BAO) measurements from 6dFGS survey [149], the Sloan Digital Sky Survey (SDSS) DR7 Main Galaxy Sample (MGS) [150], and BOSS DR12 [151]. The first two measure the expansion history through the redshift-distance and redshift-Hubble relations combined through the relation, $D_{\rm V} = (D_{\rm A}^2(1+z)^2 z/H)^{1/3}$, where $D_{\rm V}$ is the angle-averaged distance, $D_{\rm A}$ - the angular diameter distance and z is the redshift BOSS DR12 constrains both the angular diameter distance, $D_{\rm A}$ and the Hubble parameter, H. We do not consider the correlation between the BOSS measurements and the 6dF and MGS survey as those surveys cover different patches of the sky and hence any such correlation would be negligible.

RSD: We use Redshift Space Distortions (RSD) measurements derived form 6dFGS [232] and BOSS DR12 [151], where for BOSS we use the full covariance between the 3 $f(z)\sigma_8(z)$ measurements at different redshifts and the BAO measurements of $H(z)$ and $D_{\rm A}(z)$.

SNe Ia: We use the new Pantheon Supernovae (SNe) Ia sample [233], which combines observations from the Pan-STARRS1 Medium Deep Surveyat redshift $0.03 < z < 0.65$ with ones from the SDSS, SuperNova Legacy Survey (SNLS), and various low-redshift and HST samples. In total 1048 SNe Ia in the redshift range $0.01 < z < 2.3$.

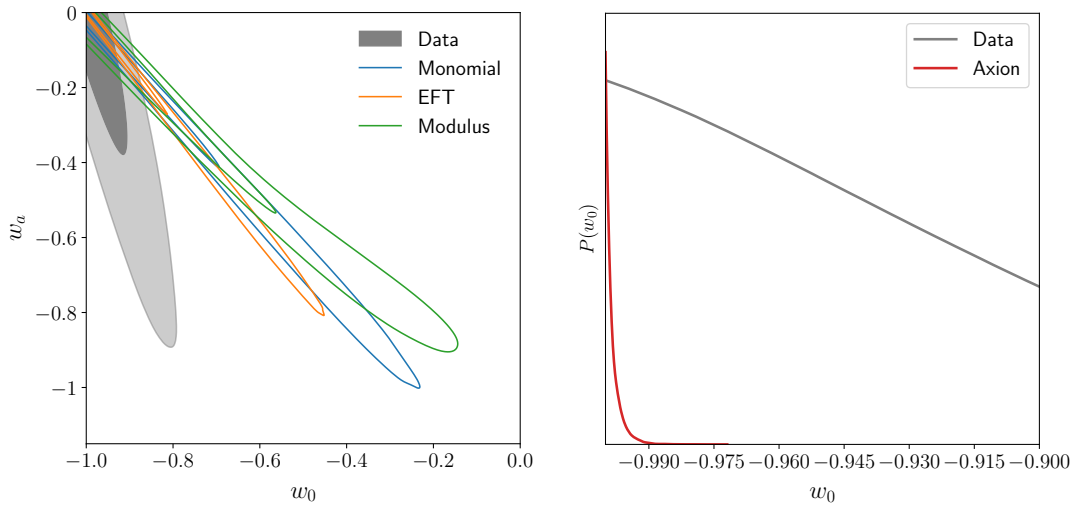


Figure 2.10: Distribution of $\{w_0, w_a\}$ for the CMB+BAO+RSD+SN combined datasets and the theoretical priors. On the left panel we show Monomial, Modulus and EFT and on the right panel Axion quintessence priors.

We note that, throughout, we assume that the cross-correlation between the different datasets is negligible. To obtain the combined constraints from data and theory we implemented the priors as a likelihood module[3] in `MontePython` and plotted the results with the python package for analysing MCMC samples GetDist [234].

We begin by showing the results of a likelihood analysis without including our model for the theoretical priors in the left hand panel Fig. 2.10. The likelihood analysis with uniform priors on the equation of state parameters prefers a distinct direction in the $w_0 - w_a$ plane which, interestingly, is not colinear with the $\bar{w}_a(w_0)$ we derived in the previous section; this is clear from the overlay of the theoretical priors (and was already apparent in [137]). The Axion model, as has been repeatedly mentioned, is a special case, with an equation of state which is very concentrated at $w_0 = -1$. For this model, we compare the widths of the posterior from the likelihood analysis with uniform priors on $\{w_0, w_a\}$ with the theoretical priors studied in this chapter; clearly the theoretical prior is much tighter than the posterior. As mentioned above, Fig. 2.10, to some extent, echoes similar plots used in contour plots for (n_S, r) for constraining the inflationary landscape. There one tends to plot inflationary "tracks" for specific models, overlaying the contours from a likelihood analysis assuming uniform priors for (n_S, r).

[3] Available at: https://gitlab.com/ardok-m/horndeski-priors/tree/master/montepython_lkl_quint_thawing_priors

Data	$w_0 = -1.012 \pm 0.088$	$w_a = 0.05 \pm 0.36$
Data + Mono.	$w_0 = -0.966 \pm 0.027$	$w_a = -0.058 \pm 0.036$
Data + EFT	$w_0 = -0.968 \pm 0.023$	$w_a = -0.040 \pm 0.035$
Data + Mod.	$w_0 = -0.967 \pm 0.025$	$w_a = -0.054 \pm 0.037$
Data + Axion	$w_0 = -0.998 \pm 0.002$	$w_a = 0.0$

Table 2.5: Confidence limits of w_0 and w_a each model from the analysis with data alone (where "Data" is the combination CMB+BAO+RSD+SN), as well as from the combined analysis including also the theoretical priors for each model.

Even though the two sets of contours overlap, i.e. there is no "tension" between them, we do not expect them to be aligned: very different physical considerations go into generating each set. Our choices were broad and uninformative in order to completely explore the phenomenology of the studied models. Furthermore the operational assumptions to build the analytical approximations of the PDF's cannot bias our result as they almost perfectly recover the exact w_0-w_a distributions.

If we invert the perspective and plot the theoretical priors individually and then incorporate them in the likelihood analysis of the current data, we see the power of combining the two. On the left panel of Fig. 2.11, we can see a substantial reduction in the areas of the contours when the data is folded in. We see that the width of the likelihood contours of $\{w_0, w_a\}$ in the analysis that included the theoretical priors is a factor of few times smaller than for the theoretical priors alone. While one would expect the uncertainty in $\{w_0, w_a\}$ for the combination of priors and data to be substantially better than for an analysis with uniform priors and data, we can see how the non-colinearity of the prior and data contours works to our advantage and that, even with current data, combining with theoretical priors gives us greatly improved constraints.

To emphasise the power of including correct theoretical priors, in Table 2.5 we present constraints on $\{w_0, w_a\}$ for the likelihood analysis with uniform priors and with theoretical priors. Clearly there is a dramatic improvement in constraints. For completeness, again, we single out the case of the Axion model (the right panel of Fig. 2.11) to see that in this case the prior is so tightly centred at $w_0 = -1$, combining it with data (also centred at ~ -1) does not improve the constraints significantly.

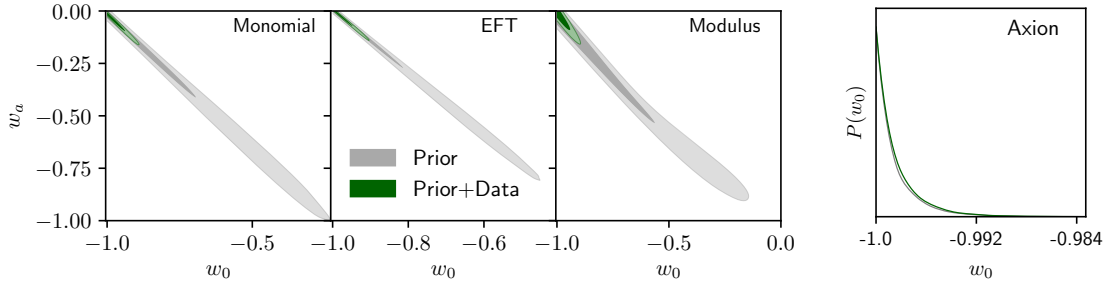


Figure 2.11: Constraints on $\{w_0, w_a\}$ for the four different quintessence models from the CMB+BAO+RSD+SN combined datasets and including the priors.

2.7 Discussion

In this chapter we have proposed a simple, analytic model, for the priors of the equation of state, $w(a)$ of thawing quintessence. We have developed it for four specific thawing models but are confident it could be extended to any thawing model, given the observed similarities on the $\{w_0, w_a\}$ space [137, 225]. It can now be used to either demarcate the physically allowed subset of the $w_0 - w_a$ plane or be incorporated into any future MCMC parameter estimation analysis. In Section 2.6 we have trialled our proposal with existing data.

The prior for the equation of state factorises easily into one probability distribution function for w_0 and another for w_a conditional on the value of w_0. The model we propose is reasonably robust on the choice of fundamental parameters for each theory (i.e. fundamental constants in the quintessence action and initial values of the scalar field). We mean by this that the priors are unchanged when we vary these fundamental parameters or that the shape of the priors remains invariant (albeit with smaller or larger variances). We believe our choice of fundamental parameters is physical, erring on the conservative side. As a result, any future likelihood analysis is greatly simplified and it is no longer necessary to run the full scalar field dynamics to find the correct distribution of $\{w_0, w_a\}$.

One interesting, and important, consequence of having accurate physical priors is that, within the context of thawing models, constraints on $\{w_0, w_a\}$ are greatly improved. While this is not initially surprising – the physical priors we have characterised are much more restrictive than the usual uniform priors one uses for $\{w_0, w_a\}$ – the fact that the orientation of the prior distribution relative to that of the posterior constructed from the uniform prior

with data also plays a key role. In fact, even though the posterior constructed from a uniform prior with data is much broader than the theoretical prior, the fact that they are not co-linear means that combining the two greatly improves the constraints on $\{w_0, w_a\}$ relative to the prior alone. As the data improves, we expect this situation to be further exacerbated.

We have focused on thawing models but our approach must be extended to other models. Within the scope of quintessence, we have touched on tracker models which lead to freezing behaviour (we do not believe non-tracking, freezing models are physically realistic; these models need to be tuned so that $V(\phi_i) \gg V(\phi_0)$ and a sufficiently flat potential to correctly approximate to $w \sim -1$, as is exemplified in Fig. 2.4). Tracking models are not amenable to such a simple parametrisation. One possible reason is due to the "quasi-nonanalyticity" of $w(a)$: in this case, the shape of the equation of state mimics that of rational functions which do not have well behaved Taylor expansions. Nevertheless, there may be alternative ways of parametrising the equation of state (through, for example Pade approximants) that are amenable to the treatment here.

Naturally, we would like go beyond quintessence and we have tried to couch the task in as general way as possible, as a first step in completely characterising Horndeski theories. For the case of quintessence, it has been an easy first step given that quintessence models have been extensively studied for over two decades and there is a detailed understanding of how the scalar field evolves in these scenarios. In the case of more general Horndeski theories, pockets have been studied well (such as Galileons or extended Jordan-Brans-Dicke theories) but a complete, generic framework for the scalar field evolution is still lacking. Only once such a framework is in hand can one start discussing physical priors for the parametrised versions of these theories, the $\mathcal{P}[\vec{\alpha}]$ discussed in the introduction.

Chapter 3

Shift-symmetric Horndeski priors

Attempts at constraining theories of late-time accelerated expansion often assume broad priors for the parameters in their phenomenological description. Focusing on shift-symmetric scalar-tensor theories with standard gravitational wave speed, we show how a more careful analysis of their dynamical evolution leads to much narrower priors. In doing so, we propose a simple and accurate parametrisation of these theories, capturing the redshift dependence of the equation of state, $w(z)$, and the kinetic braiding parameter, $\alpha_{\rm B}(z)$, with only two parameters each, and derive their statistical distribution (a.k.a. theoretical priors) that fit the cosmology of the underlying model. We have considered two versions of the shift-symmetric model, one where the energy density of dark energy is given solely by the scalar field, and another where it also has a contribution from the cosmological constant. By including current data, we show how theoretical priors can be used to improve constraints by up to an order of magnitude. Moreover, we show that shift-symmetric theories without a cosmological constant are observationally viable. We work up to quartic order in first derivatives of the scalar in the action and our results suggest this truncation is a good approximation to more general shift-symmetric theories. This work establishes an actionable link between phenomenological parameterisations and Lagrangian-based theories, the two main approaches to test cosmological gravity and cosmic acceleration.

3.1 Introduction

There is some hope that the evidence of accelerated expansion [11,12,109,151,196,197] is an indication that new physics is at play on cosmological scales. Thus, by characterising the evolution of the Universe in detail [198–202], it should be possible to measure and constrain physical parameters that capture this novel behaviour. As discussed in Chapters 1 and 2, often the new physics associated with these parameters involves an additional scalar field, ϕ.

Scalar-tensor theories of gravity involve a host of possible couplings of the scalar field, both with itself and the metric (see [40, 41, 235, 236] for a review). In principle, it should be possible to constrain such theories with observations, pinning down the fundamental parameters that enter the action. However, given the generality of the construction, the prospects are daunting. It turns out that it is possible to completely characterise a broad class of scalar-tensor models on cosmological scales in terms of a handful of time dependent functions, $\alpha_i(a)$ (as well as $w(a)$), as detailed in Section 1.4.3. A particular Horndeski model can be associated with a choice of w and α_i. In this way, the exercise of constraining scalar-tensor gravity, reduces to finding constraints on these free functions. There have been a number of attempts at constraining these functions but current uncertainties are at around the 10 to 50% level [237–248] (see also related forecasts [249, 250]).

The typical approach for models that use phenomenological functions such as $w(a)$ and the $\alpha_i(a)$ is to assume a parametric form for their evolution and constrain its parameters. The favoured model for w is the Chevallier-Polarski-Linder (CPL) parametrisation in Eq. (1.41). There exist a number of well-motivated parametrisations of $\alpha_i(a)$ that assume these functions scale in some way with the fractional density parameter of dark energy (DE), $\Omega_{\rm DE}$, or the scale factor, a (see e.g [90, 237, 241, 250–255]). However, what is often overlooked by making such a choice is that there are underlying physical models which may limit the ranges (and behaviours) of these functions. One way of putting this is that the underlying physical model will impose quite strict physical priors on these functions and these should be taken into account when undertaking parameter constraints with cosmological data.

In Chapter 2 we tackled this problem in the case of thawing quintessence where, re-

markably, we could construct an analytic prior for $w(a)$. By parametrising it as Eq. 1.41, we found that if $\{w_0, w_a\}$ were chosen to fit the observables, those could be reproduced with the accuracy required by next-generation surveys up to recombination. Furthermore, the prior, $\mathcal{P}$, was factorisable, $\mathcal{P}[w_0, w_a] = \mathcal{P}[w_a|w_0]\mathcal{P}[w_0]$ and the shape of $\mathcal{P}$ was such that it was not collinear with current constraints on $\{w_0, w_a\}$ and thus, if incorporated could reduce the uncertainties in w by up to an order of magnitude.

Emboldened by what we have found in the case of thawing quintessence, we now wish to generalise this approach to more general scalar-tensor theories. From the outset, it is a somewhat challenging task to construct a multidimensional probability distribution function for w and α_i. We have therefore established a more modest goal and focused on a sub-class of theories that are shift-symmetric, i.e. theories which are invariant under a scalar field transformation of the form

$$\phi \to \phi + C\,, \tag{3.1}$$

where C is a constant. Such theories are, in a sense we will make more precise below, well-defined and natural. In this case, the theory is completely determined by $w(a)$, $\alpha_{\rm B}(a)$ and $\alpha_{\rm K}(a)$; however, it is well known that $\alpha_{\rm K}(a)$ is unconstrained by observations [237], so we are seeking a prior distribution function for $w(a)$ and $\alpha_{\rm B}(a)$. As we will see, exploring this restricted set of scalar tensor models already sheds light on the hurdles we need to tackle in the general case. Note that, motivated by recent observations [94, 256, 257] and associated theoretical bounds [95–98], in the above we have implicitly required that the speed of gravitational waves is luminal.

Outline: In Section 3.2 we outline the theoretical aspects of and motivation for the shift-symmetric Horndeski model that we focus on here. In Section 3.3 we justify the choice of physical priors we impose on the theory. In Section 3.4 we describe the approximation scheme we use here and explain how we evaluated the required accuracy. Further, in Section 3.5 we present the constructed prior functions on w and $\alpha_{\rm B}$. In Section 3.6 we combine these priors with a set of cosmological data. Finally in Section 3.7 we discuss our findings.

3.2 Shift-Symmetric Scalar-Tensor Gravity

Here we extend the work in Chapter 2 and focus on the more general sub-set of Horndeski theories: the *shift-symmetric* model. This subset of theories is also known as 'weakly broken Galileons' [258], since the shift symmetry ensures that radiative corrections are parametrically suppressed around (quasi) de Sitter backgrounds, reminiscent of non-renormalisation theorems for Galileons [259, 260].[1] By focusing on this subset of solutions we are therefore already implicitly ensuring that a theoretical prior requiring the radiative stability of the theory is satisfied.[2]

As we are ultimately interested in investigating concrete cosmological observables for shift-symmetric Horndeski theories (and the effect theoretical priors have on them), we need to choose a concrete parametrisation of the (in principle infinite) freedom inherent in the G_i functions [Eq. 1.10]. As a concrete illustration we therefore focus on the following subset of theories

$$\begin{aligned} G_2 &= c_{01}X + \frac{c_{02}}{\Lambda_2^4}X^2, & G_3 &= -\frac{1}{\Lambda_3^3}(d_{01}X + \frac{d_{02}}{\Lambda_2^4}X^2)\,, \\ G_4 &= \tfrac{1}{2}M_P^2, & G_5 &= 0\,. \end{aligned} \tag{3.2}$$

belonging to the Kinetic Gravity Braiding (KGB) [63] class. Here the reduced Planck mass is $M_P^2 = 1/8\pi G$ and conventionally $\Lambda_2^4 = M_{\rm P}^2 H_0^2$, $\Lambda_3^3 = M_{\rm P} H_0^2$, ensuring all the above interactions can give $\mathcal{O}(1)$ contributions to the cosmological background evolution today. The choice for G_4 and G_5 is dictated by constraints on the speed of gravitational waves [92–94, 256, 257] – see [95–98] and references therein for why this implies the above restrictions on the G_i, at least as long as the cosmological Horndeski theory is valid up to energy scales of Λ_3 [262]. For $G_{2,3}$ we keep the first two orders in X, where the c_{01} and d_{01} terms capture the Galileon symmetric contributions, while the c_{02} and d_{02} capture the lowest order (in X) shift-symmetric corrections to this.[3] This will afford us with a fairly

[1] Although see [242, 261] for examples of shift-symmetry breaking theories that maintain this property.

[2] By this we mean radiative stability of the Horndeski scalar interactions considered here. We have nothing new to say about the old cosmological constant problem.

[3] If higher order terms in X/Λ_2^4 are suppressed (while terms such as $(\Box\phi)^n/\Lambda_3^{3n}$ are not), then this will fully capture the leading order terms as well as next-to-leading-order corrections for a generic $G_{2,3}$. If higher-order terms are not suppressed and e.g. all powers of X/Λ_2^4 equally contribute to $G_{2,3}$, this is not the case. A truncation like Eq. (3.2) is therefore not generically valid, but instead it should be viewed as a specific illustrative example of a shift-symmetric Horndeski theory.

minimal, yet suitably rich testbed in which to investigate the effect of theoretical priors on shift-symmetric Horndeski theories. Note that, for simplicity, we have excluded the (equally shift-symmetric) tadpole term $c_{10}\phi$ in our test case, Eq.(3.2). The shift-symmetric model has been explored previously in Refs. [263] and [264], where the authors put cosmological constraints on the parameters of the model, defined in Eq. (3.2), and on the parameters of the shift-symmetric generalisation of the Cubic Covariant Galileon model, respectively.

We will be considering a homogeneous and isotropic cosmological (FRW) background solution, $\mathrm{d}s^2 = -\mathrm{d}t^2 + a^2(t)(\mathrm{d}\mathbf{x})^2$, populated by matter, radiation and the dark energy scalar ϕ. The Friedmann equations then are

$$H^2 = \frac{1}{3M_{\rm P}^2}\rho_{\rm tot}\,, \qquad\qquad \dot{H} = -\frac{1}{2M_{\rm P}^2}\left(\rho_{\rm tot} + p_{\rm tot}\right)\,, \tag{3.3}$$

where $H \equiv \dot{a}/a$ as usual, $\rho_{\rm tot} = \rho_m + \rho_r + \rho_\phi$ and $p_{\rm tot} = p_r + p_\phi$ (subscripts refer to matter, radiation and dark energy, respectively). For Eq. (3.2), $\rho_{\rm DE}$ and $p_{\rm DE}$ then satisfy

$$\begin{aligned}
\rho_\phi &= \frac{1}{2}\left(c_{01} + \frac{3}{2}\frac{c_{02}}{\Lambda_2^4}\dot{\phi}^2\right)\dot{\phi}^2 - \frac{3}{\Lambda_3^3}\left(d_{01} + \frac{d_{02}}{\Lambda_2^4}\dot{\phi}^2\right)H\dot{\phi}^3, \\
p_\phi &= \frac{1}{2}\left(c_{01} + \frac{1}{2}\frac{c_{02}}{\Lambda_2^4}\dot{\phi}^2\right)\dot{\phi}^2 + \frac{1}{\Lambda_3^3}\left(d_{01} + \frac{d_{02}}{\Lambda_2^4}\dot{\phi}^2\right)\dot{\phi}^2\ddot{\phi}\,.
\end{aligned} \tag{3.4}$$

Note that in the case where we include a cosmological constant Λ, described in more detail below, the dark energy density, $\rho_{\rm DE}$, and pressure, $P_{\rm DE}$, will have a contribution from Λ in addition to ϕ. However, in both cases we take $w(a) = P_\phi/\rho_\phi$.

The background scalar equation of motion can be written in terms of a conserved current [90] as

$$\dot{J} + 3HJ = 0\,, \tag{3.5}$$

where

$$J = \left(c_{01} + \frac{c_{02}}{\Lambda_2^4}\dot{\phi}^2\right)\dot{\phi} - \frac{3}{\Lambda_3^3}\left(d_{01} + \frac{d_{02}}{\Lambda_2^4}\dot{\phi}^2\right)H\dot{\phi}^2\,. \tag{3.6}$$

There are a few key points to note about the background evolution. First of all, we have that Eq. (3.5) implies that there is a tracker solution as $J \propto a^{-3} \to 0$ as a grows.

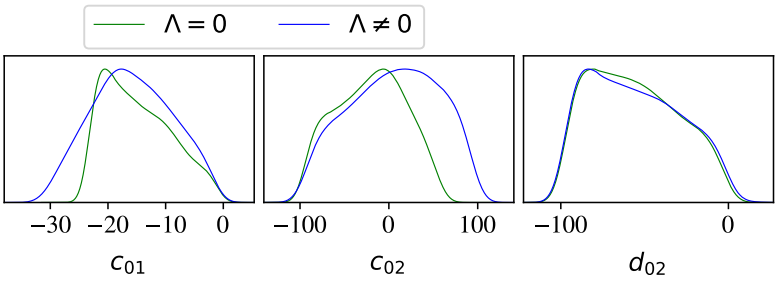


Figure 3.1: Distributions of the parameters of the action for the $\Lambda = 0$ (green) and $\Lambda \neq 0$ (blue) variants of the shift-symmetric model, where we have fixed $d_{01} = -1$. $\Lambda = 0$ is the first version of shift-symmetric theories we consider, where there is no explicit cosmological constant, Λ, and the density of DE is given solely by the scalar field ϕ; in the case of $\Lambda \neq 0$, Ω_{DE} has contributions both from ϕ and Λ.

This greatly simplifies the dynamics and, as we will reiterate further down, the priors we need to assume on the various ingredients of this model. Second, we will consider two versions of this theory. In the first version the scalar field is entirely responsible for the late-time acceleration and thus there is no explicit cosmological constant, Λ (or a constant term V_0 in the scalar field potential); we will dub this the $\Lambda = 0$ *self-accelerating* version. [4] The $\Lambda = 0$ version is, in some sense, the more interesting as it can be invoked as an alternative to cosmological constant driven acceleration. But we also have experience from other theories that self-accelerating solutions are more tightly constrained and potentially easier to rule out (for example in the case of GDP gravity [265–268]). This means that the dark energy density is solely given in terms of the energy density associated to the scalar field: $\Omega_{\rm DE} = \Omega_\phi$.

A key aspect of self-accelerating solutions is that they require "negative kinetic energy" $G_2 < 0$, at least in the class of theories under consideration [63]. For shift-symmetric Horndeski theories up to cubic term (Kinetic Gravity Braiding), the energy density can be written as [63]

$$\rho_\phi = \dot{\phi} J - G_2 \to -G_2 \,, \tag{3.7}$$

where the latest limit corresponds to the tracker solution. Because G_2 is even in $\dot{\phi}$, $\rho_\phi > 0$ requires that at least one of c_{01}, c_{02} to be negative (the tracker condition $J = 0$ on Eq. (3.6) might impose further constraints on the relative signs). We will find that generically

[4] We mean self-acceleration in the sense that the scalar field provides accelerating expansion, i.e. $w_\phi < -1/3$. Note that some authors use the term self-acceleration to mean that only the Jordan-frame scale factor is accelerating (while its Einstein-frame counterpart is not) [260]. This can not be the case in the theory at hand, as both frames are equivalent.

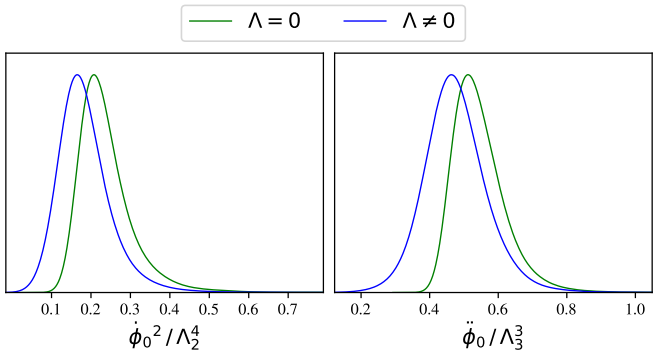


Figure 3.2: Distributions of the parameters of $\dot{\phi}_0^2/\Lambda_2^2$ and $\ddot{\phi}_0/\Lambda_3^3$, where ϕ_0 is the amplitude of the scalar field today. The fact that they are lower than 1 means that higher order terms in our expansion of the Lagrangian, Eq. (3.2), should be suppressed unless large values of the coefficients $\{c_{ij}, d_{ij}\}$ were chosen. Therefore, this could be seen as a posteriori justification of our ansatz, Eq. (3.2).

$c_{01} < 0$, i.e. the "wrong" sign of the standard kinetic term, Fig. 3.1. This means that Minkowski space with $\dot{\phi} = 0$ is not a stable solution of these models nor can we apply the usual battery of consistency conditions that have been developed in the standard vacuum (see discussion in the next section). [5]

Another interesting feature of the self-accelerating solutions is illustrated in Fig. 3.2. There we can see that both $\dot{\phi}_0^2/\Lambda_2^4$ and $\ddot{\phi}_0/\Lambda_3^3$ are smaller than unity. This is encouraging in that it provides a posteriori justification for our ansatz, Eq. (3.2): the higher order terms omitted in Eq. (3.2) scale with higher powers of $\dot{\phi}_0^2/\Lambda_2^4$ and $\ddot{\phi}_0/\Lambda_3^3$. So if these higher powers are indeed suppressed, then omitting higher order terms in the first place is consistent. This is also related to the above discussion of the sign of c_{01}. If higher order terms with coefficients c_{0i} and $i > 1$ are increasingly suppressed, then obtaining a positive scalar energy density, Eq. (3.7), with positive c_{01} becomes very challenging. Note, however, that the suppression illustrated in Fig. 3.2 is rather mild and can easily be compensated for by coefficients c_{ij} and d_{ij} that are somewhat larger than unity. Fig. 3.1 shows that this is in fact the case for the lower order interactions in our ansatz, Eq. (3.2), so we emphasise that our findings here are certainly not conclusive evidence that the higher order interactions omitted cannot yield $\mathcal{O}(1)$ contributions to the scalar energy density or the background and perturbative evolutions in general.

[5] The theories under consideration have some other generic properties: for instance the equation of state is phantom $w_\phi < -1$ in the tracker, approaching de Sitter $w_\phi \to -1$ from below as $\rho_m \to 0$ [63].

The second variant that we will consider does include Λ; we will dub it the $\Lambda \neq 0$ version. In this case the signs of c_{01}, c_{02} are less restricted by requiring the scalar field to dominate the expansion, Eq. (3.7). If we were to restrict ourselves to $c_{01} > 0$ (which we do not here) we would be looking at what is conventionally dubbed the normal branch. In the cubic Galileon limit (c_{02}, $d_{02} = 0$) $\Omega_\phi > 0$ requires $c_{01} < 0$, in agreement with Eq. (3.7). Normal-branch Galileons ($c_{01} > 0$) are driven towards a trivial tracker with $\dot{\phi} \to 0$, $\rho_\phi \to 0$ unless shift-symmetry is broken [269]. We will not fix a sign of c_{02} to be able to capture more general behaviour in the $\Lambda \neq 0$ case. Note that the cosmological constant is allowed and does not break shift symmetry. Here the dark energy density is the sum of the energy density associated to the scalar field and the cosmological constant: $\Omega_{\rm DE} = \Omega_\phi + \Omega_\Lambda$.

As we will focus on large scale observables, we are particularly interested in linearised perturbations around the cosmological background solution described above. The freedom in the dynamics of such perturbations for a general Horndeski theory, as specified in Eqs. (1.9) and (1.10), is controlled by just four functions α_i of time with $X \in \{K, B, M, T\}$. For the general form of these α_i see [90]. In the shift-symmetric subset of theories we are considering here, with $G_{4X} = 0 = G_{5X}$, we find that the effective Planck mass seen by linear perturbations is simply $M_{\rm P}$ (and hence has no time-dependence), while the speed of gravitational waves $c_{\rm GW} = 1$ by construction. We are therefore left with only two non-trivial α_i controlling linear perturbations, namely

$$\begin{aligned} H^2 M_P^2 \alpha_{\rm K} &= 2X \left[G_{2X} + 2X G_{2XX} + 6\dot{\phi} H \left(G_{3X} + X G_{3XX} \right) \right], \\ H^2 M_P^2 \alpha_{\rm B} &= 2X \dot{\phi} H G_{3X}, \end{aligned} \tag{3.8}$$

where all functions are evaluated at the background level. Upon substituting Eq. (3.2) into Eq. (3.8), it is then straightforward to express these two α_i in terms of the c_{ij}, d_{ij} in Eq. (3.2) and the background degrees of freedom, a and ϕ.

3.3 Establishing Physical Priors

It has been well established that cosmological observables are insensitive to $\alpha_{\rm K}$ [237], a direct manifestation of the fact that $\alpha_{\rm K}$ drops out in the quasi-static limit (which applies to

the vast majority of observable scales at late times) at leading order [250]. The challenge, then, is to construct physical priors for w and $\alpha_{\rm B}$. There are a number of steps in working towards this goal, the first one of which is to map out the space of possible histories for the scalar field ϕ and the metric $g_{\alpha\beta}$. In fact, as we saw in the previous section, w and $\alpha_{\rm B}$ are completely determined in terms of $\phi(t)$ and $a(t)$ so we will only have to focus on the evolution of the background in these theories.

We then have a number of parameters which need to be chosen. The standard cosmological parameters will be included in the analysis, whether we work with the scalar field action directly or we work with the parametrised form, in terms of w and $\alpha_{\rm B}$; therefore, we will not be specially concerned with the choice of their priors; indeed we will consider a standard range such as $\Omega_{\rm cdm} \in [0.15, 0.35]$ and $H_0 \in [60, 80]\,{\rm km\,s^{-1}\,Mpc^{-1}}$, which ensures our findings will be compatible with current constraints of these parameters, while not too broad to explore values that are already ruled (e.g. $H_0 = 0$). We then have the parameters in the action which we have distilled down to $\{c_{01}, c_{02}, d_{01}, d_{02}\}$ and $\{\Lambda_2.\Lambda_3\}$. Two dimensionless $\{c_{ij}, d_{ij}\}$ can be absorbed into the Λ_i. In our concrete implementation, however, we find it more practical to follow a different (yet physically equivalent) prescription and fix $\Lambda_2^4 \equiv M_{\rm P}^2 H_0^2$ and $\Lambda_3^3 \equiv M_{\rm P} H_0^2$, varying only the coefficients $\{c_{01},\, c_{02},\, d_{02}\}$. In order to decouple the effects of H_0 on the coefficients and avoid possible inconsistencies due to the way we choose to sample our parameters, we set this normalisation H_0 to a fiducial value. We use the fact that we can set $d_{01} = -1$ due to the normalization of the field [270]. [6] The physics of the model does not change depending on which of the c_{0i} (up to its sign) and d_{0i} parameters one chooses to fix, and hence our priors would be unaffected by this choice.

And finally, we must also consider the initial conditions of the scalar field, ϕ_i and $\dot{\phi}_i$. As we have seen in the previous section, shift-symmetric theories come endowed with tracking behaviour. This means that irrespective of the initial condition, the field will (quite rapidly) evolve towards a universal solution which is uniquely determined in terms of the coupling constants of the theory. And, because the theory is shift-symmetric, the result is completely independent of ϕ_i. This means that the prior will also be completely

[6] Fixing the sign of d_{0i} bears no loss of generality: because L_3 contains only odd powers of ϕ, changing the sign of d_{0i} is equivalent to flipping the sign in the initial $\dot{\phi}$. In contrast, normalizing the field to fix a coefficient in L_2 restricts the theory, cf. Eq, 11 in Ref. [269].

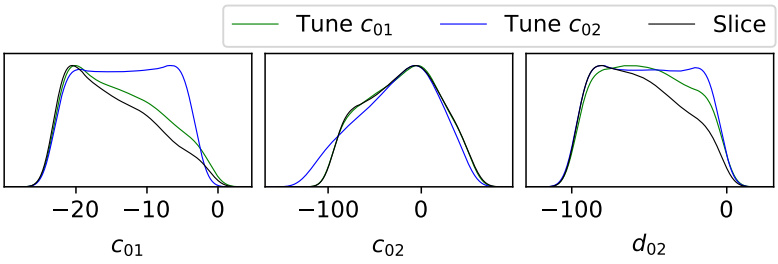


Figure 3.3: Distributions of the parameters given different ways of sampling. In the case of *tuning* one parameter, one samples the other two and chooses the value of the former that result in the desired H_0. In contrast, in the case of *slicing*, one varies the all three parameters simultaneously and keeps only the sets that give $\sum \Omega_i = 1$. As can be seen above, the *tuning* method is subject to projection effects.

independent of ϕ_i and $\dot{\phi}_i$.

With regards to $\{c_{01}, c_{02}, d_{02}\}$, it makes sense to consider uniform, uncorrelated priors over a fixed range; as with all uniform priors, one needs to define hard limits to their ranges. One may expect that naturalness criteria suggest one should only vary these dimensionless constants within a range of $\mathcal{O}(1)$ (around 0). However, note that the shift-symmetric nature of the theories at hand means that radiative corrections to the c_{0i} and d_{0i} are parametrically suppressed [258], more specifically these corrections scale as $\{\delta c_{ij}, \delta d_{ij}\} \sim (\Lambda_3/\Lambda_2)^4 \sim 10^{-40}$ [98, 258]. So considerably wider prior ranges can be explored without running into naturalness issues. We have explored different choices for the ranges of these parameters and have found that, once we allow them to vary within a range of $\mathcal{O}(2)$, the final results are unchanged. We also check that the constraints with data are consistent with these bounds, and indeed we find distributions that are well within the range of $\mathcal{O}(2)$. This confirms that this is a wide enough range so that our results are not biased by the bounds we have chosen, while at the same time we exclude regions of space that are ruled out by data. We use such an extended range in all our subsequent results.

There is a further complication, however, which is that we are interested in cosmologies which are reasonably close to the one we observe, i.e. one in which $\Omega_{\rm r}+\Omega_{\rm m}+\Omega_{\rm DE} = 1$ (note that our definition of $\Omega_{\rm DE}$ differs between the cases with and without Λ); one can loosen this statement and say that we do not want $\Omega_{\rm DE} \simeq 0$ or $\Omega_{\rm DE} \simeq 1$. This immediately imposes additional restrictions on $\{c_{01}, c_{02}, d_{02}\}$. In other words, one can see such a restriction due to $\Omega_{\rm DE}$ as a deformed slab cutting through $\{c_{01}, c_{02}, d_{02}\}$, picking out a lower dimensional

space. Projecting such a cut onto each of the $\{c_{01}, c_{02}, d_{02}\}$ will naturally lead to non-uniform 1-D priors.

One might think that an alternative approach is to solve for one of the $\{c_{01}, c_{02}, d_{02}\}$ for a fixed range of $\Omega_{\rm DE}$ and indeed it is possible to do so using a well established shooting method. Unfortunately the resulting combined priors depend heavily on which of the constants one chooses to solve for. One can understand this if one takes two examples. In one case, one assumes a uniform prior for $\{c_{02}, d_{02}\}$ and solves for c_{01}. The resulting distribution c_{01} will not, generally be uniform. Alternatively one might consider a uniform prior for $\{c_{01}, d_{02}\}$ and solves for c_{02}. Now the prior on c_{01} *will* be uniform while the prior on c_{02} will not be uniform. We illustrate this in Fig. 3.3. This is not surprising as this approach effectively introduces a non-linear correction to the measure which is highly dependent on the constant one is solving for. Thus we have opted to use our original approach – to sample all the parameters and then project down the constraint slice (or slab) [7].

A comment is in order about imposing priors related to the validity of the underlying theory itself. Firstly, these come in the form of stability priors. We have already alluded to radiative stability above and we will complement this by requiring the absence of ghost and gradient instabilities for our cosmological solution, using the implementation of [220]. Note that these instabilities directly manifest themselves in the effective (low-energy and classical) theory we are considering, i.e. Eq. (3.2).[8] Secondly, there are priors not directly linked to any easily recognisable sickness in the low-energy theory, but instead to ensuring that this low-energy theory can be embedded in a sensible UV completion. These bounds turn out to be powerful, even if the UV completion is not known. In this context we will focus on so-called positivity bounds, requiring that the underlying fundamental theory (and hence the UV completion as well) is consistent with a "standard" Wilsonian field theory description – one in which Lorentz invariance, unitarity (well-defined probabilities), analyticity (causality) and polynomial boundedness (locality) are respected. These basic principles turn out to be sufficient in order to derive a variety of additional constraints

[7] Note that, by default, `hi_class` adjusts one of the parameters to fulfil the Friedman equation. In order to prevent this, you must set `Omega_smg_debug` and unset `Omega_smg`.

[8] A direct consequence of this is that instability-infested regions of parameter space generically give very poor fits to the data. In other words, had we not imposed these priors, the data would still generically have excluded these regions of parameter space.

on the low energy parameters of the theory, in our case encoded in the c_{ij} and d_{ij} – see [271–289] for constraints directly applicable to our present scalar-tensor context. The simplest such bounds can be derived via considering tree-level $2 \to 2$ scattering on a flat (Minkowski) background. For general Horndeski theories the resulting bounds are presented in [282]. Specialised to Eq. (3.2), these reduce to

$$\begin{aligned} \bar{G}_{2,XX} \geq 0 \qquad &\Rightarrow \qquad c_{02} \geq 0\,, \\ \bar{G}^2_{3,X} \geq 0 \qquad &\Rightarrow \qquad d^2_{01} \geq 0\,, \end{aligned} \tag{3.9}$$

where a bar denotes that the function is evaluated on a flat background ($\langle\phi\rangle = 0$) and constraints are subsequently ported to cosmological backgrounds. While the second bound is trivially satisfied, the first imposes a non-trivial constraint. However, and crucial to the results of this chapter, these bounds will turn out to *not* be applicable here. This is because we will find that, for our ansatz, Eq. (3.2), cosmological constraints push c_{01} to be overwhelmingly negative. While this condition is consistent with obtaining healthy solutions on cosmological backgrounds, around a flat (Minkowski) space-time it renders ϕ into a ghost. But the existence of a well-defined and ghost-free Minkowski solution is an essential ingredient for the derivation of the above positivity bounds. So, at least for our specific ansatz, Eq. (3.2), we will not be able to identify regions of parameter space here, where observational constraints are satisfied *and* where we can consistently apply the above positivity bounds – for a more detailed discussion see [290].

3.4 Approximating the time dependence of w and $\alpha_{\rm B}$

We now proceed to determine the best way to parametrise the time dependence of w and $\alpha_{\rm B}$. We recall that, in the case of thawing quintessence, we found that $w = w_0 + w_a(1-a)$ was an excellent approximation to the equation of state; this was not the case for tracking quintessence. On the left panel of Fig. 3.4 we plot the two typical shapes of the evolution of w for the shift-symmetric model that we consider; although, on the face of it, the true curve and the fit do not seem to agree particularly well, we find that $w = w_0 + w_a(1-a)$ approximates the evolution of equation of state well enough in a sense that will be clear

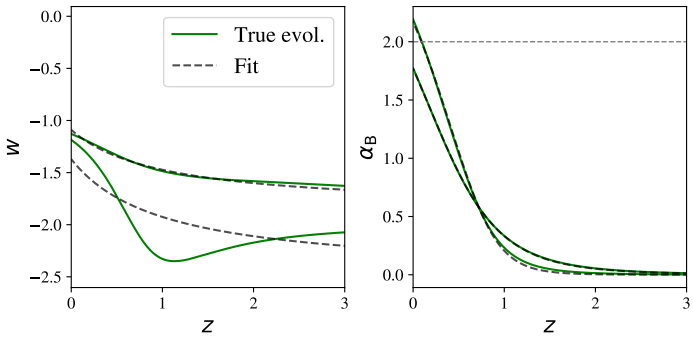


Figure 3.4: The time evolution of w (left) and α_B (right) for two representative models and their approximate fits using the parametrisations we choose. Note that we have highlighted the $\alpha_B = 2$ line here and in the following plots, as evolutions that cross this line (as shown here α_B typically increases monotonically in time) display some singular behaviour – see Appendix A for a more detailed discussion.

soon.

A natural first choice for the time-dependence of α_B was the commonly assumed scaling with fractional density of DE, Ω_{DE}, however, we found this parametrisation to only provide a good fit to a small fraction of the models we calculated. We found similar results for a proportionality with the scale factor, a. A Taylor expansion in terms of either a or Ω_{DE} worked better than a single constant factor, however, in order to reach our desired error for a the majority of models, it was necessary to include at least seven coefficients in the expansion. We had similar success with other parametrisations, such as inverse power law, binomial expansion, exponential power law and others. Finally, we note that in a simplified version of our model, i.e. the cubic galileon,[9] its exact time dependence is $\alpha_B \propto H^{-4}$. The tracker solution, $J = 0$ in Eq. (3.6), provides a solution for the scalar field evolution $\dot{\phi} \propto H^{-1}$, which can be substituted into Eq. (3.8) to get the expected result. It is also possible to prove that this time-dependence approximately holds for a more general case too, i.e. $c_{02} \neq 0$ and $d_{02} = 0$. Therefore we expect that a function of $(H_0/H)^4$ should fit the evolution of α_B in the shift-symmetric case. We find the following function to fit the true models extremely well,

$$\alpha_B = \hat{\alpha}_B \left(\frac{H_0}{H}\right)^{4/m}, \tag{3.10}$$

[9]The cubic galileon model is equivalent to a special case of the shift-symmetric we consider here with $c_{02} = d_{02} = 0$.

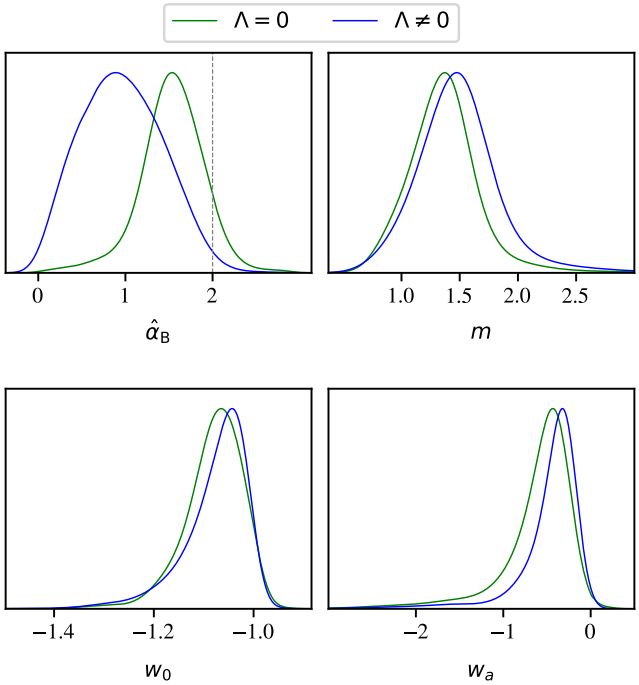


Figure 3.5: Probability distributions of the $\{w_0, w_a, \hat{\alpha}_B, m\}$ parameters obtained minimising Eq. (3.14) as explained in Sections 3.4 and 3.5. The presence of a cosmological constant term in the theory modifies the probability distributions of the parameters. Their correlations can be seen in Fig. 3.9. $\Lambda = 0$ is the case where $\Omega_{DE} = \Omega_\phi$ and $\Lambda \neq 0$ is where $\Omega_{DE} = \Omega_\phi + \Omega_\Lambda$. Fig. 3.1 shows the different distributions of the $\{c_{01}, c_{02}, d_{02}\}$ parameters given these two cases. For details on the vertical line at $\hat{\alpha}_B = 2$ we refer the reader to the Appendix A

where $\hat{\alpha}_B$ and m are constant parameters. On the right of Fig. 3.4 we plot two typical representative α_B and the lines that fit to those given the function that we chose. As will be discussed in more detail in the following section 3.5 this parametrisation fits incredibly well (to less than 1% error) more than 98% of the large set of randomly generated models.

In the spirit of [1], we now want to find the set of parameters $\{w_0, w_a, \hat{\alpha}_B, m\}$ that reproduce the Hubble rate (H), the angular diameter distance (D_A) and the growth factor ($f = \mathrm{d}\ln\delta_m/\mathrm{d}\ln a$),

$$H^2 = \frac{1}{3M_P^2}\sum_i \rho_i\,, \tag{3.11}$$

$$D_A = \int_0^z \frac{\mathrm{d}z'}{H(z)}\,, \tag{3.12}$$

$$f' + f^2 + \left(2 + \frac{\dot{H}}{H^2}\right) f - \frac{3}{2}\Omega_m\left(1 + \frac{\alpha_B^2}{2{c_{sN}}^2}\right) = 0\,, \tag{3.13}$$

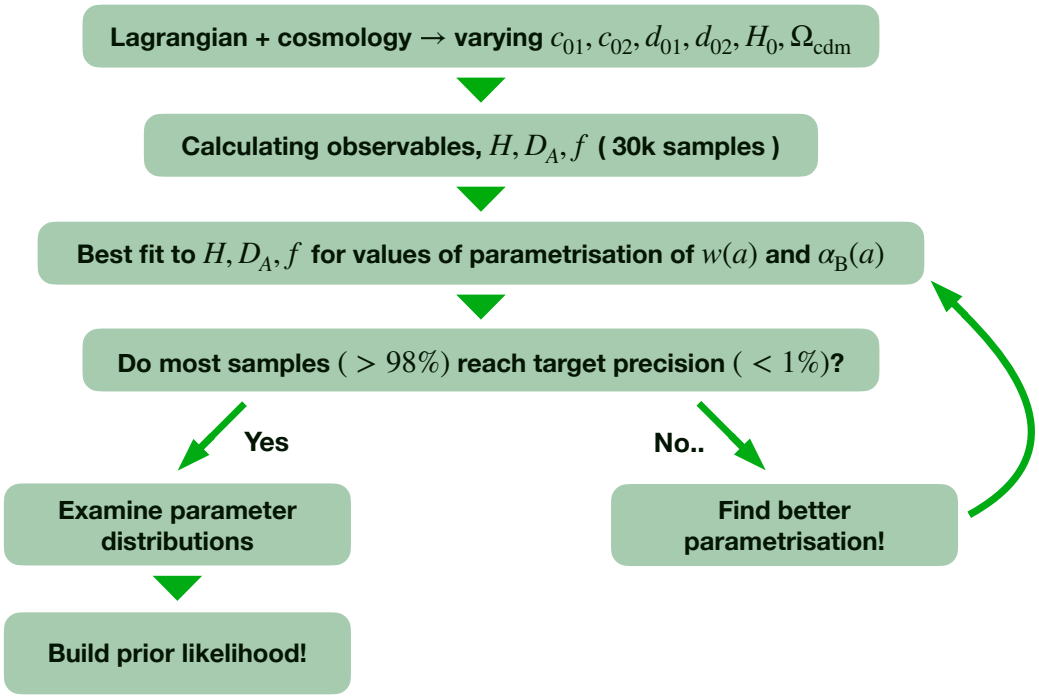


Figure 3.6: Diagram summarising the method presented in Section 3.4 that we use for determining the correct evolution functions of the model, $w(a)$ and $\alpha_{\rm B}(a)$ and the set of coefficients $\{w_0, w_a, \hat{\alpha}_{\rm B}, m\}$ that best fit the observables computed from the Lagrangian.

where

$$c_{\rm sN}{}^2 = \left[(\alpha_{\rm B} - 2)\left(\dot{H} - H^2\alpha_{\rm B}/2\right) + H\dot{\alpha}_{\rm B} - \rho_{\rm m} - p_{\rm m}\right]/H^2\,,$$

computed from the Lagrangian with parameters $(c_{01}, c_{02}, d_{01}, d_{02})$ with the accuracy required by next-generation surveys; i.e. 1% at $z < 10$ [198, 199, 201, 223]. and 0.3% at recombination for D_A [109], for 99% of the models. In order to find $\{w_0, w_a, \hat{\alpha}_{\rm B}, m\}$ we minimise

$$\chi^2 = \sum_z \frac{(\mathcal{O}(w_0, w_a, \hat{\alpha}_{\rm B}, m)_z - \mathcal{O}(c_{01}, c_{02}, d_{01}, d_{02})_z)^2}{\sigma^2_{\mathcal{O}_z}}\,, \tag{3.14}$$

where $\mathcal{O}(w_0, w_a, \hat{\alpha}_{\rm B}, m)_z$ and $\mathcal{O}(c_{01}, c_{02}, d_{01}, d_{02})_z$ are the observables at redshift z computed with the parametrisations of w and $\alpha_{\rm B}$ and the exact from the full evolution of the field equations for a shift-symmetric model given by the set of parameters $\{c_{01}, c_{02}, d_{01}, d_{02}\}$, respectively. The variable $\sigma_{\mathcal{O}_z}$ weights each point so that we can require different precision depending on the variable and redshift. For instance, we set $\sigma_{\mathcal{O}_z} = 10^{-3}$ for all observables at $z < 10$ and $\sigma_{D_{\rm A}(z_{\rm rec})} = 10^{-4}$ at recombination for the angular diameter distance. The software used to make these fits is a modified version of RUFIAN [1] and can be found at

https://gitlab.com/dinatraykova/horndeski-priors.

Let us emphasise that, with this approach, we do not choose the set $\{w_0, w_a, \hat{\alpha}_{\rm B}, m\}$ that best fit the equation of state and $\alpha_{\rm B}$ curves obtained from the Lagrangian, which are not observable quantities. Instead, we minimise the error in the background evolution H and D_A, and f for the linear perturbations. In this sense, allowing $\{w_0, w_a, \hat{\alpha}_{\rm B}, m\}$ to differ from their best fit values with respect to the exact w and $\alpha_{\rm B}$, we find the set of parameters that minimise the error on the observables. It is important to note that, in comparison with quintessence, the equation of f, Eq. (3.13), has the source term modified as

$$\frac{3}{2}\Omega_{\rm m} \longrightarrow \frac{3}{2}\Omega_m \left(1 + \frac{\alpha_{\rm B}^2}{2{c_{\rm sN}}^2}\right) , \tag{3.15}$$

which introduces an extra dependency on $\alpha_{\rm B}$ in the source term and means that a more precise fit to $\alpha_{\rm B}$ would be required to get a good fit to the observables than is the case for w.

In Fig. 3.5 we show the distributions for $\{w_0, w_a, \hat{\alpha}_{\rm B}, m\}$ set of parameters for the shift-symmetric model with and without Λ recovered by minimising the error on the observables, as detailed here; correlations between these variables will become apparent as we construct a complete model for the priors in the next section.

In Fig. 3.6, we present a summary diagram of the method explained in this Section that allows us to derive the approximate time dependent functions that describe the shift-symmetric model, $w(a)$ and $\alpha_{\rm B}(a)$, and find the best fit coefficients $\{w_0, w_a, \hat{\alpha}_{\rm B}, m\}$ that better reproduce the observable quantities obtained from the evolution of the Lagrangian $\{c_{0i}, d_{0i}\}$.

3.5 Results

We now have a robust process for determining $\{w_0, w_a, \hat{\alpha}_{\rm B}, m\}$ for each choice of the physical priors: minimising Eq. (3.14) allows us to find the set of parameters that reproduce the observables H, D_A and f with the accuracy needed by next-generation surveys. The next step is to obtain the *probability distribution* that will be used as theoretical priors for the shift-symmetric Horndeski models. For that, we sample 30,000 random models with parameters $\{c_{01}, c_{02}, d_{01}, d_{02}\}$ and store their corresponding observables at specific

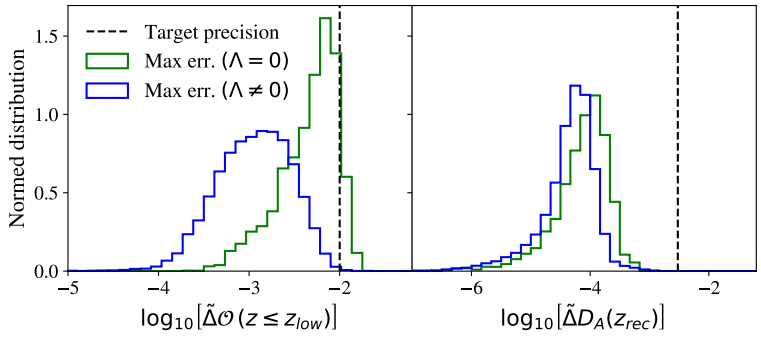


Figure 3.7: Left panel: distribution of the maximum relative deviation between the observables computed from the theory ($\mathcal{O}(c_{01}, c_{02}, d_{01}, d_{02})$) and the parametrisation ($\mathcal{O}(w_0, w_a, \hat{\alpha}_{\rm B}, m)$) at $z < 10$ for each fit. Right panel: distribution of the relative error between the $D_A(z_{\rm rec})$ computed from the theory and the parametrisation for each fit.

redshifts (100 points at $z < 10$ and at $z_{\rm rec}$, in the case of D_A). After minimising Eq. (3.14) for each of this set of 30,000 observables, we end up with having 30,000 $\{w_0, w_a, \hat{\alpha}_{\rm B}, m\}$ that can be used to build our theoretical priors. We obtain the observables quantities for each realisation using `hi_class` [220,221], an extension to the Boltzmann code `CLASS` [222] that solves the cosmological equations for a broad range of sub-sets of the Horndeski class of theories.

Let us note that the choice of 30,000 samples and 100 points at $z < 10$ is just a matter of computational efficiency and has no physical insights. We checked that after 30,000 samples the probability distributions had already converged and increasing its size to 100,000 does not alter the results. In addition, for each set of $\{w_0, w_a, \hat{\alpha}_{\rm B}, m\}$ obtained minimising Eq. (3.14) with 100 points for each observable below $z = 10$ and D_A at $z_{\rm rec}$, we saw that the new observables satisfy the requirement of having an error below 1% at $z < 10$ and below 0.3% for $D_A(z_{\rm rec})$ for the 99% of the cases. This can be seen in Fig. 3.7.

The probability distributions for the parametrised shift-symmetric Hordenski models can be seen in Fig. 3.5, which shows mild correlations between different parameters. We note that these correlations do not have the usual elliptical shape that one expects for a multivariate Gaussian. Clearly there is a non-linear correction that must be taken into account in the next steps.

If we are to construct theoretical priors that can be used in a Markov chain Monte Carlo (MCMC), we need to find a sufficiently good approximation of the probability distribution

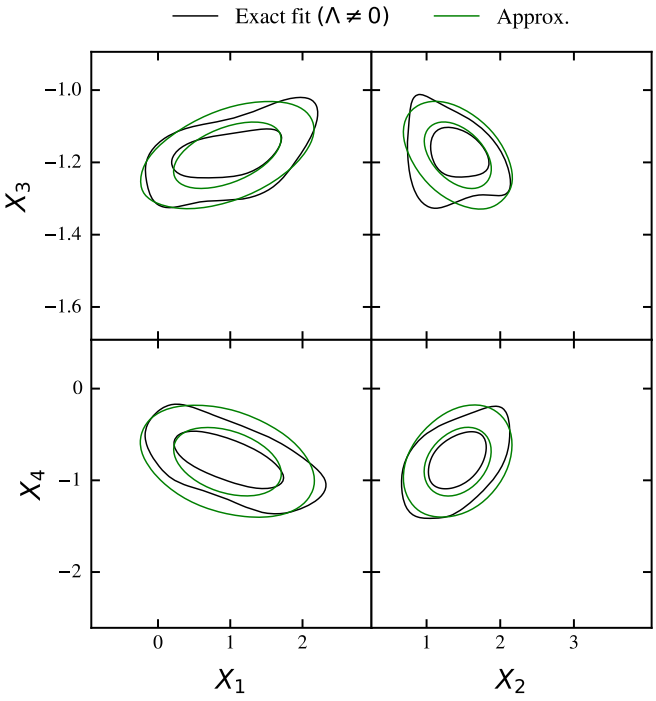


Figure 3.8: Approximate fit to the probability distribution of the $\{X_1, X_2, X_3, X_4\}$ for the $\Lambda = 0$ model. In black, the contours from the original set of parameters transformed by Eq. (3.16). In green, those obtained from a multivariate Gaussian distribution. As one can see, their differences are small and have little effect on the original parameters $\{w_0, w_a, \hat{\alpha}_{\rm B}, m\}$ (Fig. 3.9), the observables (Fig. 3.10) and, therefore, in an MCMC.

that allows us to recover the same distribution of the parameters and the observables when sampling from it. We do this in two steps. We first transform to a new set of parameters

$$\begin{aligned} X_1 &= \hat{\alpha}_{\rm B}\,, \\ X_2 &= m\,\hat{\alpha}_{\rm B}^{1/6}\,, \\ X_3 &= w_0\,m^{1/4}\,, \\ X_4 &= w_a\,m^2\,, \end{aligned} \tag{3.16}$$

which effectively Gaussianise the distributions (Fig. 3.8).

We find that a multivariate normal distribution fits the distribution of $\{X_1, X_2, X_3, X_4\}$ and that, once transformed back to $\{w_0, w_a, \hat{\alpha}_{\rm B}, m\}$ recovers the correlations between the variables to a very good approximation; this can be seen in Fig. 3.9. Of course, a crucial test is to see the impact on the observables and whether one is able to recover the correct distribution for those. We do so in Fig. 3.10 where we compare the observables obtained

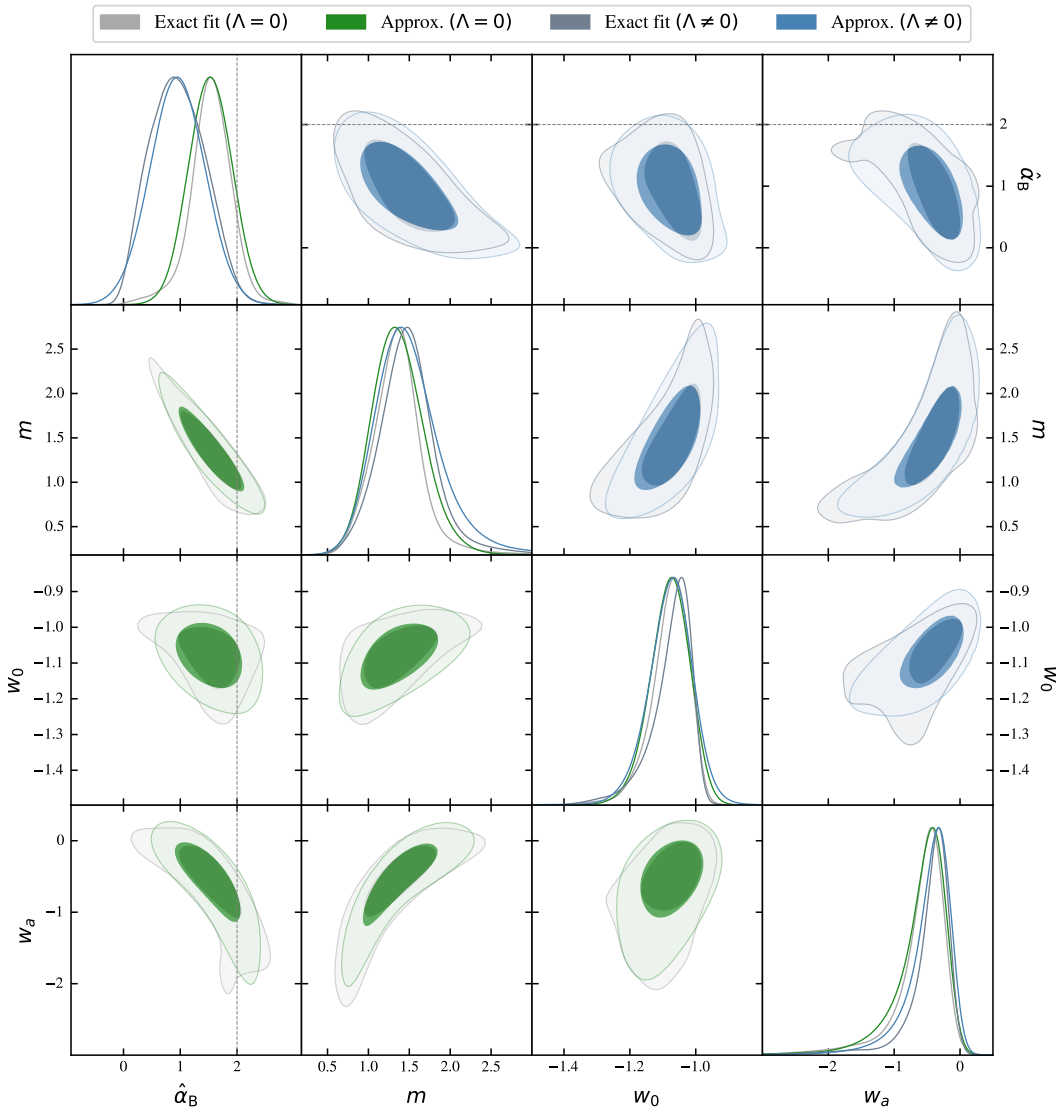


Figure 3.9: Probability density distributions of the $\{w_0, w_a, \hat{\alpha}_B, m\}$ parameters for the $\Lambda = 0$ (lower left) and $\Lambda \neq 0$ (upper right) shift-symmetric theories studied. We compare the exact distributions obtained fitting the observables with those obtained sampling from the new Gaussianised space $\{X_1,\ X_2,\ X_3\, X_4\}$ and transforming back using Eq. (3.16). The differences are small and do not affect the observables significantly (Fig. 3.10). Here we have highlighted the $\alpha_B = 2$ line to separate the region where the evolutions can display some singular behaviour (see Appendix A).

by integrating the field equations of motion to the ones obtained by sampling from the distribution. Note that we only show the distances at $z = 1$ and at recombination, as they have the largest differences, yet these are still small and should have little impact on the posterior distributions of the parameters when combined with data.

Using the Gaussianised distribution we can construct an analytic model and calculate

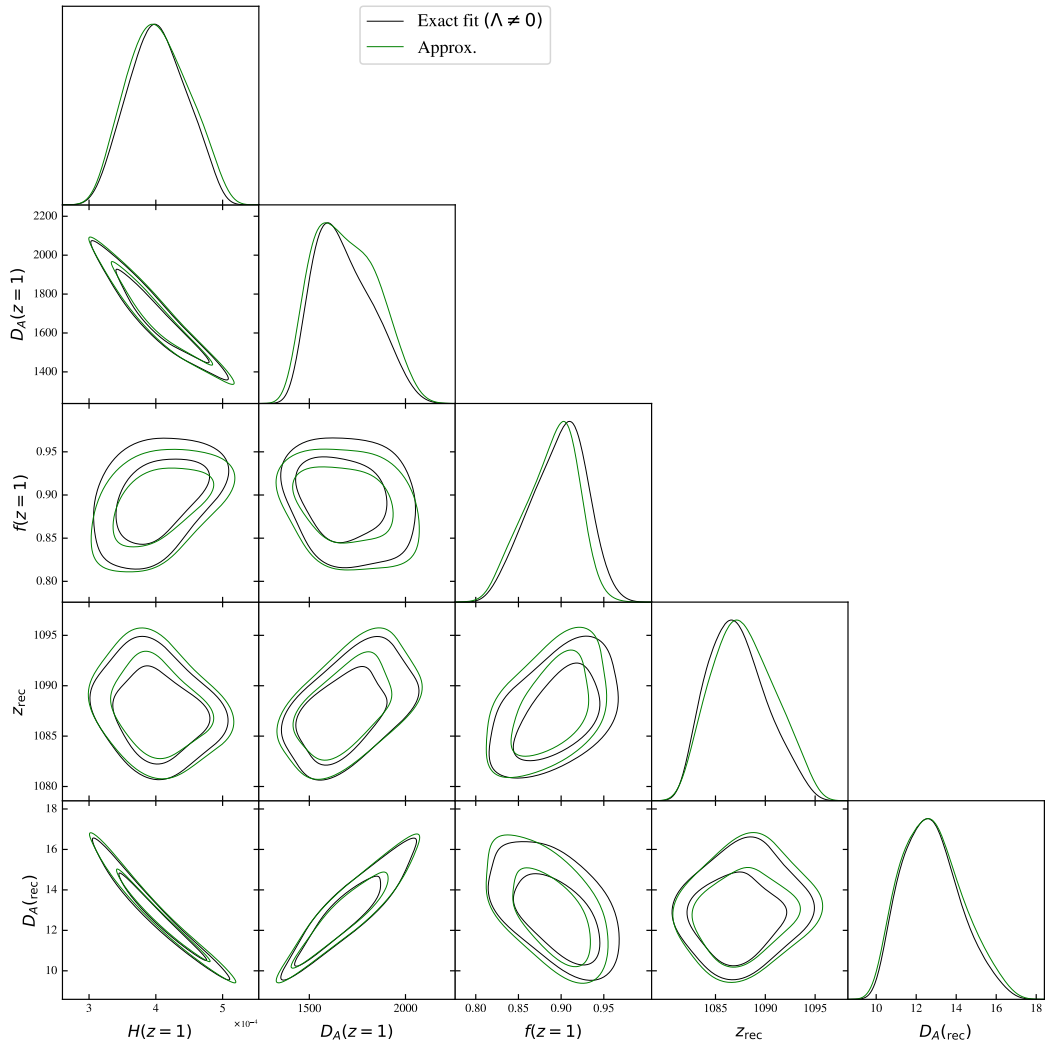


Figure 3.10: Distributions of the observables at $z = 1$ and recombination obtained integrating the field equations of motion (black lines) compared to those obtained using the parameters $\{w_0, w_a, \hat{\alpha}_B, m\}$, recovered after sampling from the multivariate Gaussian distribution (green lines) in the $\{X_1, X_2, X_3, X_4\}$ space, with Eq. (3.16). As we advanced, the differences on the observables are small, justifying the Gaussian approximation and giving confidence on the theoretical priors we have built, Eqs. (3.17)–(3.19)).

the probability density in the transformed parameter basis,

$$p(X|\mu,\Sigma) = \frac{1}{(2\pi)^2|\Sigma|^{1/2}} \exp\left(-\frac{1}{2}(X-\mu)^T \Sigma^{-1} (X-\mu)\right) \tag{3.17}$$

where μ is the vector of mean values and Σ is the covariance matrix of our prior parameter distribution in the transformed basis $\{X_1, X_2, X_3, X_4\}$. For the model without Λ we find

$$\mu(\Lambda = 0) = (1.5346, 1.4461, -1.1592, -0.8841) \ ,$$
$$\Sigma(\Lambda = 0) = \begin{pmatrix} 0.1475 & -0.0916 & 0.0160 & -0.0469 \\ -0.0916 & 0.0776 & -0.0087 & 0.0326 \\ 0.0160 & -0.0087 & 0.0041 & -0.0079 \\ -0.0469 & 0.0326 & -0.0079 & 0.0516 \end{pmatrix} . \tag{3.18}$$

For the case with Λ we have

$$\mu(\Lambda \neq 0) = (0.9545, 1.4255, -1.1803, -0.7962) \ ,$$
$$\Sigma(\Lambda \neq 0) = \begin{pmatrix} 0.2311 & -0.0511 & 0.0136 & -0.0415 \\ -0.0511 & 0.0875 & -0.0075 & 0.0218 \\ 0.0136 & -0.0075 & 0.0035 & -0.0017 \\ -0.0415 & 0.0218 & -0.0017 & 0.0589 \end{pmatrix} . \tag{3.19}$$

We use this to infer the a priori likelihood of a given sample used in the combined analysis with data in Section 3.6.

We might want to compare our current results with those of our work in Chapter 2. There, we found that the phenomenology of different highly dimensional theories is well described by the usual w_0-w_a parametrisation. In that case, we went from having many parameters in the Lagrangian to just two, accurately accounting for their cosmologies. In this chapter, however, we start from a Lagrangian with three parameters (after fixing $d_{01} = -1$) and end up with four parameters to describe its phenomenology. However, this phenomenological parametrisation is still advantageous: it does not require solving the field equations, allows to clearly split the background and linear perturbations effects and shows that both w and $\alpha_{\rm B}$ are simpler than one would a priori think. We expect this to also be the case in other more general theories.

3.6 Comparison with current data

Here we present the constraints on $\alpha_{\rm B}$ and w from current cosmological data and compare and combine these with our theoretical priors. To do this we use a combination of cosmic microwave background (CMB), Baryon Acoustic Oscilations (BAO), Redshift Space

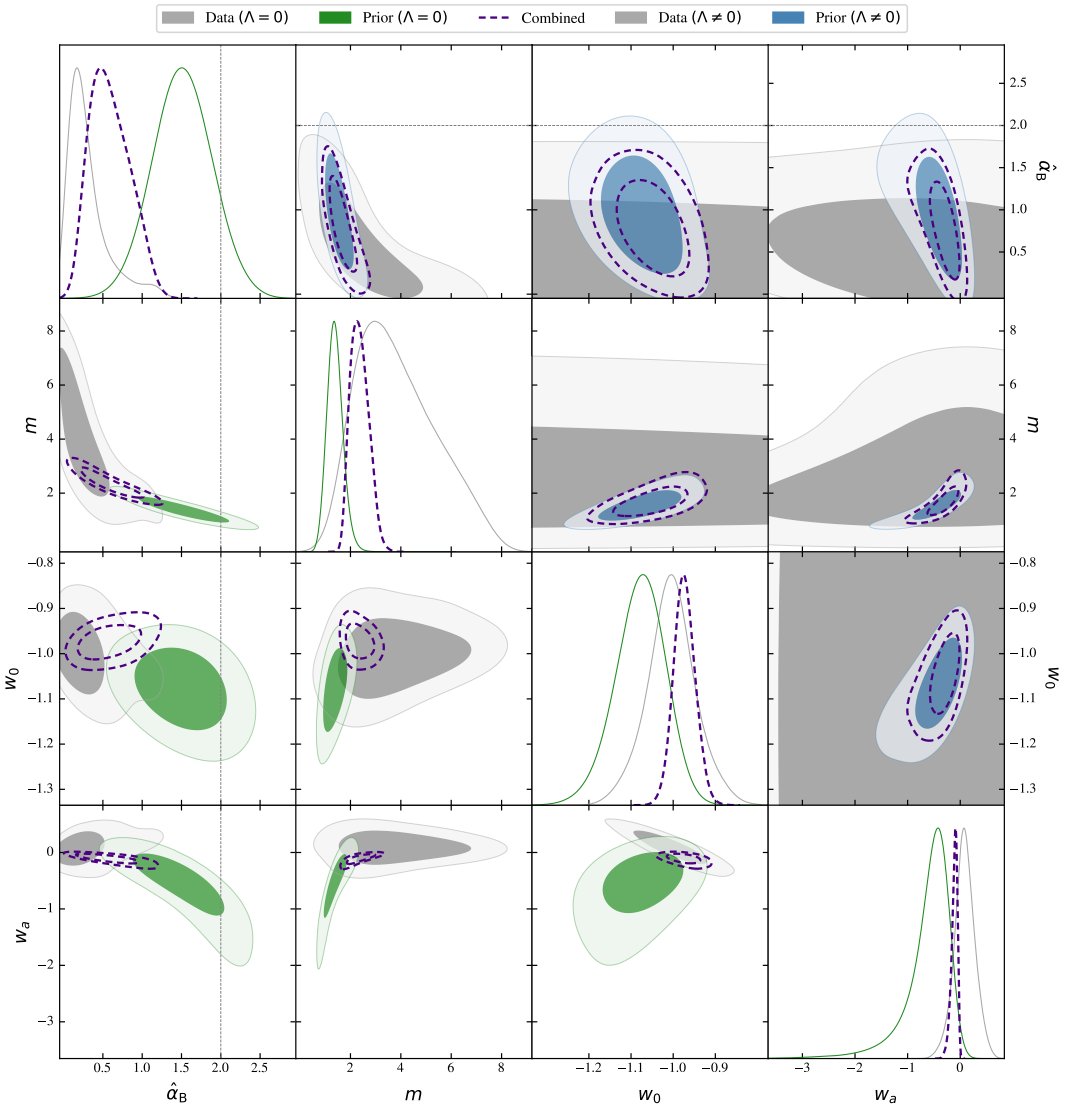


Figure 3.11: Comparison between data and the prior distributions for the two shift-symmetric variants we have considered, $\Lambda = 0$ (lower left corner) and $\Lambda \neq 0$ (upper right). The grey filled contours show the distributions of the parameters when constrained with 'data' alone, the green or blue filled contours show our 'priors' for the $\Lambda = 0$ and $\Lambda \neq 0$ cases respectively, and the purple dashed contours are from the combined analysis. Note that the 'prior' likelihood is built in the Gaussianised $\{X_i\}$ basis, as discussed in Sections 3.5 and 3.6 and takes into account the underlying physical properties of the model (not to be confused with the flat uncorrelated priors we put on the parameters in the 'data' runs). We have only plotted the 1D pdf's for the case $\Lambda = 0$ for clarity and again we have marked the line where $\alpha_B = 2$ (see Appendix A). This plot demonstrates how combining data with theoretical priors can result in much tighter constraints on some of the parameters of the model.

Distorsions (RSD) and Supernovae Type IA (SN Ia) data.

From Planck 2018 [109,291,292], we use the auto- and cross-correlations of the temperature (T) and polarisation (E) fluctuations of the Cosmic Microwave Background, together

with measurements of the lensing potential; i.e. the TT, TE, EE+lowE+lensing likelihoods, which denotes the combination of the high-l TT, TE, and EE spectra ($l \geq 30$), the low-l ($2 \leq l < 30$)) TT and EE likelihoods and the lensing likelihood (with temperature and polarisation lensing reconstruction) in the multipole range $l = 8 - 400$.

Additionally we use the BAO and RSD measurements from BOSS DR12 [151], as well as BAO from the 6dFGS survey [149]. The BAO measurements are of the Hubble rate, H and the angular diameter distance D_A, while RSD measures the growth rate of the universe through $f(z)\sigma_8(z)$. We use the full covariance between the $f(z)\sigma_8(z)$ measurements at different redshifts and the BAO measurements of $H(z)$ and $D_{\rm A}(z)$ from BOSS. However, we do not consider the correlation between the BOSS and 6dF measurements as those cover different areas of the sky and thus any such correlation would be negligible.

Finally, we also include the Pantheon SNe Ia sample [233], which combines the Pan-STARRS1 Medium Deep Survey with ones from the SDSS, SNLS, and various low-redshift and HST samples, 1048 SNe Ia in total in the redshift range $0.01 < z < 2.3$. We also note that, throughout, we assume that the cross-correlation between the different datasets is negligible.

We built our prior likelihood in the Gaussianised basis $\{X_1, X_2, X_3, X_4\}$ and, in order to be consistent, we use the same basis for the sampling in all cases, from which we then convert the resulting distributions back to $\{w_0, w_a, \hat{\alpha}_{\rm B}, m\}$. We sample through the parameter set $\{X_1, X_2, X_3, X_4\}$ together with the standard cosmological parameters in a Markov Chain Monte Carlo (MCMC) with `MontePython` [226, 227] using the Metropolis-Hastings algorithm [228, 229]. We do not consider any prior bounds on the standard cosmological parameters in the MCMC run (apart from $\tau > 0.004$), but just start from a known good fit point from Planck for the set $\{\Omega_{\rm cdm,0}, \Omega_{\rm b,0}, H_0, A_s, n_s, \tau\}$. For the X_i we set the following ranges,

$$X_1 \in (0, 10)\,, \qquad X_3 \in (-10, 0)\,, \tag{3.20}$$

$$X_2 \in (0, 15)\,, \qquad X_4 \in (-15, 30)\,. \tag{3.21}$$

In the case of $\Omega_\Lambda \neq 0$ we also set $\Omega_\Lambda \in (0, 1)$. Using the Gelman-Rubin convergence criterion [230] we require $R - 1 < 0.02$. The contour plots were produced using GetDist

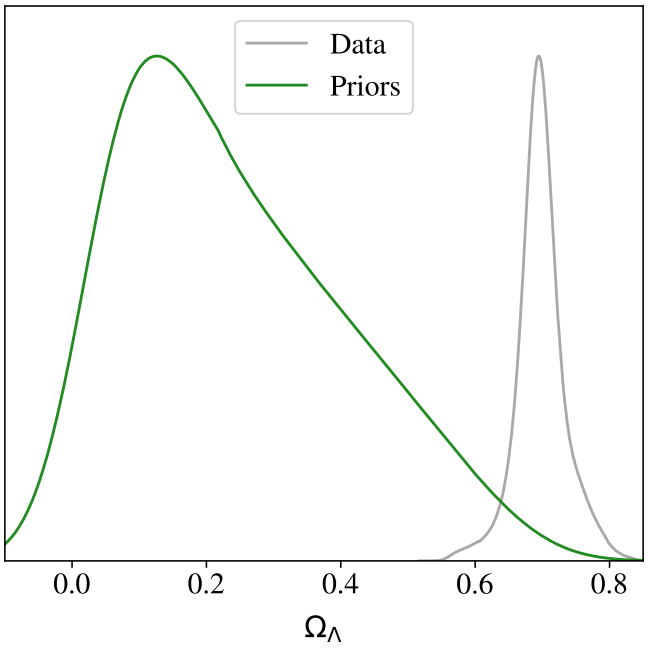


Figure 3.12: Probability distributions of Ω_Λ from the analysis with data alone (grey solid line), our priors (green solid line). Let us note that $\Omega_\Lambda \sim 0.7$ in the data run implies that data seems to prefer a universe mainly filled with a cosmological constant and only a small contribution of the scalar field to DE.

[234].

In order to obtain the combined constraints from data and the theoretical priors, we implemented Eqs. (3.17)–(3.19) in `MontePython` as a new likelihood module[10]. In the analysis with data only we assume uniform priors on the $\{X_1, X_2, X_3, X_4\}$ parameters.

We present the results in Fig. 3.11, where in the bottom half of the triangle we show the contours for the $\Lambda = 0$ case of the shift-symmetric model and on the top half we have the case with additional Λ. On this plot we show the parameters data constraints (grey solid line, filled contours) overlaid with the distributions of the priors. (in green for $\Lambda = 0$ and blue for $\Lambda \neq 0$). In addition, we show the combined constraints (dashed line) from both the data and the priors. In this figure, note that we only show the $\Lambda = 0$ 1D distributions since the $\Lambda \neq 0$ data-only constraints are much broader than any of the others, making it difficult to read.

If we focus only on the bottom left corner of Fig. 3.11 ($\Lambda = 0$), we note that although the data and the priors appear to be equally as constraining for $\hat{\alpha}_{\rm B}$, w_0 and w_a, the

[10] Available at: https://github.com/dinatraykova/shift_priors

contours are misaligned and only overlap away from their respective centres (i.e. regions of high probability). Nevertheless they are statistically consistent and combining the two results in tighter bounds on these parameters. Further, data alone does not provide a very strong bound on m, which makes including the prior likelihood crucial in constraining the time evolution of $\alpha_{\rm B}$. Looking at the combined constraints (dashed line) one may expect that the contours should lie in between the data and priors alone. However, due to the high dimensionality of the problem and the correlations between different parameters, the 2D and 1D projections of the distributions from the combined analysis can end up off the centre of the distributions of the data and the priors runs alone. In the case of w_0 this effect can be seen quite clearly, where the combined histogram appears to be to the right of both the data and priors alone. This is not surprising looking at the 2D contours of w_0 and the other three parameters, where we see that the data and priors contours overlap only at their edges, which could result in such a shift in the 1D projections of one or more parameter.

In the top right corner of Fig. 3.11 we show the contours for the case where we include a contribution of Λ to the DE density ($\Lambda \neq 0$). In this case we find that while data alone (grey solid contours) constrains the $\hat{\alpha}_{\rm B}$ and m parameters well, the distributions of w_0 and w_a are very wide, compared to the priors (blue solid contours) and the combined constraints are almost fully driven by our priors. We note that these distributions cover almost the full range that we have set for these parameters in the data run. The distributions of Ω_Λ are shown in Fig. 3.12 from the sampling with data (grey line) and the ones recovered when deriving the priors (green line). This plot shows that the data prefers the majority of the DE density contribution to come from Λ, as it is consistent with $\Omega_\Lambda \sim 0.7$. This leaves only a very small portion of $\Omega_{\rm DE}$ to come from the scalar field ϕ. Our definition of $w(a)$, Eq. (3.4) includes only the contribution of the scalar field, so we can expect that in a case where Ω_Λ dominates the DE density, it would not be possible to get a strong constraint on the equation of state parameters of the field, w_0 and w_a.

To emphasise the benefit of including theoretical priors into the likelihood analysis in constraining these models, in Table 3.1 we present the parameter ranges for the $\{w_0, w_a, \hat{\alpha}_{\rm B}, m\}$ set from the likelihood analysis with uniform priors and with theoretical priors. In the $\Lambda = 0$ case we find that for m there is a significant improvement in the

	$\hat{\alpha}_{\rm B}$	m	w_0	w_a
$(\Lambda = 0)$				
Data	0.3 ± 0.3	3.8 ± 1.6	-1.0 ± 0.06	0.1 ± 0.2
Prior	1.5 ± 0.4	1.4 ± 0.4	-1.08 ± 0.06	-0.6 ± 0.4
Combined	0.6 ± 0.3	2.4 ± 0.4	-0.97 ± 0.03	-0.11 ± 0.06
$(\Lambda \neq 0)$				
Data	0.5 ± 0.4	2.6 ± 1.4	$--$	$--$
Prior	1.0 ± 0.5	1.5 ± 0.4	-1.08 ± 0.07	-0.5 ± 0.4
Combined	0.8 ± 0.4	1.7 ± 0.4	-1.05 ± 0.06	-0.3 ± 0.2

Table 3.1: Best fit and confidence limits of w_0 and w_a for the data set CMB+BAO+RSD+SN, the theoretical priors and the combined analysis for the shift-symmetric models both with and without Λ, ($\Lambda = 0$ and $\Lambda \neq 0$). Note that we have not written the means and errors for w_0 and w_a from the data run in the $\Lambda \neq 0$ case, as data is not constraining on these; the errors are determined by the ranges we set and the means are consistent with ΛCDM. This is related to the fact that, in this work, w is defined as the scalar field equation of state and that data seems to prefer a negligible contribution of the scalar field to the DE density with the majority coming from Λ (Fig. 3.12).

error after including our theoretical priors, compared to the constraints with data using uniform uncorrelated priors (from ± 1.6 to ± 0.4). For the other three parameters ranges from the data run with uncorrelated priors and our derived correlated ones are comparable but combining them still results in slight improvement of the errors. In the case of $\Lambda \neq 0$, we see that there is a similar improvement on the constraint of m as we find in the $\Lambda = 0$ case (from ± 1.4 to ± 0.4). However, as we saw from the contours in Fig. 3.11, w_0 and w_a cannot be constrained with data using the uniform priors on the parameter set due data preferring Ω_Λ to be the dominant contribution to the DE density. The addition of the theoretical priors in this case is, therefore, crucial as the only way to fully constrain the parameter space.

3.7 Discussion

In this chapter we have taken a further step towards constructing a set of physical priors for Horndeski theories of gravity. Building on the experience of constructing such a prior for thawing quintessence, we have focussed on a physically well motivated subset of Horndeski gravity: shift-symmetric theories with standard speed of gravitational waves. While these theories are less general than the full Horndeski space of theories, they are more general

than the much studied Galileon scalar-tensor theories.

Working with shift-symmetric theories has allowed us to explore a situation in which one needs more than just the equation of state, w, to fully characterise its behaviour on cosmological scales. For such theories one needs to also include an accurate model for the "braiding" parameter, $\alpha_{\rm B}$. We have done so, constructing a prior distribution function, $\mathcal{P}$ for four constant parameters defined in Eqs. (1.41) and (3.10). Remarkably, and very much like in the case of thawing quintessence, we have come up with a simple analytical form for $\mathcal{P}$ which can be easily deployed in future cosmological parameter analysis.

We have learnt a number of lessons from focusing on shift-symmetric theories which give us a sense of the challenge of tackling more general Horndeski theories. For a start, the theories we have looked at here are endowed with a tracking behaviour which eliminates the need to pin down a prior for initial conditions. This will not be true in general for full Horndeski theories.

We have had to face the problem of sampling over a multi-dimensional space of parameters (in this case $\{c_{01}, c_{02}, d_{01}, d_{02}\}$) which is subjected to some form of constraint. The way one implements the constraint can greatly affect the prior distribution function. For example, explicitly solving the constraint can bias the resulting prior, depending on which of the parameters one is solving for. We have argued that one should sample over all parameters and exclude points which lie outside the constraint sub-region. This is, nevertheless, a computationally costly approach to the problem which will become far more severe, the more general the theory one is looking at.

With an appropriate algorithm for sampling over $\{c_{01}, c_{02}, d_{01}, d_{02}\}$, we have proposed a functional form for the phenomenological parameters, w and $\alpha_{\rm B}$. We have found that the usual form for w is still remarkably effective while, building on our knowledge of Galileons, we have come up with a suitably simple form for $\alpha_{\rm B}$, if we choose the parameters by minimising the error on the observables (a crucial aspect of this approach). The latter insight is useful and points to the fact that, in general, the α_i parameters may have a simple functional form in the more general theory. This means that a reanalysis of current cosmological data may lead to far tighter constraints than have until now been found.

An important step has been to find non-linear transformations that, to some extent, "Gaussianises" the distributions of our parameters. Such a transformation has been re-

markably effective allowing us to determine, rather more easily than one would naively expect, an analytic expression for the prior. Again, one would expect this approach to be useful when looking at more general theories.

An interesting aspect of the theories we have focused on – shift-symmmetric theories – is that they are, in some sense, viable and complete. In other words, Including terms $\propto X^2$ in G_2, G_3 give viable generalisations of the cubic Galileon (Fig. 3.11), even with $\Lambda = 0$. In this model $\dot{\phi}^2/\Lambda_2^4 \lesssim 0.2$ (Fig. 3.2), suggesting that higher order corrections are subdominant and can be neglected.

An important aspect, which from our understanding has been somewhat unexplored, is that $c_{01} < 0$ is more generic than just for the Covariant Galileon. This is important, since this regime disconnects these theories from the Minkowski solution and constraints derived for that solution. Note that there may be other solutions where, for example, higher orders in X^n contribute. In that situation, the constraints on c_{01} may be markedly different.

Note that, while we have considered and taken into account a number of theoretical priors and observational constraints throughout this work, these are of course not complete and one may wish to add additional priors/constraints to this analysis in the future. One such example to highlight are constraints from dark energy-gravitational wave interactions, specifically related to dark energy (gradient) instabilities that can be induced by gravitational wave sources such as massive binaries [293]. Requiring the absence of these instabilities in general can be used to significantly tighten cosmological parameter constraints [246]. In the specific shift-symmetric context of the theories considered here, avoiding such instabilities amounts to requiring $|\alpha_{\rm B}| \lesssim 10^{-2}$. This effectively renders the cubic Horndeski interactions we have considered into an afterthought for cosmology. We will leave a more detailed investigation of this and other additional priors in the context of shift-symmetric theories for future research.

Finally, our brief comparison with current data shows that this theory is a viable self-accelerating model: the physical priors are consistent with the cosmological constraints. This is somewhat promising given the dearth of theoretically viable models of self-acceleration, currently compatible with cosmological data. A thorough analysis of shift-symmetric cosmologies, along the lines of [294] will allow us to assess if such shift-symmetric gravity is a credible contender for the late-time acceleration of the Universe.

Chapter 4

Beyond Horndeski

We study the phenomenology of the beyond Horndeski class of scalar-tensor theories of gravity, which on cosmological scales can be characterised in terms of one extra function of time, $\alpha_{\rm H}$, as well as the usual four Horndeski set of free functions. We show that $\alpha_{\rm H}$ can be directly related to the damping of the matter power spectrum on both large and small scales. We also find that the temperature power spectrum of the cosmic microwave background (CMB) is enhanced at low multipoles and the lensing potential is decreased, as a function of $\alpha_{\rm H}$. For a particular choice of time dependence we find constraints on $\alpha_{\rm H}$ of order $\mathcal{O}(1)$ using measurements of the temperature and polarisation of the CMB, as well as the lensing potential derived from it, combined with large scale structure data. We find that redshift space distortion measurements can play a significant role in constraining these theories. Finally, we comment on the implications of the recent observation of an electromagnetic counterpart to a gravitational wave signal; we find that these measurements reduce the number of free parameters of the model but do not significantly change the constraints on the remaining parameters.

4.1 Introduction

In the last two decades, there has been tremendous progress in testing gravity on cosmological scales. We can now measure the expansion history, the Cosmic Microwave Background (CMB) and the Large Scale Structure (LSS) of the universe with incredible precision. As discussed in the previous Chapters, this can allow us to determine the nature of DE, caus-

ing the observed accelerated expansion of the universe, and compare the ΛCDM model to particular scalar-tensor theories, which can also account for this effect. The Horndeski class of theories [60–62] has received a lot of attention as it is given by a general scalar-tensor action that leads to at most second-order equations of motion on any background and also satisfies the weak equivalence principle, i.e. all matter (except from the scalar, ϕ) is coupled minimally and universally to the same metric. It has been shown, however, that Horndeski can be further extended to the so-called beyond Horndeski theories [71,87]. While in general beyond Horndeski has higher (than second) order equations of motion, this does not necessarily lead to Ostrogradski instabilities [70,71,295]. Indeed, it is possible to show that the time-derivatives remain second-order in the equations of motion for the propagating degrees of freedom for any ADM decomposition [91, 296, 297]. As expected, beyond Horndeski theories lead to new interesting phenomenological properties that are not described by the Horndeski class [298]. For example, a recent study [299] shows that the scalar field in beyond Horndeski theories can significantly modify the speed of sound in the atmosphere of the Earth. The question of whether this set of theories is viable for explaining dark energy has been studied extensively in [300–302]; self-acceleration solutions exist that can lead to a de Sitter universe at late times without the need of a cosmological constant.

The aim of this work is to explore the phenomenology of beyond Horndeski models and constrain the free parameters of the theory using the latest CMB and large scale structure data. Such fits to data have been performed previously on specific modified gravity models [270,303,304] or specific data sets [212,305]. More generally this was done for the Horndeski models considering a collection of latest CMB and large scale structure data in [238, 241, 306].

We use the formalism introduced in [90] for Horndeski and used in [220, 250, 306, 307] and extended to beyond Horndeski in [89] (see also [85–87,91,308] for a different approach to the linear perturbation theory in the Horndeski and beyond Horndeski Lagrangian). In this approach the evolution of linear perturbations is described fully by the fraction of matter density today, the Hubble parameter $H(t)$ and five other functions of time. We have chosen the parametrisation for these five functions proposed in [90], in which these are proportional to the fractional energy density of dark energy, $\Omega_{\rm DE}(t)$. In this way the

effective freedom of the model is reduced to just five free parameters.

The structure of this work is as follows. In Section 4.2 we review the theoretical properties of the beyond Horndeski action and the equations of motion that it leads to. Then in Section 4.3 we discuss the phenomenology of this model. We present our results for the constraints on the parameters of this model with data in Section 4.4. Finally we discuss our findings in Section 4.5.

4.2 Theoretical framework

In this section we discuss the general properties of the beyond Horndeski class of theories, present its Lagrangian, background equations and stability. We then briefly discuss the recent restrictions arising from GW170817 and finally present the linear perturbation equations for the model. The action for beyond Horndeski reads as the Horndeski one in Eq. (1.9), with two additional functions F_4 and F_5 to the efinitions of the Lagrangians [70, 71],

$$\begin{aligned}
\mathcal{L}_2 &= \mathcal{L}_{2,\mathrm{H}}\,, \\
\mathcal{L}_3 &= \mathcal{L}_{3,\mathrm{H}}\,, \\
\mathcal{L}_4 &= \mathcal{L}_{4,\mathrm{H}} + F_4(\phi,\, X)\epsilon^{\mu\nu\rho}{}_{\sigma}\epsilon^{\mu'\nu'\rho'\sigma}\phi_{;\mu}\phi_{;\mu'}\phi_{;\nu\nu'}\phi_{;\rho\rho'}\,, \\
\mathcal{L}_5 &= \mathcal{L}_{5,\mathrm{H}} + F_5(\phi,\, X)\epsilon^{\mu\nu\rho\sigma}\epsilon^{\mu'\nu'\rho'\sigma'}\phi_{;\mu}\phi_{;\mu'}\phi_{;\nu\nu'}\phi_{;\rho\rho'}\phi_{;\sigma\sigma'}\,,
\end{aligned} \tag{4.1}$$

Where $\mathcal{L}_{i,\mathrm{H}}$ are the Horndeski Lagrangians, defined in Eq. (1.10).

As suggested in Ref. [309] and shown in Ref. [297], this action as it is written can lead to an extra propagating degree of freedom. However, this issue can be avoided by imposing the following condition [310] ,

$$2XG_{5X}F_4 = -3F_5\left[G_4 + 4XG_{4X} + XG_{5\phi}\right]\,. \tag{4.2}$$

This is visible in the context of beyond Horndeski when non-linear terms are considered. However, in this work we only consider linear perturbations and do not need to impose this condition in obtaining our results.

Starting from this action, one has to choose the functional form of the G_i (and F_i),

initial conditions for the scalar field, and get predictions solving for the background and the perturbations. However, this can be expensive and inefficient if the objective is to test the robustness of the standard cosmological model just by detecting deviations from it. A more practical approach for this purpose is to use parametrised frameworks which were built to compress the information of a general class of models into a few functions of time. In particular we are going to use the framework introduced in [89, 90], where it was shown that the expansion history of the universe and the linear perturbations can be described completely by six functions of time: one responsible for the background evolution – $H(a)$ or $w(a)$ – and the remaining affecting only the perturbations. It is possible to show that for a general theory that can be described as a sub-class of beyond Horndeski these functions are completely independent of the background and each other, which means that they represent the minimal set of functions that can describe all models within this set of theories. Here we describe their physical meaning and definitions in terms of the G_i and F_i functions:

- The kineticity, $\alpha_{\rm K}$, is a generalisation of the standard kinetic term of simple DE models. On its own this parameter describes some of the simpler DE models, with the only modification to ΛCDM being the addition of an extra fluid (e.g. quintessence). It is defined as,

$$\begin{aligned}\alpha_{\rm K}M_*^2 = \frac{2X}{H^2}&\left[G_{2X} - 2G_{3\phi} + 2X\left(G_{2XX} - G_{3\phi X}\right)\right]\\ &+ 4H\dot{\phi}X\left[3G_{5X} + X\left(7G_{5XX} - 120F_5 + 2X\left(G_{5XXX} - 66F_{5X} - 12XF_{5XX}\right)\right)\right]\\ &+ \frac{12\dot{\phi}X}{H}\left[G_{3X} - 3G_{4\phi X} + X\left(G_{3XX} - 2G_{4\phi XX}\right)\right]\\ &+ 12X\left[G_{4X} - G_{5\phi} + X\left(8G_{4XX} - 5G_{5\phi X} + 2X\left(2G_{4XXX} - G_{5\phi XX}\right)\right)\right]\\ &+ 12X\left[X\left(24F_4 + 2X\left(18F_{4X} + 4XF_{4XX}\right)\right)\right]\,.\end{aligned} \tag{4.3}$$

- The braiding, $\alpha_{\rm B}$, describes the mixing of the scalar field and metric kinetic terms. It contributes to the kinetic energy of the scalar, partially sourced through its mixing

with the metric. In terms of G_i and F_i,

$$\begin{aligned}\alpha_{\rm B}M_*^2 = {} & 2H\dot{\phi}X\left(3G_{5X}+2XG_{5XX}-60XF_5-24X^2F_{5X}\right)\\ & +\frac{2\dot{\phi}}{H}\left[-G_{4\phi}+X\left(G_{3X}-2G_{4\phi X}\right)\right]\\ & +8X\left[G_{4X}-G_{5\phi}+X\left(2G_{4XX}-G_{5\phi X}+8F_4+4XF_{4X}\right)\right].\end{aligned} \tag{4.4}$$

- The effective Planck mass,

$$M_*^2 = 2G_4-2X\left[2G_{4X}+H\dot{\phi}G_{5X}-G_{5\phi}+2X\left(2F_4-6H\dot{\phi}F_5\right)\right], \tag{4.5}$$

can be absorbed in the densities and pressures of matter and the scalar and be effectively hidden in the equations of motion. But this is not the case for the Planck mass run rate,

$$\begin{aligned}\alpha_{\rm M}M_*^2 \equiv \frac{{\rm d}\ln M_*^2}{{\rm d}\ln a} = {} & \frac{2\dot{H}\dot{\phi}X}{H}\left(-G_{5X}+12XF_5\right)\\ & +2H\dot{\phi}X\left[3G_{5X}+2X\left(G_{5XX}-30F_5-12XF_{5X}\right)\right]\\ & -2\ddot{\phi}X\left[3G_{5X}+2X\left(G_{5XX}-30F_5-12XF_{5X}\right)\right]\\ & -\frac{2\dot{\phi}\ddot{\phi}}{H}\left[G_{4X}-G_{5\phi}+X\left(2G_{4XX}-G_{5\phi X}+8F_4+4XF_{4X}\right)\right]\\ & +\frac{2\dot{\phi}}{H}\left[G_{4\phi}+X\left(G_{5\phi\phi}-2G_{4\phi X}-4XF_{4\phi}\right)\right]\\ & +4X\left[G_{4X}-G_{5\phi}+2X\left(G_{4XX}-G_{5\phi X}+4F_4+2X\left(F_{4X}+3F_{5\phi}\right)\right)\right],\end{aligned} \tag{4.6}$$

which measures the variation in time of the Planck mass. This function is non-zero in models where in the action the scalar field couples directly to curvature, and it produces anisotropic stress in the gravitational potentials.

- The tensor speed excess, $\alpha_{\rm T}$, signifies deviations of the speed of gravitational waves from the speed of light and has an effect on the scalar perturbations too. As $\alpha_{\rm M}$, it is present in non-minimally coupled theories and can be written as,

$$\alpha_{\rm T}M_*^2 = X\left[2G_{5X}\left(2H\dot{\phi}-\ddot{\phi}\right)+4\left(G_{4X}-G_{5\phi}+2X\left(F_4-3F_5H\dot{\phi}\right)\right)\right]. \tag{4.7}$$

- $\alpha_{\rm H}$ is non-zero for beyond Horndeski theories. It has been shown that even when

ordinary mater is minimally coupled to the metric, in the theories beyond Horndeski, the higher order derivatives in the conformal transformation of the metric can lead to coupling between the sound speeds of dark energy and matter [70, 91, 311]. This mixing between the scalar and matter can be measured by the $\alpha_{\rm H}$ parameter,

$$\alpha_{\rm H} M_*^2 = 8X^2 \left(F_4 - 3F_5 H\dot{\phi} \right) . \tag{4.8}$$

Here, the dots denote derivatives with respect to proper time. As a shorthand notation in the rest of this work we may refer to these functions as α_i.

It is possible to derive the linear perturbation equations and an evolution equation for the perturbation of the scalar in term of these functions. These equations, combined with the evolution equations for the matter species, provide the full system that one has to solve to obtain the linear matter and CMB power spectra and any other prediction within linear theory. Given the constraining power of current datasets, any practical use of the α_i implies the choice of a parametric form to describe their time evolution. There are many different parametrisations that can be used. Although they cannot fully represent the beyond Horndeski class of theories, we have to make a choice in order to evolve the equations of motion in time. For example one could choose to keep the α_i constant, split them in redshift bins, or evolve them as proportional to a power of the scale factor a^n or the fractional density of the DE/MG component Ω_ϕ^n, with $n = const.$ Here we pick the parametrisation proposed in [90],

$$\alpha_i = \Omega_\phi \hat{\alpha}_i \, , \tag{4.9}$$

where $\hat{\alpha}_i$ are constants. We choose this time evolution because we are interested in DE/MG models that aim at explaining the late-time acceleration of the universe, so it is reasonable to assume that the α_i will become more important as the DE density grows and the universe starts to accelerate. If all the $\hat{\alpha}_i$ turn out to be negligibly small, that would suggest that the accelerated expansion is mainly due to a cosmological constant. Furthermore, this parametrisation provides more freedom than the constant or binned α_i, but has a smaller parameter space to sample from than for $\alpha_i = \sum_n \Omega_\phi^n \hat{\alpha}_{i,n}$, where n is a positive integer. While the reasons we have invoked are practical, we note, however, that the study of specific

beyond Horndeski models is in its infancy; specifically, there is, as yet, little understanding of the type of behaviour one might expect if constructing a model from the ground up (i.e. via an action). It would be important to explore the range of possible behaviours (as has been done for the case of the equation of state and the CLP parametrisation in the case of dark energy and, to a lesser extent, as has been done for "normal" Horndeski models) – only then can we be assured that such a parametrisation is representative of a model space.

4.2.1 Background

The Friedmann equations for a flat Friedmann-Robertson-Walker (FRW) metric read

$$\begin{aligned} 3H^2 &= \tilde{\rho}_\mathrm{m} + \tilde{\rho}_\phi \,, \\ 2\dot{H} &= -3H^2 - \tilde{p}_\mathrm{m} - \tilde{p}_\phi \,, \end{aligned} \tag{4.10}$$

where the subscript m stands for all matter species and ϕ for the additional scalar field of DE/MG. Here we have absorbed the Planck mass into the definitions of the densities and the pressures of matter and the scalar, e.g. $\tilde{\rho} \equiv \rho/M_*^2$ (see [90] for notation). As a consequence, the matter and DE densities are not conserved anymore

$$\begin{aligned} \dot{\tilde{\rho}}_\mathrm{m} + 3H(\tilde{\rho}_\mathrm{m} + \tilde{p}_\mathrm{m}) &= -\alpha_\mathrm{M} H \tilde{\rho}_\mathrm{m} \,, \\ \dot{\tilde{\rho}}_\phi + 3H(\tilde{\rho}_\phi + \tilde{p}_\phi) &= \alpha_\mathrm{M} H \tilde{\rho}_\mathrm{m} \,. \end{aligned} \tag{4.11}$$

This can be interpreted as energy density being exchanged between matter and the scalar whenever M_*^2 varies. Thus in this framework we need to integrate the densities of all matter species appropriately according to the equations above. With different definitions of DE/MG energy density and pressure we could have assumed the standard evolution for these quantities at the price of keeping track the value of M_*^2. Clearly the two approaches are equivalent and one uses whichever is more convenient. The expressions for $\tilde{\rho}_\phi$ and $\tilde{p}_\phi$

in terms of the Horndeski G_i and F_i functions are given by,

$$\begin{aligned} M_*^2\tilde{\rho}_\phi \equiv & -G_2 + 2X\left(G_{2X} - G_{3\phi}\right) + 6\dot{\phi}H\left(XG_{3X} - G_{4\phi} - 2XG_{4\phi X}\right) \\ & + 12H^2X\left(G_{4X} + 2XG_{4XX} - G_{5\phi} - XG_{5\phi X} + 8XF_4 + 4X^2F_{4X}\right) \\ & + 4\dot{\phi}H^3X\left(G_{5X} + XG_{5XX} - 24XF_5 - 12X^2F_{5X}\right) , \end{aligned} \tag{4.12}$$

$$\begin{aligned} M_*^2\tilde{p}_\phi \equiv & \, G_2 - 2X\left(G_{3\phi} - 2G_{4\phi\phi}\right) + 4\dot{\phi}H\left(G_{4\phi} - 2XG_{4\phi X} + XG_{5\phi\phi} - 4X^2F_{4\phi}\right) \\ & - M_*^2\alpha_{\rm B}H\frac{\ddot{\phi}}{\dot{\phi}} - 4H^2X^2\left(G_{5\phi X} - 12XF_{5\phi}\right) + 2\dot{\phi}H^3X\left(G_{5X} - 12F_5\right) . \end{aligned} \tag{4.13}$$

4.2.2 Stability conditions

The price of introducing new degrees of freedom is that the resulting theory may be unstable on a given background. Indeed, it is possible for specific choices of the α_i that the perturbations grow exponentially. In this section we show the conditions to avoid two types of instabilities, i.e. *ghost* and *gradient*. *Ghost instabilities* happen when we choose the wrong sign of the kinetic term of a d.o.f., while *gradient instabilities* can occur when the sound speed of the fluid is imaginary.

After decoupling from auxiliary variables the quadratic action for scalar and tensor modes in beyond Horndeski with no matter reads [87, 312],

$$S^{(2)} = \int \mathrm{d}^4x a^3 \left[Q_{\rm S}\left(\dot{\zeta}^2 - \frac{c_{\rm s}^2}{a^2}(\partial_i\zeta)\right) + Q_{\rm T}\left(\dot{h_{ij}}^2 - \frac{c_{\rm T}^2}{a^2}(\partial_k h_{ij})^2\right)\right] , \tag{4.14}$$

where h_{ij} are the tensors modes (gravitational waves), and ζ the scalar. To ensure that the propagating degrees of freedom are not ghost-like, we require that their kinetic terms are positive, i.e.

$$\begin{aligned} & Q_{\rm S} \equiv \frac{2M_*^2 D}{(2-\alpha_{\rm B})^2} > 0\,, \qquad D \equiv \alpha_{\rm K} + \frac{3}{2}\alpha_{\rm B}^2\,, \\ & Q_{\rm T} \equiv \frac{M_*^2}{8} > 0\,. \end{aligned} \tag{4.15}$$

To avoid gradient instabilities we need to require that the speed of sound of the scalar and

tensor degrees of freedom are positive. This means that,

$$c_{\rm s}^2 = \frac{(2-\alpha_{\rm B})^2}{2D}\left\{-c_{\rm T}^2 + \frac{4}{aM_*^2}\frac{\rm d}{{\rm d}t}\left[\frac{aM_*^2(1+\alpha_{\rm H})}{H(2-\alpha_{\rm B})}\right]\right\} - \frac{\tilde{\rho}_{\rm m}+\tilde{p}_{\rm m}}{DH^2}(1+\alpha_{\rm H})^2 > 0\,,$$
$$c_{\rm T}^2 = 1+\alpha_{\rm T} > 0\,. \tag{4.16}$$

Note that the only condition affected by the beyond Horndeski terms is the gradient condition for the scalar sector, while the remaining are the same as for Horndeski models [62,90].

There have been studies of the impact that stability conditions have on the constraints obtained for parametrised models [129, 313, 314] and `hi_class` gives you the freedom to relax or disable the restrictions imposed by these conditions. From a brief inspection of the results that we obtain with and without these restrictions we find that the combinations of α_i that get rejected by the stability conditions are also in regions of extremely low likelihood; if the tests are disabled they lead to exponential growth of the perturbations (and hence are an extremely bad fit to data). While it is safe to ignore the restrictions, we have decided to keep them in our analysis, as this speeds up sampling significantly.

4.2.3 Recent implications from GW170817 and GRB 170817A

After the detection of an electromagnetic counterpart (GRB 170817A) to the gravitational wave signal (GW170817) from a binary neutron star merger [94, 256, 257], it has been shown that the speed of gravitational waves (GW) has to be incredibly close to the speed of light and thus $|\alpha_{\rm T}| < 10^{-15}$ (we note that Current constraints on $\alpha_{\rm T}$ using cosmological data are $\mathcal{O}(1)$). This implies that, as pointed out in [95–98], this result imposes strict constraints on general scalar-tensor and vector-tensor theories that are much tighter than current cosmological constraints and therefore it is safe to take

$$\alpha_{\rm T} = 0\,, \quad c_{\rm T}^2 = 1\,. \tag{4.17}$$

It has been suggested that this constraint can be avoided for some scalar-tensor theories if one takes into account the dynamics of the scalar field directly, when it is not coupled directly to matter [315].

Furthermore, in Ref. [316] the authors claim that any model with $\alpha_{\rm H} \neq 0$ predicts a

copious decay of GW into DE scalar fluctuations. Given that we do observe GW, suggests that we must rule out any beyond Horndeski model. The only way to avoid decay of GW and have $\alpha_{\rm H} \neq 0$ is to impose the propagation speed of scalar perturbations, $c_{\rm s}^2$, to be equal to the speed of light. While the authors mention that there could be power-law divergent terms even in this case, here our objective is to give a purely phenomenological idea of the behaviour of beyond Horndeski theories. Our main analysis is then performed letting $\alpha_{\rm H}$ free to vary and without any additional condition on $c_{\rm s}^2$ (beside the stability condition mentioned in the previous section). However, for completeness we compare this case with the one where we fix $c_{\rm s}^2 = 1$ and show the results in Section 4.4.

It is possible to get models with $c_{\rm s}^2 = 1$ by expressing one of the α_i in terms of the others. In this paper we choose to fix $\alpha_{\rm K}$, which obeys this relation

$$\alpha_{\rm K} = -\frac{3}{2}\alpha_{\rm B}^2 - \frac{1}{2}(2-\alpha_{\rm B})^2\left\{c_{\rm T}^2 - \frac{4}{aM_*^2}\frac{\rm d}{{\rm d}t}\left[\frac{aM_*^2(1+\alpha_{\rm H})}{H(2-\alpha_{\rm B})}\right]\right\} - \frac{\tilde{\rho}_{\rm m}+\tilde{p}_{\rm m}}{H^2}(1+\alpha_{\rm H})^2\,. \quad (4.18)$$

This ensures that the speed of sound of the scalar is unity for all the models we consider at all times. As shown in [306], the value of $\alpha_{\rm K}$ is generally unconstrained by data and varying this parameter has negligible effect on the background. In Section 4.3, we can see that $\alpha_{\rm K}$ is not present in the equations of motion in the quasi-static approximation, Eqs. (4.30) and (4.31), so it also has no effect on the observables we are looking at in this limit. In Section 4.4.3 we present the results for $\alpha_{\rm K}$ as given by Eq. (4.18) and compare those to the case where $\alpha_{\rm K} = 1$.

4.2.4 Perturbations

We assume that the universe is spatially flat and is well described by small perturbations to the Friedmann-Robertson-Walker (FRW) metric. Taking into account only scalar perturbations, the line element in Newtonian gauge (with the notation of [105]) reads,

$${\rm d}s^2 = -(1+2\Psi)\,{\rm d}t^2 + a^2(t)\,(1-2\Phi)\,{\rm d}\mathbf{x}^2\,. \quad (4.19)$$

Following [90] we redefine the perturbations of the scalar field as

$$v_X \equiv -\frac{\delta\phi}{\dot{\phi}}\,. \tag{4.20}$$

Here we present the linear perturbation equations for the Fourier components of the Lagrangian given in Eq. (4.1) in Newtonian gauge and physical time. In Appendix B.1 we present these in synchronous gauge, as implemented in `hi_class`. These equations have been derived previously in [70, 71].

The modified Einstein (00) equations has the form,

$$\begin{aligned}&3\left(2-\alpha_{\rm B}\right)H\dot{\Phi}+\left(6-\alpha_{\rm K}-6\alpha_{\rm B}\right)H^2\Psi+\left(1+\alpha_{\rm H}\right)\frac{2k^2}{a^2}\Phi-\left(\alpha_{\rm K}+3\alpha_{\rm B}\right)H^2\dot{v_X}\\&-H\left[\left(\alpha_{\rm B}+2\alpha_{\rm H}\right)\frac{k^2}{a^2}-3\alpha_{\rm B}\dot{H}+3\left(2\dot{H}+\tilde{\rho}_{\rm m}+\tilde{p}_{\rm m}\right)\right]v_X=-\tilde{\rho}_{\rm m}\delta_{\rm m}\,.\end{aligned} \tag{4.21}$$

the Einstein (0i),

$$2\dot{\Phi}+\left(2-\alpha_{\rm B}\right)H\Psi-\alpha_{\rm B}H\dot{v_X}-\left(2\dot{H}+\tilde{\rho}_{\rm m}+\tilde{p}_{\rm m}\right)v_X=-\left(\tilde{\rho}_{\rm m}+\tilde{p}_{\rm m}\right)v_{\rm m}\,, \tag{4.22}$$

the traceless part of the Einstein (ij) equation,

$$\left(1+\alpha_{\rm H}\right)\Psi-\left(1+\alpha_{\rm T}\right)\Phi+\alpha_{\rm H}\dot{v_X}-\left(\alpha_{\rm M}-\alpha_{\rm T}\right)Hv_X=-\frac{3}{2}\left(\tilde{\rho}_{\rm m}+\tilde{p}_{\rm m}\right)\sigma_m\,, \tag{4.23}$$

and the trace part,

$$\begin{aligned}&2\ddot{\Phi}-\alpha_{\rm B}H\ddot{v_X}+2\left(3+\alpha_{\rm M}\right)H\dot{\Phi}+\left(2-\alpha_{\rm B}\right)H\dot{\Psi}\\&+\left[\left(2-\alpha_{\rm B}\right)\left(3+\alpha_{\rm M}\right)H^2-\left(\alpha_{\rm B}H\right)^{\cdot}-\left(2\dot{H}+\tilde{\rho}_{\rm m}+\tilde{p}_{\rm m}\right)\right]\Psi\\&-\left[\alpha_{\rm B}\left(3+\alpha_{\rm K}\right)H^2+\left(\alpha_{\rm B}H\right)^{\cdot}+\left(2\dot{H}+\tilde{\rho}_{\rm m}+\tilde{p}_{\rm m}\right)\right]\dot{v_X}\\&-\left[2\ddot{H}+2\left(3+\alpha_{\rm M}\right)\dot{H}H+\dot{\tilde{p}}_{\rm m}+\alpha_{\rm M}H\tilde{p}_{\rm m}\right]v_X=-\frac{k^2}{a^2}\sigma_m\left(\tilde{\rho}_{\rm m}+\tilde{p}_{\rm m}\right)+\delta\tilde{p}_{\rm m}\,,\end{aligned} \tag{4.24}$$

and the equation of motion for the scalar velocity potential v_X,

$$
\begin{aligned}
&3\alpha_{\rm B}\ddot{\Phi}H + \alpha_{\rm K}H^2\dot{v_X} + 3\left[\alpha_{\rm B}\left(3+\alpha_{\rm M}\right)H^2 + \left(\alpha_{\rm B}H\right)^{\cdot} - \left(2\dot{H} + \tilde{\rho}_{\rm m} + \tilde{p}_{\rm m}\right)\right]\dot{\Phi} \\
&+ \left(\alpha_{\rm K} + 3\alpha_{\rm B}\right)H^2\dot{\Psi} - 2\alpha_{\rm H}\frac{k^2}{a^2}\dot{\Phi} - 2\left[\dot{\alpha_{\rm H}} + \left(\alpha_{\rm H}\left(1+\alpha_{\rm M}\right) + \alpha_{\rm M} - \alpha_{\rm T}\right)H\right]\frac{k^2}{a^2}\Phi \\
&+ \Big[\left(2\alpha_{\rm K} + 9\alpha_{\rm B}\right)\dot{H} + \left(\dot{\alpha_{\rm K}} + 3\dot{\alpha_{\rm B}}\right)H + \left(3+\alpha_{\rm M}\right)\left(3\alpha_{\rm B} + \alpha_{\rm K}\right)H^2 \\
&- 3\left(2\dot{H} + \tilde{\rho}_{\rm m} + \tilde{p}_{\rm m}\right)\Big]H\Psi - 3\Big\{3\dot{H}\left[\left(\alpha_{\rm B}H\right)^{\cdot} - \left(2\dot{H} + \tilde{\rho}_{\rm m} + \tilde{p}_{\rm m}\right)\right] \\
&+ 3\alpha_{\rm B}\left[\ddot{H} + \left(3+\alpha_{\rm M}\right)\dot{H}H\right]H\Big\}v_X + \Big\{\left[\left(\alpha_{\rm B} + 2\alpha_{\rm H}\right)H\right]^{\cdot} + \left(\alpha_{\rm B} + 2\alpha_{\rm H}\right)\left(1+\alpha_{\rm M}\right)H^2 \\
&+ 2\left(\alpha_{\rm M} - \alpha_{\rm T}\right)H^2 - 2\left(\dot{H} + \tilde{\rho}_{\rm m} + \tilde{p}_{\rm m}\right)\Big\}\frac{k^2}{a^2}v_X \\
&- \left(\alpha_{\rm B} + 2\alpha_{\rm H}\right)H\frac{k^2}{a^2}\Psi + \left[2\alpha_{\rm K}\dot{H} + \dot{\alpha_{\rm K}}H + \alpha_{\rm K}\left(3+\alpha_{\rm M}\right)\right]H\dot{v_X} = 0\,.
\end{aligned}
\tag{4.25}
$$

These equations, combined with the evolution equations of the matter perturbations, δ_m, v_m, $\delta\tilde{p}_{\rm m}$, and σ_m, form the complete set of equations that one has to solve to follow the linear dynamics of beyond Horndeski theories. We have implemented these equations into `hi_class` [220] and used the solutions to study the phenomenology of this class of models and constrain its parameters with current CMB, large-scale structure data in the following two sections.

4.3 Phenomenology of beyond Horndeski theories

The purpose of this work is to provide constraints on parametrised beyond Horndeski models, i.e. using $\alpha_{\rm H}$. In this section we briefly discuss the observables we use to calculate our parameter confidence regions, namely the matter power spectrum and the CMB temperature, polarisation and lensing power spectra. We present the results obtained with `hi_class` for the evolution of these quantities for different values of $\alpha_{\rm H}$ and derive the analytic expressions for these in the quasi-static approximation and observe what effects $\alpha_{\rm H}$ has on them.

4.3.1 The quasi-static approximation

The key assumption of the quasi-static approximation (QSA) is,

$$
|\dot{X}| \lesssim H|X|\,,
\tag{4.26}
$$

where X stands for any metric or scalar perturbation. This assumption states that the time evolution of all parameters and perturbations of the metric and the scalar is comparable to the evolution of the Hubble parameter. However, this can be only true on sub-horizon scales, where space-derivatives become important

$$\frac{k^2}{a^2}|X| \gg H^2|X|\,. \tag{4.27}$$

We can apply this limit to the Hamiltonian constraint equation, Eq. (4.21), and the equation of motion for the scalar perturbation, Eq. (4.25),

$$\frac{2k^2}{a^2}\left(1+\alpha_{\rm H}\right)\Phi - \frac{k^2}{a^2}\left(\alpha_{\rm B}+2\alpha_{\rm H}\right)Hv_X = -\tilde{\rho}_{\rm m}\delta_{\rm m}\,, \tag{4.28}$$

$$\begin{aligned} &2\alpha_{\rm H}\frac{k^2}{a^2}\dot{\Phi} + \left(\alpha_{\rm B}+2\alpha_{\rm H}\right)\frac{k^2}{a^2}H\Psi + 2\left[\dot{\alpha_{\rm H}} + \left(\alpha_{\rm H}(1+\alpha_{\rm M}) + \alpha_{\rm M} - \alpha_{\rm T}\right)H\right]\frac{k^2}{a^2}\Phi \\ &+ \Big\{\left[\left(\alpha_{\rm B}+2\alpha_{\rm H}\right)H\right]^{\cdot} + \left[\left(\alpha_{\rm B}+2\alpha_{\rm H}\right)\left(1+\alpha_{\rm M}\right) + 2\left(\alpha_{\rm M}-\alpha_{\rm T}\right)\right]H^2 \\ &- \left(2\dot{H} + \tilde{\rho}_{\rm m} + \tilde{p}_{\rm m}\right)\Big\}\frac{k^2}{a^2}v_X = 0\,. \end{aligned} \tag{4.29}$$

In this approximation, we neglect any contribution from the matter anisotropic stress, σ_m, and pressure, $\tilde{p}_{\rm m}$. The reason is that the QSA can give predictions only at late-times, where the dominant matter component is DM, which is modelled as a pressureless perfect fluid.

Combining these with the rest of the constraint Eqs. (4.22) – (4.24) and their time derivatives, we get the constraint equations for the perturbations Φ and Ψ in this limit,

$$\frac{k^2}{a^2}\Phi = -\frac{3}{2}H^2\Omega_{\rm m}\mu_\Phi\delta_{\rm m} + \alpha_{\rm H}\lambda_\Phi H\frac{k^2}{a^2}v_{\rm m}\,, \tag{4.30}$$

$$\frac{k^2}{a^2}\Psi = -\frac{3}{2}H^2\Omega_{\rm m}\mu_\Psi\delta_{\rm m} + \alpha_{\rm H}\lambda_\Psi H\frac{k^2}{a^2}v_{\rm m}\,, \tag{4.31}$$

where

$$\mu_\Phi = \frac{1}{1+\alpha_{\rm H}}\left(1+\frac{\alpha_{\rm B}+2\alpha_{\rm H}}{c_{\rm sN}^2}B\right)\,, \qquad \lambda_\Phi = -\frac{1}{2}\frac{\left(\alpha_{\rm B}+2\alpha_{\rm H}\right)}{c_{\rm sN}^2H^2}\tilde{\rho}_{\rm m}\,, \tag{4.32}$$

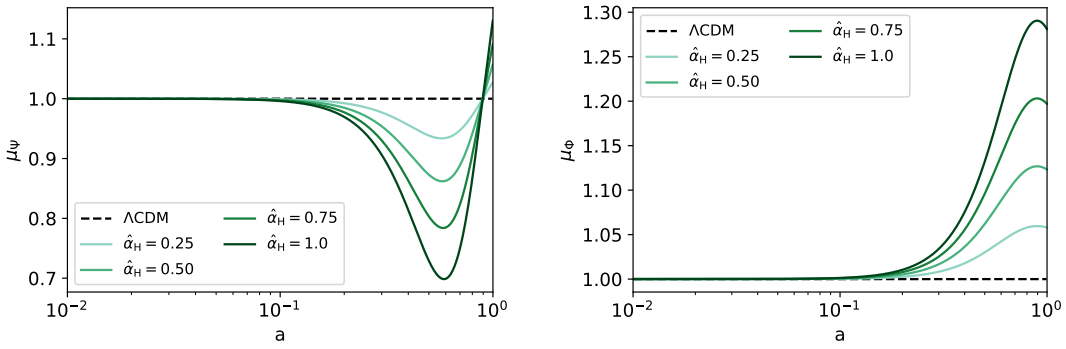


Figure 4.1: The evolution of μ_Ψ (left) and μ_Φ (right) as a function of scale factor. We have fixed $\alpha_B = \alpha_M = \alpha_T = 0$, the background cosmological parameters to their estimated values from Planck [24] and chosen background expansion history consistent with ΛCDM.

$$\mu_\Psi = \frac{1}{(1+\alpha_H^2 A)(1+\alpha_H)^2} \times \left[c_T^2 + 2\left(B + \frac{\dot{\alpha_H}}{H}\right)\frac{B}{c_{sN}^2} + \alpha_H(1+\alpha_H)aM_*^2\frac{d}{dt}\left(\frac{2B}{aHM_*^2c_{sN}^2}\right)\right], \tag{4.33}$$

$$\lambda_\Psi = \frac{\alpha_H\dot{A} + 2\dot{\alpha_H}A}{1+\alpha_H^2 A}, \tag{4.34}$$

with

$$A \equiv \frac{2\lambda_\Phi}{(\alpha_B + 2\alpha_H)H}, \qquad B \equiv \frac{1}{2}\left(\alpha_B + \alpha_B\alpha_T + 2\alpha_T\alpha_K - 2\alpha_K\alpha_H - 2\alpha_H - \frac{2\dot{\alpha_H}}{H}\right).$$

These can be combined with the Euler and continuity equations for DM, i.e.

$$\dot{\delta}_m = \frac{k^2}{a^2}v_m, \qquad \dot{v}_m = -\Psi. \tag{4.35}$$

Note that the notation we have used here is different from the commonly used effective gravitational constant, $\mu \equiv G_{eff}/G$ and gravitational slip parameter, $\gamma \equiv \Phi/\Psi$. In beyond Horndeski we have additional terms involving matter velocity that can not be neglected on sub-horizon scales, i.e. the ones proportional to λ_Φ and λ_Ψ. To avoid confusion we chose to use μ_Φ and μ_Ψ instead. In Horndeski ($\alpha_H = 0$), we would be able to relate the variables

used here to the usual μ and γ as

$$\mu_\phi \equiv \mu \qquad \mu_\Psi \equiv \mu/\gamma\,. \tag{4.36}$$

We know that in the ΛCDM model these are both equal to one. So the strength of gravity in other models can be expressed as the gravitational constant in ΛCDM plus a small correction [317],

$$\mu = 1 + \delta\mu = -\frac{2k^2\Phi}{3H^2\Omega_{\rm m}\delta_{\rm m}}\,. \tag{4.37}$$

However, here due to the presence of the beyond Horndeski parameter, $\alpha_{\rm H}$, this is not as straightforward. The effect of this additional term is non-negligible and we have taken it into account in all the calculations here. To show the significance of these terms we look at the simplified case where $\alpha_{\rm B} = \alpha_{\rm M} = \alpha_{\rm T} = 0$ and $\alpha_{\rm H} = \hat{\alpha}_{\rm H}\,\Omega_{\rm DE}$, i.e. a model with a standard kinetic term $\alpha_{\rm K}$ plus beyond Horndeski. The functions λ_Φ and μ_Φ simplify to

$$\lambda_\Phi = -\frac{3\Omega_{\rm m}}{2-3(\alpha_{\rm H}-1)\Omega_{\rm m}}\,, \qquad \mu_\Phi = 1 - \alpha_{\rm H}\lambda_\Phi\,, \tag{4.38}$$

and for λ_Ψ and μ_Ψ, we have

$$\lambda_\Psi = -\frac{9\Omega_{\rm m}\left(2-4\Omega_{\rm m}-3\Omega_{\rm m}^2\right)}{(2+3\Omega_{\rm m})\left[2+3(1-\alpha_{\rm H})\Omega_{\rm m}\right]}\,, \qquad \mu_\Psi = 1 - \alpha_{\rm H}\lambda_\Psi\,. \tag{4.39}$$

μ_Φ and μ_Ψ are plotted on Figure 4.1 as functions of the scale factor, a. In order to isolate its contribution, all α_i except for $\alpha_{\rm H}$ have been set to zero. Given that we chose the evolution of $\alpha_{\rm H}$ to be proportional to $\Omega_{\rm DE}$, we see that the deviations from $\mu_\Phi = \mu_\Psi = 1$ are very small before the onset of DE. On the left panel we have the evolution of $\mu_\Psi = 1 - \alpha_{\rm H}\,\lambda_\Psi$, which begins to decrease below one as $\alpha_{\rm H}$ becomes non negligible at late times. On the right is $\mu_\Phi = 1 - \alpha_{\rm H}\,\lambda_\Phi$. At late times $\alpha_{\rm H}\,\lambda_\Phi$ becomes negative and enhances μ_Φ.

In this case we can write $\delta\mu_\Phi \equiv -\alpha_{\rm H}\lambda_\Phi$ and so the modifications to GR coming from the two terms on the RHS of Eq. (4.30) are $\frac{3}{2}H^2\Omega_{\rm m}\alpha_{\rm H}\lambda_\Phi\delta_{\rm m}$ and $\alpha_{\rm H}\lambda_\Phi H\frac{k^2}{a^2}v_{\rm m}$, and equivalently for Eq. (4.31). The ratio of these two contributions is plotted on Figure 4.2 for four different values of $\hat{\alpha}_{\rm H}$. We can see that these are of the same order and hence have roughly equal contributions to the equations. This means that the $v_{\rm m}$ term cannot be neglected and must

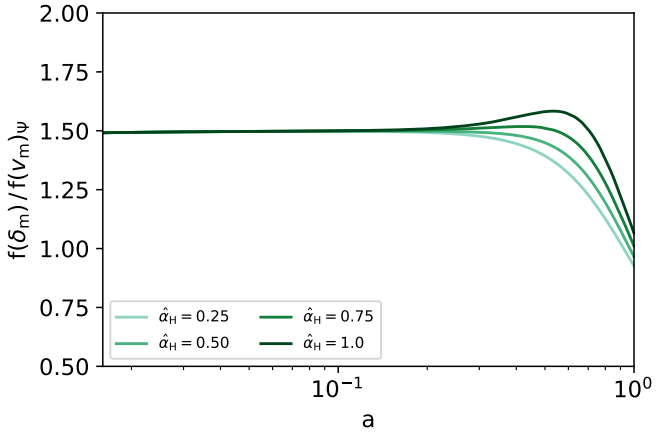


Figure 4.2: The ratio between the two terms contributing to the deviation from GR in the QSA equations, Eqs. (4.31) and (4.31) for 4 different values of $\hat{\alpha}_{\rm H}$ as a function of scale factor. On the y-axis we have abbreviated $\mathrm{f}(\delta_{\rm m}) \equiv \frac{3}{2}H^2\Omega_{\rm m}\alpha_{\rm H}\lambda_\Phi\delta_{\rm m}$ and $\mathrm{f}(v_{\rm m}) \equiv \alpha_{\rm H}\lambda_\Phi H\frac{k^2}{a^2}v_{\rm m}$.

be taken into account in the definition of the QS approximation equations. It is possible to redefine the effective gravitational constant and hence the constraint equations above using the common notation and taking into account the additional terms we have here. As usual, we define the growth factor as the logarithmic derivative of the matter overdensity

$$f = \frac{\mathrm{d}\ln\delta_{\rm m}}{\mathrm{d}\ln a}\,. \tag{4.40}$$

Using,

$$\frac{k^2}{a^2}v_{\rm m} = \dot{\delta}_{\rm m} = fH\delta_{\rm m}\,, \tag{4.41}$$

we can re-write the constraint equation for Φ in its usual form

$$\frac{k^2}{a^2}\Phi = -\frac{3}{2}H^2\Omega_{\rm m}\mu\delta_{\rm m}\,, \tag{4.42}$$

where

$$\mu = \mu_\Phi - \frac{2}{3\Omega_{\rm m}}\alpha_{\rm H}\lambda_\Phi f\,. \tag{4.43}$$

We show in Section 4.3.3 that the approximate solution for the growth factor in the quasi-static limit is very close to the exact solution, which makes this a good expression for the effective gravitational constant.

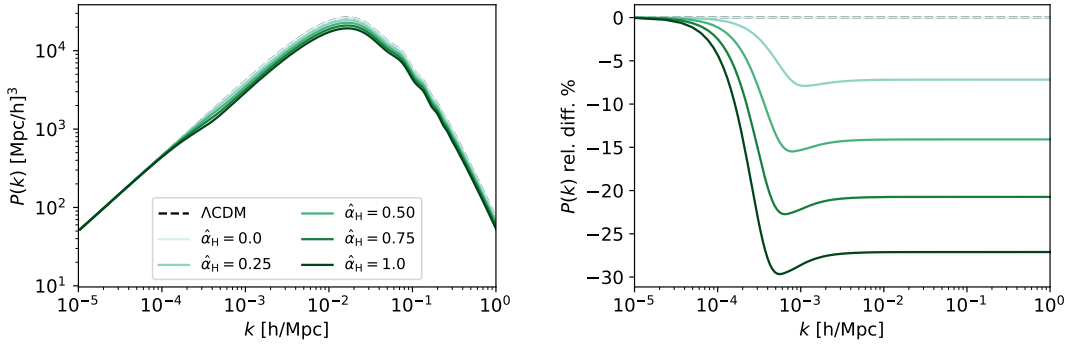


Figure 4.3: The effects of $\hat{\alpha}_{\rm H}$ on the matter power spectrum at $z = 0$. On the right graph we show the relative difference between the models we are considering and a fiducial ΛCDM model. For each line the background cosmological parameters are fixed to their estimated values from Planck [24]. For the background expansion history we assume a ΛCDM parametrisation (or $w_{\rm DE} = -1$) and for the α_i we choose the evolution proposed in [90]. Here we fix $\hat{\alpha}_{\rm K} = 1$, $\hat{\alpha}_{\rm B} = \hat{\alpha}_{\rm M} = \hat{\alpha}_{\rm T} = 0$ and vary $\hat{\alpha}_{\rm H}$.

4.3.2 Matter power spectrum

Combining Eqs. (4.31) and (4.35), we can derive the evolution equation for the matter overdensity, $\delta_{\rm m}$, in the QS limit

$$\ddot{\delta}_{\rm m} + (2 + \alpha_{\rm H}\lambda_\Psi) H \dot{\delta}_{\rm m} - \frac{3}{2} H^2 \Omega_{\rm m} \mu_\Psi \delta_{\rm m} = 0 \,. \tag{4.44}$$

As we have seen above the presence of $\alpha_{\rm H}$ decreases the effective gravitational constant μ_Ψ by $\alpha_{\rm H}\lambda_\Psi$, which in our parametrisation becomes important only at late times (see Figure 4.1). Then, increasing the value of $\hat{\alpha}_{\rm H}$, we expect a suppression of the matter power spectrum at small scales. This has two contributions acting in the same direction: (i) a decreased value of the effective gravitational constant μ_Ψ, and (ii) an enhanced friction term proportional to $\alpha_{\rm H}$. In the matter-dominated era, where $a \propto t^{2/3}$, $H = 2/(3t)$ and $\alpha_{\rm H}\lambda_\Psi \ll 1$, an approximate solution to Eq. (4.44) up to linear order in $\alpha_{\rm H}$ is given by

$$\delta_{\rm m} \propto t^{2/3(1-\alpha_{\rm H}\lambda_\Psi)} \,, \tag{4.45}$$

where in the derivation we assumed constant coefficients. This confirms that, during this period, while $\alpha_{\rm H}\lambda_\Psi > 0$, the growth of overdensities and hence the matter power spectrum have to be suppressed.

In Figure 4.3 we show the matter power spectrum as a function of k at redshift $z = 0$ as outputted from `hi_class`. We have set the other parameters, $\hat{\alpha}_{\rm K} = 1$, $\hat{\alpha}_{\rm B} = \hat{\alpha}_{\rm M} = \hat{\alpha}_{\rm T} = 0$, in order to observe the effect of $\hat{\alpha}_{\rm H}$ alone. We set the background cosmological parameters to their best fit values form Planck 2015 [24] and assume ΛCDM for the background expansion history. In this case only positive values of $\hat{\alpha}_{\rm H}$ are allowed, as negative $\hat{\alpha}_{\rm H}$ would cause a gradient instability. Assuming ΛCDM background expansion we fix $w_\phi = p_\phi/\rho_\phi = -1$, so $p_\phi + \rho_\phi = 0$ and $\dot{\rho}_\phi = 0$, and given that we chose $\alpha_{\rm H} = \Omega_\phi \hat{\alpha}_{\rm H}$, the gradient instability in Eq. (4.16) simplifies to,

$$\left[(\rho_m + p_m)(1 - \alpha_{\rm H}) + 2H^2\right] \alpha_{\rm H} > 0\,, \tag{4.46}$$

which is only satisfied when

$$\alpha_{\rm H} > 0 \qquad \text{and} \qquad \alpha_{\rm H} < 1 + \frac{2H^2}{\rho_m + p_m}\,. \tag{4.47}$$

For the time evolution of the α_i we assumed parametrisation in Eq. (4.9). On the left panel of Figure 4.3 we show the matter power spectrum generated by `hi_class` for five different values of $\hat{\alpha}_{\rm H}$ and on the right the relative difference between those and our fiducial ΛCDM. This is consistent with the results of [311]. As expected and discussed in detail in this section, $\hat{\alpha}_{\rm H}$ has a damping effect on the matter power spectrum and the deviation from ΛCDM on small scales indeed seems proportional to $\hat{\alpha}_{\rm H}$.

4.3.3 The growth rate of structure

Using the definition of the growth rate of structure, in Eq. (4.40), and the evolution equation for the matter overdensity, Eq. (4.44), we have,

$$f' + f^2 + \left(2 + \alpha_{\rm H}\lambda_\Psi + \frac{\dot{H}}{H^2}\right) f - \frac{3}{2}\Omega_{\rm m}\mu_\Psi = 0\,, \tag{4.48}$$

where primes denote a derivative with respect to $\ln a$. We can find an approximate solution to this equation in the matter-dominated era, making the following assumptions. The growth rate of structure can be expressed as the growth rate of matter in matter domination

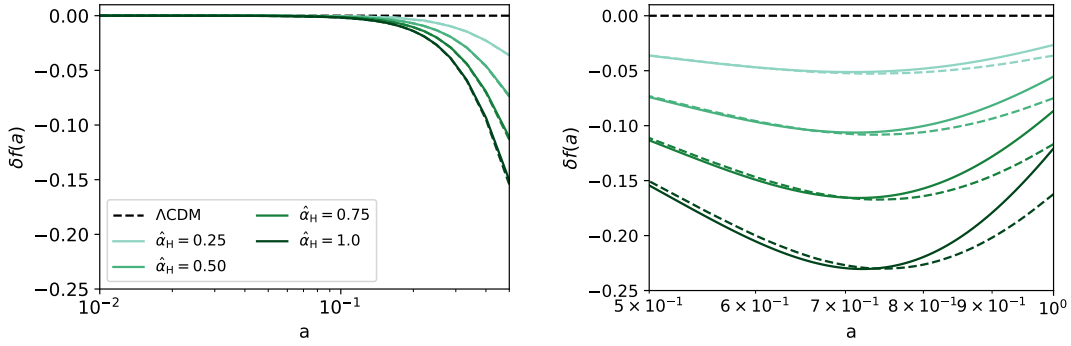


Figure 4.4: Relative difference of the growth rate, f, between 4 models with different $\hat{\alpha}_H$ and ΛCDM. On the left we have $10^{-2} < a < 0.5$ and on the right, $0.5 < a < 1$. Solid lines are the results obtained with `hi_class` and the dashed lines are the approximation, Eq. (4.52).

plus a small correction that represents the DE/MG component

$$f = f_m + \delta f \,. \tag{4.49}$$

Similarly, as argued above, we can express the effective gravitational constant μ_Ψ, as its standard value, i.e. $\mu_\Psi = 1$, plus a small correction, $\delta\mu_\Psi \equiv -\alpha_H \lambda_\Psi$. Expanding the growth equation in Eq. (4.48) to first order in the perturbation parameters, we get,

$$0^{\text{th}} \text{ order} \qquad f_m' + f_m^2 + \left(2 + \frac{\dot{H}}{H^2}\right) f_m - \frac{3}{2}\Omega_m = 0 \,, \tag{4.50}$$

$$1^{\text{st}} \text{ order} \qquad \delta f' + 2 f_m \delta f + -\delta\mu_\Psi f_m + \left(2 + \frac{\dot{H}}{H^2}\right) \delta f - \frac{3}{2}\Omega_m \delta\mu_\Psi = 0 \,. \tag{4.51}$$

We know that in ΛCDM matter-dominated universe $\Omega_m \sim 1$, $H = 2/(3t)$ and $f_m' = 0$, so $f_m = 1$. Hence we can find an approximate solution for the deviation of the growth rate from ΛCDM,

$$\begin{aligned} \delta f &\simeq \frac{5}{2} e^{-5/2 \ln a} \int e^{5/2 \ln a} \delta\mu_\Psi \, d\ln a \\ &\propto \delta\mu_\Psi \,, \end{aligned} \tag{4.52}$$

where to obtain the second line we have assumed that $\delta\mu_\Psi \sim$ const., which is reasonable in matter domination where in most realistic models the α_i are negligible.

We plot this result in Figure 4.4 and compare it to the one obtained with `hi_class`. We can see that in the matter-dominated era, the two solutions agree very well and the

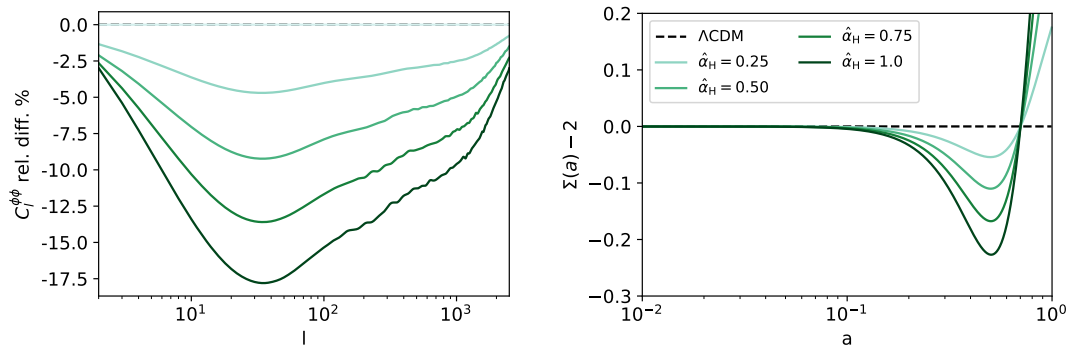


Figure 4.5: On the left is the relative difference of the CMB lensing potential for different values of $\hat{\alpha}_{\rm H}$ and ΛCDM. And on the right is the deviation from ΛCDM of the lensing parameter, $\Sigma(a) - 2$. The remaining parameters of the model are set as above.

approximation fails at later times, where the assumptions we have made do not hold.

4.3.4 CMB power spectra

The fluctuations in the CMB temperature and polarisation can be used to constrain very tightly the standard cosmological parameters in the ΛCDM model. Large scale structure gravitationally lenses the temperature and polarisation anisotropies, which makes the CMB also a good probe of the late universe where the effects that we are interested in become important. Therefore, beyond Horndeski theories are expected to modify the CMB spectra. In particular we expect to see significant deviations from ΛCDM in the lensing potential and the temperature power spectrum of the CMB. On the left panel of Figure 4.5 we show the relative difference between the CMB lensing potential, $C_l^{\phi\phi}$, of a set of MG models and our fiducial ΛCDM. As before we are looking at models where all $\hat{\alpha}_{\rm B} = \hat{\alpha}_{\rm M} = \hat{\alpha}_{\rm T} = 0$ and $\hat{\alpha}_{\rm K} = 1$ and consider five different values of $\hat{\alpha}_{\rm H}$. We can see that $C_l^{\phi\phi}$ decreases at a nearly linear rate as we increase $\hat{\alpha}_{\rm H}$, which was also shown in [311]. Again, in order to understand this behaviour, we turn to the equations describing this effect in the quasi-static approximation. The strength of the lensing potential is related to the Weyl potential, which can be obtained by summing the constraint Eqs. (4.30) and (4.31),

$$\frac{k^2}{a^2}(\Phi + \Psi) = -\frac{3}{2}H^2\Omega_{\rm m}(\mu_\Phi + \mu_\Psi)\delta_{\rm m} + \alpha_{\rm H}H(\lambda_\Phi + \lambda_\Psi)\dot{\delta}_{\rm m}\,. \tag{4.53}$$

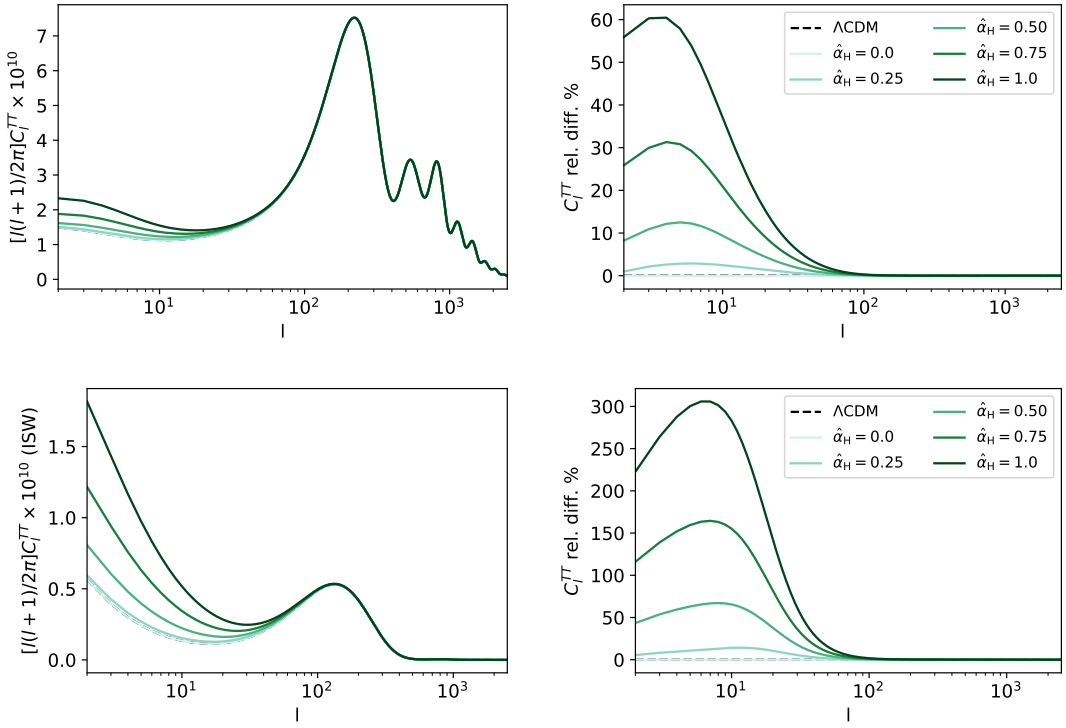


Figure 4.6: The unlensed CMB temperature power spectrum for different values of $\alpha_{\rm H}$, compared to ΛCDM.

Similarly to the case of the power spectrum, Section 4.3.2, we look at the simplest case (where $\alpha_{\rm B} = \alpha_{\rm M} = \alpha_{\rm T} = 0$). Here we have μ_Φ and μ_Ψ given by Eqs. (4.38) and (4.39) respectively. As in the case with the effective gravitational constant, the weak lensing parameter can not be defined as a function of μ_Ψ and μ_Φ as usual. Here, instead we have

$$\Sigma \equiv -\frac{2k^2(\Phi+\Psi)}{3a^2H^2\Omega_{\rm m}\delta_{\rm m}} = \mu_\Phi + \mu_\Psi - \frac{2\alpha_{\rm H}(\lambda_\Phi+\lambda_\Psi)}{3\Omega_{\rm m}} f\,, \tag{4.54}$$

where again we have used $\dot{\delta} = fH\delta$. For the case of $\hat{\alpha}_{\rm B} = \hat{\alpha}_{\rm K} = \hat{\alpha}_{\rm T} = 0$ and $\hat{\alpha}_{\rm M} = 1$ the above expression reduces to

$$\Sigma = 2 - \alpha_{\rm H}(\lambda_\Phi+\lambda_\Psi)\left(1 + \frac{2f}{3\Omega_{\rm m}}\right). \tag{4.55}$$

This expression is plotted on the right panel of Figure 4.5. In ΛCDM the lensing potential is $\Sigma = 2$, so what we are showing is the modification to this quantity due to the beyond Horndeski parameter, $\alpha_{\rm H}$. It is possible to notice that this is negative during most of the matter dominated era and decreases as $\alpha_{\rm H}$ increases, which confirms the damping effect of

$\alpha_{\rm H}$ on the lensing potential, see left panel of Figure 4.5.

The effects of beyond Horndeski can be seen also on the top panel of Figure 4.6, where we plot the CMB temperature power spectrum as obtained by `hi_class`. This result is again consistent with [311]. We can see that increasing $\hat{\alpha}_{\rm H}$ enhances the CMB temperature power spectrum at low l. This effect is well known for DE/MG models, and it is due to the integrated Sachs-Wolfe effect, which affects the power spectrum at low l, but has no significant effect at large l. The contribution from the combination of the late and early integrated Sachs-Wolfe effect to the temperature anisotropies is plotted on the bottom of Figure 4.6.

4.4 Results

In this section we present the constraints on our specific choice of beyond Horndeski parameters with data. We note that different time dependences may lead to large changes in the uncertainties and that a more systematic analysis including a broader range (or variety) of priors would be desirable. Nevertheless, this can be seen as a first step in assessing constraints on par with what has been done in the case of Horndeski theories.

4.4.1 Method

We use the Boltzmann code `hi_class` [220] to solve the equations shown in Appendix B.1. This code extends the Cosmic Linear Anisotropy Solver Software (CLASS) [318] by including the Horndeski class of theories, and it has been tested intensively against other Einstein-Boltzmann solvers in [319]. On top of the public version of `hi_class`, we have added the extra beyond Horndeski terms to the perturbation equations, the definitions of the DE density, pressure and $\alpha_{\rm H}$. We then interfaced it with the modular cosmological parameter estimation code CosmoSIS [320], which runs Monte Carlo Markov Chains (MCMC). We used the Metropolis-Hastings sampler to obtain our chains and consider those converged when the Gelman and Rubin parameter $R-1<0.01$ [230].

The full set of beyond Horndeski parameters that describes the evolution of the perturbations is $\{\hat{\alpha}_{\rm K},\hat{\alpha}_{\rm B},\hat{\alpha}_{\rm M},\hat{\alpha}_{\rm T},\hat{\alpha}_{\rm H}\}$. Assuming the constraints derived from the GW detection that we discussed in Section 4.2.3, we set $\hat{\alpha}_{\rm T}=0$ for all runs and run two sets of MCMC

BAO measurements		
Survey	z	$D_{\rm V}$
6dFGS [155]	0.106	456 ± 27
SDSS-MGS [150]	0.15	664 ± 25
BOSS DR12 [151]	0.38	1477 ± 16
BOSS DR12 [151]	0.51	1877 ± 19
BOSS DR12 [151]	0.61	2140 ± 22

Table 4.1: List of BAO measurements used in this work.

RSD measurements		
Survey	z	$f(z)\sigma_8(z)$
6dFGS [321]	0.067	0.423 ± 0.055
SDSS-MGS [322]	0.15	0.53 ± 0.19
SDSS-LRG [323]	0.30	0.49 ± 0.09
WIGGLEZ [324]	0.22	0.42 ± 0.07
WIGGLEZ [324]	0.41	0.45 ± 0.04
WIGGLEZ [324]	0.60	0.43 ± 0.04
WIGGLEZ [324]	0.78	0.38 ± 0.04
BOSS DR12 [151]	0.38	0.497 ± 0.032
BOSS DR12 [151]	0.51	0.458 ± 0.025
BOSS DR12 [151]	0.61	0.436 ± 0.022
VIPERS [159]	0.60	0.55 ± 0.12
VIPERS [159]	0.86	0.40 ± 0.11

Table 4.2: List of RSD measurements used in this work.

chains, one fixing $\hat{\alpha}_{\rm K} = 1$ and another with $\alpha_{\rm K}$ given by Eq. (4.18) to ensure $c_{\rm s}^2 = 1$ for all possible sets of values of $\{\hat{\alpha}_{\rm B}, \hat{\alpha}_{\rm M}, \hat{\alpha}_{\rm H}\}$. We fix the initial effective Planck mass, $M_*^2 = 1$. We also assume two massless and one massive neutrino with $m_\nu = 0.06$eV and vary the background cosmological parameters and the relevant set of $\hat{\alpha}_i$. Given that we use a parametrisation for the evolution of the α_i [Eq. (4.9)] here we present the constraints for the coefficients that fix this proportionality, $\hat{\alpha}_i$.

4.4.2 Datasets

To constrain the parameters of the theory we include CMB data, measurements of baryon acoustic oscillations (BAO) and redshift space distortions (RSD) from large-scale structure surveys:

- CMB: We use the temperature and polarisation power spectra and the lensing potential of the Cosmic Microwave Background (CMB) from Planck 2015 [24, 25]. The

Planck 2015 likelihood is discussed in [231]. We use the high l TT likelihood with $l = 30 - 2508$, along with the joint TT, EE, BB and TE likelihood in the range $l = 2 - 29$ and the lensing likelihood, using both temperature and polarisation lensing reconstruction in the multipole range $l = 40 - 400$.

- BAO: We use BAO measurements from 6dFGS [155] and the Sloan Digital Sky Survey (SDSS) Data Release 7 Main Galaxy Sample (MGS) [150], which probes the supplied expansion history through the redshift-distance and redshift-Hubble relations combined through the relation, $D_{\rm V} = (D_{\rm A}^2(1+z)^2 z/H)^{1/3}$. Here $D_{\rm V}$ is the angle-averaged distance, $D_{\rm A}$ - the angular diameter distance and z is the redshift. We also used measurements from the Baryon Oscillation Spectroscopic Survey (BOSS) Data Release 12 [151], which are lower signal-to-noise and constrain both the angular diameter distance, $D_{\rm A}$ and the Hubble parameter, H. There are also BAO measurements from WiggleZ survey [324], but these partially overlap with the BOSS CMASS volume. We have chosen to use the BOSS measurements here. These measurements do not constrain the matter power spectrum itself, but just the positions of the BAO peaks. They are presented in Table 4.1 and plotted on the left panel of Figure 4.7.

- RSD: Finally, we use Redshift Space Distortions (RSD) data. This effect probes the growth of structure and therefore is sensitive to late-time effects and can be used to probe MG. We use measurements derived form from 6dFGS [321], SDSS MGS [322] and Luminous Red Galaxy (LRG) [323] samples, WiggleZ [324], and VIPERS [159]. We also use the RSD measurements from BOSS DR12 [151] with the full covariance between the 3 $f(z)\sigma_8(z)$ measurements at different redshifts and the BAO measurements of $H(z)$ and $D_{\rm A}(z)$. All RSD measurements are quoted on Table 4.2 and on the right panel of Figure 4.7.

In [306] the authors also included data for the full matter power spectrum, $P(k)$, from a number of large scale structure surveys. However, this dataset does not improve the constraints significantly and requires to choose a galaxy bias factor. So we have decided not to include it here.

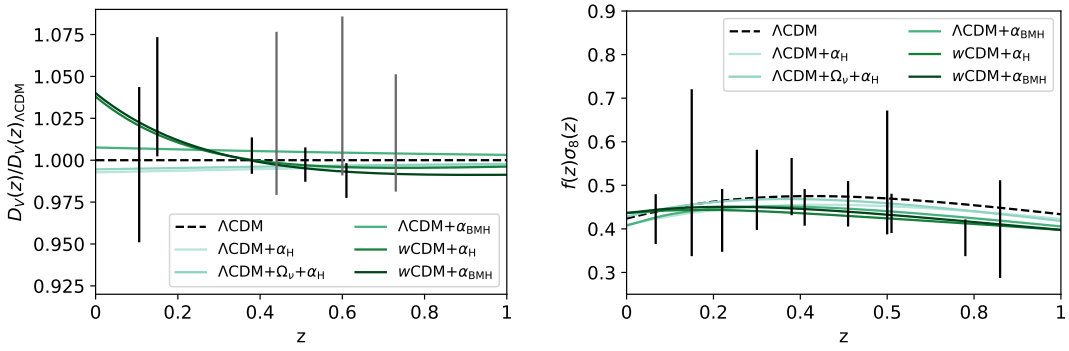


Figure 4.7: Distance measurements, D_V, (left) and the growth of structure, $f\sigma_8$, (right) as a function of redshift, z, for best fit lines of a set of MG models compared to ΛCDM. On the left plot, the black lines are the BAO measurements from Table 4.1 and the grey are the measurements from the WiggleZ survey [324]. On the right are the RSD measurement from Table 4.2.

	Data	Constraints	Marg. mean
ΛCDM+α_H	CB	$0.01 < \hat{\alpha}_H < 0.31$	$\hat{\alpha}_H = 0.12 \pm 0.10$
	CBR	$0.02 < \hat{\alpha}_H < 0.36$	$\hat{\alpha}_H = 0.17 \pm 0.11$
ΛCDM+Ω_ν+α_H	CB	$0.01 < \hat{\alpha}_H < 0.33$	$\hat{\alpha}_H = 0.12 \pm 0.10$
	CBR	$0.01 < \hat{\alpha}_H < 0.33$	$\hat{\alpha}_H = 0.14 \pm 0.10$
ΛCDM+α_{BMH}	CB	$-0.44 < \hat{\alpha}_H < 2.16$	$\hat{\alpha}_H = 0.96 \pm 0.80$
	CBR	$0.38 < \hat{\alpha}_H < 2.48$	$\hat{\alpha}_H = 1.49 \pm 0.64$
wCDM+α_H	CB	$0.13 < \hat{\alpha}_H < 0.51$	$\hat{\alpha}_H = 0.35 \pm 0.11$
	CBR	$0.02 < \hat{\alpha}_H < 0.49$	$\hat{\alpha}_H = 0.33 \pm 0.12$
wCDM+α_{BMH}	CB	$-0.53 < \hat{\alpha}_H < 2.18$	$\hat{\alpha}_H = 0.90 \pm 0.69$
	CBR	$0.07 < \hat{\alpha}_H < 2.21$	$\hat{\alpha}_H = 1.15 \pm 0.65$

Table 4.3: Constraints (95%) and marginalised mean values of α_H for the different datasets combinations (where "CB" is CMB+BAO and "CBR" – CMB+BAO+RSD) and different sets of other parameters being varied.

4.4.3 Constraints on the beyond Horndeski parameters

Here we present the constraints on the beyond Horndeski parameters derived using the method and datasets described above. As mentioned before, the value of $\hat{\alpha}_{\rm K}$ has little to no effect on sub-horizon scales and in particular on the observables we are looking at. We then chose either to fix $\hat{\alpha}_{\rm K} = 1$ or to get it from Eq. (4.18) and present the constraints on the other parameters.

The grid of parameters varied and datasets used is shown on Table 4.3, with the 95% confidence regions for $\hat{\alpha}_{\rm H}$ and marginalised means. Our baseline model is the standard ΛCDM, where we varied the Hubble constant H_0, the baryon and dark matter densities today, $\Omega_{\rm b}$ and $\Omega_{\rm cdm}$, the curvature fluctuation amplitude, $A_{\rm s}$, the scalar spectral index, $n_{\rm s}$ and the optical depth at reionization, τ. On top of that, in the other runs we varied: the beyond Horndeski parameter $\hat{\alpha}_{\rm H}$ keeping the other $\hat{\alpha}_i$ fixed (ΛCDM+$\alpha_{\rm H}$); $\hat{\alpha}_{\rm H}$ and the density of massive neutrinos (ΛCDM+Ω_ν+$\alpha_{\rm H}$); $\hat{\alpha}_{\rm H}$ and the Horndeski α_i (ΛCDM+α_{BMH}); $\hat{\alpha}_{\rm H}$ and we replaced the cosmological constant Λ with a time dependent equation of state parametrised as $w(a) = w_0$+$w_a(1-a)$ (wCDM+α_H); and finally a time dependent equation of state plus the Horndeski $\hat{\alpha}_i$ and $\hat{\alpha}_{\rm H}$ (wCDM+α_{BMH}).

The confidence regions of $\hat{\alpha}_{\rm H}$ seem to exclude 0 in most of these cases and are mainly positive. The lower limit at 0 is exact when considering a cosmological constant and $\hat{\alpha}_{\rm B} = \hat{\alpha}_{\rm M} = 0$, and can be inferred by inspecting Eq. (4.16). For the remaining cases the contours are smooth around 0 since the other MG parameters modify the stability conditions, but Eq. (4.16) still plays a central role in excluding negative values of $\hat{\alpha}_{\rm H}$. Both the upper and lower limits seem to be affected largely by the combination of datasets used and the freedom in some of the other parameters. We see that varying Ω_ν has little effect on the constraints of $\hat{\alpha}_{\rm H}$ and the largest difference seems to be due to the other MG parameters $\hat{\alpha}_{\rm B}$ and $\hat{\alpha}_{\rm M}$. It is possible to notice from Table 4.3, and Figures 4.8 and 4.9, that the contours of the MG parameters are greatly improved by adding the RSD dataset. This can be explained by the fact that RSD is the only dataset that probes the growth rate of structure, $f\sigma_8$, at high significance. And given that we chose for the α_i to evolve as the dark energy density parameter, $\Omega_{\rm DE}$, we would expect it to have an effect at late times.

Model	CMB	BAO+RSD	Total
ΛCDM	5636.61 (–)	4.78 (–)	5641.39 (–)
ΛCDM+$\alpha_{\rm H}$	5636.05 (0.56)	3.55 (1.23)	5639.60 (1.79)
ΛCDM+Ω_ν+$\alpha_{\rm H}$	5636.29 (0.35)	3.72 (1.03)	5640.01 (1.38)
ΛCDM+α_{BMH}	5633.84 (2.77)	2.95 (1.83)	5636.79 (4.60)
wCDM+α_H	5634.19 (2.42)	3.27 (1.51)	5637.46 (3.93)
wCDM+α_{BMH}	5632.62 (3.99)	2.82 (1.96)	5635.44 (5.95)

Table 4.4: Best fit likelihoods for each model and probe, when running the full CMB+BAO+RSD dataset. In the brackets we show the difference of the likelihood for the given model from ΛCDM.

In Table 4.4 we show the absolute log likelihood values for the models considered, measured at their best fit values. It is possible to notice that the total likelihood generally decreases as we increase the number of free parameters. A better fit to data is expected when enlarging the parameter space, but in this case the improvement does not appear enough to justify the price of adding new parameters. The best fit models are also plotted, together with the measurements we used, on the left panel of Figure 4.7 for the BAO datasets and on the right for the RSD dataset. We show how these measurements are fitted by the models we have considered here (green lines) and ΛCDM (black dashed lines). The beyond Horndeski models, and particularly when combined with the DE equation of state clearly provide more flexibility to fit these measurements than the best likelihood model of ΛCDM. However, given that most of these models fit within the error bars of these measurements, we cannot conclude that these differences point towards either of the models being a better fit.

On Figure 4.8 we have plotted the confidence regions for the relevant parameters of the ΛCDM+Ω_ν+$\alpha_{\rm H}$ run. The lighter and darker contours represent the 95% and 68% confidence regions respectively. In this case the only MG parameter we vary is $\hat{\alpha}_{\rm H}$, while the remaining $\hat{\alpha}_i$ are fixed to $\hat{\alpha}_{\rm K} = 1$, $\hat{\alpha}_{\rm B} = \hat{\alpha}_{\rm M} = \hat{\alpha}_{\rm T} = 0$. As mentioned the gradient stability condition in Eq. (4.16) requires $\hat{\alpha}_{\rm H} > 0$, which can be clearly seen in the contours. Interestingly, $\hat{\alpha}_{\rm H}$ does not seem to have any degeneracy with the density of neutrinos Ω_ν, which was the main motivation to study this extension to the baseline ΛCDM model.

Figure 4.9 shows the contours for the wCDM+α_{BMH} model. In particular, we focus on the posterior distributions of the (beyond) Horndeski parameters, $\{\hat{\alpha}_{\rm B}, \hat{\alpha}_{\rm M}, \hat{\alpha}_{\rm H}\}$, and the DE EoS parameters, w_0 and w_a. As mentioned, by comparing the two dataset com-

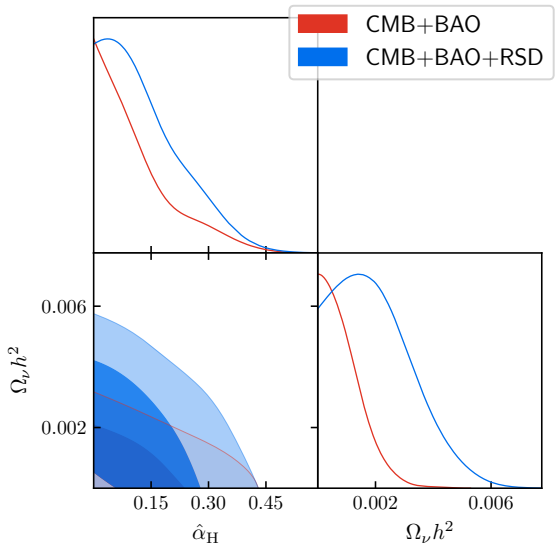


Figure 4.8: Constraints on Ω_ν and $\hat{\alpha}_{\rm H}$ from the combination of CMB+BAO (red) and CMB+BAO+RSD (blue) datasets from the ΛCDM+Ω_ν+$\alpha_{\rm H}$ run, with $\alpha_{\rm H} = \hat{\alpha}_{\rm H}\,\Omega_{\rm DE}$, $\hat{\alpha}_{\rm K} = 1$ and $\hat{\alpha}_{\rm B} = \hat{\alpha}_{\rm M} = \hat{\alpha}_{\rm T} = 0$.

binations, CMB+BAO and CMB+BAO+RSD, it is possible to notice the effect of RSD in tightening the contours. The most significant differences seem to be for $\hat{\alpha}_{\rm K}$ and $\hat{\alpha}_{\rm H}$. Unlike in the previous case, here there is no hard bound on 0 on the value of $\hat{\alpha}_{\rm H}$ coming from the stability conditions. This allows it to go negative, since the combination with the other parameters may preserve the stability of the theory. In the case where we had $\hat{\alpha}_{\rm B} = \hat{\alpha}_{\rm M} = 0$, the data seem to peak the distribution of $\hat{\alpha}_{\rm H}$ around zero and no large values were allowed. On the contrary here, the degeneracy between $\hat{\alpha}_{\rm H}$, $\hat{\alpha}_{\rm B}$ and $\hat{\alpha}_{\rm M}$, spreads out the distribution of $\hat{\alpha}_{\rm H}$ in the positive direction relaxing significantly the contours. We see that $\alpha_{\rm H}$ is not degenerate with the $w_{\rm DE}$.

On Figure 4.10 we show the different constraints on the parameters for the two cases discussed in Section 4.2.3. The combination of datasets used for both contours here is CMB+BAO+ RSD and the model considered is ΛCDM+α_{BMH}. The red contour represents the case where we set $\hat{\alpha}_{\rm K} = 1$ and let the speed of sound of the scalar degree of freedom vary with the other $\hat{\alpha}_i$. The blue is for the case where the speed of sound of the scalar $c_{\rm s}^2 = 1$ and $\alpha_{\rm K}$ is determined by the relation in Eq. ((4.18)). We can see that there is no significant difference in the contours for those two cases, which confirms that the choice for $\alpha_{\rm K}$ has little effect on current constraints, and that the $c_{\rm s}^2 = 1$ branch of the results of [316] may not have an effect on the estimated values of the rest of the α_i.

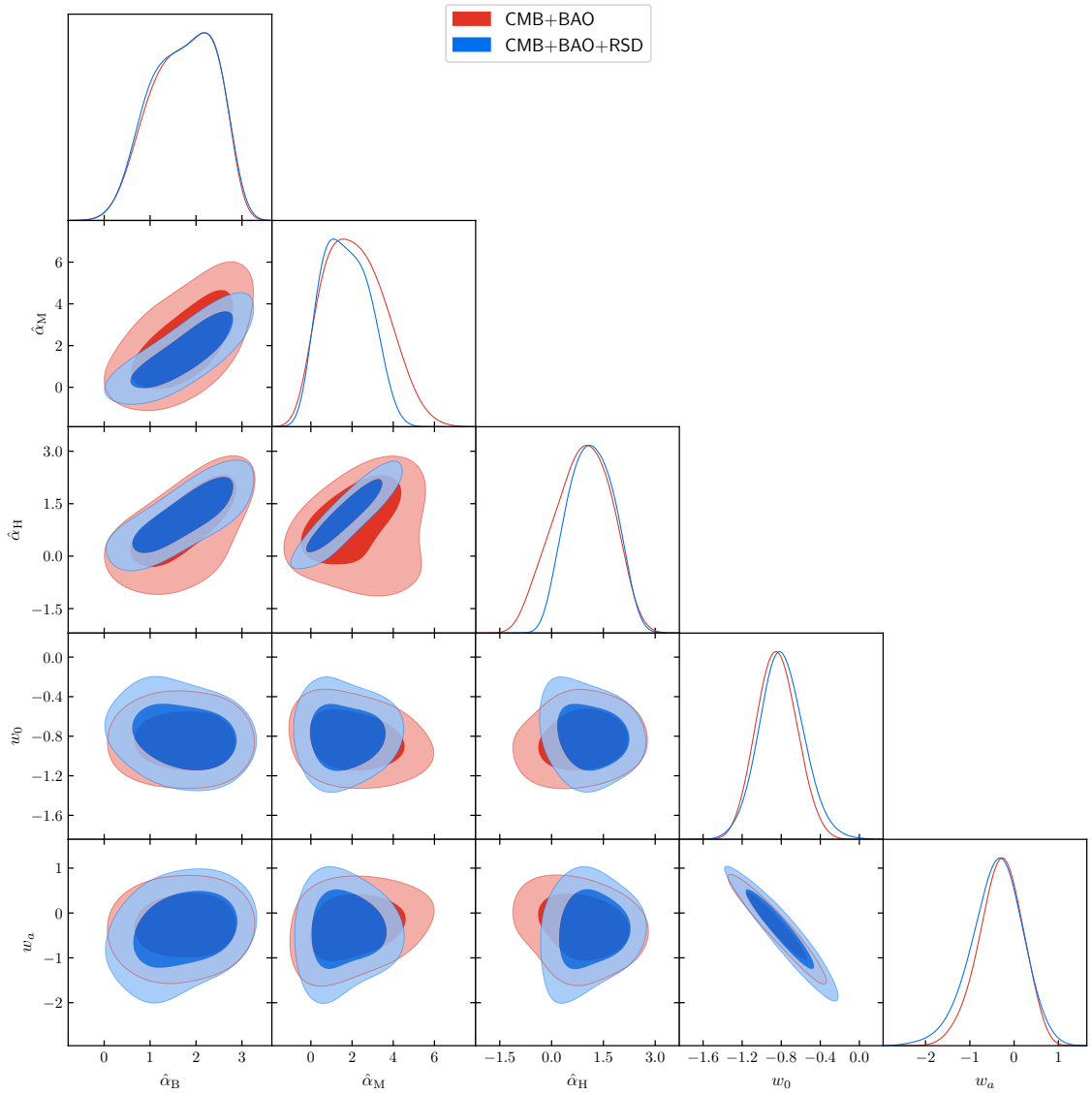


Figure 4.9: Constraints on the MG parameters, $\hat{\alpha}_{\rm B}, \hat{\alpha}_{\rm M}, \hat{\alpha}_{\rm H}$, and the DE equation of state parameters, w_0 and w_a. These contours are from the full parameter run (wCDM+$\alpha_{\rm BMH}$) with the combination of CMB+BAO (red) and CMB+BAO+RSD (blue) datasets.

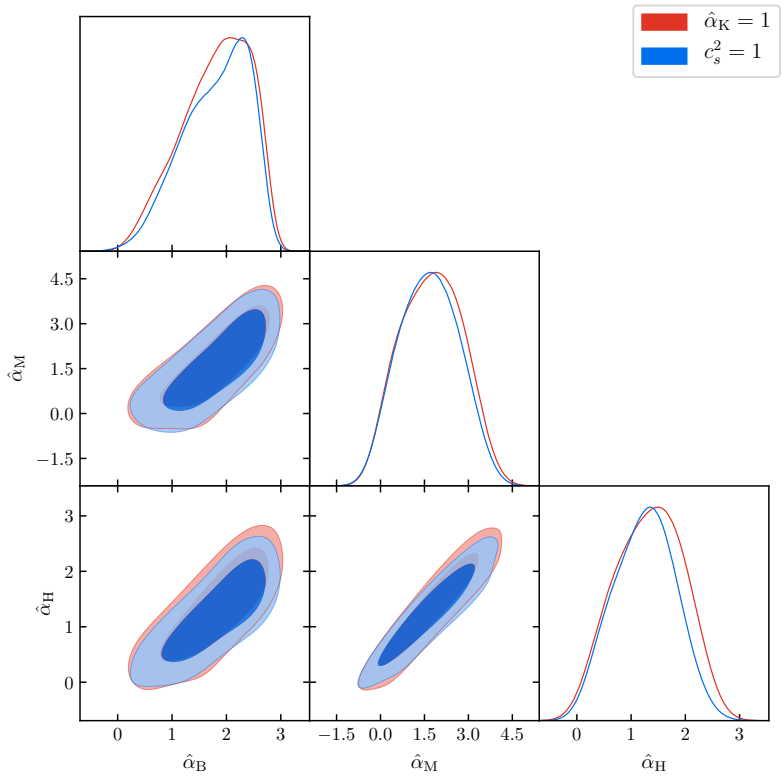


Figure 4.10: Constraints on $\hat{\alpha}_B$, $\hat{\alpha}_M$ and $\hat{\alpha}_H$ from the combination of CMB+BAO+RSD datasets. The background expansion history is again ΛCDM and the evolve the α_i is proportional to Ω_{DE}, with $\hat{\alpha}_K = 1$ (red), and $c_s^2 = 1$ and α_K given by Eq. (4.18)) (blue). We also vary the standard cosmological parameters.

4.5 Discussion

In this paper, we studied the phenomenology of the beyond Horndeski class of theories. This class of theories includes the most popular DE and MG models that aim at explaining the accelerated expansion of the Universe and has been shown to have self-accelerating solutions. The minimal set of functions that can describe the evolution of linear perturbations in this model is $\{\alpha_{\rm K}, \alpha_{\rm B}, \alpha_{\rm M}, \alpha_{\rm T}, \alpha_{\rm H}\}$. To find the solutions of these equations a parametric form for these functions has to be assumed. Here we chose the time evolution to be given by the fractional density of dark energy, so that $\alpha_i = \hat{\alpha}_i \, \Omega_{\rm DE}$. Taking into account the implications from the observation of the binary neutron star merger (GW170817) and its electromagnetic counterpart (GRB170817A), we have set the tensor speed excess, $\hat{\alpha}_{\rm T} = 0$.

Constraints on $\hat{\alpha}_{\rm K}$, $\hat{\alpha}_{\rm B}$, $\hat{\alpha}_{\rm M}$ and $\hat{\alpha}_{\rm T}$ from cosmological data are $\mathcal{O}(1)$. In this work our aim was to constrain the parameter $\hat{\alpha}_{\rm H}$, which is peculiar of the theories beyond Horndeski, using a combination of CMB, BAO and RSD datasets.

Studying the phenomenology of this model and in particular the case where $\hat{\alpha}_{\rm K} = 1$, $\hat{\alpha}_{\rm B} = \hat{\alpha}_{\rm M} = \hat{\alpha}_{\rm T} = 0$, we found that $\hat{\alpha}_{\rm H}$ suppresses the matter power spectrum and the CMB lensing potential, and enhances the temperature power spectrum of the CMB at low l. These findings are consistent with other results in the literature. The quasi-static approximation was used to derive analytic solutions to evolution equations of the matter overdensity, $\delta_{\rm m}$ the growth rate parameter, f and the weak lensing parameter, Σ, which agreed with the exact solutions obtained using `hi_class`. We discuss the commonly used notation for the quasi-static approximation and suggest how that may be amended to account for the extra terms that come from the presence of the beyond Horndeski parameter, $\alpha_{\rm H}$.

We perform parameter estimation using CMB temperature, polarisation and lensing data from the Planck 2015 dataset and measurements of the BAO and RSD from a number of different large scale structure surveys. From the MG parameters we set $\hat{\alpha}_{\rm K} = 1$, as varying this parameter has been shown to have no effect on the other parameters, as mentioned above we also set $\hat{\alpha}_{\rm T} = 0$, and varied $\hat{\alpha}_{\rm B}$, $\hat{\alpha}_{\rm M}$ and $\hat{\alpha}_{\rm H}$. We performed different runs where we varied $\hat{\alpha}_{\rm H}$ and the six standard cosmological parameters, h_0, $\Omega_{\rm b}$, $\Omega_{\rm cdm}$, A_s,

n_s and τ, combined with either Ω_ν, $\hat{\alpha}_{\rm B}$ and $\hat{\alpha}_{\rm K}$, w_0 and w_a, or a combination of all. We present the confidence contours for two of these runs and show that the beyond Horndeski parameter, $\hat{\alpha}_{\rm H}$, is degenerate with the other MG parameters, $\hat{\alpha}_{\rm B}$ and $\hat{\alpha}_{\rm M}$, but not with either the ΛCDM parameters, Ω_ν, w_0 or w_a. The constraints on $\hat{\alpha}_{\rm H}$ that we get from these runs are $\mathcal{O}(1)$. We also show that setting the speed of sound of the scalar $c_{\rm s}^2 = 1$ does not have a substantial effect on the results. Comparing the likelihood of the best fit models for the different runs we have done, we find that the MG models seem to fit the data slightly better than ΛCDM. However, the difference in the likelihood is too small to comment on the validity of either model over the others and most probably is simply due to the fact that there are more free parameters in the MG models than there are in ΛCDM.

Chapter 5

Dynamical friction from scalar dark matter

Light bosonic scalars (e.g. axions) may form clouds around black holes via superradiant instabilities, or via accretion if they form some component of the dark matter. It has been suggested that their presence may lead to a distinctive dephasing of the gravitational wave signal when a small compact object spirals into a larger black hole. Motivated by this, we study numerically the dynamical friction force on a black hole moving at relativistic velocities in a background scalar field with an asymptotically homogeneous energy density. We show that the relativistic scaling is analogous to that found for supersonic collisional fluids, assuming an approximate expression for the pressure correction which depends on the velocity and scalar mass. While we focus on a complex scalar field, our results confirm the expectation that real scalars would exert a force which oscillates between positive and negative values in time with a frequency set by the scalar mass. The complex field describes the time averaged value of this force, but in a real scalar the rapid force oscillations could in principle leave an imprint on the trajectory. The approximation we obtain can be used to inform estimates of dephasing in the final stages of an extreme mass ratio inspiral.

5.1 Introduction

Black holes (BHs) provide us with a unique laboratory to study matter in strong gravity conditions. The interplay of new forms of matter with BHs can help us shed light on

the matter composition and properties. Such investigations are particularly timely given the recent imaging of a BH at the centre of the galaxy M87 [325], ongoing detections of gravitational wave (GW) signals from the collisions of BH binary systems by the Advanced LIGO/Advanced Virgo/KAGRA network [171, 326–328], and the promise of future detections by third-generation ground-based detectors [329–331] and space based-detectors like LISA, Tianqin and Taiji [332–335].

Light bosonic scalar particles, such as axions, provide a well-motivated extension of Standard Model physics [336, 337] (see [338, 339] for reviews). They are a potential candidate for dark matter (DM) [48, 49] (see [340–342] for reviews), and in such scenarios their accretion onto BHs may result in the formation of distinctive structures [343–345]. Furthermore, superradiant instabilities can give rise to gravitationally bound clouds of axions around spinning BHs by amplifying small fluctuations in the field [346–351], in which case they need not be a major component of the DM (see [180] for a review).

In the case of superradiant clouds, it has been proposed that the GW signal from a smaller compact object orbiting the BH, passing through the bosonic environment, may carry distinctive signatures of its presence, detectable via LISA observations of extreme mass ratio inspiral (EMRI) signals [178,352–354]. In Ref. [353], such effects were contrasted with the impact of dark matter spikes that may cause a similar dephasing [179, 187, 355–360], and found to be distinguishable. Whilst Ref. [353] considered dephasing of the orbit due to the gravitational field of the cloud, dynamical friction should also play an important role, and potentially enhance the effect of the cloud on the evolution of the binary. In this chapter we seek to expand existing results for dynamical friction in light scalar DM to the relativistic regime, which would be relevant for the final stages of inspiral.

Dynamical friction, first studied by Chandrasekhar [361], is a drag force experienced by an astrophysical object moving in a fluid or bath of heavy particles. The gravitational attraction of the larger object creates an overdensity behind it (a "gravitational wake"), resulting in a drag force with a form that depends on the nature of the fluid and the perturber. In the nonrelativistic limit the dynamical friction force scales with velocity, v, as

$$F_{\rm d,nonrel} \sim \frac{\log(v)}{v^2}\,. \tag{5.1}$$

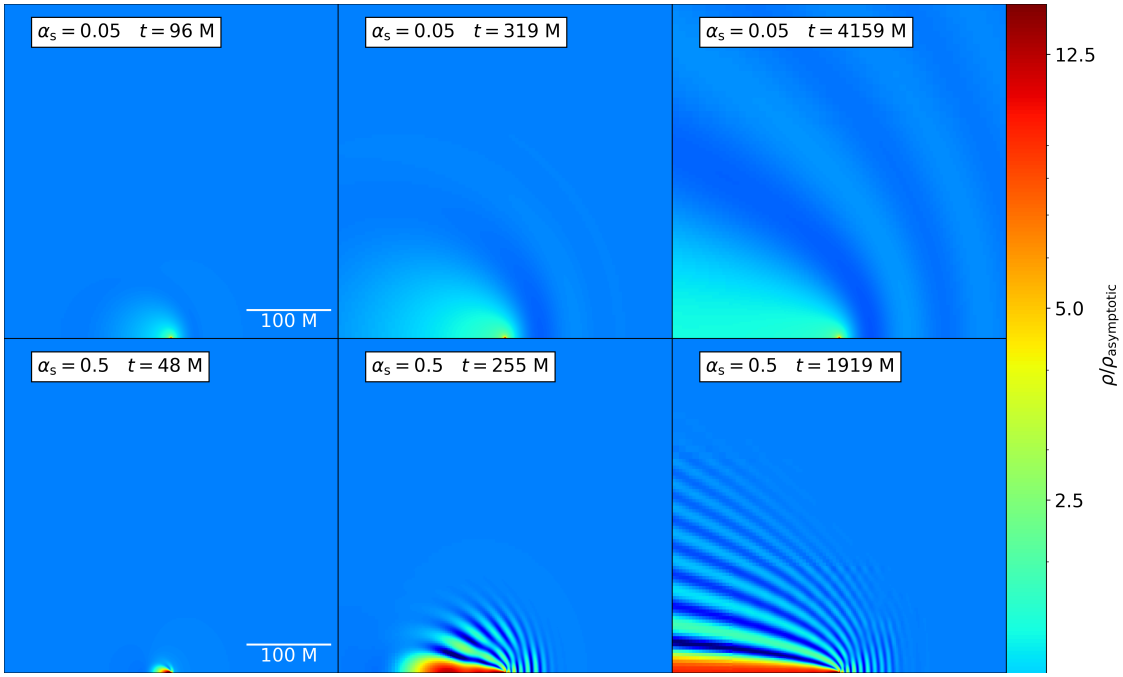


Figure 5.1: Image illustrating our numerical setup: the density distribution, ρ, of the scalar cloud (normalised to the asymptotic value of the density, $\rho_{\rm asymptotic}$) around a BH that is boosted relative to the matter rest frame. The two rows show different scalar field masses, $\alpha_{\rm s} = 0.05$ and 0.5, from top to bottom, increasing in time from left to right (the full time evolution for these simulations can be found at `https://youtu.be/5ZDfSwW9NHA` and `https://youtu.be/XUACRBfZX-w` for $\alpha_{\rm s} = 0.05$ and 0.5 respectively). This illustrates the known result that for smaller scalar field masses the tail is less dense and dynamical friction is suppressed.

This scaling does not hold in the relativistic regime where $v \sim 1$. (It also breaks down as $v \to 0$, where as expected $F_{\rm d,nonrel}(v) \to 0$). The case of a single point object immersed in scalar matter was studied in the nonrelativistic limit in Ref. [49], where it was shown that the dynamical friction force is suppressed for light scalar matter. This happens when their wave-like behaviour becomes relevant on the scale of the accretion radius $\sim GM/v^2$ where M is the mass of the object.

In this work we investigate the corrections to the scaling of the dynamical friction force with velocity for scalar matter in the relativistic regime, following similar methods to those used by Petrich et al. [362] for collisional fluids, where the fluid is numerically evolved to a stationary state from which the force can be measured.

Our setup is illustrated in Fig. 5.1, with examples of the time evolution (increasing from left to right) of the density patterns around the BH for different scalar masses. Time and distance scales are in units of the BH mass, M. The mass of the scalar field, m, is

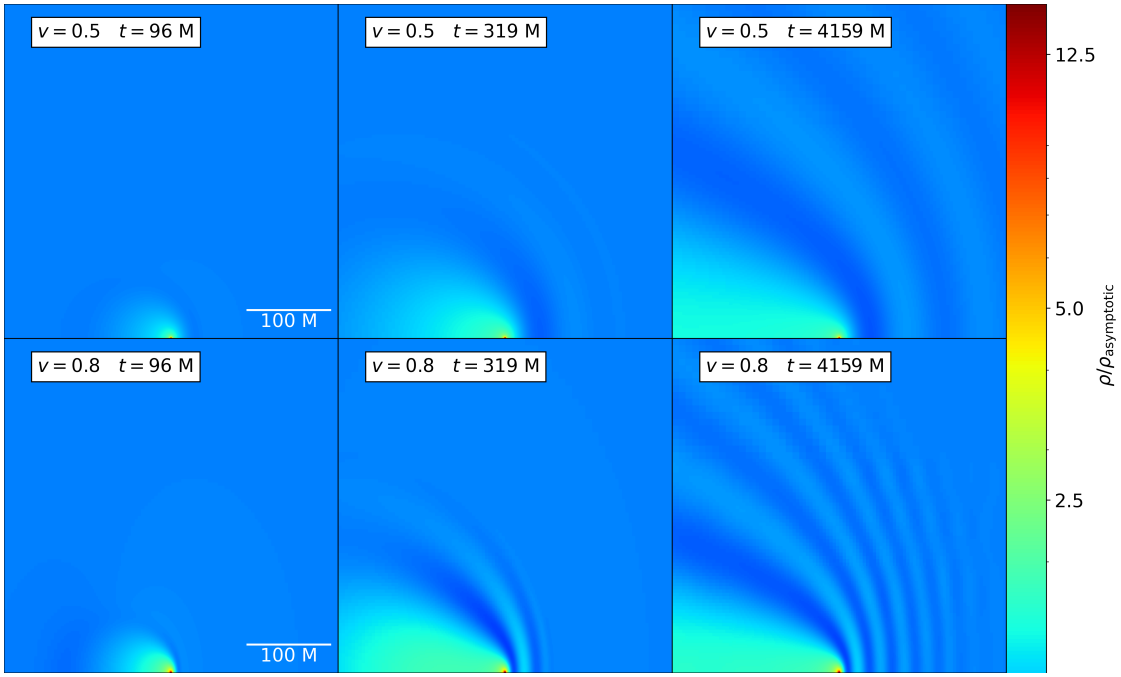


Figure 5.2: The time evolution (from left to right) of the density profiles of the cloud (normalised to the asymptotic value of the density, $\rho_{\rm asymptotic}$) for two different velocities, $v = 0.5$ and 0.8, and the same scalar mass, $\alpha_{\rm s} = 0.05$. This illustrates the change in the profile from the non relativistic to the relativistic regime. We find that, contrary to the nonrelativistic scaling, the dynamical friction force does not decrease with velocity, with the density of matter in the cloud slightly higher at $v = 0.8$ than $v = 0.5$.

also fixed to the mass of the BH, through the dimensionless variable $\alpha_{\rm s} = Mmc/\hbar$. We present two of the cases studied in this work: $\alpha_{\rm s} = 0.05$ (on the top), which covers the wave-like small mass regime, and $\alpha_{\rm s} = 0.5$ (on the bottom), where the wave-like effects begin to be suppressed. As in Ref. [49], we can see that larger scalar masses result in higher densities in the stationary cloud that forms behind the BH, leading to a larger dynamical friction force. Unlike Ref. [362], we carry out our simulations in the rest frame of the scalar matter, such that it has asymptotically zero momentum and a constant energy density far from the BH. The BH is boosted relative to the scalar fluid with relativistic velocity $v \sim 0.3 - 0.8$, and we measure the force experienced by the BH as $F_d = {\rm d}P/{\rm d}t$ in that frame (where P is the momentum of the BH), which can be shown to be equal to the proper force ${\rm d}P/{\rm d}\tau$ measured in the rest frame of the BH (see Sec. 5.2.1). This facilitates comparison to known results which tend to be quoted in the rest frame of the perturber. Fig. 5.2 illustrates the time evolution (left to right) of the density profiles that form behind the BH for two different velocities: $v = 0.5$ on the top and $v = 0.8$ on the bottom. One can

see that the overall amplitude of the density and the spread of the tail is dependent on the velocity, and that the force does not decrease significantly as one might expect from the nonrelativistic scaling in Eq. (5.1). It is in fact larger for the higher velocity case, where the density has a slightly larger amplitude in the cloud behind the BH.

For collisional fluids, Refs. [362] and [363] showed that there is an overall relativistic correction factor related to the increased effective mass of the perturber at relativistic velocities, plus an adjustment to account for the pressure of the fluid, and we find a similar trend. However, since inhomogeneous scalar dark matter does not have a well-defined equation of state, we approximate the relation between density and pressure by assuming a plane-wave solution, which makes the pressure contribution velocity-dependent, unlike in normal fluids. The plane wave description holds far from the BH, but as shown in Fig. 5.2, the solution close to the BH will be more complex. Nevertheless, using this approximation, we find good agreement with an expression of the form

$$F_{\rm d} = F_{\rm d,nonrel} \times \gamma^2(1+v^2)^2 \times \left(1+\kappa\frac{v^2}{1+v^2}\right) , \tag{5.2}$$

where $\gamma = 1/\sqrt{1-v^2}$ and $\kappa = \kappa(\alpha_{\rm s}) \in (0,1)$ characterises the dependence of the pressure correction on the scalar mass, with an $O(1)$ value in the limit of small masses. For larger masses where the wave-like behaviour is no longer significant on the scale of the BH we expect the pressure correction to reduce to zero, ie, $\kappa \sim 0$. The κ values obtained in the intermediate mass range studied here can be fit with an approximate linear dependence, as shown in Fig. 5.8.

We structure the chapter as follows. In Sec. 5.2 we describe in detail the physical set up, our numerical implementation, and how the relativistic force is measured. In Sec. 5.3 we summarise previous relevant studies of dynamical friction and use them to justify our approximation. In Sec. 5.4 we present our simulations, confirming the scaling of the dynamical friction force for a range of scalar masses. In Sec. 5.5 we discuss our results and propose applications and areas for further work.

For the remainder of the chapter we use geometrical units in which $G = c = 1$, with the scalar field mass parametrised by the inverse length scale μ. One can relate this to the scalar mass m via $\mu = mc/\hbar$. We vary the dimensionless quantity $\alpha_{\rm s} = M\mu$, which sets

the mass of the BH if the mass of the particle is specified, and vice versa. As an example, for the case $\alpha_{\rm s} = 1$, this could correspond to a solar mass BH and a scalar with mass $m \sim 10^{-10}$ eV, or a supermassive BH of $M = 10^{10} M_\odot$ with a scalar mass $m \sim 10^{-20}$ eV. In all of our simulations we set $M = 1$.

5.2 Framework

We work in the decoupling limit in which the backreaction of the scalar field onto the metric is neglected, such that the dynamical friction force is calculated to first order in the density of the field as the rate of change of momentum of the BH spacetime $F_i = \partial_t P_i$.

Therefore our numerical system is composed of a fixed boosted BH metric, and a complex scalar field that evolves dynamically on this background according to the relativistic Klein-Gordon equation. We describe these components, the force calculation and our numerical implementation in more detail in this section.

5.2.1 Background metric

We choose to work in the rest frame of the scalar fluid, which allows us to implement spatially homogeneous boundary conditions at large distance from the BH. In this frame the BH is moving with velocity v, and has ADM momentum in the x direction $P_x^{\rm ADM} = \gamma M v$, where $\gamma = 1/\sqrt{1-v^2}$ is the usual boost factor.

To obtain the appropriate coordinates we boost the Schwarzschild metric in isotropic coordinates $(\bar{t}, \bar{x}, \bar{y}, \bar{z})$ by a factor of γ in the x direction. To make the metric time-independent (effectively to prevent the BH from moving across the grid), we add a spatially constant shift to fix the x coordinate to the centre of the BH. We thus obtain our simulation coordinates (t, x, y, z) as

$$\bar{t} = (t/\gamma - \gamma v x) \quad \bar{x} = \gamma x \quad \bar{y} = y \quad \bar{z} = z \ . \tag{5.3}$$

The $3+1$ ADM decomposition of the Schwarzschild metric in these coordinates is

$$\mathrm{d}s^2 = -\alpha^2 \, \mathrm{d}t^2 + \gamma_{ij} (\mathrm{d}x^i + \beta^i \, \mathrm{d}t)(\mathrm{d}x^j + \beta^j \, \mathrm{d}t) \, , \tag{5.4}$$

where $x^i = x_i$ are the Cartesian coordinates on the grid, and the lapse, shift and nonzero components of the spatial metric are, respectively,

$$\begin{aligned} \alpha^2 &= \frac{AB}{\gamma^2(B - Av^2)}\,, \qquad \beta_i = \delta_{ix} A v\,, \\ \gamma_{xx} &= \gamma^2(B - Av^2)\,, \qquad \gamma_{yy} = \gamma_{zz} = B\,, \end{aligned} \tag{5.5}$$

where

$$A = \left(\frac{1 - M/2\bar{r}}{1 + M/2\bar{r}}\right)^2 \qquad \text{and} \qquad B = \left(1 + \frac{M}{2\bar{r}}\right)^4\,,$$

with $\bar{r}^2 = \gamma^2 x^2 + y^2 + z^2$. Noting that in these coordinates $\partial_t \gamma_{ij} = 0$, the extrinsic curvature K_{ij} can be obtained from its definition, as

$$2\alpha K_{ij} = D_i \beta_j + D_j \beta_i\,. \tag{5.6}$$

Since the BH is not moving in our chosen frame, we find that it has momentum $P^x = 0$, but $P_x = \gamma M v$, the latter quantity reflecting the fact that the normal observers are in the rest frame of the fluid.

Most of the literature to date calculates the dynamical friction force in the rest frame of the BH, since this is analytically more convenient. We therefore need to take care of the frame dependence of the measured force.

Consider the coordinate transformations in Eq. (5.3) and their inverse:

$$t = \gamma(\bar{t} + v\bar{x}) \quad x = \bar{x}/\gamma \quad y = \bar{y} \quad z = \bar{z}\,. \tag{5.7}$$

If an object experiences a change in four-momentum $dP_{\bar{\mu}}$ in the unboosted frame, the transformation to our frame is:

$$dP_\mu = \frac{\partial x^{\bar{\mu}}}{\partial x^\mu} dP_{\bar{\mu}}\,. \tag{5.8}$$

Thus

$$dP_x = \gamma dP_{\bar{x}} \tag{5.9}$$

(for small $dP_{\bar{x}}$, we have $dP_{\bar{t}} \sim 0$). The proper time elapsed during this change is $d\tau = d\bar{t} =$

dt/γ. Thus

$$\frac{dP_x}{dt} = \frac{dP_{\bar{x}}}{d\bar{t}} \,. \tag{5.10}$$

This implies that the result for the (coordinate) time derivative of the momentum is the same in both frames.

In terms of the proper time derivative (i.e., the acceleration four-vector) we have

$$\frac{dP_x}{d\tau} = \gamma \frac{dP_{\bar{x}}}{d\tau} \,, \tag{5.11}$$

as expected (but note that ours is not a simple Lorentz transformation, differing also by a coordinate shift).

5.2.2 Scalar field evolution

We simulate a complex scalar φ minimally coupled to gravity, with action

$$S = \int \mathrm{d}^4x\sqrt{-g}\left[\frac{1}{2}g^{\mu\nu}\nabla_\mu\varphi^*\nabla_\nu\varphi - V(|\varphi|)\right] \,, \tag{5.12}$$

where $V(|\varphi|) = \frac{1}{2}\mu^2|\varphi|^2$. We solve the second-order Klein-Gordon equation for the real and imaginary parts of the complex scalar field by decomposing them into two coupled first-order equations. The real part and the imaginary part both then obey

$$\partial_t\varphi = \alpha\Pi + \beta^i\partial_i\varphi \,, \tag{5.13}$$

$$\partial_t\Pi = \alpha\gamma^{ij}\partial_i\partial_j\varphi + \alpha\left(K\Pi - \gamma^{ij}\Gamma^k_{ij}\partial_k\varphi - m^2\varphi\right) + \partial_i\varphi\partial^i\alpha + \beta^i\partial_i\Pi \,, \tag{5.14}$$

where Π is the conjugate momentum density, as defined by Eq. (5.13), $K_{ij} = \frac{1}{2\alpha}(-\partial_t\gamma_{ij} + D_i\beta_j + D_j\beta_i)$ is the extrinsic curvature, and K is its trace.

For all simulations, the initial conditions for the scalar field are set to a constant across the grid as $\mathrm{Re}[\varphi(t=0,r)] = \varphi_0$, $\mathrm{Im}[\varphi(t=0,r)] = 0$, $\mathrm{Re}[\partial_t\varphi(t=0,r)] = 0$ and $\mathrm{Im}[\partial_t\varphi(t=0,r)] = \mu\varphi_0$. The initial amplitude φ_0 is arbitrary since we neglect the backreaction of the matter on the metric, but we use a value of order unity that can then be rescaled for different physical densities. Here we have chosen $\varphi_0 = 0.1$.

The stress energy tensor for the complex scalar field is

$$T_{\mu\nu} = \frac{1}{2}\left[(\nabla_\mu\varphi\nabla_\nu\varphi^* + \nabla_\nu\varphi\nabla_\mu\varphi^*) - g_{\mu\nu}\left(\nabla^\lambda\varphi\nabla_\lambda\varphi^*\right)\right] - g_{\mu\nu}V\left(|\varphi|\right) \ . \tag{5.15}$$

This can be expressed in terms of the energy, momentum and stress densities measured by the normal observers, as defined by the decomposition

$$T_{\mu\nu} = \rho n_\mu n_\nu + S_\mu n_\nu + n_\mu S_\nu + S_{\mu\nu}\,, \tag{5.16}$$

where

$$\rho = n_\mu n_\nu T^{\mu\nu}\,, \tag{5.17}$$

$$S_i = -\gamma_{i\mu} n_\nu T^{\mu\nu}\,, \tag{5.18}$$

$$S_{ij} = \gamma_{i\mu}\gamma_{j\nu}T^{\mu\nu}\,. \tag{5.19}$$

Since we do not include the backreaction of the scalar field onto the metric, or self-interactions, the results for a purely real scalar field can be obtained by simply considering the contributions of the real part of the field in the above expressions.

5.2.3 Diagnostic quantities

In the Newtonian description, the dynamical friction force in the i-direction F_i is simply the integral of the gravitational force from each element of the fluid density acting on the BH, that is

$$F_i = \int \frac{M\rho}{r^2}\frac{x^i}{r}\,\mathrm{d}V \ . \tag{5.20}$$

In the regime where the matter reaches a stationary state, this will equal the net i-momentum flux of the fluid out of a closed surface around the volume:

$$F_i = \int T_i^j \mathrm{d}S_j \ . \tag{5.21}$$

In the fully relativistic case the first expression is no longer valid but the second expression may be, provided that one adopts a coordinate system that approaches Minkowski space-

time sufficiently quickly at spatial infinity.[1] In this case we are quantifying approximately the change in the ADM momentum of the spacetime

$$F_i = \partial_t P_i^{ADM} \approx \int T_i^j \mathrm{d}S_j \ . \tag{5.22}$$

The approximation here comes from the fact that we are measuring at a large but finite radius (and not at spatial infinity, where the ADM momentum is actually defined). We are also neglecting the effect of the metric changing due to the presence of the fluid. Assuming that the fluid energy density is $O(\epsilon)$, the corresponding correction in the metric is $\delta g_{\mu\nu} \sim O(\epsilon)$, but this backreaction effect will only enter our force calculation at $O(\epsilon^2)$, firstly in neglecting the change in the flux calculated above as a result of $\delta g_{\mu\nu}$, and secondly by not accounting for any momentum loss from gravitational wave fluxes (which are $O(\delta g_{\mu\nu}^2)$). For small matter energy densities $\rho M^2 \ll 1$ the fixed background calculation will therefore be a good approximation. In superradiant clouds we expect $\rho M^2 \sim 10^{-5}$ in the most optimistic scenarios [183], and even lower densities are expected for accretion, making the approximation suitable for the intended applications.

However, as noted above, Eq. (5.21) can only be applied once the system has reached a stationary state. Before such a state is reached the momentum flux feeds both the momentum of the accumulating cloud, in addition to exerting a drag on the BH via $\delta g_{\mu\nu}$. What we are interested in measuring is only the latter of these two quantities. For our simulations, we therefore found it useful to derive a relativistic equivalent to the volume integral in Eq. (5.20), since this converged to a constant value far earlier than the flux integral. Such an expression can be obtained by considering Gauss's law in the four-dimensional volume for the current $J^\mu = T^\mu_\nu \zeta^\nu$. Here $\zeta^\nu = \delta^\nu_\mu$ must be a Killing vector in the μ direction for the asymptotically flat space far from the BH (see [365]), then the quantity we want to extract is

$$\mathcal{S}_\mu = \int_\Sigma \sqrt{g}\ T^\rho_\nu \nabla_\rho \delta^\nu_\mu \ \mathrm{d}^3x \tag{5.23}$$

[1] See Gourgoulhon [364] for the exact requirements on the ADM quantities. Note that these are satisfied by the boosted isotropic coordinates we have used, but would not be, for example, in Cartesian Kerr-Schild coordinates.

For the spatial direction i we have $\zeta^\nu = \delta^\nu_i$ and

$$\begin{aligned}\mathcal{S}_i &= \int_\Sigma \sqrt{g}\; T^\mu_\nu\; {}^{(4)}\Gamma^\nu_{\mu i}\; \mathrm{d}^3x \\ &= \int_\Sigma (-\rho\partial_i\alpha + S_j\partial_i\beta^j + \alpha S^k_j\; {}^{(3)}\Gamma^j_{ki})\; \sqrt{\gamma}\mathrm{d}^3x\,.\end{aligned} \tag{5.24}$$

Here we have used the fact that the components of ζ^μ are constant in space, whilst in the second line we express the integrand in terms of the 3+1 ADM quantities. Whilst clearly the expression is coordinate-dependent within the volume, the asymptotic behaviour guarantees that the volume integral is that measured by observers at infinity, such that the total four-vector F_μ transforms as expected under the Poincaré group (although note the comments in the previous section regarding the effect of our time-independent coordinate choice).

To account for the presence of a singularity in the volume we must replace the full three-dimensional volume Σ_{out} with the sum of the volume outside some inner surface $\partial\Sigma_{\text{in}}$ enclosing the singularity and the flux through that surface:

$$F_i = \underbrace{\int_{\Sigma_{\text{out}}-\Sigma_{\text{in}}} \sqrt{g}\; T^\mu_\nu\; {}^{(4)}\Gamma^\nu_{\mu i}\; \mathrm{d}^3x}_{\text{dynamical friction, } \mathcal{S}_i} \quad + \quad \underbrace{\int_{\partial\Sigma_{\text{in}}} \alpha T^j_i\; \mathrm{d}S_j}_{\text{momentum accretion, } \mathcal{F}_{i,\text{in}}} \tag{5.25}$$

Clearly the latter term should be identified with Bondi accretion of the fluid onto the BH, which also contributes to the drag force on the BH. We note that in the relativistic case the division of the force between accretion and dynamical friction is highly observer-dependent: consider for example an observer at infinity, who will not see any accretion onto the BH as the fluid will freeze at the horizon. As a result we measure the sum of both contributions, which is the most physically relevant quantity. For verification, we also extract the surface integral of the momentum flux at the boundary of the spatial volume

$$\mathcal{F}_i = \int_{\partial\Sigma_{out}} \alpha N_j T^j_i\; \mathrm{d}S = \int_{\partial\Sigma_{out}} N_j(\alpha\gamma^{jk}S_{ki} - \beta^j S_i)\; \mathrm{d}S \tag{5.26}$$

and the volume integral of the momentum density of the cloud

$$\mathcal{Q}_i = \int \alpha T^0_i\; \mathrm{d}V = \int S_i\; \mathrm{d}V \tag{5.27}$$

in order to check that these reconcile with F_i in the expected way, and to demonstrate that the scalar cloud does at late times settle into a steady state such that the flux agrees with the volume integral. We describe these tests in more detail in Appendix C.1.

5.2.4 Numerical methods

We explore a range of four values of the scalar mass, $\alpha_{\rm s} = (0.05, 0.2, 0.5, 1.0)$, and for each measure the force for a range of velocities v, choosing (without loss of generality) the velocity to be in the x direction.

We use an adapted version of the open source numerical relativity code GRChombo [366] to solve Eqs. (5.13) and (5.14) on a fixed metric background in the boosted isotropic coordinates described above. The scalar field is evolved by the method of lines with fourth-order finite difference stencils, Runge-Kutta time integration, and a hierarchy of grids with 2:1 resolution. The value of the metric and its derivatives are calculated locally from the analytic expressions at each point.

We choose the size of the simulation domain L such that the outer radius r over which we integrate the flux will be larger than the de Broglie wavelength of the field, i.e. such that $\mu v r \gg 1$. This corresponds to the regime of validity for the nonrelativistic analytic results we compare to, and is most challenging to achieve numerically for cases of small $\alpha_{\rm s}$. Therefore for the case of $\alpha_{\rm s} = 0.05$ we choose $L = 4096M$, for $\alpha_{\rm s} = 0.2$ and $\alpha_{\rm s} = 0.5$ we use $L = 2048M$, and for $\alpha_{\rm s} = 1$, $L = 1024M$. We use 9 $(2:1)$ refinement levels for $\alpha_{\rm s} = 0.05$, 8 for $\alpha_{\rm s} = 0.2$ and $\alpha_{\rm s} = 0.5$, and 7 for $\alpha_{\rm s} = 1$, with the coarsest level having 128^3 grid points, although we exploit the quadrant symmetry of the problem in Cartesian coordinates to reduce the domain to $64^2 \times 128$ points. This ensures that we maintain a spatial resolution of $dx = 0.0625M$ around the horizon of the BH, which is at $r \sim M/2$, in each case.

In order to resolve the temporal oscillations of the field sufficiently, we use a coarsest time step $dt_{\rm coarse}$ such that we have at least 32 time steps per period of oscillation, i.e. $T = 2\pi/\mu > 32\ dt_{\rm coarse}$.

The form of the metric naturally imposes ingoing boundary conditions at the horizon, due to the causal structure of the BH. We implement nonzero, time oscillating boundary conditions for the scalar field by setting the field to be spatially constant in the radial

direction, extrapolating from the values within the numerical domain. This simulates the effects of a roughly constant energy density, but can introduce unphysical effects in very long simulations. These effects can be easily identified by varying the domain size, but ultimately limit the time for which the growth of the cloud can be studied. For all our setups we perform code validation and convergence tests, the details of which can be found in Appendix C.1.

5.3 Background on dynamical friction

In this section we summarise previous results in dynamical friction that are relevant to this work, and formulate the relativistic approximations to which we will fit our numerical results.

The effect of an object losing momentum due to the gravitational interaction with the medium it moves through was first introduced by Chandrasekhar [361]. The idea was formulated to describe the force exerted on a nonrelativistic star propagating through a gas of heavy noninteracting particles (other stars). Since then Chandrasekhar's dynamical friction result has been applied to many other astrophysical problems, such as a relativistic projectile moving through a gaseous medium [362,363,367–370], and to scalar dark matter in the nonrelativistic regime [49,371–373]. The impact of such environments on the dynamics of compact objects and the potential for the resulting dephasing of GW signals to act as a probe of the matter has been considered in several works [178,179,187,352–360].

The classic Chandrasekhar result for a nonrelativistic perturber in a collisionless medium [361] is

$$F_{\rm Chandra} = 4\pi\rho \left(\frac{M}{v}\right)^2 \ln\left(\frac{b_{\rm max}}{b_{\rm min}}\right) , \tag{5.28}$$

where $b_{\rm min} \sim M/v^2$ is the size of the perturber or the capture impact parameter, and $b_{\rm max}$ is the maximum impact parameter. Relativistic corrections to this result were found in Ref. [367] for the weak-scattering limit and in Ref. [362] for a collimated flow, showing that the Chandrasekhar result was modified by the relativistic correction

$$\text{Relativistic correction} = \gamma^2 \left(1 + v^2\right)^2 , \tag{5.29}$$

as a multiplicative factor to the nonrelativistic Chandrasekhar result of Eq. (5.28). Here the factor of $(1+v^2)^2$ comes from the increase in the deflection angle of the fluid at relativistic velocities, $\theta = 2M(1+v^2)/bv^2$ (notice that in the limit where $v = 1$ we recover the factor $1+v^2 = 2$ that differentiates the deflection of photons from non relativistic particles). The factor of γ^2 accounts for the relativistic momentum of the fluid as seen in the frame of the perturber. This is $\tilde{\rho}\gamma v$, taking $\tilde{\rho}$ to be the asymptotic energy density in the perturber frame. Noting that $\rho = \tilde{\rho}/\gamma$ is the energy density in the rest frame of the fluid gives the second γ factor.

In supersonic collisional fluids (with Mach number $\mathcal{M} = v/c_s > 1$, where c_s is the sound speed of the fluid), a further correction is required such that the rest mass density ρ is replaced by the sum of the density and the (isotropic) pressure of the fluid p [362,368–370]. That is, we introduce another multiplicative factor of

$$\text{Pressure correction} = \frac{\rho + p}{\rho} \tag{5.30}$$

to Eq. (5.28), in addition to the relativistic correction in Eq. (5.29). For collisional fluids in the subsonic case, Ostriker [368] worked out the Newtonian case and Barausse [363] extended the calculation to the relativistic case, but these results will not be relevant to the present study, since we expect to always be in the supersonic regime, as discussed below. Another interesting correction comes from finite size effects of the surrounding fluid, as studied in [372,374]. These give a nontrivial correction to the results that assume an infinite homogeneous reservoir, but such effects are neglected in this work.

The analytic expression for the dynamical friction force on a point-like object generated by a scalar field cloud, derived in Ref. [49], relates the force to the relative velocity between the object and the fluid v, the Compton wavelength of the scalar $\lambda_{\rm C} = 1/\mu$, the BH mass M and the size of the perturbed region r.[2] It has the form

$$F_{\rm d,nonrel} = 4\pi\rho\left(\frac{M}{v}\right)^2 \left\{\ln(2kr) - 1 - \mathrm{Re}[\Psi(1+i\beta)]\right\} , \tag{5.31}$$

[2]The value of r is dependent on the environment and the past history of the BH passage through the fluid. The spatial extent of the surrounding fluid provides an upper limit on r, but in the case where the BH enters a cloud of fluid and progresses through it, r will initially be zero and then increase over time as the wake behind it forms, such that $r \sim vt$. This time dependence in r was captured by the dynamical calculations of Ref. [372].

where $k = \mu v$, $\beta = \alpha_{\rm s}/v$ is the ratio between the impact parameter where deflection becomes significant and accretion dominates ($b_{\rm min} \sim M/v^2$) and the de Broglie wavelength of the scalar ($\lambda_{\rm dB} = 1/k$), and Ψ is the digamma function.[3] Depending on the ratio $\beta = \alpha_{\rm s}/v$ this takes the form

$$F_{\rm d}|_{\beta\to 0} \sim \frac{4\pi\rho}{v^2}\left[\log(2kr) - 1 + 0.577 - 1.202\beta^2\right], \tag{5.32}$$

$$F_{\rm d}|_{\beta\to \infty} \sim \frac{4\pi\rho}{v^2}\left[\log(\frac{2v^2 r}{M}) - 1 - \frac{1}{12\beta^2}\right], \tag{5.33}$$

where again $k = \mu v$, ρ is the asymptotic value of the scalar field rest mass density, and r is the size of the perturbed volume – normally the size of the dark matter cloud in which the perturber is immersed. (This can now be identified with the maximum impact parameter in the standard Chandrasekhar result $b_{\rm max} \sim 2r$ in the limit of large β [49].)

These expressions are valid only in the case where r is larger than the de Broglie wavelength of the field, $kr \gg 1$. For small kr, Ref. [49] provides an alternative expression which is in principle valid for any radius r but only for the case of smaller β, which is

$$F_{\rm d}|_{\beta<1} = 4\pi\rho\left(\frac{M}{v}\right)^2\left[{\rm Cin}(2kr) + \frac{\sin(2kr)}{2kr} - 1\right], \tag{5.34}$$

where ${\rm Cin}(z) = \int_0^z (1-\cos(t))dt/t$ is the cosine integral. In this work we fit the regime described by Eq. (5.31), which allows us to cover a wider range of scalar masses. We leave a full approximation for the small kr regime to future work.

Note that dynamical friction is distinct from the drag force created by Bondi accretion [375,376], i.e. accretion of the fluid momentum onto the BH as it moves through the cloud

$$F_{\rm Bondi} = 4\pi\lambda M^2\rho v(v^2 + c_s^2)^{-3/2}, \tag{5.35}$$

with λ an $O(1)$ number and c_s the speed of sound of the fluid. In the small-$\alpha_{\rm s}$ regime, Bondi accretion is negligible in comparison to the effect of dynamical friction. This is the case for our results for $\alpha_{\rm s} = 0.05$. However, we find that for larger masses of the scalar field its contribution becomes nonnegligible, and we must include it in order to better fit our simulation results. Physically, this is because the surface integral calculated in [49]

[3] https://mathworld.wolfram.com/DigammaFunction.html

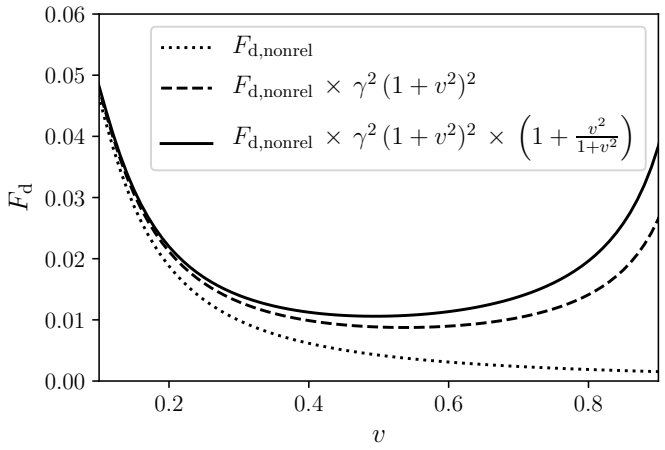


Figure 5.3: Analytic approximation for the nonrelativistic case for a scalar field cloud (dotted line) and with a relativistic correction term (dashed line) and a further correction for a pressure-like term, as for supersonic collisional fluids (solid line).

assumes a point mass perturber. This neglects several finite size effects, one of which is accretion. In the low-mass scalar case that was considered there, the impact of accretion is small because the incoming waves are mostly scattered rather than absorbed. In the particle regime, and at lower velocities where deflection is more significant, accretion can no longer be neglected.

To apply this to our relativistic scenario, we start with the nonrelativistic result of Eq. (5.31), and take as an ansatz the relativistic correction required for collisional fluids as above,

$$\text{Relativistic correction} = \gamma^2 \left(1+v^2\right)^2 , \tag{5.36}$$

assuming as before that it enters as a multiplicative factor. We also assume that the rest-mass density ρ will be replaced with the sum of the density and pressure $\rho + p$. Whilst an inhomogeneous scalar field does not have a well defined equation of state, we can consider a plane wave solution, which is what the BH will "see" in the asymptotically flat region, in its rest frame,

$$\varphi(x,t) = \varphi_0 \, e^{i(\omega t - kx)} , \tag{5.37}$$

where $\omega^2 = \mu^2 + k^2$ and $k = \mu v$. We can then obtain approximate expressions for ρ and p from the stress-energy tensor as

$$\rho = \frac{1}{2}\dot{\varphi}\dot{\varphi}^* + \frac{1}{2}(\partial_i \varphi \partial_i \varphi^*) + V = \mu^2 |\varphi|^2 (1+v^2) , \tag{5.38}$$

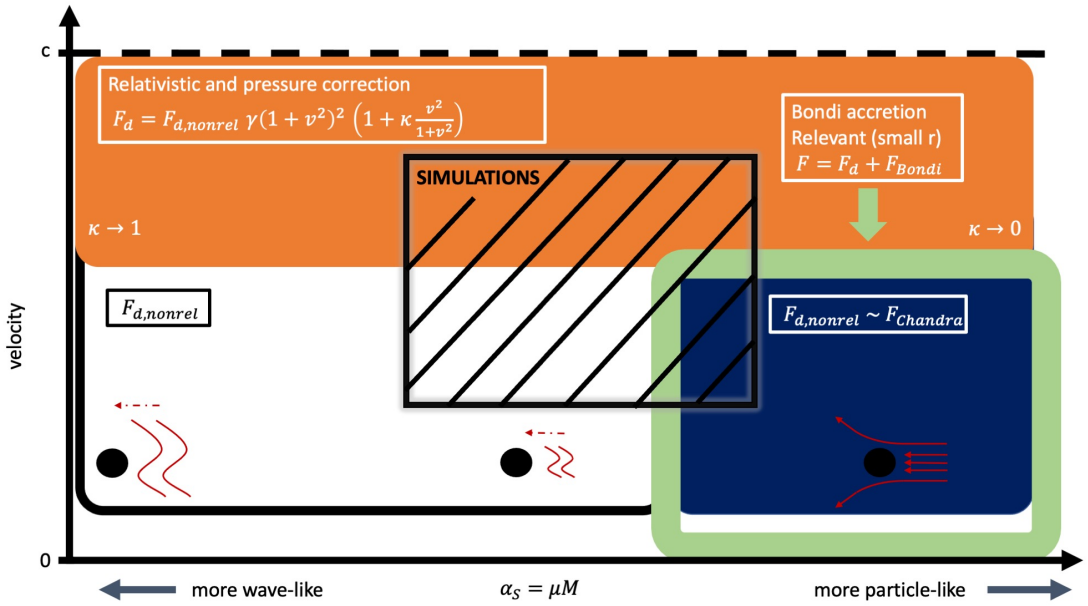


Figure 5.4: The diagram shows schematically the regime covered by our simulations in the $\alpha_s = \mu M$ - velocity plane. We consider a range of intermediate masses which cover the wave regime of $\alpha_s = 0.05$ up to $\alpha_s = 1$, where wave effects begin to turn off on the scale of the BH horizon and accretion onto the BH becomes non negligible. We study velocities $0.2 < v < 0.8$ at which relativistic corrections become significant. The expression for F_d describes the dynamical friction, with the α_s-dependent parameter κ describing pressure effects fitted to our numerical results. See the main text for further details.

$$p_x = \frac{1}{2}\dot{\varphi}\dot{\varphi}^* + \frac{1}{2}(\partial_x\varphi\partial_x\varphi^*) - V = v^2\mu^2|\varphi|^2\,. \tag{5.39}$$

$$p = \frac{1}{2}\dot{\varphi}\dot{\varphi}^* - \frac{1}{6}(\partial_i\varphi\partial_i\varphi^*) - V = \frac{1}{3}v^2\mu^2|\varphi|^2\,. \tag{5.40}$$

Note that since the fluid is no longer isotropic, we could consider the pressure correction as either $\rho + p$, where p is the averaged pressure in all three spatial directions, or as $\rho + p_x$, where p_x is the pressure in the direction of the BH motion. Either choice will be an approximation, but we find the latter to be a better fit and more physically intuitive – the pressure in the x direction is what plays the greatest role in resisting the BH motion.[4]

Using this, we estimate the pressure correction as

$$\text{Pressure correction} = \frac{\rho + p_x}{\rho} = 1 + \frac{v^2}{(1+v^2)}\,. \tag{5.41}$$

Note that this also justifies the assumption that for our setup we are always in the su-

[4]In particular, we find that the value of the parameter κ that we introduce below, tends to a value ~ 1 with this choice at lower scalar masses, which is the expected behaviour.

personic regime, since we have $c_s \sim v^2$ and thus a Mach number $\mathcal{M} \sim 1/v$ greater than 1.

The expected effect of such relativistic corrections on the result of [49] is illustrated in Fig. 5.3. The final expression that we use to fit our results has the form

$$F_{\rm d} = F_{\rm d,nonrel} \times \gamma^2(1+v^2)^2 \times \left(1+\kappa\frac{v^2}{1+v^2}\right) , \tag{5.42}$$

where κ is a factor we add to control the strength of the pressure-like correction. We include this factor as we expect this correction to become weaker (or completely turn off) as we increase the mass of the scalar field, where it would start to behave more like a particle than a wave. As we will show, this approximation turns out to be a very good fit to our results for all values of the mass, with the lower masses corresponding to $\kappa \sim 1$.

A diagram illustrating schematically the different scalar mass and velocity regimes, and placing our simulations within them, is given in Fig. 5.4.

5.4 Results

In this section we present the results we obtain for the dynamical friction force and its scaling with velocity derived from our simulations. We compare these results to the expected analytic expression, as detailed in Sec. 5.3, and fit the value of $\kappa(\alpha_{\rm s})$ for each value of $\alpha_{\rm s}$.

As explained in Sec. 5.2.4 above, we consider four different values of $\alpha_{\rm s}$, and for each case calculate the force for velocities in the range $v \in (0.3, 0.9)$, except in the case of $\alpha_{\rm s} = 1$, where we add an extra point at $v = 0.2$ to better explore the effect of Bondi accretion.

The different scalar masses we choose, $\alpha_{\rm s} = (0.05, 0.2, 0.5, 1)$, probe the two different regimes of validity of the expression in Eq. (5.31). In particular, as detailed in Appendix C.2, the smallest mass we consider ($\alpha_{\rm s} = 0.05$) is consistent with the expression in Eq. (5.32), valid for $\beta \ll 1$. The cases of $\alpha_{\rm s} = 0.5$ and 1 probe the large-β regime of Eq. (5.33). We also chose a point from the an intermediate mass range ($\alpha_{\rm s} = 0.2$), where neither of the approximations is valid and one needs to consider the exact expression in Eq. (5.31).

As outlined in Sec. 5.2.3, we extract the quantities in Eq. (5.25). For the radius r of

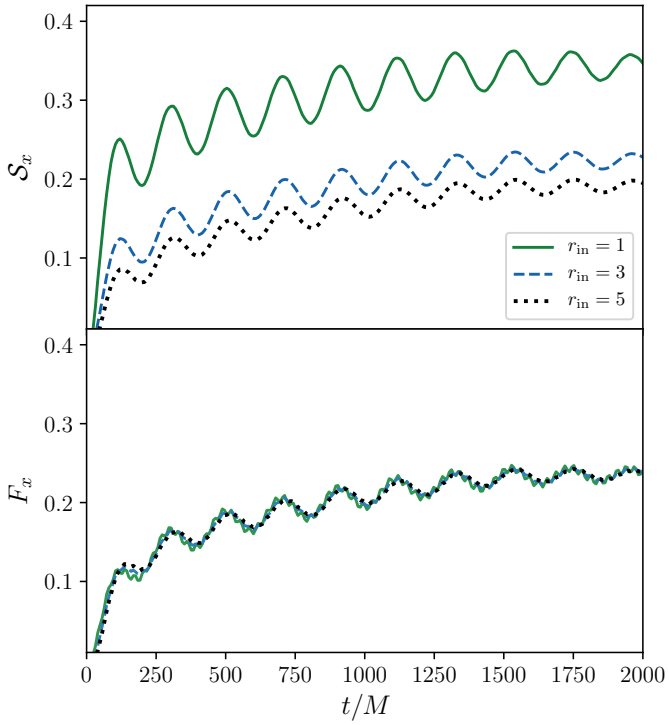


Figure 5.5: Dynamical friction force as a function of time extracted from one of our simulations. Top panel: contribution to the total force coming only from the "dynamical friction" term $\mathcal{S}_x$ in Eq. (5.25). This is calculated excising a volume of three different radii $r_{\rm in}$ around the BH: $r_{\rm in} = 1$ (green solid line), $r_{\rm in} = 3$ (blue dashed line) and $r_{\rm in} = 5$ (black dotted line). Bottom panel: total force F_x in Eq. (5.25), including the contribution $\mathcal{F}_{x,\,\rm in}$ from the flux through the inner surface $\Sigma_{\rm in}$ containing the BH. Including both terms, the total force is independent of the value of $r_{\rm in}$.

the volume $\Sigma_{\rm out}$ we take an outer extraction radius $r = r_{\rm out}$ large enough for the analytic approximation that we want to compare with [Eq. (5.31)] to be valid: $r_{\rm out} \gg 1/(\mu v)$. Therefore $r_{\rm out}$ varies depending on the value of $\alpha_{\rm s}$.[5] We choose the inner extraction radius such that the the BH horizon is fully enclosed in this region, $r_{\rm in} \gtrsim r_{\rm hor}$ (in isotropic Schwarzschild coordinates, $r_{\rm hor} = 0.5$). In principle we could use the same value for all our simulations, but we found that the flux is noisy when $r_{\rm in}$ is chosen to be too close to the horizon, and we require larger radii for the larger $\alpha_{\rm s}$. Recall that the inner radius is used to measure the flux $\mathcal{F}_{x,\,\rm in}$, which we can identify with the Bondi accretion contribution to the drag force.

For the cases where the flux is nonnegligible compared to $\mathcal{S}_x$, the choice of $r_{\rm in}$ determines

[5]Note that at larger radii the field takes longer to settle into a stationary profile and the force takes much longer to reach a constant value. The competition between this timescale and the accumulation of noise from the outer boundaries puts an upper limit on the outer extraction radius, $r_{\rm out}$ at which we can extract the force.

α_s	r_{in}	r_{out}	L	T_{final}
0.05	5	900	4096	$\gtrsim 5000$
0.2	5	700	2048	$\gtrsim 2500$
0.5	5	600	2048	$\gtrsim 2000$
1	10	300	1024	$\gtrsim 1000$

Table 5.1: Parameters that vary in our simulations for each value of α_s, which compares the Compton wavelength of the scalar to the BH size. In the first two columns are the the inner and outer extraction radii for the force, r_{in} and r_{out}, followed by the simulation box size, L, and the final time (at which we extract the diagnostic quantities) T_{final}. These are all in units of the BH mass M, which we set to 1 in our simulations.

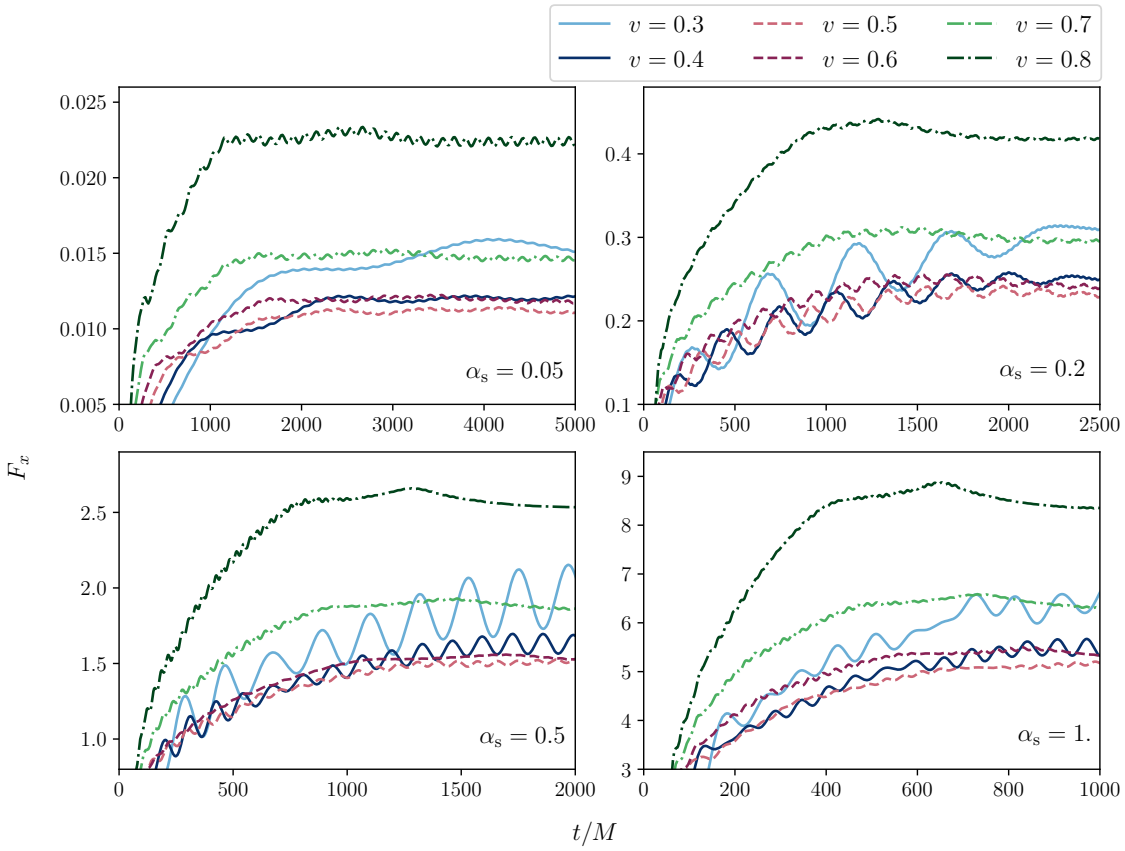


Figure 5.6: Time evolution of the total force F_x extracted from the simulations [Eq. (5.25)]. The four blocks show the the different scalar field masses we consider: $\alpha_s = 0.05$ (top left), $\alpha_s = 0.2$ (top right), $\alpha_s = 0.5$ (bottom left) and $\alpha_s = 1$ (bottom right). For each case we plot the evolution of the field for the range of velocities $v = 0.3 - 0.8$. In lighter and darker solid blue are $v = 0.3$ and 0.4, dashed red (light to dark) – $v = 0.5$ and 0.6 and dash-dotted green (light to dark) are $v = 0.7$ and 0.8.

the split between Bondi accretion drag and dynamical friction. Such a split is inherently gauge dependent, and so we measure the sum of the dynamical friction and accretion forces, which does not vary according to the choice of r_{in}. We demonstrate this in Fig. 5.5, where

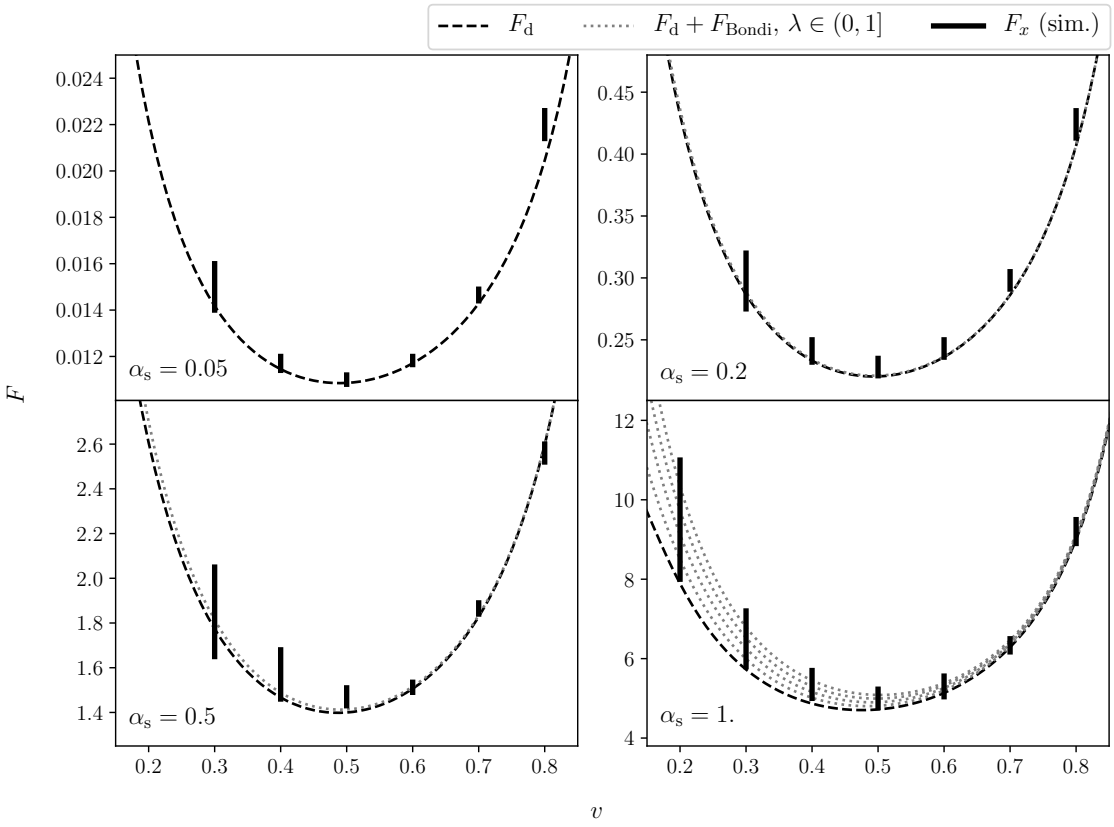


Figure 5.7: Scaling of the total force, F, on the BH due to the scalar field with relative velocity v. The four blocks again represent this result for the four mass cases we consider. The dashed lines in these plots show the analytic expression for the dynamical friction force $F_{\rm d}$ including the relativistic corrections, Eq. (5.42); the dotted lines show the analytic approximation of the total force on the BH, including both the contributions from dynamical friction and Bondi accretion, $F_{\rm Bondi}$. We include a range of values for the order one parameter λ in Eq. (5.35). The error bars (solid black) represent the total force we extract from the simulations, F_x [Eq. (5.25)], with the size of the error bars coming mainly from the amplitude of the oscillations of the force, as seen in Fig 5.6. Further details are given in Appendix C.1.

we see that although the "dynamical friction" term $\mathcal{S}_x$ in Eq. (5.25) can differ significantly depending on the choice of $r_{\rm in}$ (this is shown on the top panel), once we add the contribution $\mathcal{F}_{x,\,\rm in}$ from the flux through the inner surface the total force is the same regardless of the choice of $r_{\rm in}$.

In Table 5.1 we give the different extraction radii we have used to obtain our results from the simulations for the four different mass cases. We also show the box size L for each of these cases and the approximate time $T_{\rm final}$ at which we extract the diagnostic quantities. The larger simulation times and box sizes for the smaller velocities come from the fact that a scalar field with a longer wavelength compared to the BH light-crossing

time will take longer (in units of M) to settle into a stationary profile.

The time evolution for the force is shown in Fig 5.6. The four panels present the four different scalar mass cases, and for each case we show the evolution for the range of velocities we consider. We find that in all cases the force grows initially and settles into a roughly constant value after some time, with some remaining oscillations, which tend to be larger for smaller velocities. As the velocity decreases the overall amplitude of the force gets smaller in the regime $v \sim 0.3 - 0.5$, after which this pattern shifts and the force starts to grow again quite rapidly. Note that the time scale for the four different plots is different, since the higher the mass of the field, the faster it settles into a stationary profile and a constant value for the force. The approximate simulation times for each case are given in the $T_{\rm final}$ column of Table 5.1. However, note that due to the field taking longer to settle in the lower-velocity cases (both into a constant value and a lower amplitude of oscillation), we needed to run some cases longer before extracting a final value for the force. Values on the y axis are also not shown since they are different for all four cases and vary depending on the radius of the sphere we are considering; what is important is the overall trend in each case. Our goal is not to obtain a specific value for the force in each case, but rather to fit the dependence on v in our expression, which can then be applied at all radii r, provided that $r \gg (1/\mu v)$. Note that we have confirmed that different radii give consistent results for the scaling of the force with velocity.

Fig. 5.7 illustrates the scaling of the force with velocity for each of the scalar masses, $\alpha_{\rm s}$. The black dashed lines represent the analytic expression for the dynamical friction force $F_{\rm d}$, and the grey dotted lines represent the total force on the BH due to the combined effect of dynamical fiction and Bondi accretion, $F = F_{\rm d} + F_{\rm Bondi}$. The error bars are the force F_x that we extract from our simulations. We estimate the size of the error bars from the amplitude of the field oscillations at the time of extraction, plus the errors coming from finite resolution as identified by our convergence tests (discussed in more detail in Appendix C.1).

We find that Eq. (5.42) gives a good fit to the results in each case (black dashed line in the plots on Fig. 5.7). As expected, we find that low-mass cases fit well with the pre-factor for the pressure-like correction $\kappa \sim 1$, and for higher masses κ starts to decrease. The values of κ that give us the best fit to our results (with their estimated errors) for

the different scalar mass cases, as well as an approximate linear fit for these is shown in Fig. 5.8. As the field gets heavier, it starts to behave less like a wave and more like a

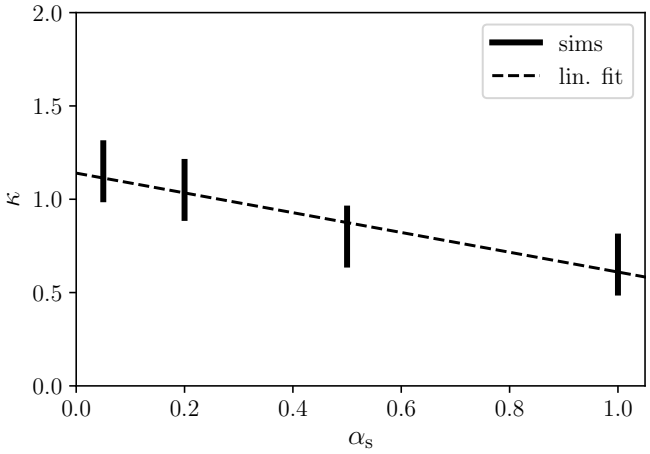


Figure 5.8: This plot shows the scaling of the pressure correction factor κ with scalar mass, α_s. The error bars are derived from our simulations (see Fig. 5.7). We fit a straight line though these, with equation $\kappa = 1.14 - 0.53\alpha_s$ (dashed line). Note that this expression is only valid in the range of scalar masses we consider, $\alpha_s \in (0.05, 1)$. We would expect that κ has a value ~ 1 for smaller α_s and tends to zero for higher α_s, and we see that this is consistent with our result.

particle, so it is not surprising that in the critical mass regime (where the wavelength of the field becomes comparable to the size of the BH, $\alpha_s \sim 1$), this pressure-like correction derived from a plane-wave solution would weaken, and the field will start to behave more like a pressureless fluid. We find that κ decreases from $\kappa \sim 1$ for $\alpha_s \sim 0.05$ to $\kappa \sim 0.5$ for $\alpha_s \sim 1.0$ and can expect that for even larger field masses, this pressure correction will fully disappear.

As discussed above, for all masses except for $\alpha_s = 0.05$, the momentum accretion onto the BH starts to have a significant contribution the total force that we measure. This can be associated with Bondi accretion, discussed in Sec. 5.3 [Eq.(5.35)], and so we cannot assume that its effect is negligible compared to dynamical friction. The grey dotted lines in Fig. 5.7 represent the expected total force onto the black hole, including this contribution, so that $F = F_d + F_{\rm Bondi}$. In the case of $\alpha_s = 0.2$ (top right) accretion is negligible, and this line fully overlaps with the dashed black line showing F_d alone. However in the cases of $\alpha_s = 0.5$ and $\alpha_s = 1$ (bottom left and right) we find that the effect is significant at lower velocities. For $\alpha_s = 1$, especially by taking the additional point at $v = 0.2$, where

the difference between the two lines becomes larger, we can show that the line including Bondi accretion (with $\lambda \sim 0.5$) is most consistent with our results.

5.5 Discussion

In this chapter we have numerically studied the dynamical friction force $F_{\rm d}$ on a BH immersed in a uniform-density region of scalar fluid of extent r as a function of the relativistic boost velocity v. We have demonstrated that the scaling of the total drag force experienced by the BH goes as

$$\begin{aligned} F =& F_{\rm d} + F_{\rm Bondi} \\ =& F_{\rm d,nonrel} \times \gamma^2(1+v^2)^2 \times \left(1+\kappa\,\frac{v^2}{1+v^2}\right) \\ &+ 4\pi\lambda M^2 \rho v (v^2+c_s^2)^{-3/2}\,, \end{aligned} \tag{5.43}$$

where we find $\kappa = \kappa(\alpha_{\rm s}) \in (0,1)$, $\lambda \in (0,1)$ and $c_s = \kappa\, v^2/(1+v^2)$.[6] This is consistent with the case of a supersonic collisional fluid, combining a relativistic correction of $\gamma^2\,(1+v^2)^2$ with the assumption that the (now velocity-dependent) pressure correction of the scalar is well described by the approximate relation

$$\rho + p_x \sim \rho\left(1+\kappa\,\frac{v^2}{1+v^2}\right)\,. \tag{5.44}$$

We find that the constant κ depends on the scalar mass, decreasing from $\kappa \sim 1$ for $\alpha_{\rm s} \sim 0.05$ to $\kappa \sim 0.5$ for $\alpha_{\rm s} \sim 1.0$. We expect it to approach zero in the limit of large $\alpha_{\rm s}$, thus recovering a result consistent with collisionless particles. An approximate linear fit for the intermediate mass regime that we study is provided in Fig. 5.8.

Our result can be applied to studies of EMRI dephasing in the final orbits around a SMBH with a superradiant or accretion-driven cloud. However, some care will need to be given to the value of r that is chosen to represent the size of the cloud that influences the BH. As we have shown, the cloud takes time to develop dynamically, and therefore at each point in the orbit, the size of the cloud will depend on both the local extent of the scalar

[6] Note that our results are not sensitive to the exact value of c_s in the expression for the Bondi accretion, and we find consistency for any $c_s \in (0, 0.5)$. The exact form we quote here is simply taken to match the form of p_x/ρ in the dynamical friction expression.

density, and also on the inspiral history. As shown in Ref. [372] in the nonrelativistic case, this can change the result significantly compared to the naive picture of an infinite uniform density environment. In addition, the effective pressure of the scalar fluid depends on the scalar mass, and this will determine the extent to which the cloud recovers to its original configuration over successive orbits - that is, one should consider whether the cloud is significantly depleted by the Bondi accretion, or alternatively whether its local density is enhanced on subsequent orbits. The full problem of simulating a relativistic BH orbiting a larger one immersed in a superradiant scalar cloud profile remains open, with the main challenge being the difference in the timescales involved.

The results in this work are derived for the case of a complex scalar field in order to avoid having to deal with the high frequency amplitude oscillations expected for a real scalar field. Nevertheless, we confirm for a few of the cases that the real field oscillates with the expected frequency of $\omega = 2\alpha_{\rm s}$, and the average value of these oscillations is consistent with the result we obtain for the complex field. We provide more detail on this in Appendix C.3. Whilst the average effect over time for a real scalar would be consistent with the complex case, in principle the impact of the higher frequency oscillations on the trajectory of the perturber is another distinctive signature of this type of scalar matter.

In addition to providing specific results for scalar dark matter, the framework that we have described and validated provides the groundwork for the study of a wider range of bosonic candidates, and could be simply extended to include nontrivial self-interactions such as those of axions (as in [377]) or dark photons through the implementation of a massive vector (Proca) field. One could also study the impact of adding spin to the BH perturber, or a curved trajectory in an asymptotically curved spacetime (as in [363]), by updating the metric background used.

Chapter 6

Discussion and conclusions

6.1 Conclusions

It is established that at most scales in the universe, the standard model of cosmology (GR+ΛCDM) provides an incredibly good fit to data. At very large and very small scales, however, current constraints are not tight enough to categorically rule out deviations from this model. The multitude of powerful upcoming large scale structure surveys are expected to be able to pin down the expansion of the universe and constrain the beyond GR parameters that govern it to a few percent level. Moreover, including theoretically informed priors for these parameters can help to improve these constraints by up to an order of magnitude.

On small scales, in the coming years both current and future surveys will provide us not only with a wealth of GW data, but also observations of events at different frequency ranges than ones we currently have. Until then, there is a need to focus on gravitational waveform modelling for different beyond GR theories and systems of compact objects, so that we can constrain parameters using this data. Bayesian statistics and MCMC algorithms have long been employed as part of the methods for parameter inference of beyond GR models of gravity on large scales using cosmological data. With the large amount of new GW data expected in the coming decade, now is the ideal time to build the analysis tools needed for constraining beyond GR parameters on small scales.

The aim of this thesis was to explore a range of beyond GR models and extend the large set of already existing tools for testing them at different scales. Chapters 2 – 4 focused

on large scale tests of a range of additional scalar field DE/MG models using cosmological data and deriving theory informed priors to include in the data analysis. Chapter 5 focused on small scale tests for a scalar field model of DM.

In Chapter 2 we started with quintessence, a minimally coupled scalar field model of DE. We used properties of the underlying theory to derive the time dependence of the DE equation of state, $w(a)$, for a range of quintessence potentials. For each of these potentials we calculated a set of observable quantities for a large set of models and used those to find an analytic form for the prior distribution of the parameters of the CPL parametrisation, given by

$$w(a) = w_0 + (1 - a)w_a \,, \tag{6.1}$$

with w_0 and w_a chosen to best fit the observables. By doing this we created a link between the phenomenological parametrisation and the action-based theory, simplifying any future likelihood analysis by providing an accurate phenomenological description and eliminating the need to evolve the full scalar field dynamics. This greatly reduces the number of parameters one needs to constrain in the analysis, while keeping all the information of the full scalar field dynamics. Moreover, we found that the prior distributions of the CPL parameters $\{w_0, w_a\}$ were not co-linear with the ones obtained considering cosmological data, which led to a large improvement on the constraints on $\{w_0, w_a\}$ when priors were included in the analysis.

Expanding on this work, in Chapter 3 we looked at the shift-symmetric sub-model of Horndeski. The only non-zero phenomenological parameters in this model are the DE equation of state, $w(a)$, the kinetic gravity braiding function, $\alpha_{\rm B}(a)$, and the kineticity, $\alpha_{\rm K}(a)$. The last of these is known to not be constrained by cosmological experiments, so we focused on finding suitable forms for the evolution of $\alpha_{\rm B}(a)$ and $w(a)$ only. Similar to before we calculated a set of observables for a range of randomly generated models for the shift-symmetric action and found what phenomenologcal description best fit those. For the DE equation of state, $w(a)$, we confirmed that as in the case of quintessence, here the CPL parametrisation provided a good enough fit to match the constraining power of future surveys. For $\alpha_{\rm B}(a)$, however, after investigating multiple possibilities, we proposed a new parametric form that fits the shift-symmetric model extremely well with a minimal

number of parameters,

$$\alpha_{\rm B}(a) = \hat{\alpha}_{\rm B} \left(\frac{H}{H_0} \right)^{4/m} , \tag{6.2}$$

where $\hat{\alpha}_{\rm B}$ and m are constant parameters. Including constraints from current cosmological data, we confirmed that shift-symmetric models without a cosmological constant are viable observationally and showed that including theoretical priors in the analysis can improve the constraints by up to an order of magnitude.

In Chapter 4 we studied the beyond Horndeski set of models, for which higher (than second) order derivatives are allowed to enter the equations of motion. We implemented the model into the Einstein-Boltzmann solving code `hi_class` and used this to explore the phenomenology of the model in detail. We found the additional beyond Horndeski function, $\alpha_{\rm H}(a)$, to suppress the matter power spectrum and the CMB lensing potential, and to enhance the temperature power spectrum of the CMB on large scales. Further, we used the quasi-static approximation to derive an analytic approximation for the growth rate of structure, $f(a)$, and the weak lensing parameter, $\Sigma(a)$, and found that those agree with the exact solutions obtained using `hi_class`. Moreover, we put the first constraints from cosmological data on the parameter setting the evolution of the beyond Horndeski function, $\hat{\alpha}_{\rm H}$, where

$$\alpha_{\rm H} = \Omega_{\rm DE}\, \hat{\alpha}_{\rm H} \, . \tag{6.3}$$

We varied $\hat{\alpha}_{\rm H}$ along with the other $\hat{\alpha}_i$ (apart from $\hat{\alpha}_{\rm K} = 1$ and $\hat{\alpha}_{\rm T} = 0$) and the six standard cosmological parameters $\{H_0, \Omega_{\rm b}, \Omega_{\rm cdm}, A_s, n_s, \tau\}$ and found constraints on $\hat{\alpha}_{\rm H}$ of order $\mathcal{O}(1)$.

In Chapter 5 we switched the focus to the smaller scales. We used numerical simulations to find an analytic expression for the dynamical friction force on a moving black hole from a uniform density scalar field cloud. We determined the exact scaling of the total force on the BH as a function of its velocity. For up to $v \sim 0.5c$, we found that the force decreased with increasing velocity (scaling roughly as $\log(v)/v^2$), as expected from the non-relativistic description of DF. At relativistic velocities, however, this behaviour changed and we started to observe a rapid increase in the force again. This effect can be characterised by a couple of relativistic corrections, which need to be accounted for and we found to be consistent

with the supersonic collisional fluid case,

$$F_{\rm d} = \underbrace{F_{d,\rm nonrel}}_{\propto \log(v)/v^2} \times \underbrace{\gamma^2(1+v^2)^2 \times \left(1+\kappa\,\frac{v^2}{1+v^2}\right)}_{\text{Relativistic corrections}}, \tag{6.4}$$

where $\gamma = 1/\sqrt{1+v^2}$ is the Lorentz boost factor and κ is a constant factor, which depends on the mass of the field. This result can be applied to find the expected de-phasing of the gravitational wave signal in the final orbit of an extreme mass ratio inspiral, caused by the presence of a superradiant or accretion-driven DM cloud.

6.2 Future Directions

In the future we plan to extend further the work in Chapters 2 and 3 by considering a more general Horndeski Lagrangian to test the validity of the expression we found for the time evolution of $\alpha_{\rm B}(a)$ in these more complex cases and check if it also represents the evolution of the other α_i parameters as accurately. Further, given that we found that the shift-symmetric model without a cosmological constant is consistent with observations, we wish to perform a detailed analysis of its phenomenology, studying the effects of the parameters setting the evolution of $\alpha_{\rm B}(a)$ on different observable quantities, as done in Chapter 4 for the beyond Horndeski class. Finally, we also plan to constrain the $\hat{\alpha}_{\rm B}$ and m parameters of the phenomenological description of the shift-symmetric model with a more complete data set, including cosmic shear weak lensing data, ISW measurements and galaxy clustering in addition to the CMB, BAO, RSD and SN data we used for the data analysis in Chapter 3. This will allow us to conclude whether the shift-symmetric model without a cosmological constant is a good model for explaining the late acceleration of the universe and determine how it compares to ΛCDM.

We intend to use the numerical framework that we built in Chapter 5 to validate an expression for the force on a moving BH at much smaller radii. In addition, this provides us with the groundwork for exploring a wider range of bosonic DM candidates by considering a scalar field with self-interactions, such as axions or dark photons, by implementing a massive vector field. It is also straightforward to implement the full evolution of the moving BH, using the full BSSN decomposition, to find any small corrections to the DF

force coming from the backreaction of the field onto the BH perturber. Further, by changing the background metric that we use, we plan to study the effects on a spinning BH, rather than a Schwarzschild one. Finally, using Bayesian statistical modelling with EMRI data we plan to check the consistency of the wave-like DM hypothesis from Chapter 5. Looking further ahead, we also intend to build tools for testing Horndeski models of DE, as done in Chapters 2 and 3, but on small scales in the presence of a BH, evolving the fully non-linear theory using NR.

References

[1] García-García C, Bellini E, Ferreira PG, Traykova D, Zumalacárregui M. Theoretical priors in scalar-tensor cosmologies: Thawing quintessence. Phys Rev D. 2020;101(6):063508.

[2] Traykova D, Bellini E, Ferreira PG, García-García C, Noller J, Zumalacárregui M. Theoretical priors in scalar-tensor cosmologies: Shift-symmetric Horndeski models; 2021.

[3] Traykova D, Bellini E, Ferreira PG. The phenomenology of beyond Horndeski gravity. JCAP. 2019;08:035.

[4] Traykova D, Clough K, Helfer T, Ferreira PG, Berti E, Hui L. Dynamical friction from scalar dark matter in the relativistic regime; 2021.

[5] Einstein A. Die Feldgleichungen der Gravitation. Sitzungsberichte der Königlich Preußischen Akademie der Wissenschaften (Berlin. 1915 Jan:844–847.

[6] Einstein A. Die Grundlage der allgemeinen Relativitätstheorie. Annalen der Physik. 1916;354(7):769–822. Available from: https://onlinelibrary.wiley.com/doi/abs/10.1002/andp.19163540702.

[7] Baker T, Psaltis D, Skordis C. Linking Tests of Gravity On All Scales: from the Strong-Field Regime to Cosmology. Astrophys J. 2015;802:63.

[8] Lundmark K. Über die Bestimmung der Entfernungen, Dimensionen, Massen und Dichtigkeit fur die nächstgelegenen anagalacktischen Sternsysteme. Meddelanden fran Lunds Astronomiska Observatorium Serie I. 1930 Jan;125:1–13.

[9] Zwicky F. Die Rotverschiebung von extragalaktischen Nebeln. Helv Phys Acta. 1933;6:110–127.

[10] Rubin VC, Ford J W Kent. Rotation of the Andromeda Nebula from a Spectroscopic Survey of Emission Regions. . 1970 Feb;159:379.

[11] Riess AG, et al. Observational evidence from supernovae for an accelerating universe and a cosmological constant. Astron J. 1998;116:1009–1038.

[12] Perlmutter S, et al. Measurements of Omega and Lambda from 42 high redshift supernovae. Astrophys J. 1999;517:565–586.

[13] Riess AG, et al. New Hubble Space Telescope Discoveries of Type Ia Supernovae at $z \geq 1$: Narrowing Constraints on the Early Behavior of Dark Energy. Astrophys J. 2007;659:98–121.

[14] Kowalski M, et al. Improved Cosmological Constraints from New, Old and Combined Supernova Datasets. Astrophys J. 2008;686:749–778.

[15] Springel V, Frenk CS, White SDM. The large-scale structure of the Universe. Nature. 2006;440:1137.

[16] Anderson L, et al. The clustering of galaxies in the SDSS-III Baryon Oscillation Spectroscopic Survey: baryon acoustic oscillations in the Data Releases 10 and 11 Galaxy samples. Mon Not Roy Astron Soc. 2014;441(1):24–62.

[17] Blake C, Kazin EA, Beutler F, Davis TM, Parkinson D, Brough S, et al. The WiggleZ Dark Energy Survey: mapping the distance-redshift relation with baryon acoustic oscillations. . 2011 Dec;418:1707–1724.

[18] Spergel DN, et al. First year Wilkinson Microwave Anisotropy Probe (WMAP) observations: Determination of cosmological parameters. Astrophys J Suppl. 2003;148:175–194.

[19] Bennett CL, et al. First year Wilkinson Microwave Anisotropy Probe (WMAP) observations: Preliminary maps and basic results. Astrophys J Suppl. 2003;148:1–27.

[20] Spergel DN, et al. Wilkinson Microwave Anisotropy Probe (WMAP) three year results: implications for cosmology. Astrophys J Suppl. 2007;170:377.

[21] Dunkley J, et al. Five-Year Wilkinson Microwave Anisotropy Probe (WMAP) Observations: Likelihoods and Parameters from the WMAP data. Astrophys J Suppl. 2009;180:306–329.

[22] Ade PAR, et al. Planck 2013 results. XVI. Cosmological parameters. Astron Astrophys. 2014;571:A16.

[23] Ade PAR, et al. Planck 2013 results. I. Overview of products and scientific results. Astron Astrophys. 2014;571:A1.

[24] Ade PAR, et al. Planck 2015 results. XIII. Cosmological parameters. Astron Astrophys. 2016;594:A13.

[25] Adam R, et al. Planck 2015 results. I. Overview of products and scientific results. Astron Astrophys. 2016;594:A1.

[26] Carroll SM. The Cosmological constant. Living Rev Rel. 2001;4:1.

[27] Peebles PJE, Ratra B. The Cosmological Constant and Dark Energy. Rev Mod Phys. 2003;75:559–606.

[28] Copeland EJ, Sami M, Tsujikawa S. Dynamics of dark energy. Int J Mod Phys. 2006;D15:1753–1936.

[29] Tsujikawa S. Quintessence: A Review. Class Quant Grav. 2013;30:214003.

[30] Friedmann A. Über die Krümmung des Raumes. Zeitschrift fur Physik. 1922 Jan;10:377–386.

[31] Lemaitre G. The expanding universe. Annales Soc Sci Bruxelles A. 1933;53:51–85.

[32] Robertson HP. Kinematics and World-Structure. . 1935 Nov;82:284.

[33] Walker AG. On Milne's Theory of World-Structure. Proceedings of the London Mathematical Society. 1937 Jan;42:90–127.

[34] Schwarzschild K. On the gravitational field of a mass point according to Einstein's theory. Sitzungsber Preuss Akad Wiss Berlin (Math Phys). 1916;1916:189–196.

[35] Kerr RP. Gravitational field of a spinning mass as an example of algebraically special metrics. Phys Rev Lett. 1963;11:237–238.

[36] Reissner H. Über die Eigengravitation des elektrischen Feldes nach der Einsteinschen Theorie. Annalen der Physik. 1916;355(9):106–120. Available from: https://onlinelibrary.wiley.com/doi/abs/10.1002/andp.19163550905.

[37] Lovelock D. The Einstein tensor and its generalizations. J Math Phys. 1971;12:498–501.

[38] Lovelock D. The four-dimensionality of space and the einstein tensor. J Math Phys. 1972;13:874–876.

[39] Horava P. Quantum Gravity at a Lifshitz Point. Phys Rev D. 2009;79:084008.

[40] Amendola L, Tsujikawa S. Dark Energy: Theory and Observations. Cambridge University Press; 2010.

[41] Clifton T, Ferreira PG, Padilla A, Skordis C. Modified Gravity and Cosmology. Phys Rept. 2012;513:1–189.

[42] Brans C, Dicke RH. Mach's Principle and a Relativistic Theory of Gravitation. Phys Rev. 1961 Nov;124:925–935. Available from: https://link.aps.org/doi/10.1103/PhysRev.124.925.

[43] Wetterich C. Cosmology and the Fate of Dilatation Symmetry. Nucl Phys. 1988;B302:668–696.

[44] Ratra B, Peebles PJE. Cosmological Consequences of a Rolling Homogeneous Scalar Field. Phys Rev. 1988;D37:3406.

[45] Preskill J, Wise MB, Wilczek F. Cosmology of the Invisible Axion. Phys Lett B. 1983;120:127–132.

[46] Abbott LF, Sikivie P. A Cosmological Bound on the Invisible Axion. Phys Lett B. 1983;120:133–136.

[47] Dine M, Fischler W. The Not So Harmless Axion. Phys Lett B. 1983;120:137–141.

[48] Hu W, Barkana R, Gruzinov A. Cold and fuzzy dark matter. Phys Rev Lett. 2000;85:1158–1161.

[49] Hui L, Ostriker JP, Tremaine S, Witten E. Ultralight scalars as cosmological dark matter. Phys Rev D. 2017;95(4):043541.

[50] Carroll SM, Duvvuri V, Trodden M, Turner MS. Is cosmic speed - up due to new gravitational physics? Phys Rev D. 2004;70:043528.

[51] Hu W, Sawicki I. Models of f(R) Cosmic Acceleration that Evade Solar-System Tests. Phys Rev D. 2007;76:064004.

[52] Sotiriou TP, Faraoni V. f(R) Theories Of Gravity. Rev Mod Phys. 2010;82:451–497.

[53] De Felice A, Tsujikawa S. f(R) theories. Living Rev Rel. 2010;13:3.

[54] Armendariz-Picon C, Damour T, Mukhanov VF. k - inflation. Phys Lett B. 1999;458:209–218.

[55] Armendariz-Picon C, Mukhanov VF, Steinhardt PJ. Essentials of k essence. Phys Rev D. 2001;63:103510.

[56] Khoury J, Weltman A. Chameleon fields: Awaiting surprises for tests of gravity in space. Phys Rev Lett. 2004;93:171104.

[57] Khoury J, Weltman A. Chameleon cosmology. Phys Rev. 2004;D69:044026.

[58] Brax P, van de Bruck C, Davis AC, Khoury J, Weltman A. Detecting dark energy in orbit - The Cosmological chameleon. Phys Rev. 2004;D70:123518.

[59] Hinterbichler K, Khoury J. Symmetron Fields: Screening Long-Range Forces Through Local Symmetry Restoration. Phys Rev Lett. 2010;104:231301.

[60] Horndeski GW. Second-order scalar-tensor field equations in a four-dimensional space. Int J Theor Phys. 1974;10:363–384.

[61] Deffayet C, Gao X, Steer DA, Zahariade G. From k-essence to generalised Galileons. Phys Rev. 2011;D84:064039.

[62] Kobayashi T, Yamaguchi M, Yokoyama J. Generalized G-inflation: Inflation with the most general second-order field equations. Prog Theor Phys. 2011;126:511–529.

[63] Deffayet C, Pujolas O, Sawicki I, Vikman A. Imperfect Dark Energy from Kinetic Gravity Braiding. JCAP. 2010;10:026.

[64] Deffayet C, Esposito-Farese G, Vikman A. Covariant Galileon. Phys Rev. 2009;D79:084003.

[65] Kobayashi T. Horndeski theory and beyond: a review; 2019.

[66] Woodard RP. Avoiding dark energy with 1/r modifications of gravity. Lect Notes Phys. 2007;720:403–433.

[67] Woodard RP. Ostrogradsky's theorem on Hamiltonian instability. Scholarpedia. 2015;10(8):32243.

[68] Ostrogradsky M. Mémoires sur les équations différentielles, relatives au problème des isopérimètres. Mem Acad St Petersbourg. 1850;6(4):385–517.

[69] Motohashi H, Suyama T. Third order equations of motion and the Ostrogradsky instability. Phys Rev D. 2015;91(8):085009.

[70] Gleyzes J, Langlois D, Piazza F, Vernizzi F. Healthy theories beyond Horndeski. Phys Rev Lett. 2015;114(21):211101.

[71] Zumalacárregui M, García-Bellido J. Transforming gravity: from derivative couplings to matter to second-order scalar-tensor theories beyond the Horndeski Lagrangian. Phys Rev D. 2014;89:064046.

[72] Arnowitt RL, Deser S, Misner CW. The Dynamics of general relativity. Gen Rel Grav. 2008;40:1997–2027.

[73] Alcubierre M. Introduction to 3+1 Numerical Relativity. Introduction to 3+1 Numerical Relativity. 2006 04.

[74] Kaplan DB. Five lectures on effective field theory; 2005. .

[75] Burgess CP. Introduction to Effective Field Theory. Ann Rev Nucl Part Sci. 2007;57:329–362.

[76] Weinberg S. Effective Field Theory for Inflation. Phys Rev D. 2008;77:123541.

[77] Cheung C, Creminelli P, Fitzpatrick AL, Kaplan J, Senatore L. The Effective Field Theory of Inflation. JHEP. 2008;03:014.

[78] Senatore L, Zaldarriaga M. The Effective Field Theory of Multifield Inflation. JHEP. 2012;04:024.

[79] Creminelli P, D'Amico G, Norena J, Vernizzi F. The Effective Theory of Quintessence: the w<-1 Side Unveiled. JCAP. 2009;02:018.

[80] Park M, Zurek KM, Watson S. A Unified Approach to Cosmic Acceleration. Phys Rev D. 2010;81:124008.

[81] Bloomfield JK, Flanagan EE. A Class of Effective Field Theory Models of Cosmic Acceleration. JCAP. 2012;10:039.

[82] Jimenez R, Talavera P, Verde L. An effective theory of accelerated expansion. Int J Mod Phys A. 2012;27:1250174.

[83] Jimenez R, Talavera P, Verde L, Moresco M, Cimatti A, Pozzetti L. The effective Lagrangian of dark energy from observations. JCAP. 2012;03:014.

[84] Khosravi N. Effective Field Theory of Multi-Field Inflation a la Weinberg. JCAP. 2012;05:018.

[85] Gubitosi G, Piazza F, Vernizzi F. The Effective Field Theory of Dark Energy. JCAP. 2013;1302:032. [JCAP1302,032(2013)].

[86] Bloomfield JK, Flanagan EE, Park M, Watson S. Dark energy or modified gravity? An effective field theory approach. JCAP. 2013;1308:010.

[87] Gleyzes J, Langlois D, Piazza F, Vernizzi F. Essential Building Blocks of Dark Energy. JCAP. 2013;08:025.

[88] Maldacena JM. Non-Gaussian features of primordial fluctuations in single field inflationary models. JHEP. 2003;05:013.

[89] Gleyzes J, Langlois D, Vernizzi F. A unifying description of dark energy. Int J Mod Phys. 2015;D23(13):1443010.

[90] Bellini E, Sawicki I. Maximal freedom at minimum cost: linear large-scale structure in general modifications of gravity. JCAP. 2014;1407:050.

[91] Gleyzes J, Langlois D, Piazza F, Vernizzi F. Exploring gravitational theories beyond Horndeski. JCAP. 2015;02:018.

[92] et al BPA. Multi-messenger Observations of a Binary Neutron Star Merger. The Astrophysical Journal Letters. 2017;848(2):L12. Available from: http://stacks.iop.org/2041-8205/848/i=2/a=L12.

[93] et al BPA. Gravitational Waves and Gamma-Rays from a Binary Neutron Star Merger: GW170817 and GRB 170817A. The Astrophysical Journal Letters. 2017;848(2):L13. Available from: http://stacks.iop.org/2041-8205/848/i=2/a=L13.

[94] et al BPA. GW170817: Observation of Gravitational Waves from a Binary Neutron Star Inspiral. Phys Rev Lett. 2017 Oct;119:161101. Available from: https://link.aps.org/doi/10.1103/PhysRevLett.119.161101.

[95] Baker T, Bellini E, Ferreira PG, Lagos M, Noller J, Sawicki I. Strong constraints on cosmological gravity from GW170817 and GRB 170817A. Phys Rev Lett. 2017;119(25):251301.

[96] Sakstein J, Jain B. Implications of the Neutron Star Merger GW170817 for Cosmological Scalar-Tensor Theories. Phys Rev Lett. 2017;119(25):251303.

[97] Ezquiaga JM, Zumalacárregui M. Dark Energy After GW170817: Dead Ends and the Road Ahead. Phys Rev Lett. 2017;119(25):251304.

[98] Creminelli P, Vernizzi F. Dark Energy after GW170817 and GRB170817A. Phys Rev Lett. 2017;119(25):251302.

[99] Piazza F, Steigerwald H, Marinoni C. Phenomenology of dark energy: exploring the space of theories with future redshift surveys. JCAP. 2014;05:043.

[100] Clarkson C, Maartens R. Inhomogeneity and the foundations of concordance cosmology. Class Quant Grav. 2010;27:124008.

[101] Ellis GFR. Inhomogeneity effects in Cosmology. Class Quant Grav. 2011;28:164001.

[102] Sarkar P, Yadav J, Pandey B, Bharadwaj S. The scale of homogeneity of the galaxy distribution in SDSS DR6. . 2009 Oct;399(1):L128–L131.

[103] Sylos Labini F. Inhomogeneities in the universe. Journal of Cosmology. 2011 Jan;15:6110–6139.

[104] Mukhanov VF, Feldman HA, Brandenberger RH. Theory of cosmological perturbations. Physics Reports. 1992 Jun;215:203–333.

[105] Ma CP, Bertschinger E. Cosmological perturbation theory in the synchronous and conformal Newtonian gauges. Astrophys J. 1995;455:7–25.

[106] Peter P. Cosmological Perturbation Theory. In: 15th Brazilian School of Cosmology and Gravitation; 2013. .

[107] Chevallier M, Polarski D. Accelerating universes with scaling dark matter. Int J Mod Phys. 2001;D10:213–224.

[108] Linder EV. Exploring the expansion history of the universe. Phys Rev Lett. 2003;90:091301.

[109] Aghanim N, et al. Planck 2018 results. VI. Cosmological parameters. Astron Astrophys. 2020;641:A6.

[110] Sprenger T, Archidiacono M, Brinckmann T, Clesse S, Lesgourgues J. Cosmology in the era of Euclid and the Square Kilometre Array. JCAP. 2019;1902:047.

[111] Sahni V, Starobinsky A. Reconstructing Dark Energy. Int J Mod Phys D. 2006;15:2105–2132.

[112] Shafieloo A, Alam U, Sahni V, Starobinsky AA. Smoothing Supernova Data to Reconstruct the Expansion History of the Universe and its Age. Mon Not Roy Astron Soc. 2006;366:1081–1095.

[113] Holsclaw T, Alam U, Sansó B, Lee H, Heitmann K, Habib S, et al. Nonparametric Dark Energy Reconstruction from Supernova Data. . 2010 Dec;105(24):241302.

[114] Seikel M, Clarkson C, Smith M. Reconstruction of dark energy and expansion dynamics using Gaussian processes. Journal of Cosmology and Astroparticle Physics. 2012;2012(06):036.

[115] Holsclaw T, Alam U, Sansó B, Lee H, Heitmann K, Habib S, et al. Nonparametric reconstruction of the dark energy equation of state from diverse data sets. Physical Review D. 2011;84(8):083501.

[116] Said N, Baccigalupi C, Martinelli M, Melchiorri A, Silvestri A. New Constraints On The Dark Energy Equation of State. Phys Rev D. 2013;88:043515.

[117] Wang Y, Pogosian L, Zhao GB, Zucca A. Evolution of dark energy reconstructed from the latest observations. Astrophys J Lett. 2018;869:L8.

[118] Shafieloo A, L'Huillier B, Starobinsky AA. Falsifying ΛCDM: Model-independent tests of the concordance model with eBOSS DR14Q and Pantheon. Phys Rev D. 2018;98(8):083526.

[119] Crittenden RG, Pogosian L, Zhao GB. Investigating dark energy experiments with principal components. JCAP. 2009;12:025.

[120] Albrecht A, Amendola L, Bernstein G, Clowe D, Eisenstein D, Guzzo L, et al. Findings of the Joint Dark Energy Mission Figure of Merit Science Working Group. arXiv e-prints. 2009 Jan:arXiv:0901.0721.

[121] Zhao GB, Pogosian L, Silvestri A, Zylberberg J. Cosmological Tests of General Relativity with Future Tomographic Surveys. Phys Rev Lett. 2009;103:241301.

[122] Hojjati A, Zhao GB, Pogosian L, Silvestri A, Crittenden R, Koyama K. Cosmological tests of General Relativity: a principal component analysis. Phys Rev D. 2012;85:043508.

[123] Asaba S, Hikage C, Koyama K, Zhao GB, Hojjati A, Pogosian L. Principal Component Analysis of Modified Gravity using Weak Lensing and Peculiar Velocity Measurements. JCAP. 2013;08:029.

[124] Crittenden RG, Zhao GB, Pogosian L, Samushia L, Zhang X. Fables of reconstruction: controlling bias in the dark energy equation of state. . 2012 Feb;2012(2):048.

[125] Shafieloo A, Kim AG, Linder EV. Gaussian process cosmography. . 2012 Jun;85(12):123530.

[126] Seikel M, Clarkson C, Smith M. Reconstruction of dark energy and expansion dynamics using Gaussian processes. . 2012 Jun;2012(6):036.

[127] Zhao GB, Crittenden RG, Pogosian L, Zhang X. Examining the Evidence for Dynamical Dark Energy. . 2012 Oct;109(17):171301.

[128] Zhao GB, et al. Dynamical dark energy in light of the latest observations. Nature Astron. 2017;1(9):627–632.

[129] Peirone S, Martinelli M, Raveri M, Silvestri A. Impact of theoretical priors in cosmological analyses: the case of single field quintessence. Phys Rev D. 2017;96(6):063524.

[130] Raveri M, Bull P, Silvestri A, Pogosian L. Priors on the effective Dark Energy equation of state in scalar-tensor theories. Phys Rev D. 2017;96(8):083509.

[131] Casas S, Kunz M, Martinelli M, Pettorino V. Linear and non-linear Modified Gravity forecasts with future surveys. Phys Dark Univ. 2017;18:73–104.

[132] Espejo J, Peirone S, Raveri M, Koyama K, Pogosian L, Silvestri A. Phenomenology of Large Scale Structure in scalar-tensor theories: joint prior covariance of $w_{\rm DE}$, Σ and μ in Horndeski. Phys Rev D. 2019;99(2):023512.

[133] Frusciante N, Papadomanolakis G, Peirone S, Silvestri A. The role of the tachyonic instability in Horndeski gravity. JCAP. 2019;02:029.

[134] Gerardi F, Martinelli M, Silvestri A. Reconstruction of the Dark Energy equation of state from latest data: the impact of theoretical priors. JCAP. 2019;1907:042.

[135] Daly RA, Djorgovski SG. A model-independent determination of the expansion and acceleration rates of the universe as a function of redshift and constraints on dark energy. Astrophys J. 2003;597:9–20.

[136] Crittenden R, Majerotto E, Piazza F. Measuring deviations from a cosmological constant: A field-space parameterization. Phys Rev Lett. 2007;98:251301.

[137] Marsh DJE, Bull P, Ferreira PG, Pontzen A. Quintessence in a quandary: Prior dependence in dark energy models. Phys Rev. 2014;D90(10):105023.

[138] Jain B, Khoury J. Cosmological Tests of Gravity. Annals Phys. 2010;325:1479–1516.

[139] Joyce A, Jain B, Khoury J, Trodden M. Beyond the Cosmological Standard Model. Phys Rept. 2015;568:1–98.

[140] Koyama K. Cosmological Tests of Modified Gravity. Rept Prog Phys. 2016;79(4):046902.

[141] Sachs RK, Wolfe AM. Perturbations of a Cosmological Model and Angular Variations of the Microwave Background. . 1967 Jan;147:73.

[142] Blanchard A, Schneider J. Gravitational lensing effect on the fluctuations of the cosmic background radiation. . 1987 Oct;184(1-2):1–6.

[143] Cole S, Efstathiou G. Gravitational lensing of fluctuations in the microwave background radiation. . 1989 Jul;239:195–200.

[144] Linder EV. Correlated gravitational lensing of the cosmic microwave background. . 1997 Jul;323:305–311.

[145] Seljak U. Gravitational lensing effect on cosmic microwave background anisotropies: A Power spectrum approach. Astrophys J. 1996;463:1.

[146] Sunyaev RA, Zeldovich IB. Microwave background radiation as a probe of the contemporary structure and history of the universe. . 1980 Jan;18:537–560.

[147] Eisenstein DJ, et al. Detection of the Baryon Acoustic Peak in the Large-Scale Correlation Function of SDSS Luminous Red Galaxies. Astrophys J. 2005;633:560–574.

[148] Cole S, et al. The 2dF Galaxy Redshift Survey: Power-spectrum analysis of the final dataset and cosmological implications. Mon Not Roy Astron Soc. 2005;362:505–534.

[149] Beutler F, Blake C, Colless M, Jones DH, Staveley-Smith L, Campbell L, et al. The 6dF Galaxy Survey: Baryon Acoustic Oscillations and the Local Hubble Constant. Mon Not Roy Astron Soc. 2011;416:3017–3032.

[150] Ross AJ, Samushia L, Howlett C, Percival WJ, Burden A, Manera M. The clustering of the SDSS DR7 main Galaxy sample – I. A 4 per cent distance measure at $z = 0.15$. Mon Not Roy Astron Soc. 2015;449(1):835–847.

[151] Alam S, et al. The clustering of galaxies in the completed SDSS-III Baryon Oscillation Spectroscopic Survey: cosmological analysis of the DR12 galaxy sample. Mon Not Roy Astron Soc. 2017;470(3):2617–2652.

[152] Jackson JC. Fingers of God: A critique of Rees' theory of primoridal gravitational radiation. Mon Not Roy Astron Soc. 1972;156:1P–5P.

[153] Kaiser N. Clustering in real space and in redshift space. Monthly Notices of the Royal Astronomical Society. 1987 07;227(1):1–21. Available from: https://doi.org/10.1093/mnras/227.1.1.

[154] Song YS, Percival WJ. Reconstructing the history of structure formation using Redshift Distortions. JCAP. 2009;10:004.

[155] Beutler F, Blake C, Colless M, Jones DH, Staveley-Smith L, Campbell L, et al. The 6dF Galaxy Survey: baryon acoustic oscillations and the local Hubble constant. . 2011 Oct;416:3017–3032.

[156] Samushia L, Percival WJ, Raccanelli A. Interpreting large-scale redshift-space distortion measurements. . 2012 Mar;420(3):2102–2119.

[157] Reid BA, Samushia L, White M, Percival WJ, Manera M, Padmanabhan N, et al. The clustering of galaxies in the SDSS-III Baryon Oscillation Spectroscopic Survey: measurements of the growth of structure and expansion rate at z = 0.57 from anisotropic clustering. . 2012 Nov;426(4):2719–2737.

[158] Blake C, Glazebrook K, Davis TM, Brough S, Colless M, Contreras C, et al. The WiggleZ Dark Energy Survey: measuring the cosmic expansion history using the Alcock-Paczynski test and distant supernovae. . 2011 Dec;418(3):1725–1735.

[159] Pezzotta A, et al. The VIMOS Public Extragalactic Redshift Survey (VIPERS): The growth of structure at $0.5 < z < 1.2$ from redshift-space distortions in the clustering of the PDR-2 final sample. Astron Astrophys. 2017;604:A33.

[160] Tanner M. Tools for statistical inference; 1993. .

[161] Gelman A, Carlin JB, Stern HS, Dunson DB, Vehtari A, Rubin DB. Bayesian Data Analysis (3rd ed.). Chapman and Hall/CRC; 2013.

[162] Abbott BP, et al. Observation of Gravitational Waves from a Binary Black Hole Merger. Phys Rev Lett. 2016;116(6):061102.

[163] Abbott BP, et al. GW151226: Observation of Gravitational Waves from a 22-Solar-Mass Binary Black Hole Coalescence. Phys Rev Lett. 2016;116(24):241103.

[164] Abbott BP, et al. GW170104: Observation of a 50-Solar-Mass Binary Black Hole Coalescence at Redshift 0.2. Phys Rev Lett. 2017;118(22):221101. [Erratum: Phys. Rev. Lett.121,no.12,129901(2018)].

[165] Abbott BP, et al. GW170608: Observation of a 19-solar-mass Binary Black Hole Coalescence. Astrophys J. 2017;851(2):L35.

[166] Abbott BP, et al. GW170814: A Three-Detector Observation of Gravitational Waves from a Binary Black Hole Coalescence. Phys Rev Lett. 2017;119(14):141101.

[167] Abbott BP, et al. GW170817: Observation of Gravitational Waves from a Binary Neutron Star Inspiral. Phys Rev Lett. 2017;119(16):161101.

[168] Abbott BP, et al. Multi-messenger Observations of a Binary Neutron Star Merger. Astrophys J Lett. 2017;848(2):L12.

[169] Abbott BP, et al. GWTC-1: A Gravitational-Wave Transient Catalog of Compact Binary Mergers Observed by LIGO and Virgo during the First and Second Observing Runs. Phys Rev X. 2019;9(3):031040.

[170] Shoemaker D. Gravitational wave astronomy with LIGO and similar detectors in the next decade; 2019.

[171] Abbott BP, et al. Prospects for Observing and Localizing Gravitational-Wave Transients with Advanced LIGO, Advanced Virgo and KAGRA. Living Rev Rel. 2018;21(1):3.

[172] Amaro-Seoane P, et al. eLISA/NGO: Astrophysics and cosmology in the gravitational-wave millihertz regime. GW Notes. 2013;6:4–110.

[173] Amaro-Seoane P, Audley H, Babak S, Baker J, Barausse E, Bender P, et al. Laser interferometer space antenna. arXiv preprint arXiv:170200786. 2017.

[174] Sathyaprakash B, et al. Scientific Objectives of Einstein Telescope. Class Quant Grav. 2012;29:124013. [Erratum: Class.Quant.Grav. 30, 079501 (2013)].

[175] Barausse E, Cardoso V, Pani P. Can environmental effects spoil precision gravitational-wave astrophysics? Phys Rev D. 2014;89(10):104059.

[176] Barausse E, Cardoso V, Pani P. Environmental Effects for Gravitational-wave Astrophysics. J Phys Conf Ser. 2015;610(1):012044.

[177] Barack L, et al. Black holes, gravitational waves and fundamental physics: a roadmap. Class Quant Grav. 2019;36(14):143001.

[178] Macedo CFB, Pani P, Cardoso V, Crispino LCB. Into the lair: gravitational-wave signatures of dark matter. Astrophys J. 2013;774:48.

[179] Eda K, Itoh Y, Kuroyanagi S, Silk J. New Probe of Dark-Matter Properties: Gravitational Waves from an Intermediate-Mass Black Hole Embedded in a Dark-Matter Minispike. Phys Rev Lett. 2013;110(22):221101.

[180] Brito R, Cardoso V, Pani P. Superradiance. Lect Notes Phys. 2015;906:pp.1–237.

[181] Cardoso V, Pani P, Yu TT. Superradiance in rotating stars and pulsar-timing constraints on dark photons. Phys Rev D. 2017;95(12):124056.

[182] Dolan SR. Superradiant instabilities of rotating black holes in the time domain. Phys Rev D. 2013;87(12):124026.

[183] Brito R, Cardoso V, Pani P. Black holes as particle detectors: evolution of superradiant instabilities. Class Quant Grav. 2015;32(13):134001.

[184] East WE, Pretorius F. Superradiant Instability and Backreaction of Massive Vector Fields around Kerr Black Holes. Phys Rev Lett. 2017;119(4):041101.

[185] Gair JR, Vallisneri M, Larson SL, Baker JG. Testing General Relativity with Low-Frequency, Space-Based Gravitational-Wave Detectors. Living Rev Rel. 2013;16:7.

[186] Ezquiaga JM, Zumalacárregui M. Dark Energy in light of Multi-Messenger Gravitational-Wave astronomy. Front Astron Space Sci. 2018;5:44.

[187] Bertone G, et al. Gravitational wave probes of dark matter: challenges and opportunities. SciPost Phys Core. 2020;3:007.

[188] Nakamura T, Oohara K, Kojima Y. General Relativistic Collapse to Black Holes and Gravitational Waves from Black Holes. Prog Theor Phys Suppl. 1987;90:1–218.

[189] Shibata M, Nakamura T. Evolution of three-dimensional gravitational waves: Harmonic slicing case. Phys Rev D. 1995;52:5428–5444.

[190] Baumgarte TW, Shapiro SL. On the numerical integration of Einstein's field equations. Phys Rev D. 1998;59:024007.

[191] Papallo G, Reall HS. On the local well-posedness of Lovelock and Horndeski theories. Phys Rev D. 2017;96(4):044019.

[192] Kovács AD. Well-posedness of cubic Horndeski theories. Phys Rev D. 2019;100(2):024005.

[193] Kovács AD, Reall HS. Well-Posed Formulation of Scalar-Tensor Effective Field Theory. Phys Rev Lett. 2020;124(22):221101.

[194] Kovács AD, Reall HS. Well-posed formulation of Lovelock and Horndeski theories. Phys Rev D. 2020;101(12):124003.

[195] Figueras P, França T. Gravitational Collapse in Cubic Horndeski Theories. Class Quant Grav. 2020;37(22):225009.

[196] Abbott TMC, et al. First Cosmology Results using Type Ia Supernovae from the Dark Energy Survey: Constraints on Cosmological Parameters. Astrophys J. 2019;872(2):L30.

[197] Hinshaw G, et al. Nine-Year Wilkinson Microwave Anisotropy Probe (WMAP) Observations: Cosmological Parameter Results. Astrophys J Suppl. 2013;208:19.

[198] Abell PA, et al. LSST Science Book, Version 2.0; 2009.

[199] Font-Ribera A, McDonald P, Mostek N, Reid BA, Seo HJ, Slosar A. DESI and other dark energy experiments in the era of neutrino mass measurements. JCAP. 2014;1405:023.

[200] Spergel D, et al. Wide-Field InfraRed Survey Telescope-Astrophysics Focused Telescope Assets WFIRST-AFTA Final Report; 2013.

[201] Aghamousa A, et al. The DESI Experiment Part I: Science,Targeting, and Survey Design; 2016.

[202] Hounsell R, et al. Simulations of the WFIRST Supernova Survey and Forecasts of Cosmological Constraints. Astrophys J. 2018;867(1):23.

[203] Caldwell RR, Dave R, Steinhardt PJ. Cosmological imprint of an energy component with general equation of state. Phys Rev Lett. 1998;80:1582–1585.

[204] Lidsey JE, Liddle AR, Kolb EW, Copeland EJ, Barreiro T, Abney M. Reconstructing the inflation potential : An overview. Rev Mod Phys. 1997;69:373–410.

[205] Barger V, Lee HS, Marfatia D. WMAP and inflation. Phys Lett B. 2003;565:33–41.

[206] Ade PAR, et al. Planck 2013 results. XXII. Constraints on inflation. Astron Astrophys. 2014;571:A22.

[207] Ade PAR, et al. Planck 2015 results. XX. Constraints on inflation. Astron Astrophys. 2016;594:A20.

[208] Akrami Y, et al. Planck 2018 results. X. Constraints on inflation. Astron Astrophys. 2020;641:A10.

[209] Ferreira PG, Joyce M. Cosmology with a primordial scaling field. Phys Rev. 1998;D58:023503.

[210] Caldwell RR, Linder EV. The Limits of quintessence. Phys Rev Lett. 2005;95:141301.

[211] Barger V, Guarnaccia E, Marfatia D. Classification of dark energy models in the (w(0), w(a)) plane. Phys Lett. 2006;B635:61–65.

[212] Ade PAR, et al. Planck 2015 results. XIV. Dark energy and modified gravity. Astron Astrophys. 2016;594:A14.

[213] Huterer D, Peiris HV. Dynamical behavior of generic quintessence potentials: Constraints on key dark energy observables. Phys Rev. 2007;D75:083503.

[214] Hildebrandt H, et al. KiDS-450: Cosmological parameter constraints from tomographic weak gravitational lensing. Mon Not Roy Astron Soc. 2017;465:1454.

[215] Joudaki S, et al. CFHTLenS revisited: assessing concordance with Planck including astrophysical systematics. Mon Not Roy Astron Soc. 2017;465(2):2033–2052.

[216] Copeland EJ, Liddle AR, Wands D. Exponential potentials and cosmological scaling solutions. Phys Rev. 1998;D57:4686–4690.

[217] Barreiro T, Copeland EJ, Nunes NJ. Quintessence arising from exponential potentials. Phys Rev. 2000;D61:127301.

[218] Ng SCC, Nunes NJ, Rosati F. Applications of scalar attractor solutions to cosmology. Phys Rev. 2001;D64:083510.

[219] de la Macorra A, Piccinelli G. General scalar fields as quintessence. Phys Rev. 2000;D61:123503.

[220] Zumalacárregui M, Bellini E, Sawicki I, Lesgourgues J, Ferreira PG. hi_class: Horndeski in the Cosmic Linear Anisotropy Solving System. JCAP. 2017;1708(08):019.

[221] Bellini E, Sawicki I, Zumalacárregui M. hi_class: Background Evolution, Initial Conditions and Approximation Schemes; 2019.

[222] Blas D, Lesgourgues J, Tram T. The Cosmic Linear Anisotropy Solving System (CLASS) II: Approximation schemes. JCAP. 2011;1107:034.

[223] Joudaki S, Kaplinghat M, Keeley R, Kirkby D. Model independent inference of the expansion history and implications for the growth of structure. Phys Rev. 2018;D97(12):123501.

[224] Fang W, Hu W, Lewis A. Crossing the Phantom Divide with Parameterized Post-Friedmann Dark Energy. Phys Rev. 2008;D78:087303.

[225] Linder EV. Quintessence's last stand? Phys Rev. 2015;D91:063006.

[226] Audren B, Lesgourgues J, Benabed K, Prunet S. Conservative Constraints on Early Cosmology: an illustration of the Monte Python cosmological parameter inference code. JCAP. 2013;1302:001.

[227] Brinckmann T, Lesgourgues J. MontePython 3: boosted MCMC sampler and other features; 2018.

[228] Metropolis N, Rosenbluth AW, Rosenbluth MN, Teller AH, Teller E. Equation of state calculations by fast computing machines. J Chem Phys. 1953;21:1087–1092.

[229] Hastings WK. Monte Carlo Sampling Methods Using Markov Chains and Their Applications. Biometrika. 1970;57:97–109.

[230] Gelman A, Rubin DB. Inference from Iterative Simulation Using Multiple Sequences. Statist Sci. 1992;7:457–472.

[231] Aghanim N, et al. Planck 2015 results. XI. CMB power spectra, likelihoods, and robustness of parameters. Astron Astrophys. 2016;594:A11.

[232] Beutler F, Blake C, Colless M, Jones DH, Staveley-Smith L, Poole GB, et al. The 6dF Galaxy Survey: $z \approx 0$ measurement of the growth rate and σ_8. Mon Not Roy Astron Soc. 2012;423:3430–3444.

[233] Scolnic DM, et al. The Complete Light-curve Sample of Spectroscopically Confirmed SNe Ia from Pan-STARRS1 and Cosmological Constraints from the Combined Pantheon Sample. Astrophys J. 2018;859(2):101.

[234] Lewis A. GetDist: a Python package for analysing Monte Carlo samples; 2019.

[235] Bergmann PG. Comments on the scalar tensor theory. Int J Theor Phys. 1968;1:25–36.

[236] Fujii Y, Maeda Ki. The Scalar-Tensor Theory of Gravitation. Cambridge Monographs on Mathematical Physics. Cambridge University Press; 2003.

[237] Bellini E, Cuesta AJ, Jimenez R, Verde L. Constraints on deviations from ΛCDM within Horndeski gravity. JCAP. 2016 Feb;2:053.

[238] Kreisch CD, Komatsu E. Cosmological Constraints on Horndeski Gravity in Light of GW170817. JCAP. 2018;12:030.

[239] Spurio Mancini A, Reischke R, Pettorino V, Schäfer BM, Zumalacárregui M. Testing (modified) gravity with 3D and tomographic cosmic shear. Mon Not Roy Astron Soc. 2018;480(3):3725–3738.

[240] Reischke R, Spurio Mancini A, Schäfer BM, Merkel PM. Investigating scalar–tensor gravity with statistics of the cosmic large-scale structure. Mon Not Roy Astron Soc. 2019;482(3):3274–3287.

[241] Noller J, Nicola A. Cosmological parameter constraints for Horndeski scalar-tensor gravity; 2018.

[242] Noller J, Nicola A. Radiative stability and observational constraints on dark energy and modified gravity; 2018.

[243] Spurio Mancini A, Köhlinger F, Joachimi B, Pettorino V, Schäfer BM, Reischke R, et al. KiDS + GAMA: constraints on horndeski gravity from combined large-scale structure probes. Mon Not Roy Astron Soc. 2019;490(2):2155–2177.

[244] Frusciante N, Perenon L. Effective field theory of dark energy: A review. Phys Rept. 2020;857:1–63.

[245] Arai S, Karmakar P, Nishizawa A. Cosmological evolution of viable models in the generalized scalar-tensor theory. Phys Rev D. 2020;102(2):024003.

[246] Noller J. Cosmological constraints on dark energy in light of gravitational wave bounds. Phys Rev D. 2020;101(6):063524.

[247] Baker T, Harrison I. Constraining Scalar-Tensor Modified Gravity with Gravitational Waves and Large Scale Structure Surveys. JCAP. 2021;01:068.

[248] Mastrogiovanni S, Steer D, Barsuglia M. Probing modified gravity theories and cosmology using gravitational-waves and associated electromagnetic counterparts. Phys Rev D. 2020;102(4):044009.

[249] Gleyzes J, Langlois D, Mancarella M, Vernizzi F. Effective Theory of Dark Energy at Redshift Survey Scales. JCAP. 2016;02:056.

[250] Alonso D, Bellini E, Ferreira PG, Zumalacárregui M. Observational future of cosmological scalar-tensor theories. Phys Rev. 2017;D95(6):063502.

[251] Linder EV, Sengör G, Watson S. Is the Effective Field Theory of Dark Energy Effective? JCAP. 2016;05:053.

[252] Linder EV. Challenges in connecting modified gravity theory and observations. Phys Rev D. 2017;95(2):023518.

[253] Denissenya M, Linder EV. Gravity's Islands: Parametrizing Horndeski Stability. JCAP. 2018;11:010.

[254] Lombriser L, Dalang C, Kennedy J, Taylor A. Inherently stable effective field theory for dark energy and modified gravity. JCAP. 2019;01:041.

[255] Gleyzes J. Parametrizing modified gravity for cosmological surveys. Phys Rev D. 2017;96(6):063516.

[256] Goldstein A, Veres P, Burns E, Briggs MS, Hamburg R, Kocevski D, et al. An Ordinary Short Gamma-Ray Burst with Extraordinary Implications: Fermi -GBM Detection of GRB 170817A. The Astrophysical Journal Letters. 2017;848(2):L14. Available from: http://stacks.iop.org/2041-8205/848/i=2/a=L14.

[257] Savchenko V, Ferrigno C, Kuulkers E, Bazzano A, Bozzo E, Brandt S, et al. INTEGRAL Detection of the First Prompt Gamma-Ray Signal Coincident with the Gravitational-wave Event GW170817. The Astrophysical Journal Letters. 2017;848(2):L15. Available from: http://stacks.iop.org/2041-8205/848/i=2/a=L15.

[258] Pirtskhalava D, Santoni L, Trincherini E, Vernizzi F. Weakly Broken Galileon Symmetry. JCAP. 2015;09:007.

[259] Luty MA, Porrati M, Rattazzi R. Strong interactions and stability in the DGP model. JHEP. 2003;09:029.

[260] Nicolis A, Rattazzi R, Trincherini E. The Galileon as a local modification of gravity. Phys Rev D. 2009;79:064036.

[261] Heisenberg L, Noller J, Zosso J. Horndeski under the quantum loupe. JCAP. 2020;10:010.

[262] de Rham C, Melville S. Gravitational Rainbows: LIGO and Dark Energy at its Cutoff. Phys Rev Lett. 2018;121(22):221101.

[263] Peirone S, Benevento G, Frusciante N, Tsujikawa S. Cosmological data favor Galileon ghost condensate over ΛCDM. Phys Rev D. 2019;100(6):063540.

[264] Frusciante N, Peirone S, Atayde L, De Felice A. Phenomenology of the generalized cubic covariant Galileon model and cosmological bounds. Phys Rev D. 2020;101(6):064001.

[265] Dvali G, Gabadadze G, Porrati M. 4D gravity on a brane in 5D Minkowski space. Physics Letters B. 2000 Jul;485(1-3):208–214. Available from: http://dx.doi.org/10.1016/S0370-2693(00)00669-9.

[266] Deffayet C. Cosmology on a brane in Minkowski bulk. Physics Letters B. 2001 Mar;502(1-4):199–208. Available from: http://dx.doi.org/10.1016/S0370-2693(01)00160-5.

[267] Fang W, Wang S, Hu W, Haiman Z, Hui L, May M. Challenges to the DGP model from horizon-scale growth and geometry. Physical Review D. 2008 Nov;78(10). Available from: http://dx.doi.org/10.1103/PhysRevD.78.103509.

[268] Schmidt F. Self-consistent cosmological simulations of DGP braneworld gravity. Physical Review D. 2009 Aug;80(4). Available from: http://dx.doi.org/10.1103/PhysRevD.80.043001.

[269] Zumalacarregui M. Gravity in the Era of Equality: Towards solutions to the Hubble problem without fine-tuned initial conditions. Phys Rev D. 2020;102(2):023523.

[270] Barreira A, Li B, Sanchez A, Baugh CM, Pascoli S. Parameter space in Galileon gravity models. Phys Rev D. 2013;87:103511.

[271] Adams A, Arkani-Hamed N, Dubovsky S, Nicolis A, Rattazzi R. Causality, analyticity and an IR obstruction to UV completion. JHEP. 2006;10:014.

[272] Jenkins A, O'Connell D. The Story of O: Positivity constraints in effective field theories; 2006.

[273] Nicolis A, Rattazzi R, Trincherini E. Energy's and amplitudes' positivity. JHEP. 2010;05:095. [Erratum: JHEP11,128(2011)].

[274] Bellazzini B, Martucci L, Torre R. Symmetries, Sum Rules and Constraints on Effective Field Theories. JHEP. 2014;09:100.

[275] Baumann D, Green D, Lee H, Porto RA. Signs of Analyticity in Single-Field Inflation. Phys Rev D. 2016;93(2):023523.

[276] de Rham C, Melville S, Tolley AJ, Zhou SY. Positivity bounds for scalar field theories. Phys Rev D. 2017;96(8):081702.

[277] de Rham C, Melville S, Tolley AJ, Zhou SY. Massive Galileon Positivity Bounds. JHEP. 2017;09:072.

[278] de Rham C, Melville S, Tolley AJ. Improved Positivity Bounds and Massive Gravity. JHEP. 2018;04:083.

[279] Bellazzini B, Lewandowski M, Serra J. Positivity of Amplitudes, Weak Gravity Conjecture, and Modified Gravity. Phys Rev Lett. 2019;123(25):251103.

[280] de Rham C, Tolley AJ. Speed of gravity. Phys Rev D. 2020;101(6):063518.

[281] Ye G, Piao YS. Positivity in the effective field theory of cosmological perturbations. Eur Phys J C. 2020;80(5):421.

[282] Melville S, Noller J. Positivity in the Sky: Constraining dark energy and modified gravity from the UV. Phys Rev D. 2020;101(2):021502.

[283] Kennedy J, Lombriser L. Positivity bounds on reconstructed Horndeski models. Phys Rev D. 2020;102(4):044062.

[284] Alberte L, de Rham C, Jaitly S, Tolley AJ. Positivity Bounds and the Massless Spin-2 Pole. Phys Rev D. 2020;102:125023.

[285] Tokuda J, Aoki K, Hirano S. Gravitational positivity bounds. JHEP. 2020;11:054.

[286] Bellazzini B, Elias Miró J, Rattazzi R, Riembau M, Riva F. Positive Moments for Scattering Amplitudes; 2020.

[287] Tolley AJ, Wang ZY, Zhou SY. New positivity bounds from full crossing symmetry; 2020.

[288] Grall T, Melville S. Positivity Bounds without Boosts; 2021.

[289] de Rham C, Melville S, Noller J. Positivity Bounds on Dark Energy: When Matter Matters; 2021.

[290] Melville S, Noller J. to appear.

[291] Aghanim N, et al. Planck 2018 results. I. Overview and the cosmological legacy of Planck. Astron Astrophys. 2020;641:A1.

[292] Aghanim N, et al. Planck 2018 results. V. CMB power spectra and likelihoods. Astron Astrophys. 2020;641:A5.

[293] Creminelli P, Tambalo G, Vernizzi F, Yingcharoenrat V. Dark-Energy Instabilities induced by Gravitational Waves. JCAP. 2020;05:002.

[294] Joudaki S, Ferreira PG, Lima NA, Winther HA. Testing Gravity on Cosmic Scales: A Case Study of Jordan-Brans-Dicke Theory; 2020.

[295] de Rham C, Gabadadze G, Tolley AJ. Helicity Decomposition of Ghost-free Massive Gravity. JHEP. 2011;11:093.

[296] Lin C, Mukohyama S, Namba R, Saitou R. Hamiltonian structure of scalar-tensor theories beyond Horndeski. JCAP. 2014;1410(10):071.

[297] Crisostomi M, Hull M, Koyama K, Tasinato G. Horndeski: beyond, or not beyond? JCAP. 2016;1603(03):038.

[298] Gleyzes J, Langlois D, Piazza F, Vernizzi F. New Class of Consistent Scalar-Tensor Theories. Phys Rev Lett. 2015 May;114:211101. Available from: https://link.aps.org/doi/10.1103/PhysRevLett.114.211101.

[299] Babichev E, Lehébel A. The sound of DHOST. JCAP. 2018;1812(12):027.

[300] Crisostomi M, Koyama K. Self-accelerating universe in scalar-tensor theories after GW170817. Phys Rev. 2018;D97(8):084004.

[301] Lim EA, Sawicki I, Vikman A. Dust of Dark Energy. JCAP. 2010;1005:012.

[302] Gao X. Unifying framework for scalar-tensor theories of gravity. Phys Rev. 2014;D90:081501.

[303] Dossett J, Hu B, Parkinson D. Constraining models of f(R) gravity with Planck and WiggleZ power spectrum data. JCAP. 2014;1403:046.

[304] Raveri M, Hu B, Frusciante N, Silvestri A. Effective Field Theory of Cosmic Acceleration: constraining dark energy with CMB data. Phys Rev. 2014;D90(4):043513.

[305] Hu B, Raveri M. Can modified gravity models reconcile the tension between the CMB anisotropy and lensing maps in Planck-like observations? Phys Rev. 2015;D91(12):123515.

[306] Bellini E, Cuesta AJ, Jimenez R, Verde L. Constraints on deviations from ΛCDM within Horndeski gravity. JCAP. 2016;1602(02):053. [Erratum: JCAP1606,no.06,E01(2016)].

[307] Bellini E, Jimenez R, Verde L. Signatures of Horndeski gravity on the Dark Matter Bispectrum. JCAP. 2015;1505(05):057.

[308] Lagos M, Bellini E, Noller J, Ferreira PG, Baker T. A general theory of linear cosmological perturbations: stability conditions, the quasistatic limit and dynamics. JCAP. 2018;03:021.

[309] Langlois D, Noui K. Degenerate higher derivative theories beyond Horndeski: evading the Ostrogradski instability. JCAP. 2016;1602(02):034.

[310] Ben Achour J, Crisostomi M, Koyama K, Langlois D, Noui K, Tasinato G. Degenerate higher order scalar-tensor theories beyond Horndeski up to cubic order. JHEP. 2016;12:100.

[311] D'Amico G, Huang Z, Mancarella M, Vernizzi F. Weakening Gravity on Redshift-Survey Scales with Kinetic Matter Mixing. JCAP. 2017;1702:014.

[312] De Felice A, Tsujikawa S. Conditions for the cosmological viability of the most general scalar-tensor theories and their applications to extended Galileon dark energy models. JCAP. 2012;1202:007.

[313] Salvatelli V, Piazza F, Marinoni C. Constraints on modified gravity from Planck 2015: when the health of your theory makes the difference. JCAP. 2016;1609(09):027.

[314] Perenon L, Marinoni C, Piazza F. Diagnostic of Horndeski Theories. JCAP. 2017;1701(01):035.

[315] Copeland EJ, Kopp M, Padilla A, Saffin PM, Skordis C. Dark energy after GW170817 revisited. Phys Rev Lett. 2019;122(6):061301.

[316] Creminelli P, Lewandowski M, Tambalo G, Vernizzi F. Gravitational Wave Decay into Dark Energy; 2018.

[317] Baker T, Ferreira PG, Skordis C. A Fast Route to Modified Gravitational Growth. Phys Rev. 2014;D89(2):024026.

[318] Blas D, Lesgourgues J, Tram T. The Cosmic Linear Anisotropy Solving System (CLASS). Part II: Approximation schemes. Journal of Cosmology and Astro-Particle Physics. 2011 Jul;2011:034.

[319] Bellini E, et al. Comparison of Einstein-Boltzmann solvers for testing general relativity. Phys Rev. 2018;D97(2):023520.

[320] Zuntz J, Paterno M, Jennings E, Rudd D, Manzotti A, Dodelson S, et al. CosmoSIS: modular cosmological parameter estimation. Astron Comput. 2015;12:45–59.

[321] Beutler F, Blake C, Colless M, Jones DH, Staveley-Smith L, Poole GB, et al. The 6dF Galaxy Survey: $z \approx 0$ measurements of the growth rate and σ_8. . 2012 Jul;423:3430–3444.

[322] Howlett C, Ross A, Samushia L, Percival W, Manera M. The clustering of the SDSS main galaxy sample – II. Mock galaxy catalogues and a measurement of the growth of structure from redshift space distortions at $z = 0.15$. Mon Not Roy Astron Soc. 2015;449(1):848–866.

[323] Oka A, Saito S, Nishimichi T, Taruya A, Yamamoto K. Simultaneous constraints on the growth of structure and cosmic expansion from the multipole power spectra of the SDSS DR7 LRG sample. Mon Not Roy Astron Soc. 2014;439:2515–2530.

[324] Blake C, Brough S, Colless M, Contreras C, Couch W, Croom S, et al. The WiggleZ Dark Energy Survey: the growth rate of cosmic structure since redshift z=0.9. . 2011 Aug;415:2876–2891.

[325] Akiyama K, et al. First M87 Event Horizon Telescope Results. I. The Shadow of the Supermassive Black Hole. Astrophys J. 2019;875(1):L1.

[326] Abbott BP, et al. Binary Black Hole Mergers in the first Advanced LIGO Observing Run. Phys Rev X. 2016;6(4):041015. [Erratum: Phys.Rev.X 8, 039903 (2018)].

[327] Acernese F, et al. Advanced Virgo: a second-generation interferometric gravitational wave detector. Class Quant Grav. 2015;32(2):024001.

[328] Somiya K. Detector configuration of KAGRA: The Japanese cryogenic gravitational-wave detector. Class Quant Grav. 2012;29:124007.

[329] Punturo M, et al. The Einstein Telescope: A third-generation gravitational wave observatory. Class Quant Grav. 2010;27:194002.

[330] Reitze D, et al. Cosmic Explorer: The U.S. Contribution to Gravitational-Wave Astronomy beyond LIGO. Bull Am Astron Soc. 2019 7;51:035.

[331] Saleem M, et al. The Science Case for LIGO-India; 2021.

[332] Amaro-Seoane P, et al. Laser Interferometer Space Antenna; 2017.

[333] Hu WR, Wu YL. The Taiji Program in Space for gravitational wave physics and the nature of gravity. Natl Sci Rev. 2017;4(5):685–686.

[334] Luo J, et al. TianQin: a space-borne gravitational wave detector. Class Quant Grav. 2016;33(3):035010.

[335] Barausse E, et al. Prospects for Fundamental Physics with LISA. Gen Rel Grav. 2020;52(8):81.

[336] Peccei RD, Quinn HR. CP Conservation in the Presence of Instantons. Phys Rev Lett. 1977;38:1440–1443.

[337] Arvanitaki A, Dimopoulos S, Dubovsky S, Kaloper N, March-Russell J. String Axiverse. Phys Rev D. 2010;81:123530.

[338] Peccei RD. The Strong CP problem and axions. Lect Notes Phys. 2008;741:3–17.

[339] Marsh DJE. Axion Cosmology. Phys Rept. 2016;643:1–79.

[340] Ferreira EGM. Ultra-Light Dark Matter; 2020.

[341] Niemeyer JC. Small-scale structure of fuzzy and axion-like dark matter. Prog Part Nucl Phys. 2019 12:103787.

[342] Hui L. Wave Dark Matter; 2021.

[343] Hui L, Kabat D, Li X, Santoni L, Wong SSC. Black Hole Hair from Scalar Dark Matter. JCAP. 2019;06:038.

[344] Clough K, Ferreira PG, Lagos M. Growth of massive scalar hair around a Schwarzschild black hole. Phys Rev. 2019;D100(6):063014.

[345] Bamber J, Clough K, Ferreira PG, Hui L, Lagos M. Growth of accretion driven scalar hair around Kerr black holes; 2020.

[346] Detweiler SL. KLEIN-GORDON EQUATION AND ROTATING BLACK HOLES. Phys Rev. 1980;D22:2323–2326.

[347] Cardoso V, Yoshida S. Superradiant instabilities of rotating black branes and strings. JHEP. 2005;07:009.

[348] Dolan SR. Instability of the massive Klein-Gordon field on the Kerr spacetime. Phys Rev. 2007;D76:084001.

[349] Herdeiro CAR, Radu E. Kerr black holes with scalar hair. Phys Rev Lett. 2014;112:221101.

[350] Arvanitaki A, Baryakhtar M, Huang X. Discovering the QCD Axion with Black Holes and Gravitational Waves. Phys Rev D. 2015;91(8):084011.

[351] Arvanitaki A, Dubovsky S. Exploring the String Axiverse with Precision Black Hole Physics. Phys Rev D. 2011;83:044026.

[352] Ferreira MC, Macedo CFB, Cardoso V. Orbital fingerprints of ultralight scalar fields around black holes. Phys Rev. 2017;D96(8):083017.

[353] Hannuksela OA, Wong KWK, Brito R, Berti E, Li TGF. Probing the existence of ultralight bosons with a single gravitational-wave measurement. Nature Astron. 2019;3(5):447–451.

[354] Zhang J, Yang H. Dynamic Signatures of Black Hole Binaries with Superradiant Clouds. Phys Rev D. 2020;101(4):043020.

[355] Eda K, Itoh Y, Kuroyanagi S, Silk J. Gravitational waves as a probe of dark matter minispikes. Phys Rev D. 2015;91(4):044045.

[356] Kavanagh BJ, Nichols DA, Bertone G, Gaggero D. Detecting dark matter around black holes with gravitational waves: Effects of dark-matter dynamics on the gravitational waveform. Phys Rev D. 2020;102(8):083006.

[357] Yue XJ, Cao Z. Dark matter minispike: A significant enhancement of eccentricity for intermediate-mass-ratio inspirals. Phys Rev D. 2019;100(4):043013.

[358] Hannuksela OA, Ng KCY, Li TGF. Extreme dark matter tests with extreme mass ratio inspirals. Phys Rev D. 2020;102(10):103022.

[359] Edwards TDP, Chianese M, Kavanagh BJ, Nissanke SM, Weniger C. Unique Multi-messenger Signal of QCD Axion Dark Matter. Phys Rev Lett. 2020;124(16):161101.

[360] Yue XJ, Han WB. Gravitational waves with dark matter minispikes: the combined effect. Phys Rev D. 2018;97(6):064003.

[361] Chandrasekhar S. Dynamical Friction. I. General Considerations: the Coefficient of Dynamical Friction. Astrophys J. 1943;97:255.

[362] Petrich LI, Shapiro SL, Stark RF, Teukolsky SA. Accretion onto a Moving Black Hole: A Fully Relativistic Treatment. . 1989 Jan;336:313.

[363] Barausse E. Relativistic dynamical friction in a collisional fluid. Mon Not Roy Astron Soc. 2007;382:826–834.

[364] Gourgoulhon E. 3+1 formalism and bases of numerical relativity; 2007.

[365] Clough K. Continuity equations for general matter: applications in numerical relativity; 2021.

[366] Clough K, Figueras P, Finkel H, Kunesch M, Lim EA, Tunyasuvunakool S. GR-Chombo: Numerical relativity with adaptive mesh refinement. Classical and Quantum Gravity. 2015 Dec;32(24):245011. Available from: http://dx.doi.org/10.1088/0264-9381/32/24/245011.

[367] Syer D. Relativistic dynamical friction in the weak scattering limit. Mon Not Roy Astron Soc. 1994;270:205.

[368] Ostriker EC. Dynamical friction in a gaseous medium. Astrophys J. 1999;513:252.

[369] Ruderman MA, Spiegel EA. Galactic Wakes. . 1971 Apr;165:1.

[370] Rephaeli Y, Salpeter EE. Flow past a massive object and the gravitational drag. . 1980 Aug;240:20–24.

[371] Annulli L, Cardoso V, Vicente R. Stirred and shaken: Dynamical behavior of boson stars and dark matter cores. Phys Lett B. 2020;811:135944.

[372] Annulli L, Cardoso V, Vicente R. Response of ultralight dark matter to supermassive black holes and binaries. Phys Rev D. 2020;102(6):063022.

[373] Hartman STH, Winther HA, Mota DF. Dynamical friction in Bose-Einstein condensed self-interacting dark matter at finite temperatures, and the Fornax dwarf spheroidal. Astron Astrophys. 2021;647:A70.

[374] Vicente R, Cardoso V, Zilhão M. Dynamical friction in slab geometries and accretion disks. Mon Not Roy Astron Soc. 2019;489(4):5424–5435.

[375] Bondi H. On spherically symmetrical accretion. Mon Not Roy Astron Soc. 1952;112:195.

[376] Bondi H, Hoyle F. On the mechanism of accretion by stars. Mon Not Roy Astron Soc. 1944;104:273.

[377] Helfer T, Marsh DJE, Clough K, Fairbairn M, Lim EA, Becerril R. Black hole formation from axion stars. JCAP. 2017;03:055.

[378] Lagos M, Baker T, Ferreira PG, Noller J. A general theory of linear cosmological perturbations: scalar-tensor and vector-tensor theories. JCAP. 2016;08:007.

Appendix A

Shift-symmetric Horndeski priors

A.1 Discontinuities for models crossing $\alpha_{\rm B} = 2$

In the main text we briefly alluded to potential issues associated with crossing $\alpha_{\rm B} = 2$. As shown in Fig. 3.4, $\alpha_{\rm B}$ generically starts strongly suppressed at high redshifts and then grows towards redshift zero, typically reaching $\mathcal{O}(1)$ values. For a small, yet significant, subset of the models discussed in this chapter (see e.g. the distributions shown in Fig. 3.5) $\alpha_{\rm B}$ eventually grows to be larger than 2. This is important, because crossing the $\alpha_{\rm B} = 2$ point is associated with a number of discontinuities. This was first noted in [90] and discussed in [308] and has resulted in evolutions crossing this point being conservatively excluded in some of the subsequent analyses – see e.g. [241, 243, 246] – so in this appendix we quickly summarise the issues associated with crossing this point and how we treat models that do so in this chapter (as this differs from the treatment in the above-mentioned papers).

Discontinuity in the number of propagating degrees of freedom: Horndeski scalar-tensor models of dark energy generically propagate two scalar degrees of freedom: one directly associated to dark energy and one to matter. Following the approach outlined in [90, 308, 378] and for concreteness modelling matter as a minimally coupled canonical scalar field ψ_M with Lagrangian $\mathcal{L} = -\frac{1}{2}\partial_\mu\psi_M\partial^\mu\psi_M - V(\psi_M)$, working on a cosmological background and in unitary gauge we find these two independent degrees of freedom can be associated with $\delta\psi_M$ and Φ (i.e. the scalar metric perturbation of the ii component of the metric). While crossing $\alpha_{\rm B} = 2$ in the evolution, the following constraint relating these

two degrees of freedom emerges

$$\psi'_M \delta\psi_M = 2M_P^2 \Phi', \tag{A.1}$$

where we have assumed that there is no cosmological running of the Planck mass, as is the case for the models considered in this chapter. This relation shows that one propagating degree of freedom is eliminated at this point, so only one dynamical degree of freedom remains here. This is alarming, since the number of propagating degrees of freedom therefore changes as we evolve through $\alpha_{\rm B} = 2$: it is two on either side, but only one remains on the divide itself. This may be an artefact of using perturbation theory, but in any case indicates a potential ill-definedness in the evolution across $\alpha_{\rm B} = 2$. Giving a definitive answer may require a non-perturbative analysis, which allows to follow the dynamics of the real degree of freedom (and not an approximated version of it), and may allow us to exclude the dangerous situation of being in a strongly coupled regime.

Discontinuity in the evolution equations: For general $\alpha_{\rm B}$, one can straightforwardly derive the (coupled) evolution equations for $\delta\psi_M$ and Φ. Using these and taking the limit as $\alpha_{\rm B} \to 2$, one recovers the constraint (A.1) from the equation of motion for $\delta\psi_M$ and can then use this constraint to solve for $\delta\psi_M$, arriving at a single second order evolution equation for Φ. This reads

$$\Phi'' + \left(2\mathcal{H} + \frac{2a^2 V_{\psi_M}}{\psi'_M}\right)\Phi' + k^2\Phi = 0, \tag{A.2}$$

where we have again assumed that there is no cosmological running of the Planck mass and will also assume that the speed of gravitational waves is precisely the speed of light in what follows – both assumptions are met for the models considered in this chapter and violating them would complicate the expressions shown here, although not the qualitative conclusions of this appendix. Now suppose we instead first set $\alpha_{\rm B} = 2$ in the full quadratic action and then derive the residual evolution equation for the remaining degree of freedom. Again we recover the constraint (A.1), this time from a Lagrange multiplier in the quadratic

action. However, the evolution equation for Φ now instead reads

$$\Phi'' + \left(2\mathcal{H} + \frac{2a^2 V_{\psi_M}}{\psi'_M}\right)\Phi' + k^2\Phi - \frac{\Phi}{2}\left((6+\hat{\alpha}_{\rm K})\,\mathcal{H}^2 + \frac{\varphi'^2}{M_P^2}\right) = 0. \tag{A.3}$$

This is identical to (A.2), except for the addition of the last term. While the last term is suppressed with respect to the second last in the sub-horizon limit, this nevertheless again hints at evolutions crossing the $\alpha_{\rm B} = 2$ point being ill-defined, since there does not seem to be a uniquely defined evolution across this point. However, carrying out the analogous calculation in Newtonian gauge gives the same equations up to terms proportional to $\alpha'_{\rm B}$, which also vanish in this limit. This suggests that the above-mentioned discontinuity in the evolution equations might be a gauge artefact.

Summarising, both these issues are alarming and should be investigated in more detail. However, a definitive answer can be given only after further investigation, and this is beyond the scope of this work. Despite the above issues, it is important to notice – as shown in Fig. A.1 – that the CMB and matter spectra do not show any discontinuity when crossing $\alpha_{\rm B} = 2$. This shows that it is possible to solve this system in such a way that they do not show any observable discontinuity at $\alpha_{\rm B} = 2$. This corresponds to the second case considered above, cf. (A.3). In addition, given that the majority of the models considered and consistent with current observational constraints never crosses $\alpha_{\rm B} = 2$, a hard bound at this point should not affect our results qualitatively. While these observations do not resolve the above issues as such, they are nevertheless encouraging and suggest that they may be resolved without invalidating other parts of the analysis. For this reason we here put these issues to one side and do evolve across $\alpha_{\rm B} = 2$ in this way.

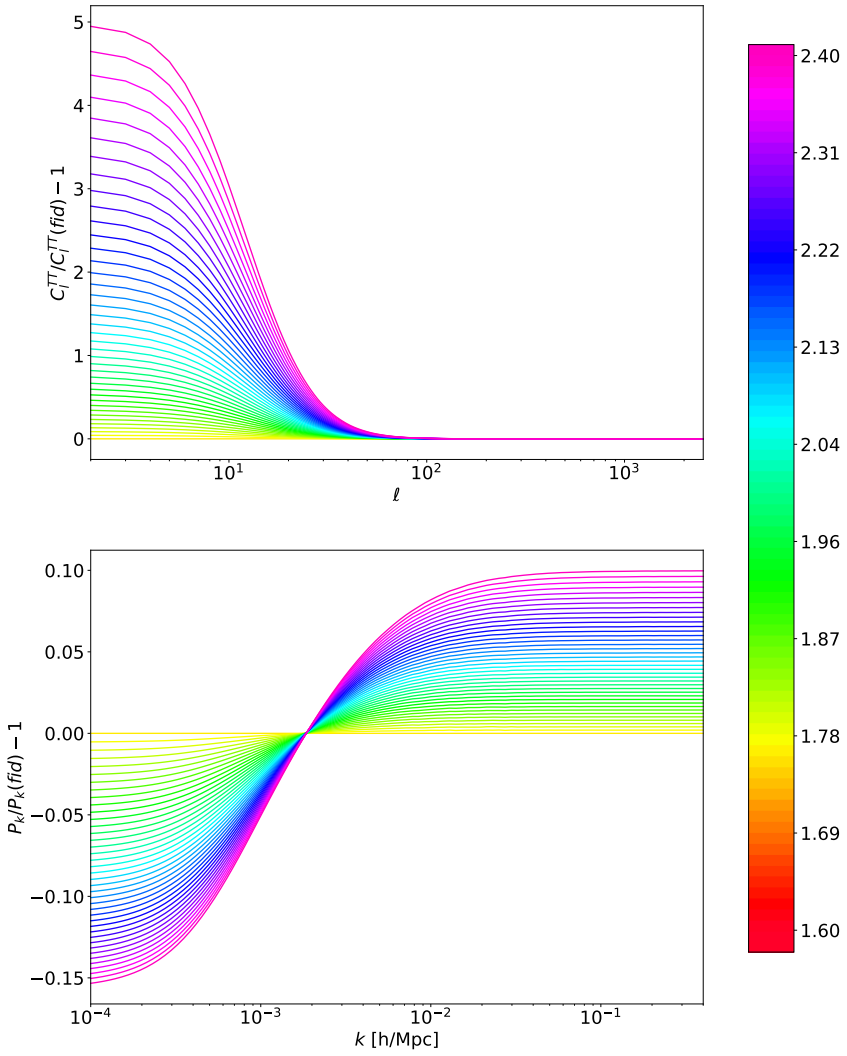


Figure A.1: We show the relative deviation of the CMB temperature-temperature (top panel) and the matter (bottom panel) power spectra w.r.t. a fiducial model for different values of $\alpha_{\rm B}\,(a=1)$ (the corresponding colour for each value is shown on the colour bar). We chose to pick models with both $\alpha_{\rm B} < 2$ and $\alpha_{\rm B} > 2$, to see if some kind of discontinuity could be detected. We notice that the spectra seems continuous and smooth at this point.

Appendix B

Beyond Horndeski

B.1 Implementing the equations into `hi_class`

In this section we present the equations we implemented into `hi_class`. In CLASS (and `hi_class`) the units are chosen so that the Friedmann equations are written as,

$$H^2 = \rho_{\rm mc} + \rho_{\phi \rm c}\,, \tag{B.1}$$

$$\frac{H'}{a} = -\frac{3}{2}\left(H^2 + p_{\rm mc} + p_{\phi \rm c}\right)\,, \tag{B.2}$$

$$\tag{B.3}$$

where the primes denote a derivative with respect to conformal time, however the Hubble parameter H is the physical one, $\rho_{\rm mc}$ and $p_{\rm mc}$ are the density and pressure of matter in the universe (excluding dark energy), and $\rho_{\phi \rm c}$ and $p_{\phi \rm c}$ are those of the scalar field.

$$\begin{aligned}\rho_{\phi \rm c} \equiv & -\frac{1}{3}G_2 + \frac{2}{3}X\left(G_{2X} - G_{3\phi}\right) - \frac{2H^3\phi' X}{3a}\left[7G_{5X} + 4X\left(G_{5XX} - 33F_5 - 12XF_{5X}\right)\right] \\ & + H^2\left[1 - \left(1-\alpha_{\rm B}\right)M_*^2 - 4X\left(G_{4X} - G_{5\phi}\right) - 4X^2\left(2G_{4XX} - G_{5\phi X} + 8F_4 + 4XF_{4X}\right)\right]\,,\end{aligned} \tag{B.4}$$

$$\begin{aligned}p_{\phi \rm c} = & \frac{1}{3}G_2 - \frac{2}{3}X\left(G_{3\phi} - 2G_{4\phi\phi}\right) + \frac{4H\phi'}{3a}\left(G_{4\phi} - 2XG_{4\phi X} + XG_{5\phi\phi} - 4X^2F_{4\phi}\right) - \\ & \frac{\left(\phi'' + aH\phi'\right)}{3\phi' a}HM_*^2\alpha_{\rm B} - \frac{4}{3}H^2X^2\left(G_{5\phi X} - 12XF_{5\phi}\right) \\ & - \left(H^2 + \frac{2H'}{3a}\right)\left(1 - M_*^2\right) + \frac{2H^3\phi' X}{3a}\left(G_{5X} - 12XF_5\right)\,.\end{aligned} \tag{B.5}$$

This form of the densities and pressures is analogous to the way they were defined in [220], so that we get the usual conservation equations,

$$\rho'_{\rm mc} = -3Ha\left(\rho_{\rm mc} + p_{\rm mc}\right) , \tag{B.6}$$

$$\rho'_{\phi{\rm c}} = -3Ha\left(\rho_{\phi{\rm c}} + p_{\phi{\rm c}}\right) . \tag{B.7}$$

In CLASS it is possible to solve the linear perturbation equations in both Newtonian and synchronous gauge. However, the current version of `hi_class` only has the synchronous gauge, so here we present the equations of Section 4.2.4 in this gauge as they are implemented into the code.

The line element to first order in the perturbations in synchronous gauge is [105],

$$\mathrm{d}s^2 = a^2\left[-\mathrm{d}\tau^2 + \left(\delta_{ij} + \tilde{h}_{ij}\right)\mathrm{d}x^i dx^j\right] , \tag{B.8}$$

with

$$\tilde{h}_{ij}(\tau,\vec{k}\,) = \hat{k}_i\hat{k}_j h + 6\left(\hat{k}_i\hat{k}_j - \frac{1}{3}\delta_{ij}\right)\eta + h_{ij} ,$$

in Fourier space, where h and η are the scalar perturbations and h_{ij} is the tensor perturbation.

The scalar field perturbation $V_{\rm X}$ here is defined as

$$V_{\rm X} \equiv a\frac{\delta\phi}{\phi'} = a\, v_{\rm X} . \tag{B.9}$$

In this gauge the Einstein equations take the form:

Einstein (0,0)

$$\begin{aligned} h' = {} & \frac{4k^2}{Ha}\left(\frac{1+\alpha_{\rm H}}{2-\alpha_{\rm B}}\right)\eta + \frac{6\rho_{\rm mc}\delta_{\rm mc}a}{HM_*^2\left(2-\alpha_{\rm B}\right)} - 2Ha\left(\frac{3\alpha_{\rm B}+\alpha_{\rm K}}{2-\alpha_{\rm B}}\right)V'_X \\ & - 2\left[3aH' + \left(\frac{\alpha_{\rm K}+3\alpha_{\rm B}}{2-\alpha_{\rm B}}\right)a^2H^2 + \frac{9a^2}{M_*^2}\left(\frac{\rho_{\rm mc}+p_{\rm mc}}{2-\alpha_{\rm B}}\right) + \left(\frac{\alpha_{\rm B}+2\alpha_{\rm H}}{2-\alpha_{\rm B}}\right)k^2\right]V_X . \end{aligned}$$

Einstein (0,i)

$$\eta' = \frac{3a^2\theta_{\rm m}}{2k^2M_*^2} + \frac{1}{2}\alpha_{\rm B}HaV'_X + \left[H'a + \frac{1}{2}\alpha_{\rm B}H^2a^2 + \frac{3a^2}{2M_*^2}\left(\rho_{\rm mc}+p_{\rm mc}\right)\right]V_X . \tag{B.10}$$

where

$$\theta_{\rm m} \equiv -\left(\rho_{\rm mc} + p_{\rm mc}\right) \frac{k^2}{a} v_m \,.$$

Einstein (i,j) traceless

$$\xi' = \left(1+\alpha_{\rm T}\right)\eta - aH\left(2+\alpha_{\rm M}\right)\xi + aH\left(\alpha_{\rm M} - \alpha_{\rm T} - \alpha_{\rm H}\right)V_X - \alpha_{\rm H}V_X' - \frac{9a^2\sigma_{\rm m}}{2k^2M_*^2}\,. \quad \text{(B.11)}$$

To simplify this equation a new perturbation $\xi(\tau, \vec{k})$ has been introduced that relates h and η through

$$\xi = \frac{h' + 6\eta'}{2k^2}\,.$$

Einstein (i,j) trace

$$\begin{aligned} Dh'' =& 2\left(\lambda_1 - \lambda_9\right)k^2\eta - \frac{6\alpha_{\rm B}\alpha_{\rm H}k^2\eta'}{Ha} + 2aH\lambda_3 h' - \frac{9\alpha_{\rm K}\delta p_{\rm mc}a^2}{M_*^2} \\ &+ \left(3a^2H^2\lambda_4 - 2\alpha_{\rm H}\alpha_{\rm K}k^2\right)V_X' + 2aHk^2\left(\lambda_{10} + \lambda_5 + 3\frac{H^2a^2}{k^2}\lambda_6\right)V_X\,, \end{aligned} \quad \text{(B.12)}$$

And the equation of the evolution of the scalar perturbations is given by

$$\begin{aligned} &D\left(2-\alpha_{\rm B}\right)V_X'' + \left[\frac{\alpha_{\rm B}\alpha_{\rm H}k^2}{Ha}\left(2-\alpha_{\rm B}\right) + 8Ha\lambda_7\right]V_X' + \left[2k^2\lambda_{11} + 2c_{\rm sN}^2k^2 - 8H^2a^2\lambda_8\right]V_X \\ =&\frac{2k^2}{Ha}\left(c_{\rm sN}^2 + \frac{3(\rho_{\rm mc}+p_{\rm mc})}{H^2M_*^2}\alpha_{\rm H}(1+\alpha_{\rm H})\right)\eta + \frac{2\alpha_{\rm H}k^2}{H^2a^2}\left(2-\alpha_{\rm B}\right)\eta' \\ &+ \frac{3a}{2HM_*^2}\left[2\lambda_2\delta\rho_{\rm mc} - 3\alpha_{\rm B}\left(2-\alpha_{\rm B}\right)\delta p_{\rm mc}\right]\,. \end{aligned} \quad \text{(B.13)}$$

where

$$\begin{aligned} D &= \alpha_{\rm K} + \frac{3}{2}\alpha_{\rm B}^2\,, \\ \lambda_1 &= \alpha_{\rm K}(1+\alpha_{\rm T}) - 3\alpha_{\rm B}(\alpha_{\rm M} - \alpha_{\rm T})\,, \\ \lambda_2 &= -\frac{3(\rho_{\rm mc}+p_{\rm mc})}{H^2M_*^2} - (2-\alpha_{\rm B})\frac{H'}{aH^2} + \frac{\alpha_{\rm B}'}{aH}\,, \\ \lambda_3 &= -\frac{1}{2}(2+\alpha_{\rm M})D - \frac{3}{4}\alpha_{\rm B}\lambda_2\,, \\ \lambda_4 &= \alpha_{\rm K}\lambda_2 - \frac{2\alpha_{\rm K}\alpha_{\rm B}' - \alpha_{\rm B}\alpha_{\rm K}'}{aH}\,, \\ \lambda_5 &= \frac{3}{2}\alpha_{\rm B}^2(1+\alpha_{\rm T}) + (D+3\alpha_{\rm B})(\alpha_{\rm M} - \alpha_{\rm T}) + \frac{3}{2}\alpha_{\rm B}\lambda_2\,, \end{aligned}$$

$$
\begin{aligned}
\lambda_6 &= \left(1-\frac{3\alpha_{\rm B}H'}{\alpha_{\rm K}aH^2}\right)\frac{\alpha_{\rm K}\lambda_2}{2}-\frac{DH'}{aH^2}\left(2+\alpha_{\rm M}+\frac{H''}{aHH'}\right)-\frac{2\alpha_{\rm K}\alpha_{\rm B}'-\alpha_{\rm B}\alpha_{\rm K}'}{2aH}-\frac{3\alpha_{\rm K}p_{\rm mc}'}{2aH^3M_*^2}\,,\\
\lambda_7 &= \frac{D}{8}\left(2-\alpha_{\rm B}\right)\left(4+\alpha_{\rm M}+\frac{2H'}{aH^2}+\frac{D'}{aHD}\right)+\frac{D}{8}\lambda_2\,,\\
\lambda_8 &= -\frac{\lambda_2}{8}\left(D-3\lambda_2+\frac{3\alpha_{\rm B}'}{aH}\right)+\frac{1}{8}(2-\alpha_{\rm B})\left[(3\lambda_2-D)\frac{H'}{aH^2}-\frac{9\alpha_{\rm B}p_{\rm mc}'}{2aH^3M_*^2}\right]\\
&\quad-\frac{D}{8}\left(2-\alpha_{\rm B}\right)\left[4+\alpha_{\rm M}+\frac{2H'}{aH^2}+\frac{D'}{aHD}\right]\,,\\
\lambda_9 &= 3\left[\alpha_{\rm B}\alpha_{\rm H}\left(1+\alpha_{\rm M}\right)+\frac{\alpha_{\rm B}\alpha_{\rm H}'}{aH}\right]\,,\\
\lambda_{10} &= \lambda_9+3\alpha_{\rm B}\alpha_{\rm H}\frac{H'}{aH^2}-\alpha_{\rm H}\alpha_{\rm K}\,,\\
\lambda_{11} &= \alpha_{\rm H}\left[\frac{1}{2}(2-\alpha_{\rm B})\left(\alpha_{\rm B}+\frac{2H'}{aH^2}\right)+\frac{3(\rho_{\rm mc}+p_{\rm mc})}{H^2M_*^2}(1+\alpha_{\rm H})\right]\,,\\
c_{\rm sN}^2 &= \frac{1}{2}(2-\alpha_{\rm B})\left[\alpha_{\rm B}+2\alpha_{\rm H}+2\alpha_{\rm M}(1+\alpha_{\rm H})-(2-\alpha_{\rm B})\alpha_{\rm T}+\frac{2\alpha_{\rm H}'}{aH}-2\frac{(1+\alpha_{\rm H})H'}{aH^2}\right]\\
&\quad+\frac{(1+\alpha_{\rm H})\alpha_{\rm B}'}{aH}-\frac{3(\rho_{\rm mc}+p_{\rm mc})}{H^2M_*^2}(1+\alpha_{\rm H})^2\,,
\end{aligned}
$$

where $c_{\rm sN}^2$ is the numerator of the speed of sound of the scalar,

$$c_s^2=\frac{c_{\rm sN}^2}{D}\,.$$

To include the effects of beyond Horndeski theories, we added the terms involving $\alpha_{\rm H}$, λ_9, λ_{10} and λ_{11} to the speed of sound of the scalar and perturbation equations and the F_i and their derivatives to the definitions of the scalar density and pressure and the α_i in `hi_class`.

For now we have only included two parametrisations for this model in `hi_class`, one where the evolution of α_i is given by the evolution of the DE density parameter $\Omega_{\rm DE}$ and and one where they are proportional to the scale factor,

$$\alpha_i=\left(1-\Omega_{\rm m}\right)\hat{\alpha}_i\,, \tag{B.14}$$

$$\alpha_i=a\,\hat{\alpha}_i\,. \tag{B.15}$$

For both of these you need to set or vary the initial set $\{\hat{\alpha}_{\rm K},\hat{\alpha}_{\rm B},\hat{\alpha}_{\rm M},\hat{\alpha}_{\rm T},\hat{\alpha}_{\rm H}\}$. For the first one we have also added the option to have the value of $\alpha_{\rm K}$ computed using Eq. (4.18). In this case the initial set of parameters you need to specify is $\{\hat{\alpha}_{\rm B},\hat{\alpha}_{\rm M},\hat{\alpha}_{\rm T},\hat{\alpha}_{\rm H}\}$.

Appendix C

Dynamical friction from scalar dark matter

In this Appendix we discuss how we validate our code results, and provide some additional details on the fixed metric background used.

C.1 Code validation

In this Appendix we discuss how we validate our code results, and provide some additional details on the fixed metric background used.

C.1.1 Code validation and coordinate choice

As discussed in the main text, we evolve the field on a fixed background metric in boosted isotropic Schwarzschild coordinates.

The metric is validated by checking that the numerically calculated Hamiltonian and momentum constraints converge to zero with increasing resolution, as do the time derivatives of the metric components, i.e. $\partial_t \gamma_{ij} = \partial_t K_{ij} = 0$ (calculated using the ADM expressions). This ensures that (ignoring the backreaction) the metric that is implemented is indeed stationary in the chosen gauge, consistent with it being fixed over the field evolution.

The advantage of using isotropic coordinates is that the asymptotic behavior is appropriate for measuring an approximate ADM momentum for the system at large r, due to the rate at which the quantities approach flat Minkowski spacetime asymptotically. The

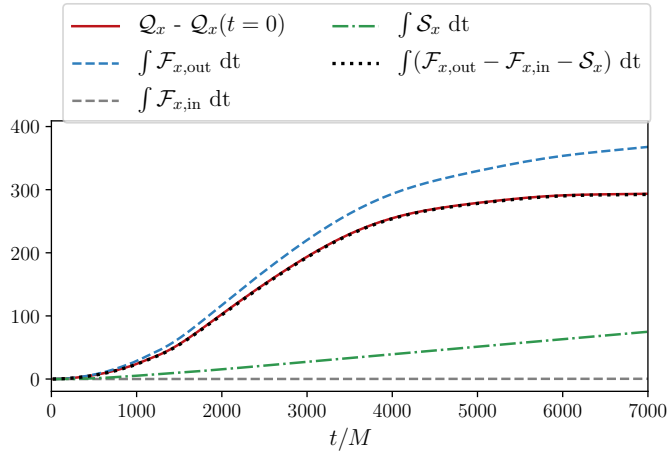


Figure C.1: Agreement between the time-integrated quantities defined in Eq. (C.2). The grey and blue dashed lines show the momentum flux through the inner and outer extraction surfaces, respectively, the green dash-dotted line is the "source" within the volume between those two surfaces, the red solid line is the momentum density in the x-direction and the black dotted line is the RHS of Eq. (C.2). We see that the momentum of the cloud settles into a roughly stationary value at around $t \sim 5000$ and that there is good agreement between the surface flux and volume integrals.

downside is that since the time coordinate corresponds to that of the asymptotic observers, the lapse goes to zero and time freezes around the horizon.[1] This means that any ingoing waves tend to "bunch up" there. Given sufficient resolution outside the outer horizon, the ingoing nature of the metric prevents the errors this introduces from propagating into the region far from the BH, and unresolved waves are effectively damped away by grid precision close to the horizon. Provided we are not interested in extracting quantities very close to the horizon, these coordinates work in practice, as shown below by the conservation of the flux and volume integrals shown in Fig. C.1, where we confirm the expected relation (see [365])

$$\partial_t \left(\int_\Sigma \mathrm{d}^3x \sqrt{\gamma}\ \mathcal{Q}_i \right) = - \int_{\partial\Sigma_{\mathrm{out}}} \mathrm{d}^2x \sqrt{\sigma}\ \mathcal{F}_i \tag{C.1}$$

$$+ \int_{\partial\Sigma_{\mathrm{in}}} \mathrm{d}^2x \sqrt{\sigma}\ \mathcal{F}_i + \int_\Sigma \mathrm{d}^3x \sqrt{\gamma}\ \mathcal{S}_i\,, \tag{C.2}$$

where we define $\partial\Sigma_{\mathrm{in}}$ to be the 2D surface cutting out the three-dimensional volume around the BH Σ_{in} (at r_{in}), $\partial\Sigma_{\mathrm{out}}$ – the 2D surface enclosing the volume of influence on the BH Σ_{out} (at r_{out}), and $\Sigma = \Sigma_{\mathrm{out}} - \Sigma_{\mathrm{in}}$. The "charge" $\mathcal{Q}_i$ is the momentum density in the i

[1] The implementation of these coordinates is improved by the use of an analytic continuation of the lapse in which its value becomes negative within the horizon, as described in [345].

direction defined by the coordinate basis vector $\zeta^\mu = \delta^\mu_i$, i.e.,

$$\mathcal{Q}_i = n_\mu \zeta^\nu T^\mu_\nu = -\alpha T^0_i = -S_i \,, \tag{C.3}$$

the "flux" $\mathcal{F}$ is the i-stress in the normal direction (aka the i-momentum flux out of the closed surface $\partial\Sigma$)

$$\mathcal{F}_i = \alpha N_j J^j_i = \alpha N_j T^j_i = N_j(\alpha\gamma^{jk} S_{ik} - \beta^j S_i) \,, \tag{C.4}$$

and the reconcilling "source" term $\mathcal{S}$ is

$$\mathcal{S}_i = \alpha T^\mu_\nu \nabla_\mu \zeta^\nu = \alpha T^\mu_\nu \ {}^{(4)}\Gamma^\nu_{\mu i} \tag{C.5}$$

$$= -\rho\partial_i\alpha + S_j\partial_i\beta^j + \alpha S^k_j \ {}^{(3)}\Gamma^j_{ik} \,. \tag{C.6}$$

Here N_i is defined to be in the direction of the covector $s_i = \partial_i r$ (so $s_i = x^i/r$ in Cartesian coordinates) and it is normalised such that $\gamma_{ij}N^iN^j = 1$, whilst $n_\mu = (-\alpha, 0, 0, 0)$ is the normal to the ADM spatial hypersurfaces.

C.1.2 Convergence testing and error estimation

We have performed convergence tests for each of the masses considered at $v = 0.3$ and $v = 0.8$. For each of these we have computed our results at three resolutions, Δ_1, Δ_2 and Δ_3. For the cases $\mu = 0.05$, 0.2 and 0.5, the high resolution, Δ_1 is for $N_x = 256$, the medium resolution Δ_2 (that we run all our simulations at) corresponds to $N_x = 128$, and the low resolution corresponds to $N_x = 64$. On the top of Fig. C.2 we show as an example the evolution of the force for the three resolutions from one of our simulations. The low resolution case is slightly more noisy than the medium and high resolution cases, but they are consistent and the difference is well within our error bars, the measurement of which is illustrated with the grey dot-dashed lines. These error bars from the oscillation of the force are the ones presented in Sec. 5.4.

The convergence factor is defined as the ratio of the relative differences between the

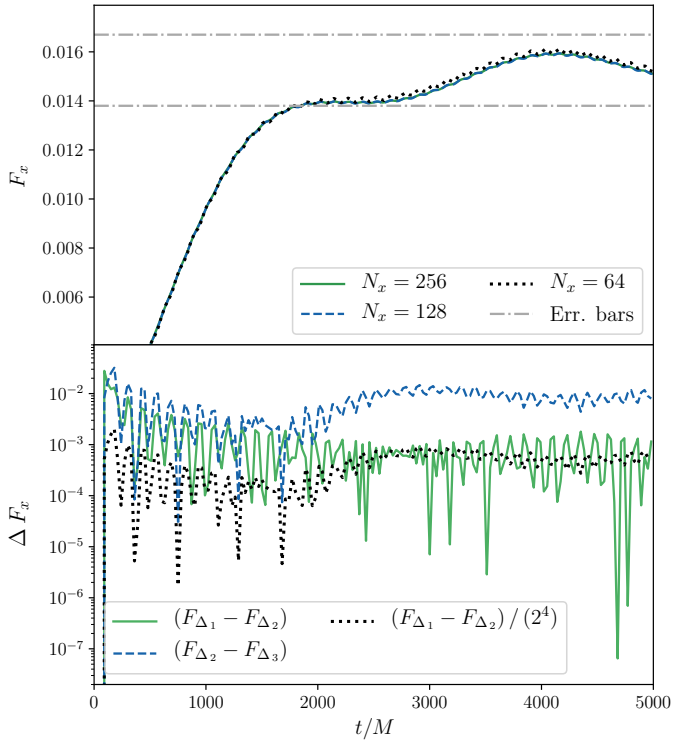


Figure C.2: Top panel: evolution of the force extracted from the simulations for $\mu = 0.05$ and $v = 0.3$ at three different resolutions. We show the the high resolution case ($N_x = 256$, solid green line), the medium resolution used for our results ($N_x = 128$, dashed blue line), and low resolution case ($N_x = 64$, dotted black). The grey dash-dotted lines show how we extract the error bars (in Fig. 5.7) from this simulation. Bottom panel: relative difference between the solutions at the high/low resolutions and the medium one in solid green and dashed blue, respectively. We also show the difference in the solutions between the low and medium resolutions divided by a convergence factor of 2^4, showing that we achieve fourth-order convergence.

solution at the medium and the low/high resolutions,

$$c(t) = \frac{||F_{\Delta_1} - F_{\Delta_2}||}{||F_{\Delta_2} - F_{\Delta_3}||}\,. \tag{C.7}$$

In the case where the three resolutions we have considered have number of grid points $N_x = (64, 128, 256)$ (so that $\Delta_1/\Delta_2 = \Delta_2/\Delta_3 = 2$), in the limit $\Delta \to 0$ the convergence factor is expected to behave as,

$$\lim_{\Delta \to 0} c(t) = 2^n\,, \tag{C.8}$$

where n is the order of the finite difference scheme used to evolve our initial configuration. We have $n = 4$, so that the expected convergence factor is $c(t) = 2^4$. We show the results of this test in the bottom panel of Fig. C.2, where the green solid line shows the difference

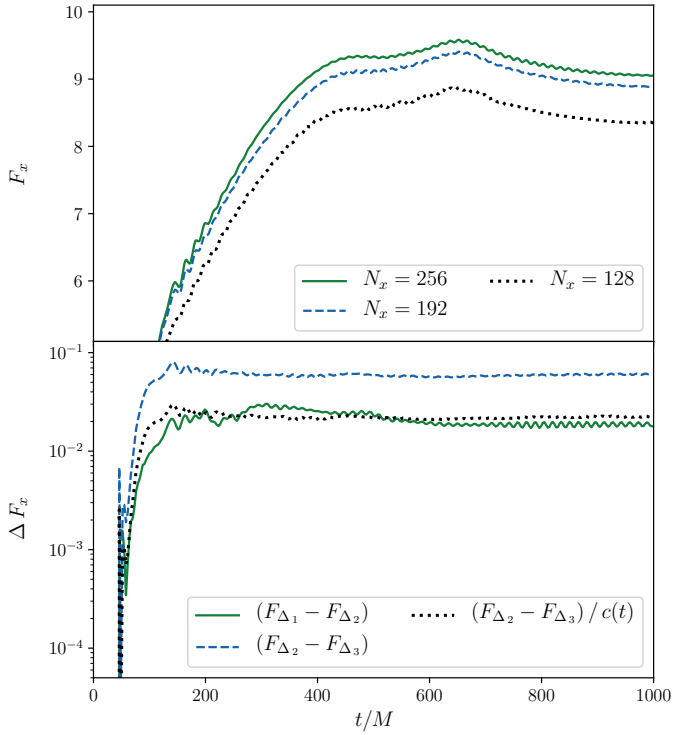


Figure C.3: The top panel shows the evolution of the force extracted from the simulations for $\mu = 1$ and $v = 0.8$ at three different resolutions, where the green solid line shows the high resolution case ($N_x = 256$), the dashed blue line is ($N_x = 192$) and the black dotted - the resolution we run all our simulations on ($N_x = 128$). The bottom panel shows the relative differences in the force between Δ_1 and Δ_2 resolutions - solid green line, and Δ_2 and Δ_3 - dashed blue line. The dotted black line is the difference in the solution between Δ_2 and Δ_3 resolutions divided by the convergence factor $c(t)$, as calculated by Eq. (C.9), showing fourth-order convergence.

in the solutions for the low and medium resolution cases, and the red dashed line is the difference between the high and medium resolution values of the force. The blue dot-dashed line, showing the the difference between the high and medium resolution cases divided by the expected convergence factor for this case, 2^4, lies on top of the solid green line, showing that indeed we get fourth-order convergence for the simulation.

The case of ($\mu = 1$, $v = 0.8$) was the most challenging from the set of simulations presented. The evolution of the force, F_x, extracted from this simulation is shown on the top panel of Fig. C.3. In this case the low resolution, $N_x = 64$, was found to be outside of the convergence regime, so instead we calculated the force at resolutions $N_x = (128, 196, 256)$. For this set of resolutions we no longer have $\Delta_1/\Delta_2 = \Delta_2/\Delta_3 = 2$ and the

convergence factor in the continuum limit is given by

$$\lim_{\Delta\to 0} c(t) = \frac{\Delta_1^n - \Delta_2^n}{\Delta_2^n - \Delta_3^n} \sim 2.7\,, \tag{C.9}$$

for $N_x = 128, 196, 256$ and $L = 1024$, so that $\Delta_1 = 0.25$, $\Delta_2 = 0.1875$ and $\Delta_3 = 0.125$, and $n = 4$. The bottom panel of Fig. C.3 shows that in this case we still achieve fourth-order convergence, with the low resolution now being $N_x = 128$.

Although we confirm that the results are converging with resolution in the expected way, the resolution errors are comparable with those computed from the oscillations. We can estimate the error on the solution at the highest resolution grid using the relation

$$\epsilon_{\Delta_1} \sim \frac{1}{(\Delta_1/\Delta_2)^n - 1}(F_{\Delta_1} - F_{\Delta_2}) \sim 0.08\,. \tag{C.10}$$

We apply this error to the highest resolution result. Note that if we were to use the lowest resolution for our results ($N_x = 128$) the error would have been larger, $\epsilon_{\Delta_3} \sim 0.7$ (around 9%). Similarly we have checked the error on the results at $N_x = 128$ for $v = 0.7$ (as that is expected to be lower) and we find that to be around 5%. We also use this error as a conservative estimate of the resolution error in the extracted force from the simulations of $v = 0.5, 0.6$, $\alpha_{\rm s} = 1$, using it to increase the error bars presented. In a few other cases, we also identify and add convergence errors to the error bars in a similar way, but these are much less significant.

C.2 Large and small β approximations

As discussed in Sec. 5.3, the analytic approximation for the dynamical friction force on a BH from a scalar cloud (for a BH moving at nonrelativistic velocities), given in Eq. (5.31), depends on the digamma function $\Psi(1+i\beta)$. Although Ψ can be evaluated and plotted with many computational packages such as Mathematica or Python, its shape is not immediately obvious, so it is useful to look at its approximate form in terms of $\beta = \alpha_{\rm s}/v$. This can be done in the two regimes, where β is either very small or very large:

$$\Re\left[\Psi(1+i\beta)\right] \sim -0.577 + 1.202\beta^2 \quad (\beta \to 0)\,, \tag{C.11}$$

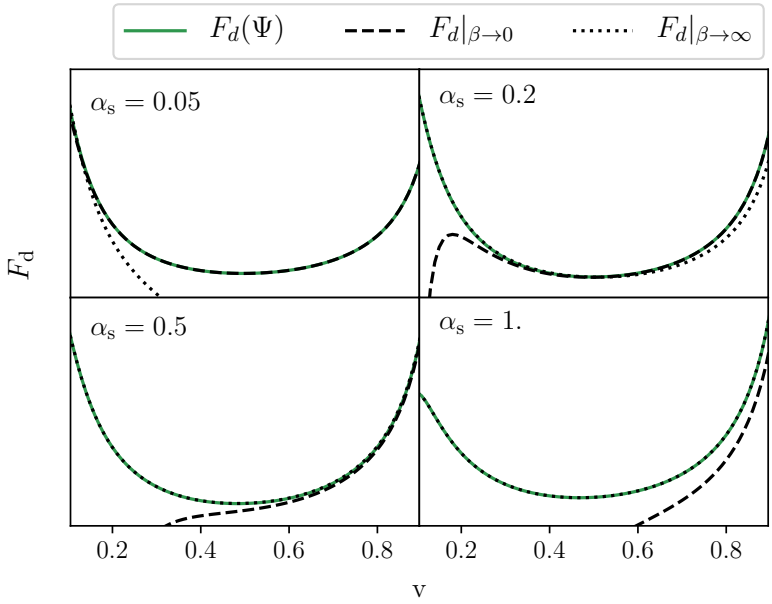


Figure C.4: The expressions in Eqs. (5.31)–(5.33) as a function of the relative velocity v of the BH with respect to the scalar field, for the four values of α_s that we simulate. The solid green lines show the exact expression in terms of the digamma function, while the dashed and dotted black lines correspond to the small-β and large-β approximations, respectively.

$$\Re\left[\Psi(1+i\beta)\right] \sim \ln\beta - \frac{1}{12\beta^2} \quad (\beta\to\infty)\,, \tag{C.12}$$

which leads to the approximate expressions in Eqs. (5.32) and (5.33).

To illustrate the range of validity of these approximate expressions, in Fig. C.4 we plot the scaling of the force F_d with velocity, given the exact expression containing the digamma function and the two approximations for small and large β. As expected for the case of $\alpha_s = 0.05$ (top left) the valid expression is the $\beta \to 0$ approximation. At large masses of the scalar, $\alpha_s = 0.5$ and 1, the solutions for $\beta \to \infty$ match the exact solution very well. In the intermediate-mass case ($\alpha_s = 0.2$), both expression match the exact solution in the range $v \sim 0.4 - 0.5$, but the small-β approximation fails at small velocities and the large-β approximation is inaccurate at large v.

C.3 Real scalar field

A uniform real scalar field has a density that oscillates with a frequency related to its mass. This gives rise to a dynamical friction force that oscillates between positive and negative values over time. This can make the results more difficult to interpret and lead

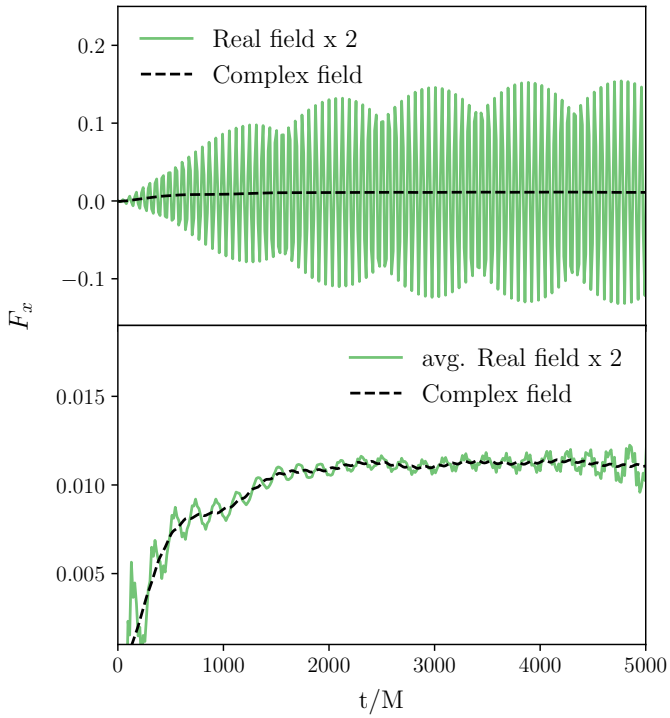


Figure C.5: Time evolution of the force in the case of a real (solid green lines) and complex (dashed black lines) scalar field, showing the agreement between the two cases.

to large error bars on the numerical results. To avoid this issue we have performed all our simulations for a complex scalar field instead, as this can provide an asymptotically constant density that is twice the average of the real field density. To confirm that this is indeed the case, we evolve the real scalar field in the case of $\alpha_{\rm s} = 0.05$ and show that the force in the complex field case is twice the average of that for the real field, as expected.

Fig. C.5 shows the evolution of the force as a function of time for $\alpha_{\rm s} = 0.05$ and $v = 0.5$ in the case of a real scalar field (solid green lines) and the complex one (dashed black lines). In the top panel, the real field force is as extracted from the simulations. As expected for the real field, the force oscillates with very high frequency and amplitude. We confirm that the frequency of the oscillations is related to the mass of the field as $\omega = 2\alpha_{\rm s}$. To confirm that the complex field gives the average of the oscillations in the real case we have removed the high-frequency oscillations using a filtered Fourier transform of the signal, as shown in the bottom panel of Fig. C.5.

We observe that in the case of a purely real field, the dynamical friction force oscillates rapidly in time. Whilst the average effect over time would be consistent with the complex

case, it should in principle be possible to observe the impact of the higher frequency oscillations on the trajectory of the perturber.